MODELLING OF THE THERMAL EVOLUTION OF STEEL STRIPS COOLED IN THE HOT ROLLING RUNOUT TABLE

by

VICTOR HUGO HERNANDEZ-AVILA

B. Sc., The National University of Mexico, 1988
M. A. Sc., The University of British Columbia, 1994

A THESIS SUBMITTED IN PARTIAL FULFILLMENT OF
THE REQUIREMENTS FOR THE DEGREE OF
DOCTOR OF PHILOSOPHY

in

THE FACULTY OF GRADUATE STUDIES
Department of Metals and Materials Engineering

We accept this thesis as conforming to the required standard

THE UNIVERSITY OF BRITISH COLUMBIA

September, 1999

In presenting this thesis in partial fulfilment of the requirements for an advanced degree at the University of British Columbia, I agree that the Library shall make it freely available for reference and study. I further agree that permission for extensive copying of this thesis for scholarly purposes may be granted by the head of my department or by his or her representatives. It is understood that copying or publication of this thesis for financial gain shall not be allowed without my written permission.

Department of Metals and Materials Eng.

The University of British Columbia
Vancouver, Canada

Date October 4, 2000

DE-6 (2/88)

ABSTRACT

The controlled cooling of steel on the runout table has become a standard practice in the production of flat hot-rolled products, and since its introduction by BISRA in 1957, has been adopted because it is a vital tool in meeting the increasing demand of steels with better quality and higher mechanical properties.

Although approximately one third of the total steel produced in the world is cooled using laminar cooling in the runout table with some degree of success, little is known about what actually happens during cooling. Even though many of the runout table operations are relatively under control, it is still not known how far these operations are from the optimum. Whereas the influence of steel chemistry has been traditionally exploited to accomplish certain mechanical properties, the recently recognized effect of cooling on mechanical properties has been exploited poorly. This increases the importance of the study of the runout table cooling.

The runout table process has been studied in detail during this work, and important observations leading to a better understanding of this operation were obtained. A mathematical model for the runout table cooling was developed, which solves the transient 1-D heat transfer in a steel strip moving through the cooling units in the runout table. The model takes into account the individual fluid flow characteristics of each jet such as its velocity, diameter, temperature, and the geometry of the nozzle arrays, and relates them to other process variables, such as strip speed, chemistry, and thickness, to predict the thermal evolution of the steel. The model was validated by comparing the predictions of the model for the processing of two plain carbon steels, A36 and DQSK,

with measurements in ten different runout table operations. Very good agreement with measurements was obtained. The boundary conditions were obtained by the mathematical modelling of the boiling curves during water jet cooling based on the application of the macrolayer evaporation mechanism, which lead to accurate predictions of the boiling curves, which compare very well with most of the reported measurements in the literature.

Table of Contents

List of Tables

List of Figures

List of Symbols

a = acceleration

A = Area, amplite of the liquid - vapor interface

A_1 = Air cooling parameter

A_i, B_i, D_i = Finite differences parameter

b_i = Avrami parameter for the transformation to the i - microconstituent

Bi = Biot number

c = Carbon concentration, constant

c^o = Steel average carbon concentration

c_* = Critical carbon concentration

c_I = γ - intefacial carbon concentration

c_P = Carbon solubility in austenite

C = Free - stream velocity gradient near stagnation line

$\overline{C}$ = Dimensionless velocity gradient = $w_j C / u_j$

$C_p = c_p$ = Heat capacity

C_{ps}= Heat capacity of steel

d = free - surface circular jet diameter

D = Shape factor

D= Jet diameter

D_C = Carbon diffusion coefficient

d_j = Distance to jet centerline

d_{jetlin} = Distance between jet lines

DX = Nucleate boiling exponent

d_α = Ferrite grain size

d_γ = Austenite grain size

E = Elastic modulus

f = Contact length

$F = A_{l-s} / A_{tot} \approx t_{l-s} / t_{tot}$, Fraction transformed

Fo = Fourier number

g = Gravity acceleration

g= Heat generation per unit volume

g_i = heat generation / volume

h = Heat - transfer coefficient, height

h_0= Heat transfer coefficient at $y=0$

h_{LS}= Heat transfer coefficient at $y=L_S$

Gr = Grashof number

H = Sensible latent heat ratio, $\frac{C_p \Delta T}{h_{fg}}$, in the film boiling model

$H_{fg} = h_{fg}$ = Latent heat of evaporation

h_l = Liquid film thickness

H_n = Nozzle height

H_i = Volumetric heat of transformation

H_t = Volumetric heat of transformation

h_v = Vapor film thickness

k = Steel thermal conductivity, thermal conductivity

k_f = Thermal conductivity of water

k_r = Equivalent thermal conductivity in the radial direction

l = Length

l_c = Characteristic length

L = Characteristic length, Macrolayer length, length

L_B = Vapor bubble length

L_c = Coil length

L_R = Distance between rolls

L_S = Strip thickness

m = Falkner - Skan power law exponent = $\theta/(\pi-\theta)$

$m_{lp} = m_{e,lp}$ = Triple - point evaporation - rate parameter

N = Number of nucleation sites

n_i = Avrami equation exponent for the i - transformation

Nu = Nusselt number

Nu_x = Nusselt number , $h_{conv} x_j / k_f$, hx/k_{air} in forced convection in air

Nu_x = Local Nusselt number, hx/k_v, in FB model

$\overline{P}$ = dimensionless pressure = $(P - P_\infty) / (1/2)\rho_l u_\infty^2$

P = Static pressure

Pe = Peclet number

Pr = Prandtl number

q = Heat flux

Q = Volumetric flow rate

r = Air cooling parameter, radial position

r = Position

R = Radius of a grown phase

R =Density/viscosity ratio,= $\rho\mu / \rho_f \mu_f$

smp = Sample

r_o = Finite differences parameter

Re_x = Reynolds number $u_j x_j / \nu$, $u_x x / \nu$, $u_p x / \nu$ for forced convection in air

$\mathrm{Re}_x = U_e x / \upsilon_l$ =Reynolds number in FB model

R_s = Stem radius

T = Temperature

t = Time

T_N = End of Nucleation Temperature

T_{start} = Transformation start temperature

t_v = Virtual time

$T0(y)$= Initial temperature profile in the steel

u = velocity, x - component of the velocity vector

U = Velocity

U =x-component of the velocity vector in the FB model

$\overline{u} = u / u_j$

U_e = Free stream velocity in the FB model

U_i =Interfacial velocity in FB model

U_i^* =Dimensionless interfacial velocity= $U_i^* = U_i / U_e$ in FB model

U_{me} = Water velocity at the entrance of the microlayer

u_j = Velocity of the impinging jet

U_l = Bulk flow liquid horizontal velocity

$U_p = u_p$ = Plate velocity

U_p^* =Dimensionless plate velocity, $= \dfrac{\Omega U_p}{U_e U_i^*}$

$U_{p_\varepsilon}^*$ =Dimensionless plate velocity, $= \dfrac{\Omega U_p}{U_\varepsilon U_i^*}$

U_{p_0} = Initial strip velocity

$\overline{u}_s = u_s / u_j$

U_v = Bulk flow vapor horizontal velocity

U_y = y - component of the water velocity

u_∞ = x component of free - stream velocity

$\overline{u}_\infty$ = Velocity ratio u_∞ / u_j

v = y - component o the velocity vector

w = Width, interaction factor

$w_j = w_{jet}$ = Width of the impinging jet

x = Position, distance from the jet centerline along the length of the strip

x, y =Boundary Layer coordinates, x in the direction of the flow, y perpendicular to the surface

x_i = Contact time ratio, t_i / t_{tot}

$\bar{x}$ = Dimensionless position = x_j / w_j

x_j = streamwise position measured from the stagnation plane

x_* = Value for $\bar{x}$ where $\overline{P} = 0$

y = normal coordinate to the surface

z = Coordinate in the direction of the width of the strip

α = Thermal diffusivity

δ = Vapor film thickness

Δ =Viscous boundary-layer thickness of liquid

Δ_o =Initial viscous boundary-layer thickness of liquid

Δ_t =Thermal boundary-layer thickness of liquid

Δ_{to} =Initial thermal boundary-layer thickness of liquid

ΔH_{sub} = Sensible enthalpy at actual temperature

Δt = Time step

ΔT =Degree of superheating, $= T_w - T_i$ in FB model

ΔT_l = Degree of subcooling,= $T_i - T_e$ in FB model

ΔT_s = Wall superheat, $T_s - T_{sat}$

ΔT_{sub} = Water subcooling, $T_{sat} - T_l$

ΔT^*_{sat} = Dimensionless wall superheat

Δx = Finite differences position step

ε = Emissivity

$\varsigma = \Delta / \Delta_t$

$\xi = \varsigma; \varsigma^*$ = Boundary-layer thickness ratio=, $\varsigma^* = \varsigma / \sqrt{\mathrm{Pr}_f}$

η, η_t =Similarity variables, $\eta = (y - \delta) / \Delta$, $\eta_t = (y - \delta) / \Delta_t$

η = displacement

$\eta = y(u / vx)^{1/2}$ *in Figure 2.3*

φ= Cooling rate

Γ =Parameter associated with the degree of subcooling,$=\left(\mathrm{Pr}/\ \mathrm{Pr}_f\right)\left(C_{p_f}\Delta T_f\ /\ C_p \Delta T\right)$

Λ =Shape factor for velocity profile in a vapor layer=$\dfrac{m}{2}\dfrac{\rho_f}{\mu}\dfrac{U_e^2\delta^2}{U_i x}$

λ = Vapor - liquid interface wavelength

μ = Viscosity

ν = water kinematic viscosity

$v_{\alpha,\beta}$ = Critical velocity of the α - γ interface for cementite nucleation

v_{∞} = y component of free - stream velocity

Ω=1 when jet velocity is in the direction of the strip motion, -1 when viceversa

ρ = Density

ρ_l = Water density

ρ_s = Steel density

σ = Surface tension, Stefan - Boltzmann constant, stress

σ_s = Stefan - Boltzmann constant

τ = Shear stress

$2\pi / \omega$ = Wave length

Ψ= Heat conducted through the liquid/total heat extracted from the surface in FB

Subscripts and superscripts:

a, b = Values at $r = r_a$ and $r = r_b$, respectively

across = Across the width of the strip

air = Enviromental medium

cond = Conduction

conv = convective

counter = Countercurrent flow

e = Evaporation, free stream

e =Boundary-layer edge

eq = Equilibrium

f = fluid, water

FB = Film boiling

i = Finite differences position or index, micro - constituent, index

i =liquid/vapor interface

imp = Impingement

j = Impinging jet

jet = Impinging jet

l = Liquid

L_1, L_2 = Hollow roll thickness, strip thickness

L_s = Strip thickness

$l - s$ = Liquid - solid contact

m = Minimum, at the minimum heat flux

$NB = FNB$ = nucleate boiling

n = Value at the nozzle, finite differences time step

noz = Nozzle

p = plate, strip, pearlite

per = Pearlite

pg = Pressure gradient zone

r, ϕ, z = Directions

rad = Radiation

ref = Reference

s = Surface, steel

sat = saturation

t = Total, time

TB = Transition boiling

tp = Triple - point

tot = statistical suficient quantity at a point on a surface

$w = wat$ = Water

w =Wall in FB model

x, y, z = Coordinates

α = Ferrite

ε =At x= ε in FB model

γ = Austenite

v = vapor

$v - s$ = Vapor - solid contact

x, y, z = Coordinates

∞ = free stream

0 = Initial value, value at $x = 0$, value at $t = 0$, nominal

o = Initial value in FB model

$1,2$ = Domain, 1 = roll, 2 = strip

Acknowledgements

I would like to express my sincere gratitude to the late Professor J. K. Brimacombe and Professor I. V. Samarasekera for their patience, supervision and guidance, and the opportunity to be part of such an interesting and challenging research project. Also the valuable discussions and encouragement from Professors E. B. Hawbolt and T. R. Meadowcroft was greatly appreciated.

Also I would like to thank Professor José Antonio Barrera Godínez, Professor Fidel Reyes Carmona, and Professor Bernardo Hernández Morales of the National University of Mexico for the encouragement and friendship during the course of my studies. The support from Dr. Jesús Guzmán was also greatly appreciated.

This work was only possible by the contribution of many people. I would like to acknowledge the contribution of Dr. D. Jin for the debugging of the computer code, Prof. M. Militzer and R. Pandi for the phase transformation model. My gratitude also to all who contribute with plant information, in particular P. E. Repas (USS Steel), S. L. Feldbauer and L. Clinger (Geneva Steel), K. R. Barnes and David E. Overby (Stelco), L. Collins (Ipsco), B. D. Nelson (Dofasco), O. Lanzi (Inland), E. G. Hamburg (Lukens), J. E. Hartmann and M. J. Crooks (LTV), D. Bosch and S. Denner (National), J. Ives (Timken), D. Aichbhaumik (Weirton).

The financial assistance of the American Iron and Steel Institute and the National University of Mexico was greatly appreciated during the course of this work.

At last, but not least, I thank all my friends in UBC for their friendship in particular C. A. Muojekwu, B. Hernández-Morales, U. Wankhede, Denisa Ionescu, R. Pandi and Anabel Thomas.

Dedication

There is always a driving force behind any motion and any creation. This work is dedicated to the driving force of my life, my wife Patricia, whose incredible beauty, encouragement and greatness is the inspiration and greater contributor to this work, and who certainly deserves to be co-author. Also I dedicate this to my son Andre and daughter Natasha, whose energy and motion is a good example of boiling... they are so incredible.

This work is also dedicated to Jehovah God, the creator of the whole universe, the greatest engineer, who permitted me to be here to try to discover a microscopic part of the greatness of his creation. He is the inspiration of my entire life and source of blessings for me and my family.

Finally I dedicate this work to all our family members: my mother Ma. Elena, and father Gabino, and mother in-law Amelia, Rosario, Tziran, Federico, Claudia, Gabino Gloria, Maricarmen, Luis y Edith and their children. Also to our spiritual family, in particular Marty, Eunice, Rebekah, Lisa, Diana, Kelly and Scott whose encouragement and good example made very enjoyable to be away from home, and to all those in the Grandview and McDonald Halls.

1. INTRODUCTION

Approximately 700 million metric tons of steel are produced in the world every year, and around 200 million of them are hot rolled to flat products with gauges from 2mm to 25mm. These flat rolled products are used in a wide variety of applications ranging from construction, hydrocarbons transport, automotive applications, household appliances, etc. The controlled cooling of steel is common practice in the production of such products.

The controlled cooling on the runout table of a hot strip mill is accomplished by supplying water to the top and bottom surfaces of the strip, using water jets issuing from circular nozzles (bars) or rectangular narrow nozzles (curtains). These kinds of cooling systems are often called laminar cooling because of the streamlined appearance of the jets, but they are not necessarily in laminar flow as defined by fluid mechanics.

Laminar cooling (jet cooling) is adopted because of the high rates of heat extraction that can be attained, which lowers the austenite decomposition temperature, leading to a smaller ferrite grain. Finer ferrite grains are obtained as a consequence of the increased ferrite nuclei rate at lower temperatures during the austenite decomposition.

A fine ferrite grain size increases both the yield and tensile strength of the steel, and improves the toughness. This reduction of the ferrite grain size together with precipitation strengthening from aluminum nitrides in Al-killed low carbon steels, or Nb, Ti, V, carbo-nitrides in HSLA steels can be manipulated to achieve steel with higher strengths even with reduced carbon contents. This considerably improves the weldability

due to the reduced hardenability of the steel and the consequent formation of the tougher equilibrium transformation products, ferrite and pearlite.

The ability of water jet cooling to extract heat from the steel at very large rates is due to the effectiveness of the boiling mechanisms that take place at the typical temperatures of the runout table. Jet boiling heat transfer is probably one of the most efficient mechanisms of cooling known to man to this date, and it is also used in other important applications such as: computer chip production, continuous casting, etc. A comparison of the magnitude of the heat-transfer coefficients for different kinds of flow is shown in Table 1.1 [1].

1.1 Description of the Hot Rolling Runout Table

A typical layout of a Hot Strip Mill is presented in Figure 1.1. Following the rolling stands, where deformation takes place, the runout table and the down coiler are the last steps of the hot rolling process.

The runout table is typically made up of, as shown in Figure 1.2, a set of cooling banks placed at the top and bottom of the strip, an array of motorized rolls and a coiler. The strip exits the finishing mill, where the final deformation takes places, and moves to the down coiler where it is coiled for storage or further processing at a velocity which in many operations is constant. The strip moves on hollow rolls, made of low carbon steel, which are placed at appropriate distances to avoid excessive bending of the strip.

The cooling banks consist of headers, or distributor pipes, which supply water to arrays of jet lines from which the water impinges on the steel through rectangular nozzles

creating a water curtain, or through round nozzles which produce water bars, as shown in Figure 1.3. The water is supplied from cooling towers, to large storage tanks located below or above the runout table level. When these tanks are below the runout table, the water is pumped to the headers and then to the jet nozzles, to ensure that the amount of water is sufficient and to maintain the stability of the water flow. When the tanks are above the runout table, water flows by gravity through the different pipes, headers and nozzles, the level of water being maintained constant in the storage tanks to control the amount and stability of the water flow. Once the water has been used for cooling, it is filtered and recycled to the cooling towers. The water usually is supplied at room temperature (18-40°C) through the top and bottom nozzles, with flow rates that are commonly constant for a given mill.

1.2 Laminar Cooling Systems

Before the adoption of laminar cooling, air-water cone sprays were used to cool the steel. However, these were not efficient enough to ensure the cooling rates necessary to attain a small ferrite grain size. The reason might be the fact that cone sprays are more prone to form an isolating vapor film between the water and the strip at the runout table temperatures, mainly because of the discontinuous nature of the flow and the air trapped.

The earliest water jet system consisted of several lines extending along the length of the runout table with arrays of circular bar jets (axisymmetric jets) placed across the width (Figure 1.3). This is probably the most common cooling system because of its intermediate cooling capacity. Water exits the nozzle at velocities typically from 1.0-3.0m/s, its velocity being modified by gravity; in the case of top jets velocities from 5 to

8m/s can be realized, whereas for bottom jets, the nozzles must be placed closer to the strip surface to maintain adequate velocity.

The water jet impinges on the strip surface, as depicted in Figure 1.3[a] and Figure 1.3[b], with a certain amount of momentum, creating a region of highly localized cooling, called hereafter the impingement region. This area is about three times the impinging jet diameter or width, across which a pressure gradient exists. In the case of bar jets, outside the impingement region, the streams of water from neighbor jets interact with each other along the width direction (interaction flow region), creating a region of intermediate cooling between the impingement region and the region where the water flows parallel to the strip motion (parallel flow region); in this region the cooling efficiency is comparatively low. The interaction of the various cooling zones depends on the geometry of the jet array as well as on the strip speed. Intrinsic inhomogeneity of the water flow across the width of the strip can cause inhomogeneous properties, but this effect has been greatly reduced by alternating the pattern of the nozzle array. On the bottom surface, water impinges in a similar fashion, but due to the gravity, the water does not remain in contact, except in a small area. Typically, top surface cooling is more efficient than bottom cooling mainly for this reason. It is noteworthy that the fluid flow patterns are very much affected by the strip motion.

In order to increase the cooling capabilities of the laminar systems, water curtains (planar jets) issuing from slot-type nozzles were developed (Figure 1.3[b]). Although this system provides the most effective cooling and provides homogenous profiles of mechanical properties across the product width, the extremely high cooling attained by it

can result in shape problems during production, such as cobbling or canoeing. As a result, the more rapid system requires a higher degree of control.

1.3 References

1.- M. N. Ozisik, Basic Heat Transfer, 1st Spanish edition, McGraw Hill, 1979, pp.6.
2.- W. L. Roberts, Hot Rolling of Steel, Marcel Dekker, Inc., 1983, p 472.

Table 1.1:Heat Transfer Coefficients for different cooling flows [1]

Kind of Flow	Heat Transfer Coefficient ($W/m^{2o}C$)
Free convection	6-28
Forced turbulent convection in pipes (water)	284-17000
Boiling water	2840-57000
Jet boiling of water	>50000

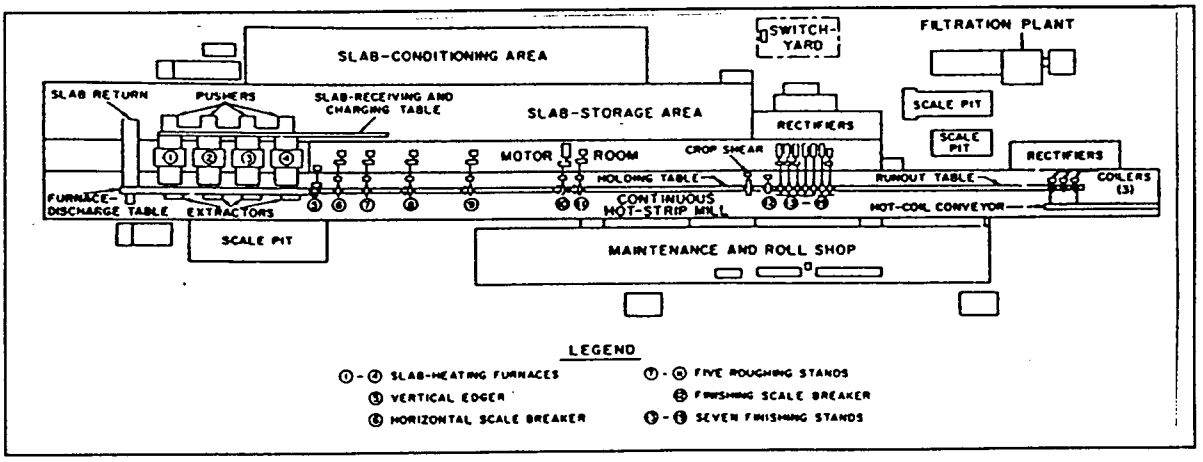

Figure 1.1:Typical Hot Strip Mill. Layout of the 84-inch Continuous Hot-Strip Mill at Gary Works of U.S. Corporation [2]

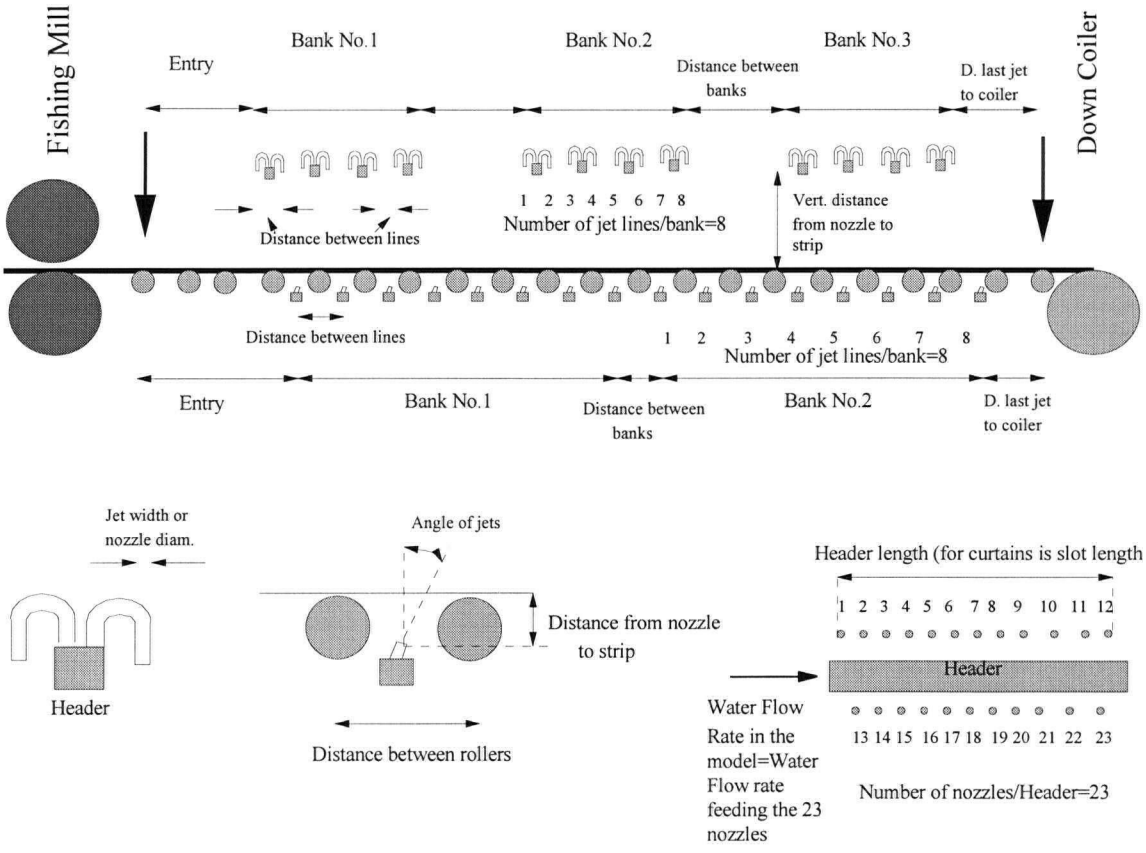

Figure 1.2:Typical Runout Table Setup

[a]

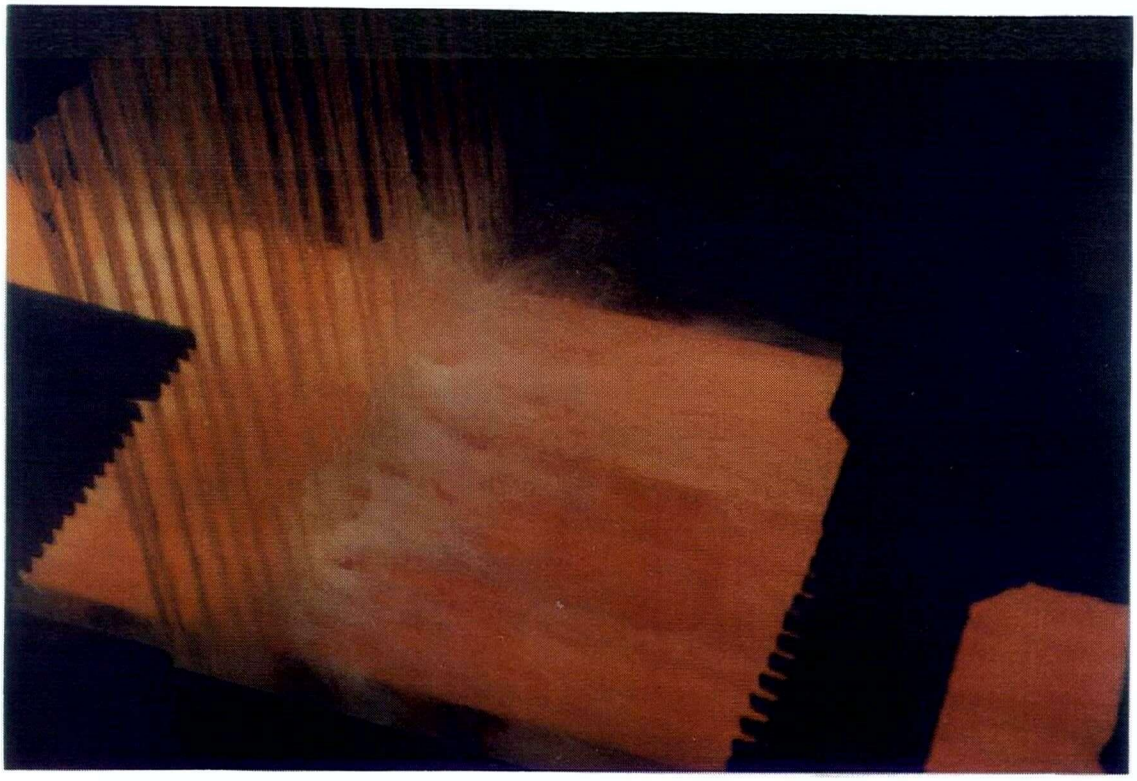

[b]

Figure 1.3:Typical Laminar Cooling Systems. [a] Laminar cooling bars, [b] Laminar water curtains

2. LITERATURE REVIEW

In this chapter, the present knowledge on runout table processing is presented, and some of the several models published in the literature are discussed. Additionally, a review of the fundamentals of heat transfer involved during processing is included.

2.1 Runout Table Models

The increasing need for a quantitative description of the thermal and microstructural events taking place during controlled cooling on the runout table has led to the development of mathematical models. Currently, the main applications of such models are in mill set up to attain a specified coiling temperature [1]; which is linked to the final mechanical properties.

Several mathematical models have been developed to predict the temperature field in the strip during laminar cooling. Most thermal field predictions are based on the solution of the 1-D heat conduction problem by applying specific heat-transfer coefficients (HTC) to the strip surfaces, corresponding to the nature of the cooling in that zone.

The major problem in creating a runout table model is the definition of the local heat flux (HF) during water jet cooling as a function of the most important operating parameters such as water temperature and flow rate, strip velocity, and the local surface temperature. Other parameters of importance are the jet arrangement along the table, and the nozzle shape, dimension, height and angle.

In jet cooling, two main fluid flow zones may be defined:

1.- Parallel flow, with and against the direction of the motion of the strip.

2.- Pressure gradient flow (Impingement zone).

Depending on the jet arrangement, there can be a relatively stagnant zone where two opposing parallel flows meet.

A realistic description of the heat transfer characteristics requires the knowledge of the heat fluxes in each of these flow zones, in terms of the operating parameters previously mentioned. However, such expressions are generally unknown, due to the wide variety of operation conditions, and the complexity of the two-phase heat transfer mechanisms occurring.

Therefore, since an experimental measurement of the heat transfer coefficients during cooling on a runout table is extremely difficult, typically the selection of an appropriate HTC has been obtained by a "fitting" process. In most cases, an "average" heat transfer coefficient is assumed which fits the experimental results [2, 3, 4]. Prasad et al. [4] highlighted the present state of knowledge in this regard by saying that there has not been a serious attempt directed at predicting the heat transfer coefficients. Given the complexity of the problem, the lack of the expressions for the heat transfer coefficients is not surprising.

However, some attempts have been made to characterize the individual jet cooling zones [5, 6, 7, 8 9]. Colas et al. [5] defined a constant heat transfer coefficient in the impingement zone and a different one in the parallel flow zones, but were unable to define a set of values which give good agreement with observations. So they assumed that an isolating oxide layer on the strip surface was responsible for the disagreement. Evans et al. [6]

assumed convection heat transfer on the top and bottom surfaces, regardless of the temperature range of the strip. Filipovic et al. [7] assumed film boiling in the parallel flow zone and unstable nucleate boiling in the impingement zone. Their model was validated using data for only two coils predicting much higher exit temperatures. The discrepancy was believed to be related to heat conduction to the rolls; once this was included, the discrepancy was reduced. Their model [8] was extended to predict the 2-D behavior of the strip during cooling with laminar bars, under the same basic assumptions, except that transition boiling was assumed in the impingement region. The predicted coiling temperature for two coils was within 16°C from the measured coiling temperatures. Guo [9] employed an alternative statistical approach to back calculate the heat-transfer coefficients obtained during the cooling of several coils, and obtained a power-law equation which included parameters such as strip thickness, velocity and temperature, and water flow rate. Process control models have also been developed under similar circumstances[10] .

Although some degree of predictive success was obtained from all these models, the fact is that they disagree fundamentally with the experimental evidence available[11]. Most of these models do not allow the prediction of the effect of specific process variables on the coiling temperature. A constant heat transfer coefficient for each zone is not consistent with the facts, neither do the assumption of forced convection nor film boiling satisfy the cooling conditions observed. Similarly, discrepancies assumed to be due to the formation of an oxide layer on the strip must be tested and validated, and probably its effect is smaller[12]. In addition, conduction to the rolls should be much smaller than

assumed by Filipovic et al. [7] since the heat transfer coefficients during the strip to roll contact are not large enough to consider continuity of the temperature at the interface[13].

With respect to the metallurgical transformations occurring during cooling, some work has been published [2, 3, 4] dealing with the prediction of the kinetics of the austenite decomposition to ferrite and pearlite. Hurkmans et al.[14] developed a model focused on the prediction of the kinetics of the austenite decomposition to ferrite, although the transformation to pearlite, bainite and martensite was also studied. The phase transformation model was based on quantitative dilatometry and was combined with a thermal analysis through the effect of cooling rate on the phase transformation. The steel chemistry included in the study ranged from C(w%)=0.04-0.17 and Mn(w%)=0.220-1.420. The heat transfer coefficients were obtained assuming spray cooling, for which transition boiling is present over the whole range of strip temperatures. Consideration of the effect of cooling conditions on the austenite decomposition to non-polygonal microstructures, such as are found in medium to high carbon steels, has not been included in any of these models.

Hernandez et al.[15,16] developed the first mechanistic model based on the assumption of transition boiling in both the impingement and parallel flow regions, where the entire boiling curve in each of these zones was modelled by assuming the existence of the "macrolayer dryout" mechanism. This boiling mechanism has also been observed experimentaly, even in the parallel flow region during cooling of a non-moving flat plate, as will be discussed later in this work. However, the model did not consider the important effect of the local water temperature increase due to the absorption of the heat released

by the strip as water flows from the jet impingement region. In operation, transition boiling changes to film boiling due to this effect, and the assumption of complete transition boiling with water at room temperature overpredicts the cooling where the parallel flow region is long. Prediction of the austenite decomposition kinetics to ferrite and pearlite was included for low carbon steels. This model constitutes the foundation of the structure of the process model presented in this work.

More recently, the existence of transition boiling as the overall cooling mechanism has been recognized, and has been adopted in on-line control models very successfully[17,18]. These models assume that the cooling of long sections of the runout table, i.e. banks of jets, follow the typical transition boiling behavior of increasing heat extraction when the steel temperature is lower.

However, from the present literature, it is clear that insufficient experimental studies have been made to allow the development of a model that incorporates the fundamental characteristics of the heat transfer processes occurring during runout table cooling. Moreover, the results from most of these models are inconsistent with mill observations and the experience of mill operators.

2.2 Air Cooling

During the cooling on the runout table the steel strip often moves through regions covered by water and dry regions, where air cooling takes place. Air cooling is a small contributor to the overall cooling on the runout table under those circumstances. However, during the production of some thick strips and plates, slow cooling is more desirable and the product is allowed to cool in air exclusively.

Cooling in air has been extensively studied both experimentally and theoretically. Given the extent of the information available, only the equations that are used in this work are presented. In the dry areas where cooling in air takes place, natural, forced and mixed convection heat transfer can occur. Natural convection occurs by the air flow driven by air density variations promoted by the high temperature of the steel in contact with air. Forced convection heat transfer takes place because of the motion of the strip, and mixed convection is the resulting contribution of these two modes of convection heat transfer which always occur. Radiation heat transfer to the environment also takes place.

Radiation heat transfer losses to the ambient have been frequently calculated by means of the following equation[19]:

$$q_{rad} = \varepsilon\sigma(T_{surface}^4 - T_{ambient}^4) \qquad [2.2.1]$$

$$\varepsilon = 1.1 + \frac{(T-273)}{1000}\left[1.25x10^{-4}(T-273) - 0.38\right];\ T\ in\ K$$

The mean natural convection heat transfer from a horizontal surface has been extensively calculated by adopting the equation[20]:

$$Nu_{nat} = c(Gr_L\ Pr)^n \qquad [2.2.2]$$

for a range of cooling conditions producing the parameters c and n, as shown in Table 2.1. The forced convection heat transfer for the runout table conditions can be expressed for laminar flow[21, 7] ($Re_x < 5x10^5$, $u_p \geq u_{air}$) as:

$$Nu_{x,forced} = \frac{Re_x^{1/2}\, Pr^{1/2}}{\left(\left[\frac{10}{3}\right]^{1/2} + \frac{20r}{27\left(Pr\, A_1\right)^{1/2}}\right)} \qquad [2.2.3]$$

and for turbulent flow[7] ($Re_x \geq 5x10^5$, $u_p \geq u_{air}$) as:

$$Nu_{x,forced} = 0.019\left(9 - 7r\right)^{0.2}\, Re_x^{0.8}\, Pr^{1/3} \qquad [2.2.4]$$

where $Re_x = U_p x/\nu$, $Nu_{x,forced} = hx/k_{air}$, and $r = 1 - u_{air}/u_p$; $A_1 = 1/(0.3 - 0.0074r)$. It should be observed that laminar forced convection can occur on the runout table. For the lower limit of the strip speeds in the runout table (2m/s), the minimum local Reynolds number for air cooling is approximately $Re_{x,min} = 1.43x10^4 * x$, and hence, laminar forced convection may be possible at a position $x < 35m$ from the beginning of each dry zone.

It is important to mention that during run out table cooling, mixed convection heat transfer always takes place, because the strip is always in motion, promoting forced convection simultaneously with the natural convection. However, mathematical expressions to describe the mixed convection heat transfer regime on the runout table do not exist. To overcome this limitation in the present work, the mixed convection heat transfer can be approximated by the following equation[22]:

$$Nu_{mixed} = \left(Nu_{forced}^n + Nu_{natural}^n\right)^{1/n} \qquad [2.2.5]$$

where n=3.5-4.0 for horizontal flow past cylinders or spheres.

2.3 Water Jet Heat Transfer

Firstly, a brief discussion of the fluid flow during jet cooling is considered in order to understand better the heat transfer phenomena, which will be discussed afterwards. A comprehensive review of jet impingement boiling for different coolants and jet characteristics was presented by Wolf et al.[11]. However, a more specific and updated overview for free surface water jet cooling is needed.

A discussion of the specific location for each cooling zone on the runout table and the state of the knowledge of the boiling curves in terms of water subcooling, jet velocity, jet dimensions, and other parameters is presented. All of the experimental data was obtained for non-moving surfaces, unless stated otherwise.

2.3.1 Fundamentals of Boiling Heat Transfer

The heat transfer behavior of a system in which boiling occurs is usually best described by a plot of heat flux as a function of the difference between the surface temperature of the solid being cooled and the saturation temperature of the coolant (superheat). This kind of curve is commonly called the "boiling curve".

It is worthwhile to differentiate between the boiling curves obtained from temperature-controlled and heat-flux controlled conditions. Typically, temperature-controlled boiling curves are obtained by transient cooling; but it is possible, in principle, to generate steady state curves. On the other hand, heat-flux controlled boiling curves are usually obtained from steady-state cooling experiments. Similarly, the heat transfer versus superheat curve is not the same for boiling and condensation. In general, the

boiling curves are very dependent on the path followed during cooling, and careful consideration of boiling data is of prime importance.

The typical shapes of temperature-controlled and heat-flux controlled boiling curves are shown in Figure 2.1. The basic difference between the temperature controlled and the heat-flux controlled boiling curve is that in the latter, the transition boiling regime does not exist. This precludes the measurement of the heat fluxes in the runout table under more controlled steady-state experiments. A variety of terms are used in the literature to describe the different boiling regimes. Throughout this work, the nomenclature shown in Figure 2.1 will be used.

Under heat-flux control, to maintain a higher heat flux than the critical heat flux, a large increase in the surface temperature is required because of the very high thermal potential needed to sustain the heat flow under conditions of pure film boiling. In contrast, with smaller temperature gradients, the liquid contacts the surface, and the cooling is very effective during that contact, generating a very high heat flow. The transition boiling mechanism is a combination of both film boiling and nucleate boiling, which is also intermediate in effectiveness of cooling.

Jet cooling on the runout table is realized over a very wide range of surface strip temperatures, typically from 900°C down to 300°C; and therefore, the cooling is carried out by different boiling mechanisms. More specifically, nucleate boiling, the critical heat flux, transition boiling and film boiling must be fully characterized in order to develop a general model.

2.3.2 Fluid Flow

A basic understanding of the fluid flow phenomena involved in jet cooling is required to understand the controlled cooling of steel, because the heat transfer processes involved are strongly dependent on how the water flows on the steel surface.

Basically, there are two different flow zones during single-phase jet cooling, as shown in Figure 2.2. In the zone adjacent to the jet center, the free stream flow changes direction, and must develop in a finite length, which is defined as the impingement or pressure gradient zone. This zone extends in a direction parallel to the strip motion (cocurrent and countercurrent). This involves a change in the pressure energy (pressure gradient) which is also parallel to the strip motion. Jet fluid flow can be well approximated in the neighborhood of the jet center by the well known Falkner-Skan power-law[23, 24]. According to this, for a top planar jet, the free stream velocities in this region are given by:

$$\begin{aligned} u_\infty &= Cx \\ v_\infty &= -Cy \end{aligned} \qquad [2.3.1]$$

$$C = \frac{\pi}{4}\frac{u_{jet}}{w_{jet}}$$

and for bottom planar jets, which usually are inclined, the velocity in the direction parallel to the surface can be estimated by the wedge flow equation:

$$u_\infty = Cx^m \qquad [2.3.2]$$

where $m=\theta/(\pi-\theta)$, θ is one-half of the angle of the wedge, and the constant C is dependent on the angle θ.

The effect of impingement angle on the dimensionless free stream velocity of a planar jet is shown in Figure 2.3. It is important to note that the overall length of the impingement region is reduced by inclining the jet. These latter expressions were used extensively in this research to describe the free stream velocity of the flowing jet.

Webb et al.[24] presented the free stream velocity of an axisymmetric jet (bar) impinging with a uniform velocity perpendicular to the surface as

$$u_{\infty} = 0.9 \frac{u_{jet}}{d_{jet}} r \qquad [2.3.3]$$

which was obtained by solving numerical the fluid flow of an impinging jet under negligible surface tension effects.

Experimental work has been conducted to define the free stream fluid flow characteristics. The pressure distribution with distance from the centerline of an impinging planar water jet was measured by Zumbrunnen[25] resulting in the following expression:

$$\overline{P} = \left(\frac{\overline{x}}{x_*}\right)^2 \left(2\frac{\overline{x}}{x_*} - 3\right) + 1 \qquad [2.3.4]$$

which is related with the free-stream velocity by the well known equation

$$\frac{d(\overline{u}_{\infty}{}^2)}{d\overline{x}} = -\frac{d\overline{P}}{d\overline{x}} \qquad [2.3.5]$$

and from both the free-stream velocity is

$$\bar{u}_\infty\big|_{0\le\bar{x}\le x_*} = \left[3\left(\frac{\bar{x}}{x_*}\right)^2 - 2\left(\frac{\bar{x}}{x_*}\right)^3\right]^{1/2} \qquad [2.3.6]$$

$$\bar{u}_\infty\big|_{\bar{x}\ge 1} = 1$$

and the dimensionless velocity gradient is:

$$\bar{C} = \frac{d\bar{u}_\infty}{d\bar{x}}\bigg|_{\bar{x}=0} = \frac{\sqrt{3}}{x_*} \qquad [2.3.7]$$

The pressure distribution is presented by the line in Figure 2.4(a), and shows that the impingement region actually extends to a distance of approximately 1.75 times the impinging jet width in each direction, as compared to the 1.3 predicted by the potential flow theory, which is more applicable close to the impingement line. Similarly, Ochi et al.[26] measured the pressure distribution on the surface for an axisymmetric jet (bar) impinging perpendicularly, and the results are shown in Figure 2.4(b). Clearly, the pressure gradient zone extends to approximately 1.3 times the jet diameter, as compared to 1.1 predicted by theory. For both, planar and axisymmetric jets, the measured length of the impingement region may be considered more accurate than the theoretical approximations. Consequently, the experimental values were used extensively in the present research to delineate the impingement region in the runout table.

For single-phase jet cooling on a stagnant plate, a similar flow solution of the momentum and energy equations for the flow near the solid at the stagnation line (jet centerline) can be easily obtained for laminar flow[23], by either the direct solution of the Navier-Stokes equation (Hiemenz solution), or by integral methods (Falkner-Skan wedge

flow solution). Even though the flow might be turbulent, the impingement of the jet tends to laminarize the flow, and usually laminar flow solutions are accurate enough. For example, Webb et al.[24] mentioned that for axisymmetric jets, unless the pre-impingement jet is characterized by extremely high turbulence, a laminar boundary layer will begin at the stagnation point and proceed outward into the radial flow zone.

The zone where the free-stream velocity is fully developed, will be called "parallel flow zone", and the free-stream velocity is:

$$u_{\infty} = u_{jet} \qquad [2.3.8]$$

2.3.3 Water Bar Impingement

The boundary of the impingement region is determined by the radial position where the pressure gradient becomes negligible. For practical purposes the pressure gradient can be considered negligible when $r/d_{jet} \approx 1.3$. It is interesting to note that the experiments show that for $r/d_{jet} > 1.3$ the pressure gradient is not zero, but asymptotically decreases with radial position.

A heat transfer analysis of the effect of the process variables on the runout table cooling can be better carried out by analyzing the effect of these on the boiling curves at each particular cooling zone. Consequently, the effect of the following variables will be considered in this section: [a] Jet subcooling; [b] Nozzle diameter and position from stagnation point; and [c] Jet velocity. It is important to mention that for the experimental information presented in sections 2.3.3 to 2.3.6, mathematical expressions that could be used in a process model were not obtained. However, these measurements were very

useful for the verification of the model presented in this work, and they were used whenever possible.

[a] *Effect of subcooling.*

Subcooling is defined as the boiling temperature of the fluid at the actual pressure minus the actual temperature of the flow. Ochi et al.[26] measured the boiling curves at the stagnation point of a water bar for a range of subcoolings from 5 to 80°C (u_{jet}=3m/s, d_{jet}=0.02m, $T_{initial}$=1100°C). The results are plotted in Figure 2.5. Film boiling appears only at subcoolings lower than 45K, and the transition boiling region extends from superheats of 200K to 800K at subcoolings higher than 45K. The strong effect of subcooling on the strength of cooling is also supported by the findings of Kokado et al.[27] in similar experiments. Consequently, in the impingement region of the bar jets used on the runout table, transition boiling always takes place, and film boiling is almost impossible.

[b] *Effect of nozzle diameter and position from the stagnation point.*

The results by Ochi et al.[26] also show that the boiling curves at the stagnation point are lowered by increasing the nozzle diameter, given a constant jet subcooling and velocity, as shown in Figure 2.6. Within the stagnation zone, the boiling curves remain nearly the same for different positions, as shown in Figure 2.7, for which the jet diameter was constant (d_{jet}=0.020m). More recent experiments by Hall et al.[28] under very similar conditions (ΔT_{sub}=25K, u_{jet}=3m/s, d_{jet}=0.005m, $T_{initial}$=650°C) show the effect of the position from the stagnation point on the boiling curves, while the flow and the diameter of the jet were maintained constant, as seen in Figure 2.8. Comparing the results by Ochi

et al.[26] with those by Hall et al.[28] , it is observed that at the stagnation point, the heat fluxes can be increased up to three times by decreasing the jet diameter from 0.020m to 0.005m. This is in agreement with results shown in Figure 2.6. Figure 2.8 also shows that the boiling curve, in general, moves downwards with increasing position from the stagnation point. In this particular figure, the boiling curves for positions higher than 5mm from the stagnation point are representative of the parallel flow region. An interesting observation from the author was that in the parallel flow region, the intensive boiling lifts up the liquid layer and breaks it into droplets.

[c] *Effect of jet velocity.*

The effect of jet velocity on the boiling curve has not been reported. However, the minimum heat flux point (also referred as Leidenfrost point) has been reported as a function of jet velocity. The Leidenfrost point shifts to higher heat fluxes and superheats with increasing jet velocity, but variations in the heat fluxes due to jet velocity are relatively small. Ochi et al.[26] give the following expression for the minimum heat flux:

$$q_{min} = 3.18x10^{5}\left(1+0.383\Delta T_{sub}\right)\left(u_{jet} / d_{noz}\right)^{0.828} \qquad [2.3.9]$$

For bottom bars, the critical heat flux (maximum heat flux in the boiling curve) has been studied[29] and was found to be dependent on jet velocity. Values lower than 10 MW/m^2 were observed, even at jet velocities higher than 10 m/s and subcoolings of 80K, as shown in Figure 2.9.

2.3.4 Water Curtain Impingement

Similarly to the previous section, the heat transfer analysis will be focused on the effect of the following variables on the boiling curve: [a] Subcooling; [b] Jet velocity and water flow rate; [c] Impingement angle and jet pressure.

[a] *Effect of subcooling.*

Ishigai et al.[30] measured the boiling curves on the stagnation line of an impinging water curtain (u_{jet}=1-3.17m/s, ΔT_{sub}=5-55°C, w_{jet}=0.0062m, L_{jet}=0.05m , $T_{initial}$=1000°C), and their results are shown in Figure 2.10. Typically, the headers of a runout table issue water at room temperature, so in the impingement region of a jet subcooling is typically from 60-80°C. This figure shows that the heat fluxes in the impingement region of a typical runout table planar jet have to be in the transition boiling regime, and their values are expected to be higher than the values presented in Figure 2.10. The effect of subcooling is very significant for lower subcoolings but tend to decrease with increasing subcooling (compare to Figure 2.5). In addition, the steel surface temperature also has a very strong effect on the local heat transfer.

[b] *Effect of jet velocity and water flow rate.*

Ishigai et al.[30] also measured the effect of jet velocity on the boiling curve. The heat fluxes increase with the jet velocity, but this effect is relatively small compared to subcooling variations, as can be seen in Figure 2.11.

The average heat transfer coefficients over an area that includes the impingement region have been reported by some other researchers[31] in terms of the ratio flow

rate/length, but inconsistent results were obtained. Increasing the flow rate/length ratio produced an increase in the average heat fluxes for bars and curtains (Figure 2.12[a]) . The same report shows that with changing nozzle height the average removal of heat is only slightly affected (Figure 2.12[b]).

[c] *Effect of impingement angle and jet pressure*

Boiling curves have been measured for a water curtain impinging perpendicularly on a vertical surface by Raudenski et al.[32] (Figure 2.13). Although the water temperature was not reported, the experimental setup does not include a water heater, and water temperature may be considered as room temperature. Clearly the heat fluxes are smaller than those in the case of the cooling of the top surface of a horizontal plate (compare with Figure 2.5 and Figure 2.10). Figure 2.13[a] shows that the effect of jet pressure is negligible. Figure 2.13[b] shows that the average heat flux from an area 11.0x45.0cm (which includes the parallel flow region) is just slightly smaller than at the jet center. No film boiling was observed in these experiments, where the surface temperatures were below 600°C. An important observation made by these authors was that if the starting temperature for such experiments was increased from 600°C to 900C°, the results obtained for the temperature range of 100°C to 500C° would be different. Therefore, the initial state of the heat-transfer mechanism influences the whole heat removal process.

2.3.5 Parallel Flow Region

Despite the importance of cooling in the parallel flow region on the overall cooling process, very little research to measure the heat transfer has been reported.

In this section, the effect of the following variables on the heat transfer process will be discussed: [a] Position from the impingement zone; [b] Subcooling; [c] Jet velocity; [d] Strip speed.

[a] *Effect of Position from the Impingement Zone.*

Early work carried out by Otomo et al.[31] and Takeda et al.[33] show that away from the stagnation line of a planar jet, the heat transfer coefficients increase with decreasing plate surface temperature, as shown in Figure 2.14. This figure also shows that the heat transfer coefficient decreases with increasing distance from the curtain. Similarly, for water bars, the heat fluxes decrease with increasing distance from the stagnation point[26], as shown in Figure 2.8.

In a more systematic study, Kumagai et al.[34] measured the boiling curves for a water curtain (u_{jet}= 3.5 m/s, ΔT_{sub} =0°C) at several distances from the jet centerline. The initial plate temperature was approximately 400°C. The heat fluxes change faster close to the stagnation line, and variations in heat fluxes are negligible after some distance , as shown in Figure 2.15. These results imply that there is little effect of distance on the development of the vapor-liquid interface or of any boundary layer and the associated heat transfer.

[b] *Effect of Subcooling.*

In order to understand the heat transfer taking place in the parallel flow region, recently Filipovic et al.[35] quenched a nickel plated (15μm thick) oxygen-free copper plate (25.2mm thick, 38.1mm wide, and 508mm long) using a nozzle that issues water flowing

completely parallel to the surface, which resembles the parallel flow region of a water curtain. Several type K thermocouples were inserted in the plate at a distance of 0.2mm below the cooling surface and along the length of the plate to record temperature measurements using a data acquisition system with sampling frequency of 0.5s. Since the thermal resistance of the copper plate was very small, direct calculation of the heat fluxes was possible without the need of solving the inverse heat conduction problem. The range of operating parameters tested were similar to those in use on typical runout table operations (u_{jet} =2-4m/s, T_{water}=25-55°C, $T_{initial}$ ≈850°C). The experiments were video recorded in order to link the temperature measurements with the visible processes taking place. Boiling curves were obtained at different locations, as shown in Figure 2.16. It is clear that the boiling curves change substantially with position from the edge where the water flow starts. The authors verified that the local subcooling decreases significantly along the surface, which reduces also the heat extraction downstream. So, the effect of position was attributed to a decrease in local subcooling. It was also mentioned that the development of any boundary layer or the vapor-liquid interface was negligible.

It is important to mention that a minimum heat flux is virtually nonexistent, and the film boiling regime (considered by the authors as the flatter response on the heat flow curves) was obtained only at relatively long distances from the edge where the water flow starts, where the water temperature is high, probably above 70°C. Under these experimental conditions, the transition boiling regime takes place at lower water temperatures and changes continuously to film boiling while the local water temperature

increases. Even though the experiments by Filipovic et al.[35] depart from the hot strip mill conditions with respect to the lack of plate motion and the differences of plate material, the effect of subcooling is in qualitative agreement with observations in runout table operations, where a water stream may be left on the strip for several meters without any overcooling observed, typically between the last working header and the sweep sprays near the coiling temperature. Since the only significant variable that changes along this stream for a particular strip is the local water temperature, it is reasonable to consider that higher local water temperatures are responsible for limiting the cooling capabilities of the water stream.. Visually the streams change from visual "direct" contact of the water with the strip to a vapor film which later on induces the breaking up the water layer into pools.

Kumagai et al.[34] also showed the effect of variations in subcooling on the critical heat flux at different locations in Figure 2.17. The critical heat flux increases with subcooling. However, this effect seems to be smaller in the parallel flow region, where increasing the distance from the centerline gives rise to a progressively smaller decrease in the CHF.

The cooling in the parallel flow region could also be compared to the quenching of a steel bar in a pipe through which water is flowing, as used by Hernandez-Morales et al.[12]. The surface heat fluxes were calculated using an inverse heat conduction method applied to thermocouple readings obtained at various depths in the quenched bar, for different water temperatures and velocities, and the results are presented in Figure 2.18. Lower water temperatures increase substantially the heat fluxes during quenching, and

film boiling appears at water temperatures in the neighborhood of 75°C at surface temperatures above 600°C.

[c] *Effect of Jet Velocity*

The effect of jet velocity cannot be seen as clearly as the effect of subcooling on the heat fluxes reported in the literature.

From the parallel flow experiments by Filipovic et al.[35] presented in Figure 2.16, some conclusions may be drawn. Comparing the curve (T_{water}=25°C, u=2m/s at x=0.4826m), which may have been subjected to a local water temperature up to 40°C, to the curve (T_{water}=55°C, u=4m/s at x=0.127m), with a local T_{water} probably above 60°C, it is clear that the latter curve exhibits higher heat fluxes, even with a difference of about 20°C in local water temperature. This indicates that the velocity variation from 2 to 4m/s produces a noticeable increase in the boiling curves.

The experiments by Hernandez-Morales et al.[12] shown in Figure 2.18 provide additional information on the effect of flow velocity. The variation in the average flow velocity in the pipe from 2.8 to 6.9 m/s has a significant effect on the boiling curves, especially for lower water temperatures. However, for this flow the maximum velocity can be significantly higher than the average, which increases the effect of water velocity to a level similar to that in the impingement region of a jet. Consequently, the effect of jet velocity has to be intermediate between the actual effect in the parallel flow region and that obtained in the impingement region.

Finally, Kumagai et al.[34] showed that the effect of jet velocity on the critical heat flux in the parallel flow region of a water curtain is small, and it becomes almost negligible with increasing distance from the impingement line, as shown in Figure 2.19.

[d] *Effect of strip speed.*

The effect of strip speed on the heat transfer was studied by Hatta et al.[36], but their results are unclear with respect to the real effect of motion on the boiling curve, although it seems to be small.

More recently, Hernandez et al.[16] measured the thermal history of a moving plate going through an array of planar water jets in a pilot-plant runout table experiment. A schematic layout of the experimental setup is presented in Figure 2.20. Three Type-K thermocouples (0.51 mm diameter) were installed in a 304 stainless steel plate. No cleaning or special treatment was applied on the surfaces of the test plates. Temperatures were recorded using the Lab Tech-Notebook data acquisition system with a sampling frequency of 500 Hz during the cooling of each sample plate under an array of six planar water jets. The plate was placed on a sled and accelerated to constant speed before being drawn through the jet array. The water curtain (u_{nozzle}=1.46m/s, u_{jet}=4.6m/s, w_{jet}=0.001m, L_{jet}=0.41m, T_{water}=24°C) impinged on the constant velocity plate (1.45 m/s). In order to measure the surface temperature directly (avoiding the solution of an inverse heat conduction problem and the effect of the "thermal capacitance" of the plate on the thermal response of the thermocouples) two thermocouple wires were spot-welded on the surface to be cooled down, and an additional thermocouple was placed at the

center of the plate. The time constant of the thermocouples was estimated to be smaller than the sampling frequency.

Hernandez et al. [16] mathematically modeled the thermal response of the surface thermocouples with reasonable results, but they did not conclude about the effect of strip motion in these experiments. A numerical analysis was performed based on a boiling heat transfer model and the authors suggested that increasing the strip speed the local heat transfer is also enhanced in both, the impingement and the parallel flow regions.

2.3.6 Interaction between jets in an array

The heat transfer characteristics of a single jet have previously been considered. However, in the runout table, arrays of jets are used to control the cooling of the steel. Consequently, the effect of neighboring jets on the heat transfer of a single jet must be characterized. Since the fluid flow involved during these operations is extremely complex, only experimental work and plant measurements and observations have been reported.

The work by Kimura et al.[37] shows clearly that the average heat-transfer coefficients for an array of jets follows the typical transition boiling shape, as previously described for both the impingement and parallel flow regions (see Figure 2.21). Also, it is evident that the effect of water temperature and flow rate is qualitatively the same as that obtained for the single jet cooling.

Slayzak et al. studied the interaction between planar jets[38] and adjoining rows of water bars[39]. Experiments were conducted to obtain the single-phase local heat transfer

coefficient along a constant heat flux surface. In the case of the curtains, nozzle widths and nozzle-to-heater separation distances were fixed at 5.1 and 89.7 mm, respectively, while two nozzle-to-nozzle pitches (81 and 51 mm) were considered. The ratio of impingement velocities for the two nozzles was varied from 0.47 to 1.0. Interacting wall jets created by the impinging jets yielded a strong upwelling of spent flow (an interaction fountain), beneath which convection coefficients were comparable to those associated with the impingement regions. With decreasing the ratio of impinging velocities, the heat transfer coefficients in the impingement region of the weaker jet were reduced by the effects of crossflow imposed by the stronger jet.

In the experiments associated with the impingement of one or two rows of circular, free-surface water jets, the nozzle diameter, the centerline-to centerline distance between nozzles in a row, and the nozzle -to-heater separation distance were fixed at 4.9, 6.3, and 89.7 mm, respectively. Two row-to row separations (81 and 51 mm) were considered, and the jet velocities were varied from 2.1 to 4.5 m/s. For an equivalent impingement velocity, maximum convection coefficients beneath a planar and a linear array of circular jets are comparable. Over a region that transcends the impingement zone, the local and average heat transfer coefficients obtained for a linear array of circular jets are less than those obtained for an equivalent planar jet. Although the convection coefficients in the stable interaction zones between the planar jets are characterized by a pronounced secondary maxima, comparable to those at impingement, a dual array of circular jets did not produce such strong peaks. The existence of such peaks was attributed to the availability of cool, free-stream fluid just prior to the flow interaction. It

is important to mention that measurements of the heat-transfer coefficient across one line of circular jets revealed that the heat transfer in the parallel flow region is increased by higher concentrations of water, even for the same jet velocity (compare Cases A and C with B and D in Figure 2.22).

Detailed information with respect to the flow characteristics and cooling performance of arrays of curtains was also presented by Takeda et al.[33]. They reported that the interference zone between two curtains presents a lower heat transfer than the impingement or the parallel flow regions, and in this region the cooling is that for a stagnant water pool. Interestingly, the water distribution across the width was not uniform. It was estimated that the 20°C temperature difference between the edge and the center could be eliminated by reducing the flow rate at the edges by 30%, with respect to that used at the center. In the case of an array of circular jets, important differences can be seen in the flow rate ratio (Flow rate at the edge/Flow rate at the center x 100) across the width related to the different water supply method employed, as it is shown in Figure 2.23.

More recently, Haraguchi and Hariki[40] studied the effects of interference flow and nozzle pitch on the uniformity and capacity of cooling of arrays of water bars at typical runout table temperatures. A 5-mm-thick copper plate (300mm long by 300mm wide) was heated to 1000°C and set into a steel plate (2200mm long by 500 mm wide) and cooled from 800°C, using water at 30°C. Two different numbers of rows of nozzles and two nozzle pitches were considered (1 and 4 rows, pitches of 40 and 80mm), and the nozzle flow rates were 12.5 and 25.0 l/min. The nozzle diameter, the row-to-row distance,

the nozzle-to-plate distance were fixed at 16.7, 450, 1500 mm, respectively. The steel plate was inclined three degrees from the horizontal in order to simulate the effect of strip motion. The heat transfer coefficients at different locations were measured, as shown in Figure 2.24. In Figure 2.24[a] the heat-transfer coefficients are plotted versus the surface temperature for three locations from a jet impingement point (P=0mm, Q=40mm, R=80mm); it is clear that the heat transfer increases substantially decreasing the surface temperature, but the effect is less significant outside the impingement region (points Q and R). Figure 2.24[b] shows the average crosswise heat transfer distributions over the temperature range from 500-800°C, for four different cooling configurations, where the number of rows, nozzle pitch and nozzle flow rate were varied (Case A1: 4, 40mm, 12.5 l/min; Case A2: 1, 40mm, 12.5 l/min; Case B1: 4, 80mm, 25.0 l/min; Case B2: 1, 80mm, 25.0 l/min). The average heat transfer over section A (region ± 40mm from the jet line axis) is significantly higher than the average over the whole section, which indicates the need of local heat transfer coefficients for predictions. Variations crosswise are smaller in Cases A1 and A2 because of the smaller pitch according to the authors, but possibly also due to the smaller diameter of the impinging jet (7mm compared to 10 in the Cases B1 and B2), which is evident in the distance between the peaks of these distributions. The authors observed that for four rows of nozzles, the interference flow is formed close to the impingement points on one side of the row, and it decreases the flow velocities and heat transfer of jets around the impingement points. Contrasting the effect of flow interference (cases A1-A2 and cases B1-B2), the interference flow has little effect on the uniformity of the heat transfer, while it decreases the heat transfer coefficient around the

impingement points. The reduction in nozzle pitch greatly improves the uniformity across the strip width, while it decreases the coefficient in the area close to the impingement points.

2.4 Principles of Boiling Curve Modeling

It has been shown that the published experimental or theoretical work although providing some general trends with respect to the effect of process variables on the heat transfer, is not sufficient to generate an empirical mathematical expression to calculate the boiling curves with sufficient generality to describe the complex cooling on the runout table. On the other hand, the experimental measurement of the boiling curves obtained for a moving strip requires an extremely large amount of work and its cost would probably be prohibitive. As a result, the mathematical modeling emerges as a cheaper and easier alternative, which, if based on fundamental principles, may help substantially in understanding the runout table operations.

This section deals with the fundamentals of heat transfer available to generate a mathematical model describing the boiling curves relevant to the runout table. A discussion of each of the individual parts required to describe the entire boiling curve is presented.

2.4.1 Transition Boiling

In the typical range of strip surface temperatures experienced on the runout table, transition boiling appears to be the boiling regime in the impingement region, whereas in the parallel flow region transition boiling takes places and continuously gives way to film boiling on moving away from the impingement zone. Given the much higher heat fluxes

in transition boiling compared to film boiling, the former is responsible for most of the cooling even though the strip cooling area under film boiling might be larger. The transition boiling regime has been defined in several different ways. In most cases, information from the boiling curve is used in defining the area where transition boiling takes place, but some researchers have used other experimental characteristics to define it, such as the differences in noise generated during boiling or the color of the cooling surface. However, throughout this work, the definition used by Kalinin et al.[41] and Auracher[42] is adopted., where the transition boiling regime is the section of the boiling curve where

$$\frac{\partial q}{\partial \Delta T_{sat}} \leq 0 \qquad [2.4.1.1]$$

discarding the minimum heat flux (MHF) and the critical heat flux (CHF).

Very little information about transition boiling has been published; this is particularly true for jet cooling[11]. Only in recent years has interest in this boiling regime increased, mainly in connection with the safety of nuclear reactors. Other fields of interest include the material quenching processes, and the design of high performance evaporators heated by a liquid or a condensing fluid, which may also be operated in the transition boiling region without the danger of instabilities because the heat transfer is temperature controlled [42]. Reviews of the present state of knowledge on transition boiling are presented elsewhere[41,42], and only the details of those reviews relating to this work are presented here.

The experimental results on the transition boiling mechanism and the estimates of heat-transfer rates show that, at a given instant, a part of the hot surface is wetted by the liquid while the remainder is covered by a vapor film. Consequently, each region of the hot surface is alternately in contact with the liquid and vapor phases of the boiling medium. The mean duration of the heating surface contact with the liquid depends on the superheat, the properties of the boiling fluid, the wall material and surface conditions. Since the heat transfer to liquid is much higher than that to vapor, the heat transfer processes occurring at the wall-liquid contacts are dominant in the case of transition boiling[41].

It is important to mention that the processes taking place during liquid-solid contact change with the local superheat. Kalinin et al.[41] distinguished three zones in the wetted part of the heating surface in the transition boiling region:

1.- A low superheat zone near the critical heat flux where the duration of the liquid-wall contact is rather large and nucleate boiling occurs at the contact place.

2.- A high superheat zone near the minimum heat flux where nucleate boiling cannot develop because of the small contact time, and heat transfer from the wall to the liquid dominates, and unsteady heat conduction occurs.

3.- A mean-superheat zone where the contributions of nucleate boiling and unsteady heat conduction are comparable.

Increasing the superheat, the duration of the periodic liquid-solid contacts is decreased. The disturbance of the hydrodynamic stability of the vapor film and the

conservation of the thermodynamic stability of the liquid at the contact place are necessary conditions for the liquid-solid contact.

Stable equilibrium of the vapor-liquid interface is possible only when the less dense phase is above the more dense one (as occurs on the underside of a water cooled horizontal surface with small free-flow velocity of both phases). For other cases, (film boiling on vertical, inclined, cylindrical, spherical surfaces and on top of a horizontal surface), the interface boundary is unstable as the more dense phase is above or adjacent to the less dense one.

The instability initiates a transverse motion of the interface boundary. However, at high superheats, the vapor film is thick, and the liquid does not touch the surface. Decreasing the superheat, the thickness of the vapor film decreases, and the vibration amplitude of the interface boundary may coincide with it, and the liquid-solid contact becomes possible from a hydrodynamic viewpoint. Whether this contact occurs depends on the thermodynamic condition and its combination with the hydrodynamic ones. When the wave peak is close to the surface, and when the liquid temperature is much higher than the saturation temperature, the intense vaporization produces a reactive force that can throw the liquid from the surface, and contact will not occur. If contact takes place, and if the liquid reaches a higher temperature than a limiting metastable liquid heating temperature, then the explosive boiling of the thinnest layer occurs and the liquid is thrown from the surface. When the liquid temperature is lower, then wetting occurs, and unsteady heat conduction (small contact time) or nucleate boiling (large contact time) will appear.

Regardless of the properties of the solid or the surface orientation, increasing the liquid subcooling, widens the transition boiling region and shifts it to higher superheats, enhancing the heat transfer. In contrast, heat removal in the NB region does not depend on subcooling; this may be attributed to two compensating factors such as increasing the temperature drop between the surface and liquid and the decreasing rate of bubble growth due to subcooled liquid condensation at their caps. In the transition region these factors act in the same direction since increasing the temperature difference between the surface and water increases the heat release during the solid-liquid contacts, while the falling bubble growth increases the duration of this contact.

The influence of the thermal properties and surface conditions (roughness and wettability) of the solid is quite important in transition boiling. Such influence has been examined mostly in pool boiling experiments, but there is no reason to doubt that the effects are similar in flow boiling[42].

According to Kalinin et al.[41], the experimental data supports the conclusion that decreasing the thermal effusivity ($\rho c_p k$) shifts the nucleate and transition boiling curves to regions of higher superheats, while film boiling is not affected. However, Auracher[42] states that the MHF point shifts to the right also.

Since nucleate boiling is very dependent on the nucleation site density, with decreasing the height of the microroughnesses on the surface, NB and CHF shift to higher superheats, while the MHF remains the same, if the micro roughness height is smaller than the vapor layer thickness. Therefore, for the same superheat, in transition boiling the heat flux increases with smoother surfaces[41,42].

Wettability has a strong influence on transition boiling. Enhancing wettability, increases the heat transfer rate by increasing the liquid-solid contact area. The resulting increase in heat flux with decreasing wetting contact angle includes both the CHF and the MHF, but this effect is greater in the MHF. The wettability also changes with oxidation or deposition. Contamination may, in a very complicated way, simultaneously affect roughness, wettability and the thermal properties of the surface, thus causing non-reproducibility in much of the experimental data available. However, at least in flow boiling, an oxidized surface shifts the CHF point to higher heat fluxes and superheats, thus higher transition boiling heat transfer rates [41,42].

A very important factor is the steadiness in the experimental boiling curves. Very different boiling curves are obtained from steady state experiments compared to transient ones. Kalinin et al. [41] pointed out that the general tendency is, the slower the unsteady process the less the boiling curves differ from the steady-state curve obtained under the same conditions. An analysis by Auracher[42] showed that the instantaneous interface temperature and the cooling rate at the surface are the primary parameters needed to describe this problem. The heat flux increases as the cooling rate at the surface increases during the heat-up processes; but the opposite is true for the cool-down processes. Finally, the transient boiling curves can generally be characterized by the cooling rate in addition to the steady-state expressions.

According to this discussion, the boiling curve from nucleate to film boiling can be described by a linear combination of the heat fluxes for the liquid and vapor contacts with the surface as follows:

$$q_{TB} = q_{l-s}F + q_{v-s}(1-F) \qquad [2.4.1.2]$$

where F is the fraction of the area in contact with the liquid, q_{l-s} and q_{v-s} are the heat fluxes realized during the liquid-solid and vapor- solid contacts respectively. This equation constitutes the foundation of most of the transition boiling studies, and it was adopted as the basis of a mathematical model for the boiling curves presented in this thesis.

Ragheb and Cheng[43] assumed that $q_{l-s} = q_{CHF}$, $q_{v-s} = q_{MHF}$. This is a good approximation, but usually the CHF and the MHF are also unknown and thus of little use for modeling purposes.

Kalinin et al.[41] proposed that $q_{l-s} = q_{NB}$, $q_{v-s} = q_{FB}$, evaluating them as the extrapolation to real superheats of known correlations for both nucleate boiling and film boiling. However, direct extrapolation of the present NB heat flux correlations to transition boiling superheats in convective boiling might overestimate by orders of magnitude the liquid-solid contact heat flux[42]. Nevertheless, this assumption seems to be the most reasonable if a mathematical expression to represent the extension of nucleate boiling was found. Such approximation was adopted in this work.

Kostiuk et al.[44], Pan et al.[45], and Farmer et al.[46] suggested a variation of Eq. [2.4.1.2], but include the effect of the transient conduction before bubble formation, which is expressed as:

$$q_{TB} = x_t q_t + x_{NB} q_{NB} + x_{FB} q_{FB} \qquad [2.4.1.3]$$

This approach has the advantage of being able to include the thermal characteristics of the surface. Nevertheless, Pan et al.[45] using a similar approach showed that the nucleate boiling mechanism contact time is of the order of 10^{-3} s, whereas the transient conduction lasts about 10^{-6} s. Since the heat flux is much higher in nucleate boiling than in transient conduction, the later mechanism is negligible. However, Pan et al. [45] include this effect to evaluate the local superheat in nucleate boiling.

2.4.2 Liquid-Solid Contact Heat Transfer

As previously mentioned, Kalinin et al.[41] distinguished three zones in the transition boiling region on the wetted part of the heating surface:(1) A low superheat zone near the CHF where the duration of the liquid-wall contact is rather large and nucleate boiling occurs at the contact place; (2) A high superheat zone near the MHF where nucleate boiling cannot develop because of the small contact time; the heat transfer from the wall to the liquid dominates, and unsteady heat conduction occurs; (3) A mean-superheat zone where the contributions of nucleate boiling and unsteady heat conduction are comparable. However, Auracher[42] has shown that unsteady heat conduction cannot be the main mechanism of heat transfer, and consequently nucleate boiling is the mechanism of heat transfer in the solid-liquid contacts.

For the range of jet velocities of interest, nucleate boiling is not affected by the jet velocity. Wolf et al.[47] suggest than in the fully-developed nucleate boiling, convection is dominated by the intense, bubble-induced mixing and latent heat effects, and therefore heat transfer is independent of jet velocity and subcooling, and it depends only on the wall superheat. This regime can be considered a linear combination of convective heat

transfer and pure pool boiling. For the fully developed nucleate boiling (FNB), the convective term takes the boiling curve to higher superheats, and heat fluxes, but only as an extension of the pool nucleate boiling curve. Water subcooling, ΔT_{sub}, has no effect on the heat flux[11,47,48]. The effect of the strip speed has been analyzed by some researchers, and it seems that the heat flux increases slightly with strip speed, but there are no conclusive results[11].

The heat flux in fully nucleate boiling (FNB) has been found in different cooling systems to follow a relationship such as:

$$q_{FNB} = C\Delta T_s^n \qquad [2.4.2.1]$$

For the specific case of planar water jets, Miyasaka et al.[48]reported $C = 79$ and $n = 3.0$ for a wall superheat of 26-90°C. Wolf et al.[11] from data by Ishigai et al.[30] obtained $C = 42$ and $n = 3.2$, and in more recent experiments Wolf et al.[47] obtained $C = 63.7$ and $n = 2.95$ for a superheat of 23-51°C.

The parameters of this equation are reported for other jet configurations. Values of n from 1.42-7.4 are found, and if jet FNB is an extension of pool FNB, then an important parameter not taken into account yet, should be considered.

A closer analysis of the origin of the superheat exponent, n, shows that the extension of pool boiling is a good approximation of jet nucleate boiling. Consequently, the heat transfer is determined by the nucleation and growth of bubbles during boiling. Boiling occurs at nucleate sites, and their number is very dependent on the physical condition of the surface, the wetting characteristics of the fluid and the efficiency of air trapped

displacement. Whalley[49] analyzed some experimental results and obtained the following expression for the heat flux:

$$q_{NB} \propto \Delta T_s^{1.2} \left(\frac{N}{A_{tot}} \right)^{0.33} \qquad [2.4.2.2]$$

where the nucleation site density, N/A_{tot}, is dependent on the heat flux (or wall superheat). It is clear that n is directly related to the mechanism of activation and deactivation of nucleation sites, which is a function of the substrate temperature.

The parameter C has been studied with some detail using the well-known correlation by Rohsenow[49]. However, the parameter C is related to specific conditions of evaporation, and usually an additional constant has to be evaluated experimentally to calculate C.

Chen et al.[50] measured q_{l-s} directly for a falling water drop on an Inconel 600 surface, and the results are presented in Figure 2.25. Water subcooling increases the solid-liquid contact heat flux, and for a large subcooling q_{l-s} increases monotonically. For saturated liquids, the heat flux encounters a maximum and decreases at higher superheats. The solid-liquid contact heat flux increases slightly with the drop velocity. These experimental results were used extensively during this work to validate a mathematical model to extrapolate the nucleate boiling regime to the transition boiling, because this is the only work known to this author with measurements of this parameter.

It is remarkable that the contact heat flux does not follow any available nucleate boiling correlation , where the superheat exponent is $n \sim 3$, as previously mentioned.

Instead, n is smaller, supporting the idea of deactivation of nucleation sites at higher surface temperatures[51].

In the case of pool nucleate boiling, there is experimental evidence of the formation of a so called "macrolayer", as shown in Figure 2.26. The macrolayer of liquid adjacent to the solid surface is punctured with vapor stems which feed bubbles by vapor formed at the liquid-vapor and solid-liquid-vapor interfaces of the stems. This mechanism has been adopted in the development of semi-empirical expressions to estimate forced convection boiling[52,53,54] and for saturated and subcooled jet boiling[55,29]. Also good results have been obtained for pool[56,45] and forced convection transition boiling in tubes[57]. The macrolayer evaporation mechanism was applied to the parallel flow region of an impinging jet by Hernandez[16], as shown in Figure 2.27. More recently, Filipovic et al.[35] video-recorded basically the same mechanism depicted in Figure 2.27 during the transient quenching of a long nickel-plated copper surface by subcooled water flowing parallel to the surface.

Pasamehmetoglu et al.[58] analyzed this mechanism numerically (see Figure 2.26). They concluded that in saturated nucleate pool boiling, most of the evaporation occurs at the triple-point; that is, at the solid-liquid-vapor interface (perimeter of the vapor stems). Accordingly, the extrapolation of the liquid-solid contact heat transfer is approximated by nucleate boiling heat transfer due to the macrolayer evaporation mechanism given by:

$$q_{triple-point} = m_{tp} H_{fg} 2\pi R_s \left(T_{tp} - T_{sat}\right) \frac{N}{A_{tot}} \qquad [2.4.2.3]$$

where the macrolayer evaporation parameter, m_{tp}, was found to be 6.0×10^{-5} $Kgm^{-1}s^{-1}\,{}^{o}C^{-1}$ for nucleate boiling of saturated water on a copper block.

Hernandez[16] applied Pasamehmetoglu's model to evaluation of the subcooled nucleate boiling heat flux, in such a way that the liquid-solid contact heat flux in equation [2.4.1.2] was calculated by:

$$q_{l-s} = q_{NB} = q_{triple-point} \qquad [2.4.2.4]$$

where the equation [2.4.2.3] was extended to:

$$q_{triple-point} = \left\{ 2 m_{tp} H_{fg} \left(117.1 \pi 0.165 \right)^{1/2} \Delta T_{sat} \right\}^{1.333} \qquad [2.4.2.5]$$

It is important to mention that the simplicity and the generality of this latter expression allowed its extensive application in this work.

2.4.3 Liquid-Solid Fractional Contact Area

The estimation of the liquid-solid fractional contact area, F, in equation [2.4.1.2] has been the subject of some of the recent transition boiling research[42,59]. Shoji et al.[59] measured F for a saturated pool boiling experiment and compared their results with the findings from other researchers, as shown in Figure 2.28. It is clear that even for pool boiling, the results can be extremely different. The experimental data that has been published was obtained for conditions very different from subcooled jet boiling, making its direct application limited.

In an attempt to calculate the parameter F, the macrolayer evaporation mechanism has been adopted by Pan et al.[57] in the transition boiling in tubes, and by

Hernandez[16]. In convection boiling, liquid enters the macrolayer according to the fluid flow depicted Figure 2.27. The rate of liquid input maintains the original thickness of the macrolayer at the entrance, but as evaporation proceeds, the macrolayer becomes thinner. Thus at a point (L) in the direction of the flow, the evaporation rate is equal to liquid input, beyond which only vapor-solid contact exists. Then, the parameter, F, may be expressed by:

$$F = \frac{L}{L_B} \qquad [2.4.3.1]$$

Hernandez[16] obtained the parameter, F, by a heat balance on the macrolayer, where the length, L_B, was assumed to be equal to the wavelength of a disturbance causing the vapor-liquid interface[60] to become unstable, according to the linear Kelvin-Helmholtz instability criterion[61,62]. While the application of equation [2.4.3.1] was successful for a variety of operating conditions, it may not be applicable to the description of transition boiling on long surfaces. This issue will be address further in another section.

2.4.4 Vapor-Solid Contact Heat Transfer

The vapor-solid contact heat flux required in equation [2.4.1.2] can be assumed to be equal to the film boiling heat flux from an isothermal surface, since small errors in this approximation are not significant. Mathematically, then

$$q_{v-s} = q_{FB} \qquad [2.4.4.1]$$

A very general equation was developed by Nakayama[64], who solved the Navier-Stokes equations for subcooled laminar wedge flow film boiling on a non-moving surface

by applying a boundary layer approach, where the solution of the equations were obtained by the integral method. This approach can be used in the impingement region of the jet, since jet cooling behaves as a Falkner-Skan wedge flow. Nakayama[64] obtained the local Nusselt number:

$$Nu_x = \left[\frac{\mu_l}{\mu}\frac{m}{2}\frac{1}{U_i^* \Lambda}\right]^{1/2} Re_x^{1/2} \qquad [2.4.4.2]$$

which is calculated by solving the non-linear system of three algebraic equations with three unknowns, $U_i^*, \Lambda, \varsigma^*$, as follows:

$$\varsigma^{*2} = \frac{15}{2}\frac{(1+m)D}{\left(1+\frac{3}{2}U_i^*\right)(1+3m)+5m} \qquad [2.4.4.3]$$

$$\frac{H}{Pr\,R}\frac{\mu}{\mu_l} = \frac{1+m}{2m}\frac{U_i^{*2}\Lambda(1+\Lambda/3)}{1-\left[(1-\Lambda)/\left(1-U_i^*\right)\right]U_i^*\varsigma^*\left(\Gamma\sqrt{Pr_f}\right)} \qquad [2.4.4.4]$$

$$\frac{\mu}{\mu_f} = \frac{4}{15}\frac{\Lambda}{mU_i^*}\left(\frac{1-U_i^*}{1-\Lambda}\right)^2\left[\left(1+\frac{3}{2}U_i^*\right)(1+3m)+5m\right] \qquad [2.4.4.5]$$

where

$$D = \frac{\left[(5\varsigma-1)+\left(10\varsigma^2-5\varsigma+1\right)U_i^*\right]}{30\varsigma^2} \quad \text{for } \varsigma \geq 1 \qquad [2.4.4.6]$$

$$D = \frac{\left[\left(10 - 10\varsigma + 5\varsigma^2 - \varsigma^3\right) + \left(10\varsigma - 5\varsigma^2 + \varsigma^3\right)U_i^*\right]}{30} \quad \text{for } \varsigma \le 1 \qquad [2.4.4.7]$$

An asymptotic expression for high subcoolings was also obtained by Nakayama[64], which is applicable for the low water temperatures found in the impingement region of the runout table:

$$Nu_x = \frac{q_{FB}x}{\Delta T_{sat}k} = \left(\frac{m(1+3m)\xi^{*3}}{10}\right)^{1/4}\left(\frac{\mu_f}{\mu}\Gamma\sqrt{Pr_f}\right)^{3/4} Re_x^{1/2} \qquad [2.4.4.8]$$

where

$$m = 1$$

$$\xi^* = \left(\frac{5}{3}\frac{1+m}{1+3m}\right)^{1/2}$$

$$\Gamma = \left(\frac{Pr}{Pr_f}\right)\left(\frac{C_{p_f}\Delta T_f}{C_p \Delta T_{sat}}\right)$$

Equations [2.4.4.2]-[2.4.4.7] are the most general equations applicable to film boiling in the runout table. They served as the basis for an extended model developed during this research.

An additional contribution of radiation heat transfer through the vapor layer has to be included. Nakanishi[65] suggested that the total heat flux in film boiling for an impinging water planar jet is given by:

$$q'_{FB} = 1.74q_{FB} + 0.75q_{rad} \qquad [2.4.4.9]$$

where

$$q_{rad} = \varepsilon\sigma\left(T^4 - T_{sat}^4\right)$$
$$\varepsilon = 0.85$$
$$\sigma = 0.56697x10^{-7}$$

For the parallel flow region, empirical equations have been proposed[66] such as the one for the parallel flow of a bar jet impinging on a non-moving surface,

$$q_{FB}' = 200\left(2420 - 21.7T_{wat}\right)\Delta T_{sat}^{0.2} \qquad [2.4.4.10]$$

or the more general equation for the turbulent subcooled boiling on a moving surface obtained by Filipovic et al.[67] using an integral analysis:

$$Nu_x = \frac{q_{FB}x}{k_v \Delta T_{sat}} = C^d\left(1+m\right)^{-a}\beta\overline{U}_l^{\,c}\frac{\mu_l}{\mu_v}\left(\frac{2\overline{u}_s + n_l\overline{u}_\infty}{\left(n_v+1\right)\left(n_v+2\right)}\right)^a Re_x^d\, Pr_l^{1-p} \qquad [2.4.4.11]$$

where a,c,d,m, and p are constants, β is a subcooling parameter, and the u's correspond to dimensionless velocities in the system. This latter equation is obviously more applicable to the runout table model than equation [2.4.4.10] because it expresses the heat transfer in terms of the process variables of interest.

A detailed knowledge of the film boiling processes is extremely important to understand the high temperature quenching processes. This is because the local position of the liquid-vapor interface determines not only whether film, transition or nucleate boiling appears, but also the magnitude of the heat fluxes encountered.

Kalinin et al.[63] reviewed the state of the overall knowledge on film boiling and suggested the following conclusions for film boiling: (1) The saturation temperature at the liquid-vapor interface is assured at any wall temperature; (2) The minimum heat flux

(MHF) and the minimum vapor film thickness possible correspond to steady laminar vapor film with a smooth steady interface; (3) Enhancing the vapor removal, the higher the heat flux resulting from a decreasing thermal resistance due to a smaller vapor thickness; (4) Heat transfer is increased by a reduction of the hydrodynamic stability of the liquid-vapor interface which increases the interface wave amplitude. Subcooling tends to stabilize the interface, but increases the heat flux through an increase in the sensible heat required for evaporation; (5) The oscillation behavior of the interface leads to fluctuations in the solid surface temperature and unsteady conduction in the solid occurs.

Recent experiments by Nigmatulin et al.[68] of quasistationary film boiling in external flow on a horizontal cylinder in a pool of saturated and subcooled water are very revealing with respect to the behavior of the liquid-vapor interface. Laser and acoustic techniques were employed to measure the mean vapor film thickness and the local wave amplitude as a function of surface superheat and water subcooling. The results are presented in Figure 2.29. The behavior of the vapor film thickness is as expected; that is, it increases with increasing superheat and decreases with increasing subcooling. Interestingly, the amplitude of the interface seems to have a similar behavior, suggesting some kind of dependence on the vapor film thickness.

2.5 Phase Transformation

The microstructure of the steel after hot rolling and cooling determines the mechanical properties of the steel. During the runout table enhanced cooling the decreasing temperature initiates the austenite decomposition to ferrite, pearlite, bainite or

martensite; whereas, the reduced cooling rate experienced subsequently in the coiled product allows precipitation strengthening take place.

At the same time, the thermal events experienced on the runout table are significantly affected by the austenite decomposition, mainly because of the heat released by the phase transformation, but also by the differences in thermal properties between austenite and the products of the transformation. Consequently, it is important to quantify these microstructural changes to predict accurately the thermal events and the final mechanical properties. However, it should be emphasized that quantifying the heat transfer characteristics obtained during runout table cooling, is the priority of this thesis. The phase transformations occurring during runout table cooling are important because of their associated heats of transformation which affect the heat flux analysis as they relate to subsequent validation of the thermal modelling. The details of the transformation occurring on the runout table can be found elsewhere [70,71,72,73,74,75].

2.6 Relationship between Mechanical Properties and Microstructure

The effect of microstructure characteristics on mechanical properties have been the subject of different research efforts. The relevant work done for this research has been published elsewhere [76,77,78].

2.7 References

1.- S. Saini, D. A. Shaw, H. Pérez R., J. Cuellar P., "Coiling Temperature Control Performance at AHMSA Hot Strip Mill Mexico", unpublished paper, 1997.
2.- C. McCulloch, M. A. Sc. Thesis, University of British Columbia, 1989.

3.- A. Kumar, C. McCulloch, E. B. Hawbolt, I.V. Samarasekera, "Modelling Thermal and Microstructural Evolution on Runout Table of Hot Strip Mill", Material Science and Technology, Vol. 7, April 1991, pp.360-368.

4.- Prasad A., Jha S., Mishra N. S., "Modelling of Microstructural Evolution during Accelerated Cooling of Hot Strip on the Runout Table", Steel Research, Vol. 66, No. 10, 1995, pp.416-423.

5.- R. Colas, C. M. Sellars, "Computed Temperature Profiles of Hot Rolled Plate and Strip during Accelerated Cooling", Proceedings of the International Symposium on Accelerated Cooling of Rolled Steel, Winnipeg, Canada, Vol. 3, Pergamon Press, London, 1987.

6.- J. F. Evans, I. D. Roebuck, H. R. Watkins, "Numerical Modeling of Hot Strip Mill Runout Table Cooling", Iron and Steel Engineer, January, 1993, pp.50-55.

7.- J. Filipovic, R. Viskanta, F. P. Incropera, T. A. Veslocki, "Thermal Behaviour of a Moving Steel Strip Cooled by an Array of Planar Water Jets", Steel Research, Vol. 63, No. 10, 1992, pp. 438-446.

8.- J. Filipovic, R. Viskanta, F. P. Incropera, T. A. Veslocki, "Cooling of a Moving Steel Strip by an Array of Round Jets", Proceedings of the 35th Mechanical Working and Steel Processing Conference, ISS-AIME, Vol. XXXI, 1994, pp.317-327.

9.- R. M. Guo, "Heat Transfer of Accelerated Steel Strip Using Laminar Flow Cooling", 10th Process Technology D. Conference Proceedings, The Iron and Steel Society, 1992.

10.- Yashiro, K., J. Yamasaki, M. Furukawa, K. Arai, M. Morita, M. Obashi, "Development of Coiling Temperature Control System on Hot Strip Mill", Kawasaki Steel Technical Report, No. 24, Apr. 1991, pp. 32-40.

11.- D. H. Wolf, F. P. Incropera, R. Viskanta, "Jet Impingement Boiling", in Advances in Heat Transfer, Vol. 23, 1993, pp.1-132.

12.- B. Hernandez-Morales, Ph.D. Thesis, UBC, February, 1996.

13.- E. Fried, "Thermal Conduction Contribution to Heat Transfer at Contacts", in Thermal Conductivity, Vol. 2, R. P. Tye Editor, Academic Press, 1969.

14.- A. Hurkmans, G. A. Duit, Th. M. Hoogendoorn, F. Hollander, "Accelerated Cooling and the Transformation of Steel", Proceedings of the Accelerated Cooling of Steel Symposium of the Metallurgical Society of AIME, Pittsburgh, Pennsylvania, August 19-21, 1985, pp. 481-499.

15.- V. H. Hernandez A., I. Samarasekera, J. K. Brimacombe, "Heat Transfer Model of Runout-Table Cooling: a Fundamental Approach", 36th Mechanical Working and Steel Processing Conference, Baltimore, October 17th, 1994.

16.- V. H. Hernandez A., "Heat Transfer Model of the Hot Rolling Runout Table-Cooling and Coil Cooling of Steel", M. A. Sc. Thesis, December, 1994.

17.- D. Auzinger, P. Franz, P. Gerhard, "Process Optimization for Laminar Cooling", Metallurgical Plant and Technology International, v. 19, No. 5, Oct 1996, pp.68-75.

18.- H. Shimizu, K. Kimura, H. Tachibana, et al., "Development of a Runout Table Cooling System for a Hot Strip Mill", La Revue de Métallurgie-CIT, July-August, 1995, pp. 893-898.

19.- F. Seredinski, "Prediction of Plate Cooling During Rolling-Mill Operation", Journal of Iron Steel Institute, Vol. 211, 1973, pp. 197-203.

20.- M. N. Ozisik, Basic Heat Transfer, 1st spanish edition, McGraw Hill, 1979, pp.6.
21.- P. R. Chappidi, F. S. Gunnerson, "Analysis of Heat and Momentum Transport Along a Moving Surface", International Journal of Heat and Mass Transfer, Vol. 32, No.7, 1989, pp. 1383-1386.
22.- F. M. White, Heat and Mass Transfer, Addison-Wesley, 1991, pp. 415.
23.- F. M. White, Viscous Fluid Flow, 2nd. Ed., Mc Graw Hill, 1991.
24.- B. W. Webb, C. F. Ma, "Single-Phase Liquid Jet Impingement Heat Transfer", Advances in Heat Transfer, Vol. 26, pp. 105-217, 1995.
25.-D. A. Zumbrunnen, F. P. Incropera, R. Viskanta, "A Laminar Boundary Layer Model of Heat Transfer due to a Nonuniform Planar Jet Impinging on a Moving Plate", Warme-und Stoffubertragung, 27, pp. 311-319, 1992.
26.- T. Ochi, S. Nakanishi, M. Kaji, S. Ishigai, "Cooling of a Hot Plate with an Impinging Circular Water Jet", Multi-Phase Flow and Heat Transfer III. Part A: Fundamentals, Elsevier Science Publishers B. V., Amsterdam , pp. 671-681, 1984.
27.- J. Kokado, N. Hatta, H. Takuda, J. Harada, N. Yasuhira, "An Analysis of Film Boiling Phenomena of Subcooled Water Spreading Radially on a Hot Steel Plate", Arch. Eisenhuttenwes, 55, Nr. 3, 1984, pp. 113-118.
28.- D. E. Hall, F. P. Incropera, R. Viskanta, "Jet Impingement Boiling from Circular Free-Surface Jets during Quenching Experiments", Proceedings of the ASME Heat Transfer Division, HTD-Vol. 333, Volume 2, ASME, 1996, pp. 131-141.
29.- M. Monde, K. Kitajima, T. Inoue, Y. Mitsutake, "Critical Heat Flux in a Forced Convective Subcooled Boiling with an Impinging Jet", 10TH International Heat Transfer Conference, paper 18-FB-19, 1994, pp. 515-520.
30.- S. Ishigai, S. Nakanishi, T. Ochi, "Boiling Heat Transfer for a Plane Water Jet Impinging on a Hot Surface", Proceedings of the 6th International Heat Transfer Conference, Vol. 1, 1978.
31.- A. Otomo, S. Yasunaga, R. Ishida, "Cooling Characteristics of Steel Sheet by Water Film in Hot Strip Mill", ISIJ, Vol. 73, 1987, (japanese), pp. 80-86.
32.- M. Raudenski, L. Bending, J. Horsky, "Experimental Study of Heat Transfer in Process of Rolls Cooling in Rolling Mills by Water Jets", Steel Research, 65, No. 1, pp. 29-35, 1994.
33.- T. Takeda, Y. Hosokawa, T. Suzuki, T. Hashimoto, K. Takashima, T. Yokoi, "Developement of Dynamic Accelerated Cooling Process", Proc. Symp. on Accelerated Cooling of Steel, The Metallurgical Society of the AIME, Pittsburgh, PA, pp. 133-149, Aug. 19-21, 1985.
34.- S. Kumagai, S. Suzuki, Y. Sano, M. Kawazoe, "Transient Cooling of a Hot Metal Slab by an Impinging Jet with Boiling Heat Transfer", Proceedings of the ASME JSME Thermal Engineering Joint Conference 1995, Lahaina, Maui, Hawaii, March 19-24, 1995, Part 2, pp. 347-352.
35.- J. Filipovic, F.P. Incropera, R. Viskanta, "Quenching Phenomena associated with a Water Wall Jet: I. Transient Hydrodynamic and Thermal Conditions", Experimental Heat Transfer, vol. 8, 1995, pp. 97-117.
36.- N. Hatta, H. Osakabe, "Numerical Modeling for Cooling Process of a Moving Hot Plate by Laminar Water Curtain", ISIJ International, 29, 1989, pp. 955-961.

37.- K. Kimura, S. Ebata, T. Uemura, "Development of Multipurpose Accelerated Cooling System (MACS)", Proc. Symp. on Accelerated Cooling of Steel, The Metallurgical Society of the AIME, Pittsburgh, PA, pp. 283-296, Aug. 19-21, 1985.

38.- S. J. Slayzak, R. Viskanta, F. P. Incropera, "Effects of Interaction between Adjacent Free Surface Planar Jets on Local Heat Transfer from the Impingement Surface", Int. J. Heat Mass Transfer, Vol. 37, No. 2, 1994, pp. 269-282.

39.- S. J. Slayzak, R. Viskanta, F. P. Incropera, "Effects of Interactions Between Adjoining Rows of Circular, Free-Surface Jets on Local Heat Transfer From the Impingement Surface", Journal of Heat Transfer, Vol. 116, February, 1994, pp.88-95.

40.- Y. Haraguchi, M. Hariki, "Analysis of Heat Transfer of Laminar Cooling for Uniform Temperature Control in Hot Strip Mill", Modelling of Metal Rolling Processes, eds. J. H. Beynon, P. Ingham, H. Teichert and K. Waterson, The Institute of Materials, London, 1996, pp. 606-611.

41.- E. K. Kalinin, I. I. Berlin, V. V. Kostiouk, "Transition Boiling Heat Transfer", Advances in Heat Transfer, Vol. 18, 1987, pp. 241-323.

42.- H. Auracher, "Transition Boiling", Proceedings of the Ninth International Heat Transfer Conference, Vol. 1, KN-5, Jerusalem, Israel, 1990, pp.69-90.

43.- H. S. Ragheb, S. C. Cheng, "Surface Wetted Area During Transition Boiling in Forced Convective Flow", Journal of Heat Transfer, Vol. 101, 1979, pp. 381-383.

44.- V. V. Kostyuk, I. I. Berlin, A. V. Karpyshev, "Experimental and Theoretical Study of the Transient Boiling Mechanism", Journal of Engineering Physics, Vol. 50, 1986, pp. 38-45.

45.- C. Pan, J. Y. Hwang, T. L. Lin, "The Mechanism of Heat Transfer in Transition Boiling", Int. J. Heat Mass Transfer, Vol. 32, No. 7, 1989, pp. 1337-1349.

46.- M. T. Farmer, B. G. Jones, R. W. Spencer, "Analysis of Transient Contacting in the Low Temperature Film Boiling Regime, Part 1: Modeling of the Process", 24th National Heat Transfer Conference on Nonequilibrium Transport Phenomena, ASME, pp. 23-29, 1987.

47.- D. H. Wolf, F. P. Incropera, R. Viskanta, "Local Jet Impingement Boiling Heat Transfer", International Journal of Heat and Mass Transfer, Vol. 39, No. 7, 1996, pp. 1395-1406.

48.- Y. Miyasaka, S. Inada, "The Effect of Pure Forced Convection on the Boiling Heat Transfer Between a Two-Dimensional Subcooled Water Jet and a Heated Surface", Journal of Chemical Engineering of Japan, Vol. 13, No.1, 1980, pp. 22-28.

49.- P. B. Whalley, Boiling, Condensation and Gas-Liquid Flow, Oxford University Press,1987.

50.- J. C. Chen, K. K. Hsu, "Heat Transfer During Liquid Contact on Superheated Surface", Proceedings of the Pool and External Flow Boiling Conference, ASME, pp. 257-261, 1992.

51.- H. Del Valle, D. B. R. Kenning, "Subcooled Flow Boiling at High Heat Flux", International J. Heat Mass Transfer, Vol. 28, No. 10, 1985, pp. 1907-1920.

52.- Y. Katto, "A Physical Approach to Critical Heat Flux of Subcooled Flow Boiling in Round Tubes", Int. J. Heat Mass Transfer, Vol. 33 No. 4, 1990, pp. 611-620.

53.- Y. Katto, "A Prediction Model of Subcooled Water Flow Boiling CHF for Pressure in the range 0.1-29 MPa", Int. J. Heat Mass Transfer, Vol. 35, No.5, 1992, pp. 1115-1123.

54.- G.P. Celata, M. Cumo, A. Mariani, "Assessment of Correlations and Models for the Prediction of CHF in Water Subcooled Flow Boiling", Int. J. Heat Mass Transfer, Vol. 37, No.2, 1994, pp. 237-255.

55.- M. Monde, "Critical Heat Flux in Saturated forced Convective boiling on a Heated Disk with an Impinging Jet,, a New Generalized Correlation", Warme Stoffubertrag, Vol. 19, 1985, pp. 205-209

56.- M. Shoji, "A Study of Steady Transition Boiling of Water: Experimental Verification of Macrolayer Evaporation Model", Proceedings of the Pool and External Flow Boiling Conference, ASME, 1992, pp. 237-242.

57.- C. Pan, K. T. Ma, "Modeling of Transition Boiling", Proceedings of the Pool and External Flow Boiling Conference, ASME, 1992, pp. 263-270.

58.- K. O. Pasamehmetoglu, P. R. Chappidi, C. Unal, R. A. Nelson, "Saturated Pool Nucleate Boiling Mechanisms at Heat Fluxes", Int. J. Heat Mass Transfer, Vol. 36, No. 15, 1993, pp. 3859-3868.

59.- M. Shoji, L. C. Witte, S. Yokoya, M. Ohshima, "Liquid-Solid Contact and Effects of Surface Roughness and Wettability in Film and Transition Boiling on a Horizontal Large Surface", Proceedings of the Ninth International Heat Transfer Conference, Vol. 2, 1-BO-23, pp.135-140, Jerusalem, Israel, 1990.

60.- C. H. Lee, I. Mudawar, " A Mechanistic Critical Heat Flux Model for Subcooled Flow Boiling Based on Local Bulk Flow Conditions", Int. J. Multiphase Flow, Vol. 14, No. 6, 1988, pp. 3859-3868.

61.- C. S. Yih, Stratified Flows, Academic Press, 1980.

62.- M. Ishii, "Wave Phenomena and Two-Phase Flow Instabilities", in the Handbook of Multiphase Systems, Hemisphere Publishing Corporation, 1982, pp. 2-95-2-96.

63.- E. K. Kalinin, I. I. Berlin, V. V. Kostyuk, "Film Boiling Heat Transfer", in Advances in Heat Transfer, Vol. 11, 1975, pp. 51-197.

64.- A. Nakayama, Subcooled Forced-Convection Film Boiling in the Presence of a Pressure Gradient, AIAA Journal, vol. 24, No.2, 1986, pp. 230-236.

65.- S. Nakanishi, S. Ishigai, T. Ochi, I. Morita, "Film Boiling Heat Transfer of Impinging Plane Water Jet", Trans. JSME, 46B, 1980, pp. 955-961.

66.- N. Hatta, Y. Tanaka, H. Takuda, J. Kokado, "A Numerical Study on Cooling Process of Hot Steel Plates by a Water Curtain", ISIJ International, 29, pp. 673-679, 1989.

67.- J. Filipovic, R. Viskanta, F. P. Incropera, "An Analysis of Subcooled Turbulent Film Boiling on a Moving Isothermal Surface", International Journal of Heat and Mass Transfer, Vol. 37, No. 17, 1994, pp. 2661-2673.

68.- B. I. Nigmatulin, A. S. Moloshnikov, D. V. Sidenkov, "Interface Oscillations and Heat Transfer Mechanism at Film Boiling", Proceedings of the 10th International Heat Transfer Conference, 1994, paper 10-PB-19A, pp.123-128.

69.- B. W. Webb, C. F. Ma, "Single-Phase Liquid Jet Impingement Heat Transfer", Advances in Heat Transfer, Vol. 26, pp. 105-217, 1995.

70.- M. Militzer, R. Pandi, E. B. Hawbolt, "Ferrite Nucleation and Growth During Continuous Cooling", Metallurgical and Materials Transactions A, Vol. 27A, June 1996, pp.1547-1555.

71.- M. Militzer, E. B. Hawbolt, T. R. Meadowcroft, "Ferrite Nucleation during Continuous Cooling", Proceedings of the International Symposium on Phase Transformations During the Thermal/Mechanical Processing of Steel, CIM, Vancouver, B. C., Canada, 1995, pp. 445-458.

72.- M. Militzer, R. Pandi, E. B. Hawbolt, T. R. Meadowcroft, "Modelling the Phase Transformation Kinetics in Low-Carbon Steels", Proceedings of the International Symposium on Hot Workability of Steels and Light Alloys-Composits, CIM, Montreal, Quebec, Canada, August 24-28, 1996.

73.- R. Pandi, M. Militzer, E. B. Hawbolt, T. R. Meadowcroft, "Modelling of Austenite Decomposition Kinetics in Steels during Run-out Table Cooling", Proceedings of the International Symposium on Phase Transformations During the Thermal/Mechanical Processing of Steel, CIM, Vancouver, B. C., Canada, 1995, pp. 459-471.

74.- R. Pandi, M. Militzer, E. B. Hawbolt, T. R. Meadowcroft, "Effect of Cooling and Deformation on the Austenite Decomposition Kinetics", 37th MWSP Conference, ISS, Hamilton, Ontario, October 1995, Warrendale, PA, Vol. XXXIII, pp. 635-643.

75.- P. C. Campbell, E. B. Hawbolt, J. K. Brimacombe, "Microstructural Engineering Applied to the Controlled Cooling of Steel Wire Rod: Part II. Microstructural Evolution and Mechanical Properties Correlations", Metallurgical Transactions A, Vol. 22A, November, 1991, pp. 2779-2790.

76.- G. E. Dieter, Mechanical Metallurgy, 2nd Edition, McGraw Hill, 1976, pp. 195-199.

77.- M. Umemoto, "Relationships between Microstructure and Mechanical Properties in Steels", Journal of the Iron and Steel Institute of Japan (Tetsu-to-Hagane), Vol. 81, No. 3, 1995, pp. 1-10.

78.- P. Choquet et al., "Modelling of Forces, Structure and Final Properties during the Hot Rolling Process on the Hot Strip Mill", Proceedings of the International Symposium on Mathematical Modelling of Hot Rolling of Steel, CIM, Hamilton, Ontario, Canada, 1990, pp.34-43.

Table 2.1: Parameters for the Natural Convection Heat Transfer in the ROT[20]

Regime	c	n	Range (Gr_LPr)	Orientation
Laminar	0.54	1/4	10^5-$2x10^7$	Upper
Turbulent	0.14	1/3	$2x10^7$-$3x10^{10}$	Upper
Laminar	0.27	1/4	$3x10^5$-$3x10^{10}$	Lower

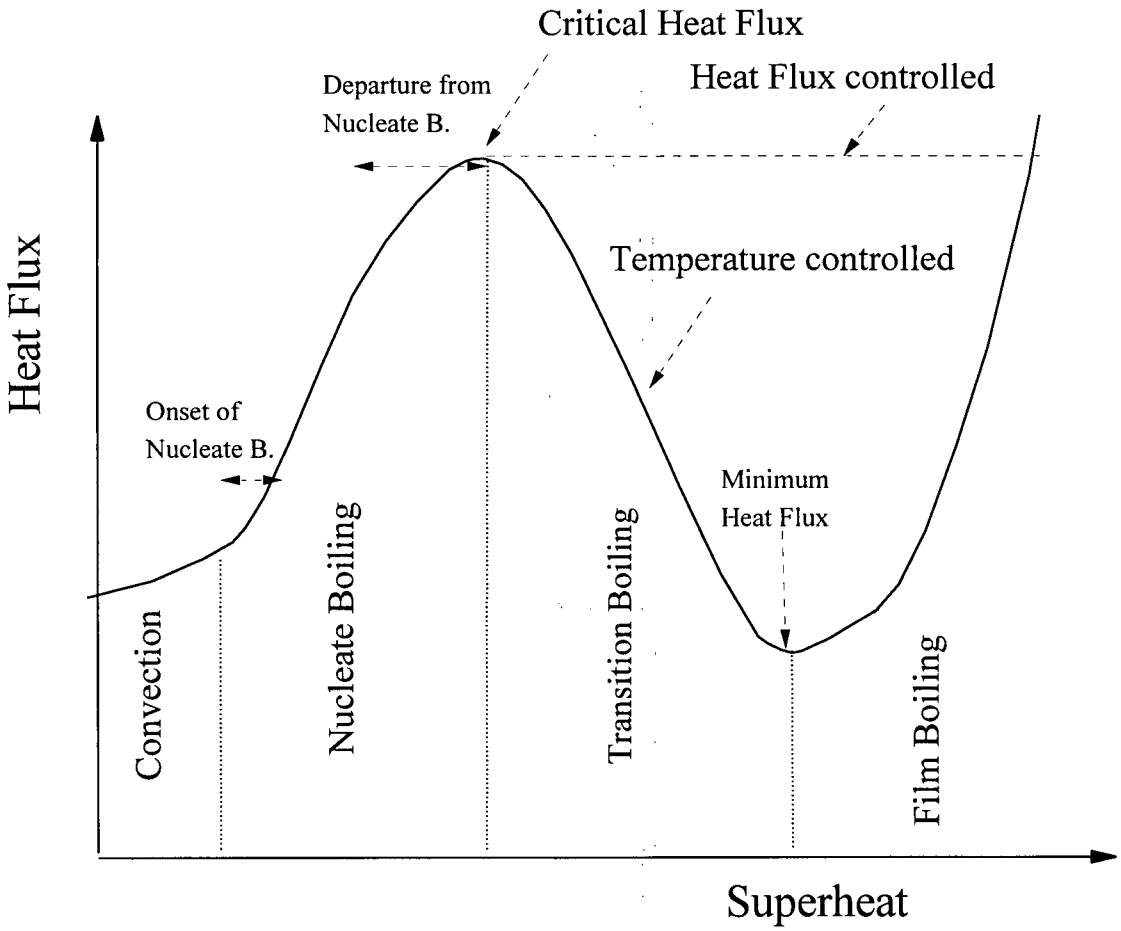

Figure 2.1:Typical Temperature and Heat Flux Controlled Boiling Curves

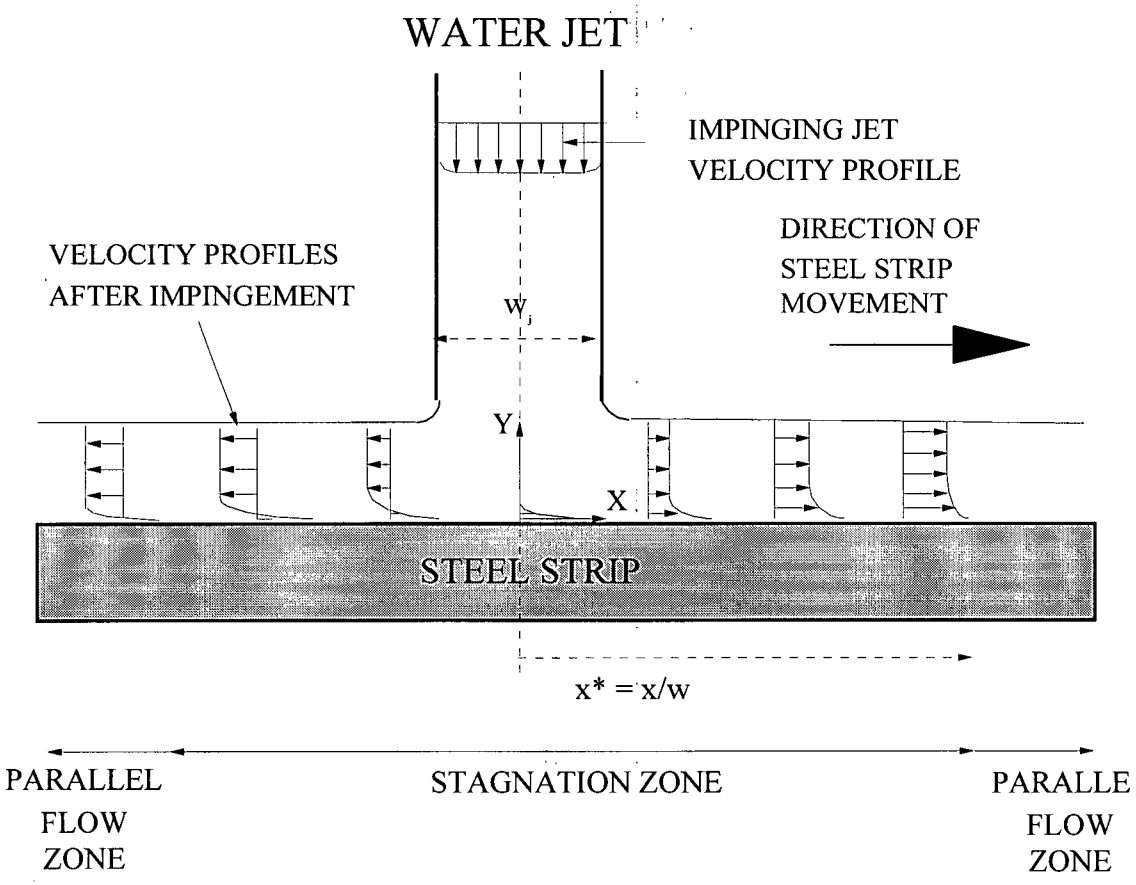

Figure 2.2: Schematic Fluid Flow during Single-Phase Jet Cooling

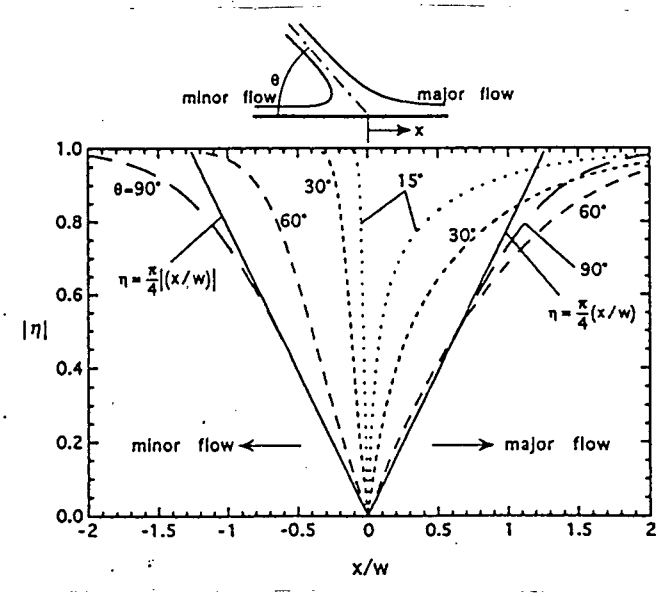

Figure 2.3:Effect of Impinging Jet Angle on the Fluid Flow of a Planar Jet[24]

(a)

(b)

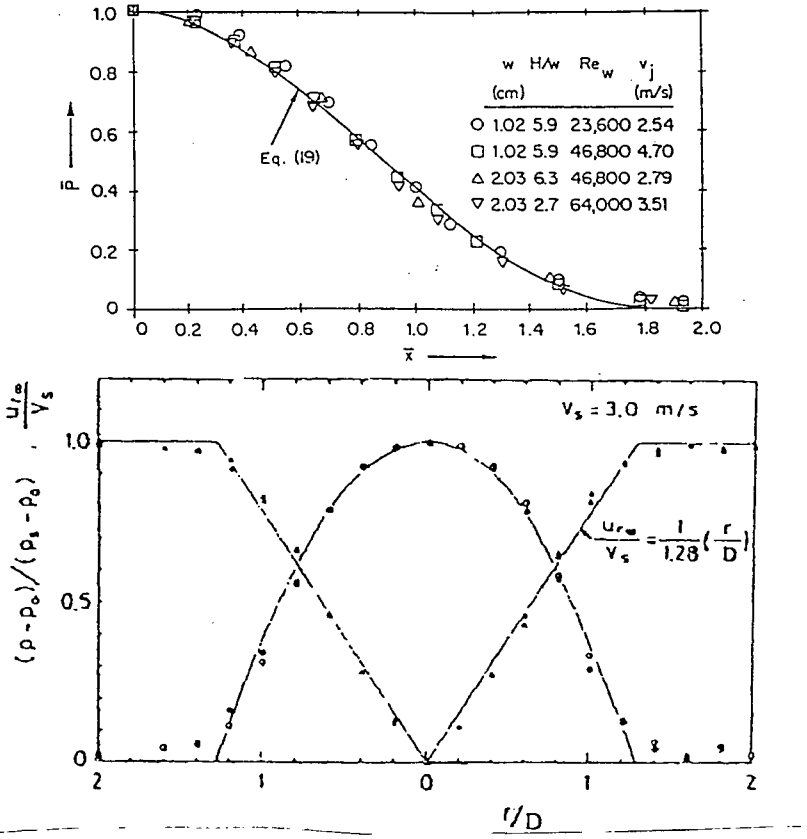

Figure 2.4 Measured Pressure Distribution on a non-moving plate for: (a) Planar Jets[25], (b) Axysimmetric Jets[26]

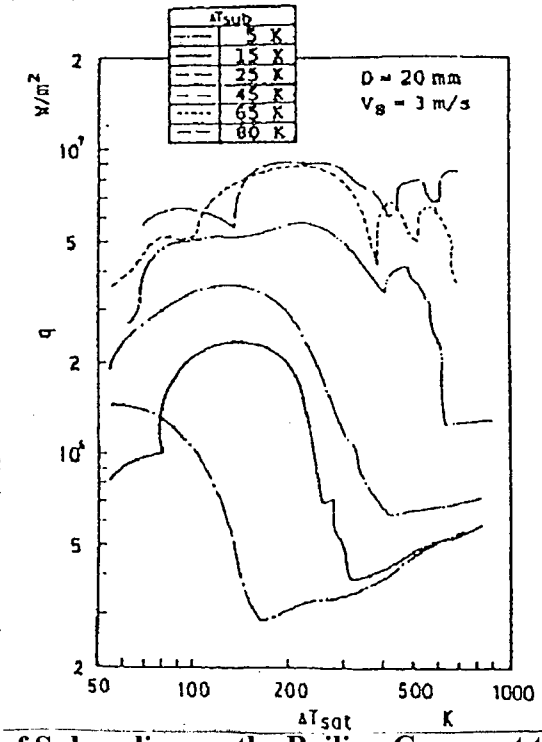

Figure 2.5: Effect of Subcooling on the Boiling Curves at the Stagnation Point of a Water Jet Bar[26] (d_{jet}=20mm, U_{jet}=3m/s)

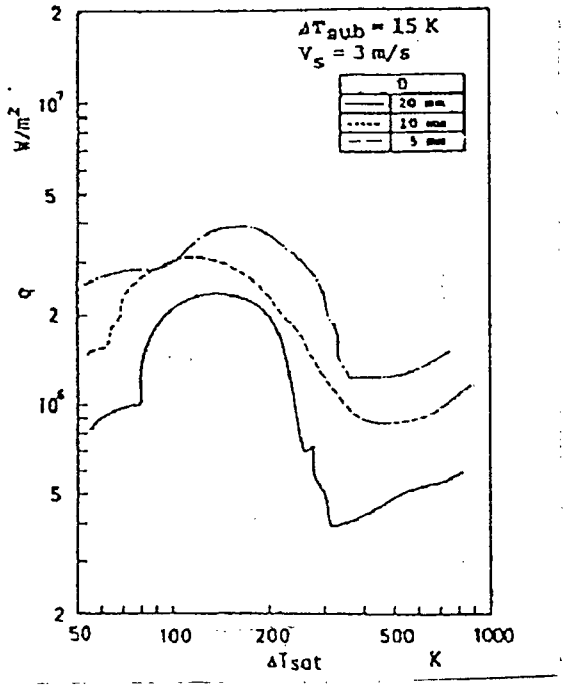

Figure 2.6: Effect of Jet Diameter on the Boiling Curves at the Stagnation Point of a Water Bar[26] (ΔT_{sub}=15°C, U_{jet}=3m/s).

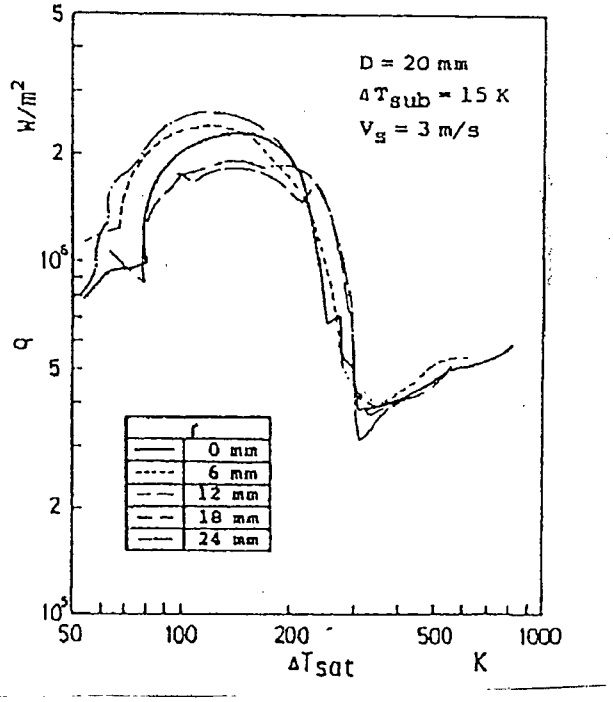

Figure 2.7: Effect of Position in the Impingement Zone on the Boiling Curves of a Water Bar[26] (d_{jet}=20mm, U_{jet}=3m/s, ΔT_{sub}=15°C)

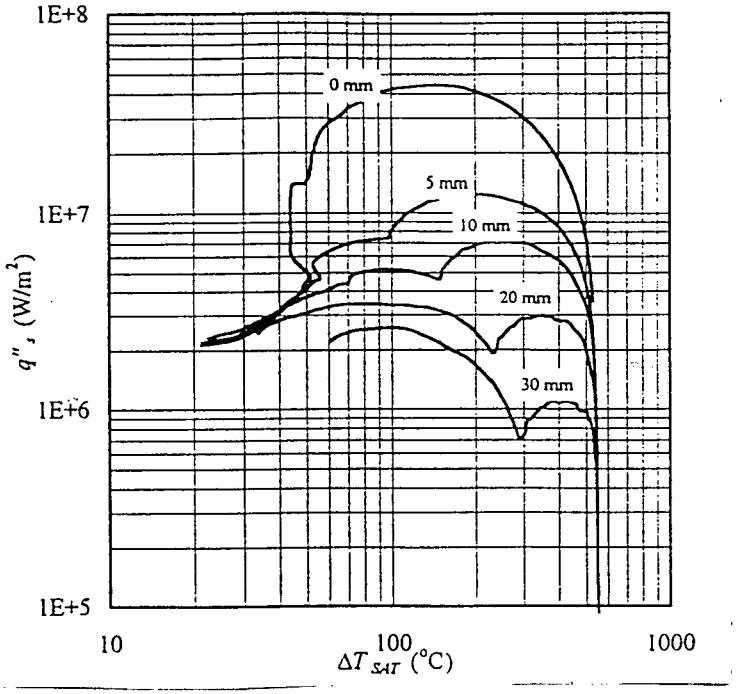

Figure 2.8:Effect of Position from the stagnation point on the Boiling Curves of a Water Bar[28] (d_{jet}=5mm, U_{jet}=3m/s, ΔT_{sub}=25°C, $T_{initial}$=650°C)

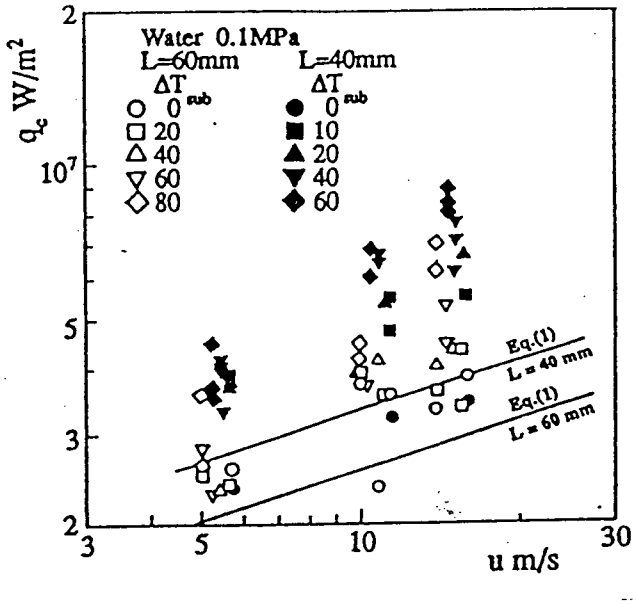

Figure 2.9: Effect of the Impinging Jet Velocity on the Critical Heat Flux of a Water Bar Impinging from the bottom[29].

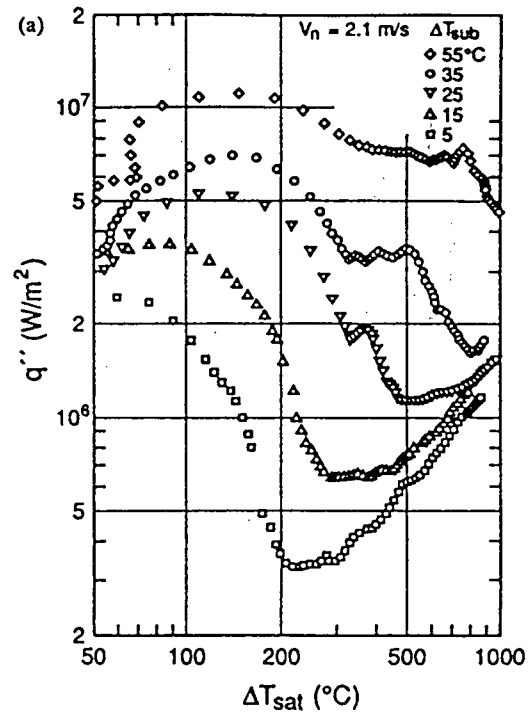

Figure 2.10: Effect of Subcooling on the Boiling Curves for a Water Curtain[30] (u_{jet}=2.1m/s, ΔT_{sub}=5-55°C, w_{jet}=0.0062m, L_{jet}=0.05m , $T_{initial}$=1000°C)

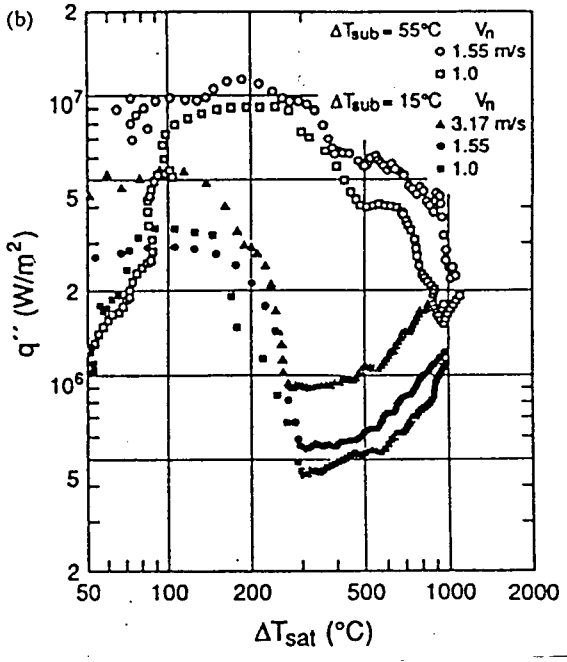

Figure 2.11: Effect of Jet Velocity on the Boiling Curves of a Water Curtain[30] (u_{jet}=1-3.17m/s, ΔT_{sub}=15, 55°C, w_{jet}=0.0062m, L_{jet}=0.05m , $T_{initial}$=1000°C)

[a] [b]

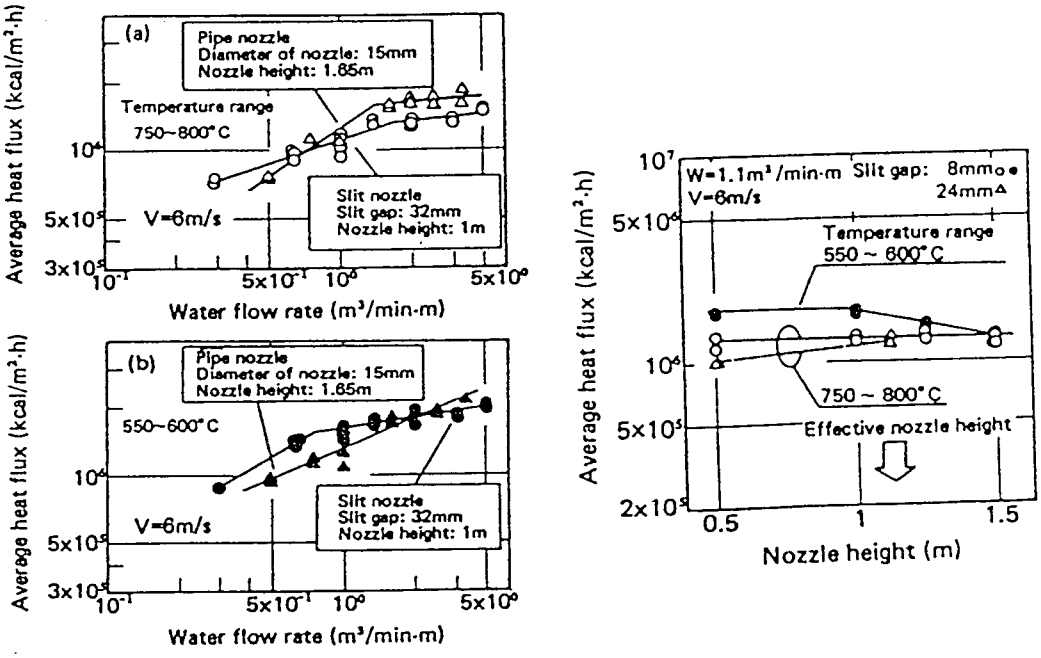

Figure 2.12: Effect of [a] Water flow rate, and [b] Nozzle height, on the Average Heat Fluxes obtained in Cooling Tests[31]

[a] [b]

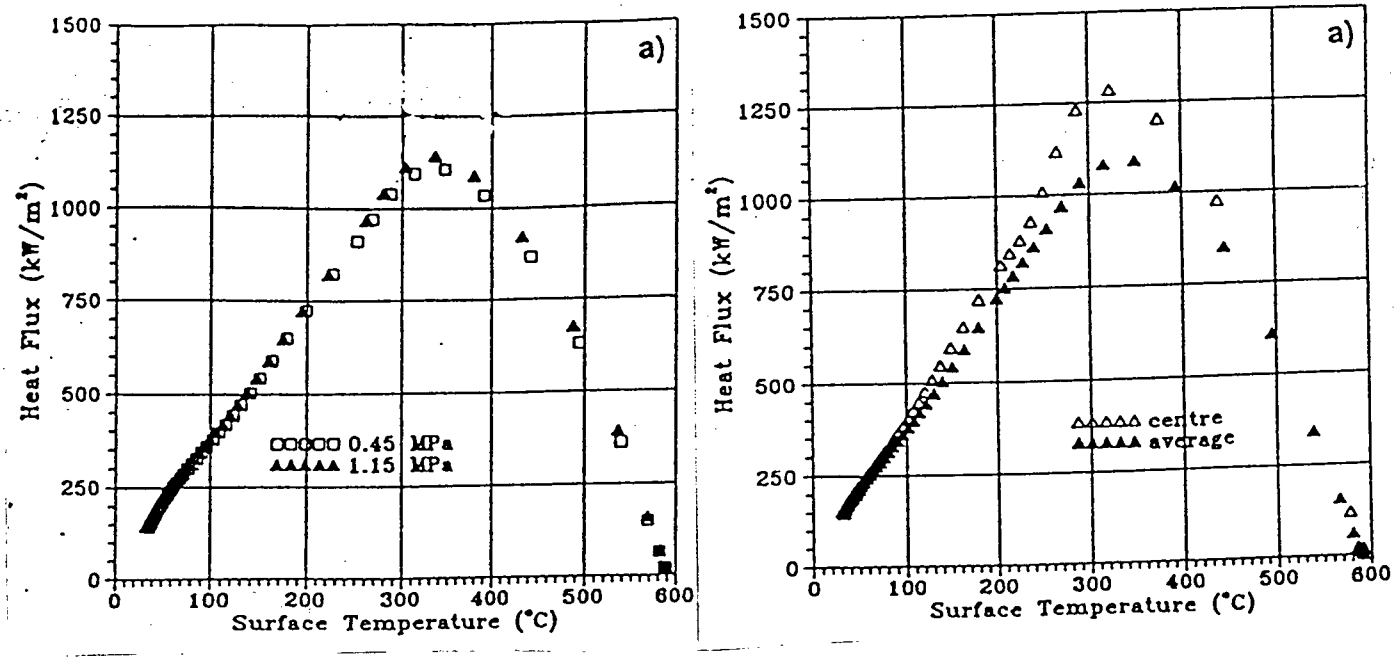

Figure 2.13: Effect of [a] Jet Pressure, and [b] Plate Area on the Boiling Curves for a Water Curtain Impinging on a Vertical Surface[32]

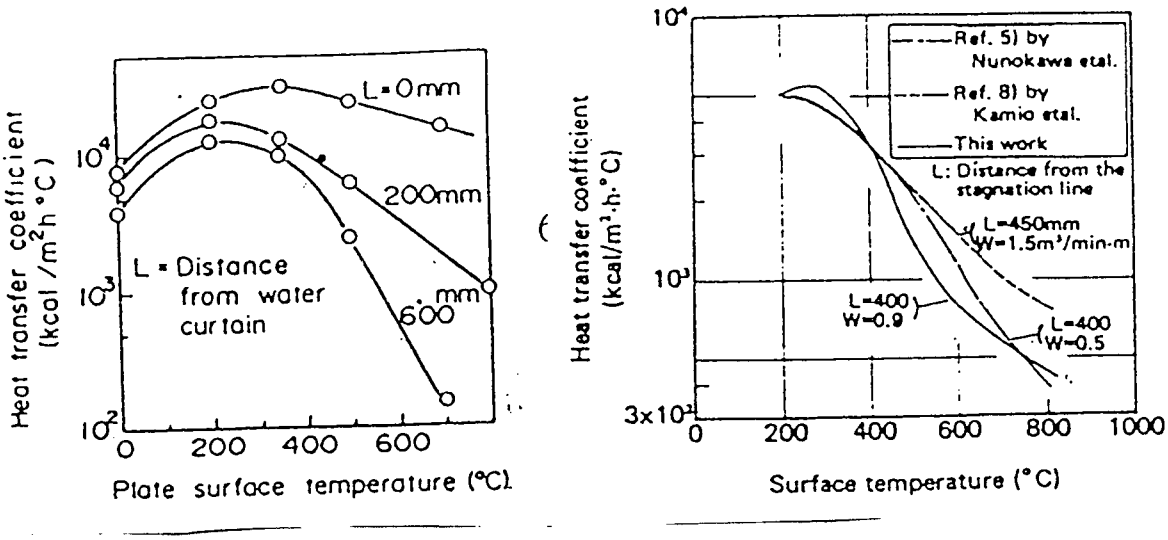

Figure 2.14: Effect of Position from the Impingement Zone of a Water Curtain on the Heat Transfer [31,33]

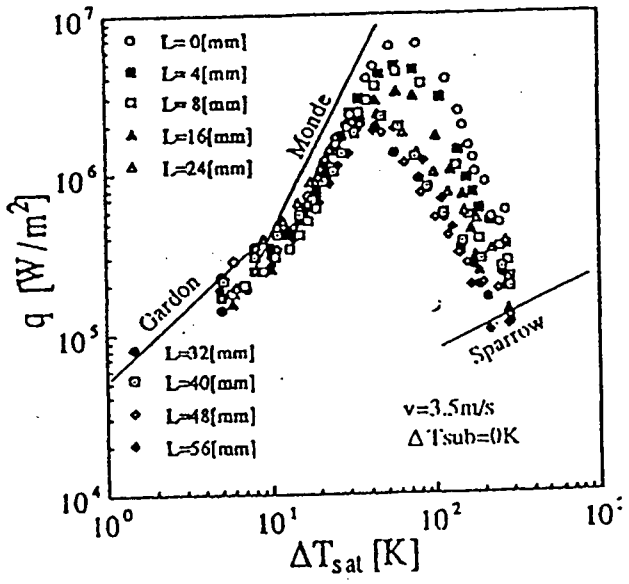

Figure 2.15: Boiling Curves at different locations of a Water Curtain[34] (u_{jet}= 3.5 m/s, ΔT_{sub} =0°C)

[a] [b]

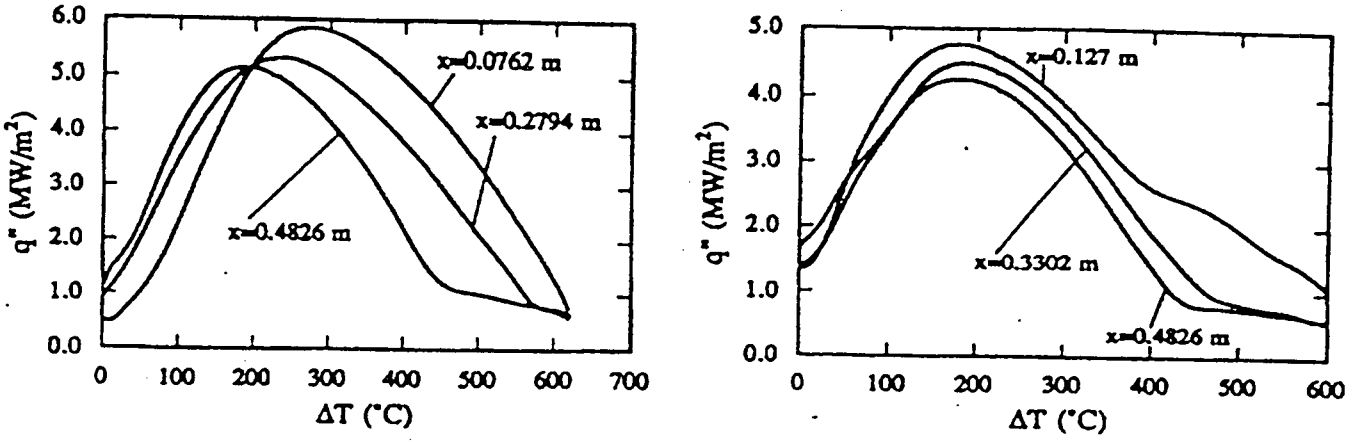

Figure 2.16: Boiling Curves in Parallel Flow [35] for: [a] T_{water}=25°C, u=2m/s, [b] T_{water}=55°C, u=4m/s.

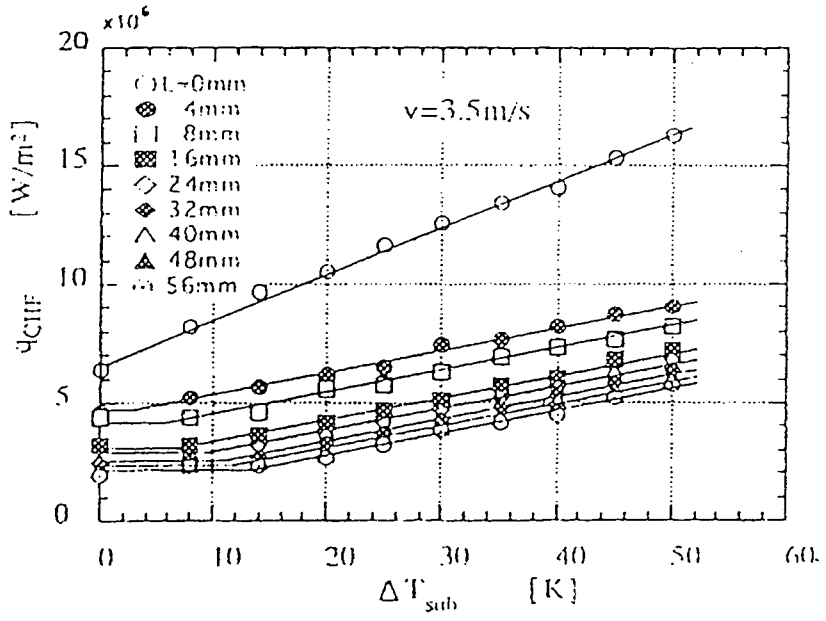

Figure 2.17: Effect of Subcooling on the Critical Heat Flux at different locations from the impingement line of a Water Curtain[34] (u_{jet}=3.5m/s)

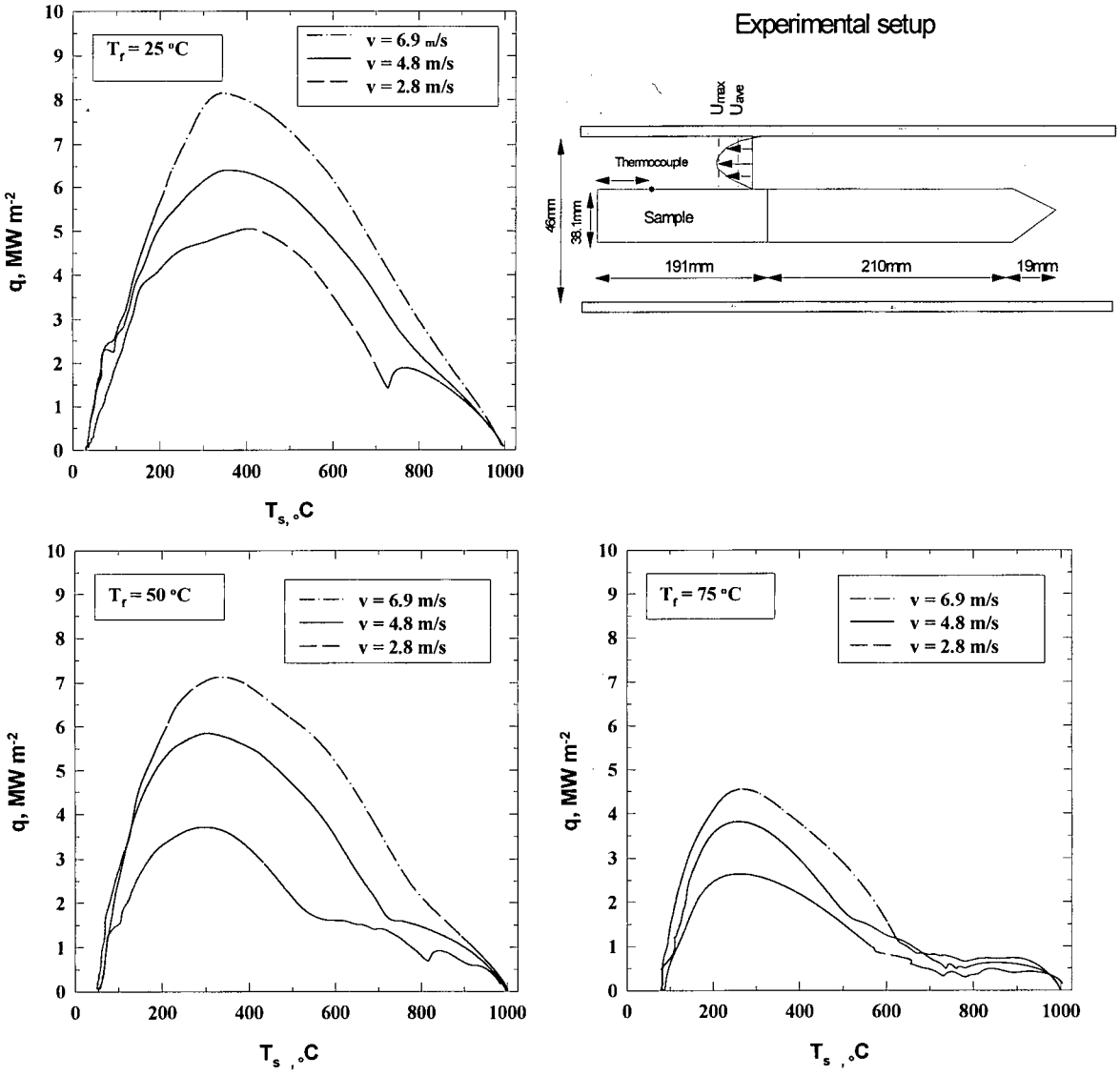

Figure 2.18:Boiling Curves during the Quenching of a Steel Bar in a Pipe under Forced Flow[12]

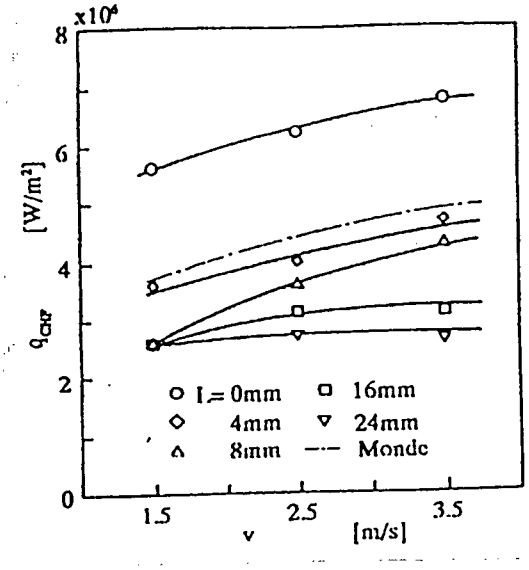

Figure 2.19: Relationship between the Critical Heat Flux and Jet Velocity for a Water Curtain[34]

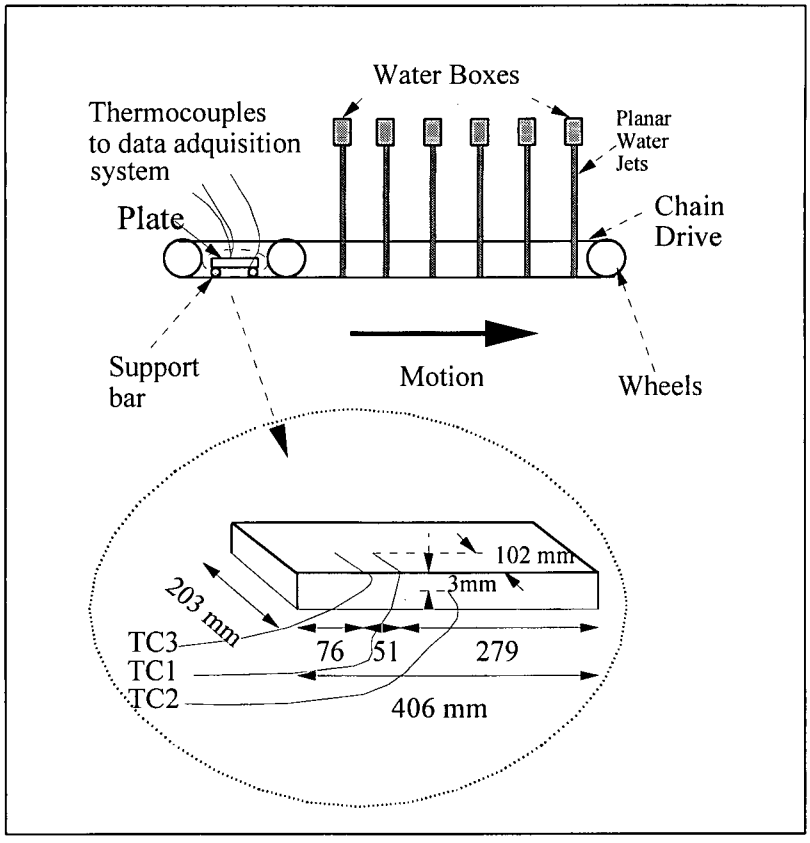

Figure 2.20: Schematic Diagram of Pilot-Plant Runout Table, and Thermocouple Placement for Surface Temperature Measurements[16]

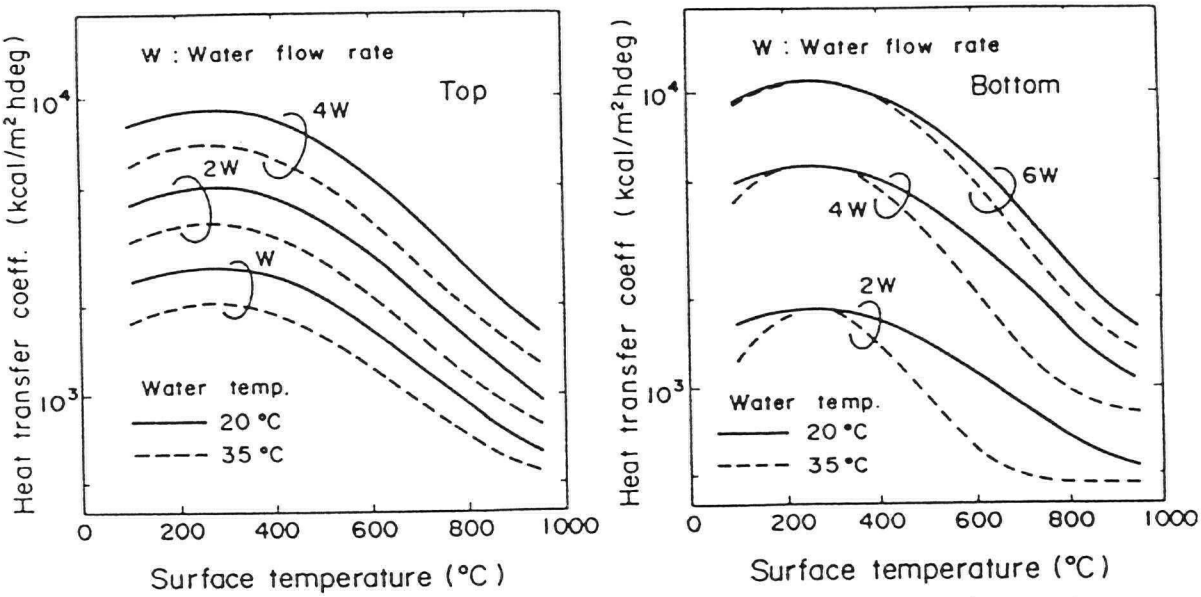

Figure 2.21: Average Heat Transfer Coefficients on the Top Surface Cooled by an Array of Water Bars[37]

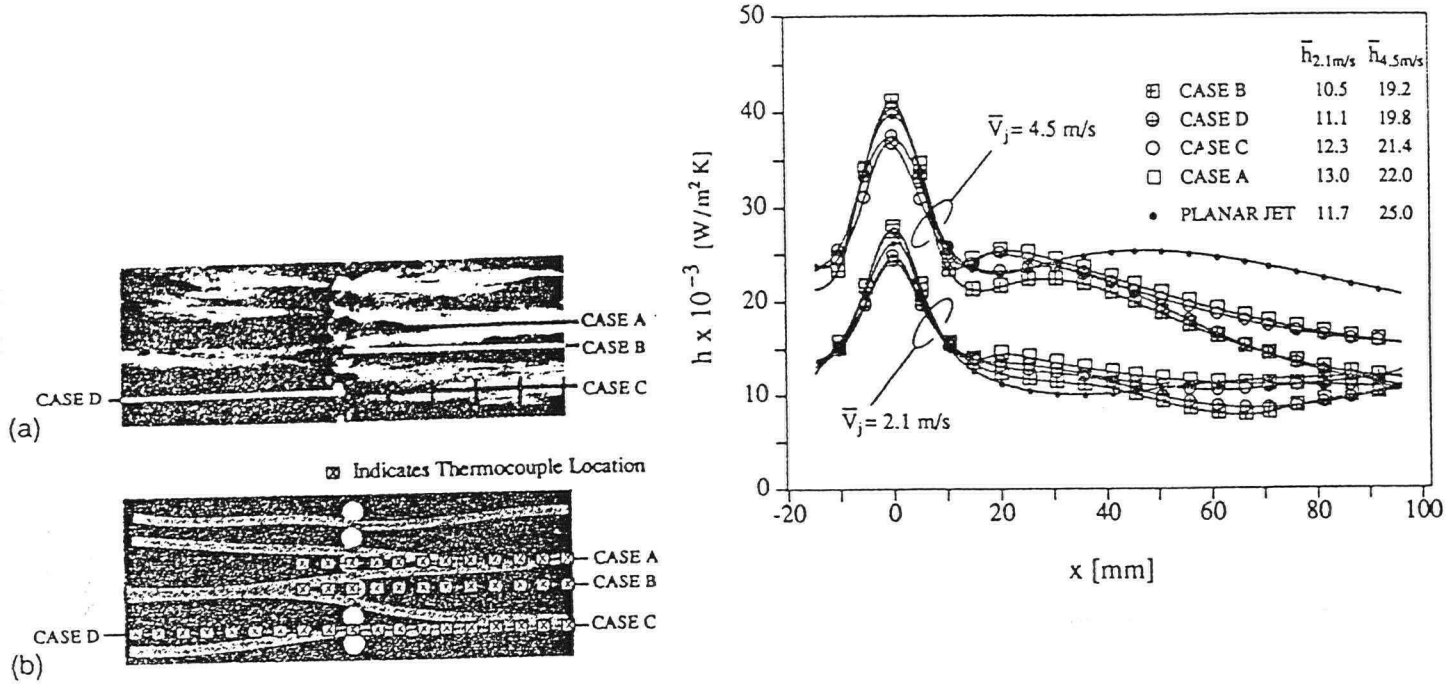

Figure 2.22: Effect of Location Along a Line of Water Jet Bars on the Local Pure-Convective Heat Transfer Coefficients[39]

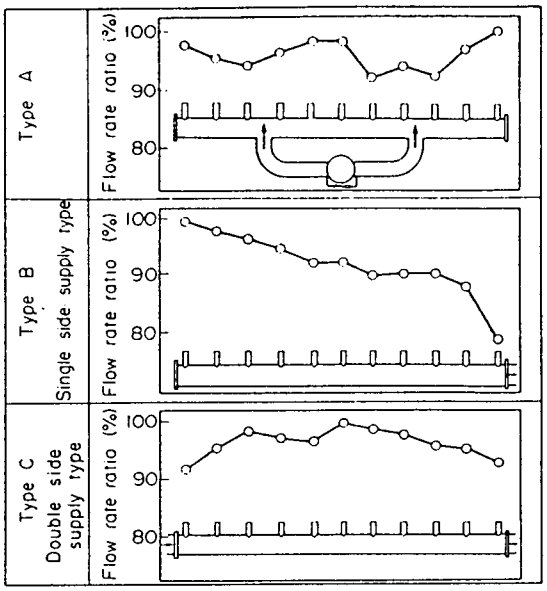

Figure 2.23: Relation between the Water Supply Method and the Flow Rate Ratio Distribution[33]

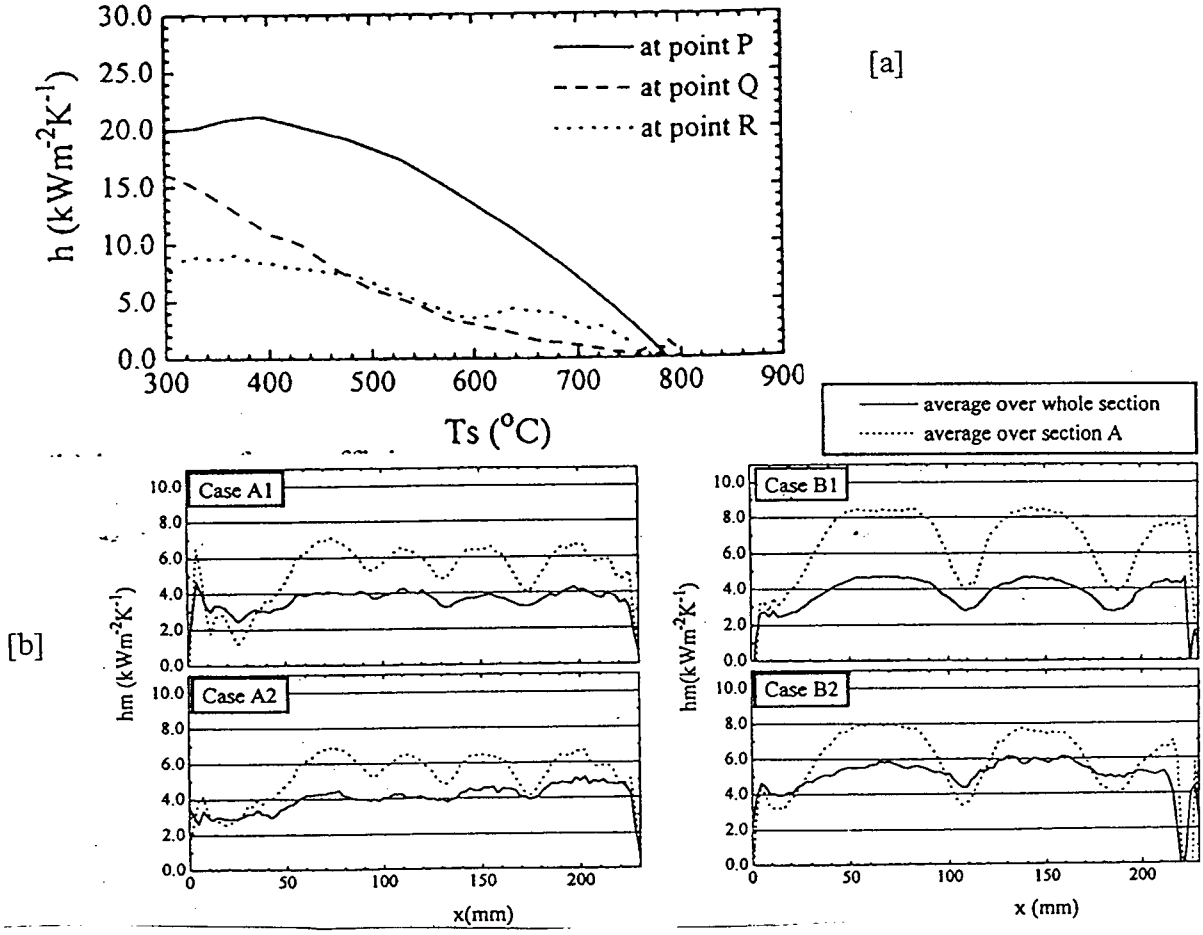

Figure 2.24: Measured Heat Transfer Coefficients for Arrays of Water Bars[40]. [a] At different locations from jet line, [b] Average crosswise distributions over the temperature range 500-800°C.

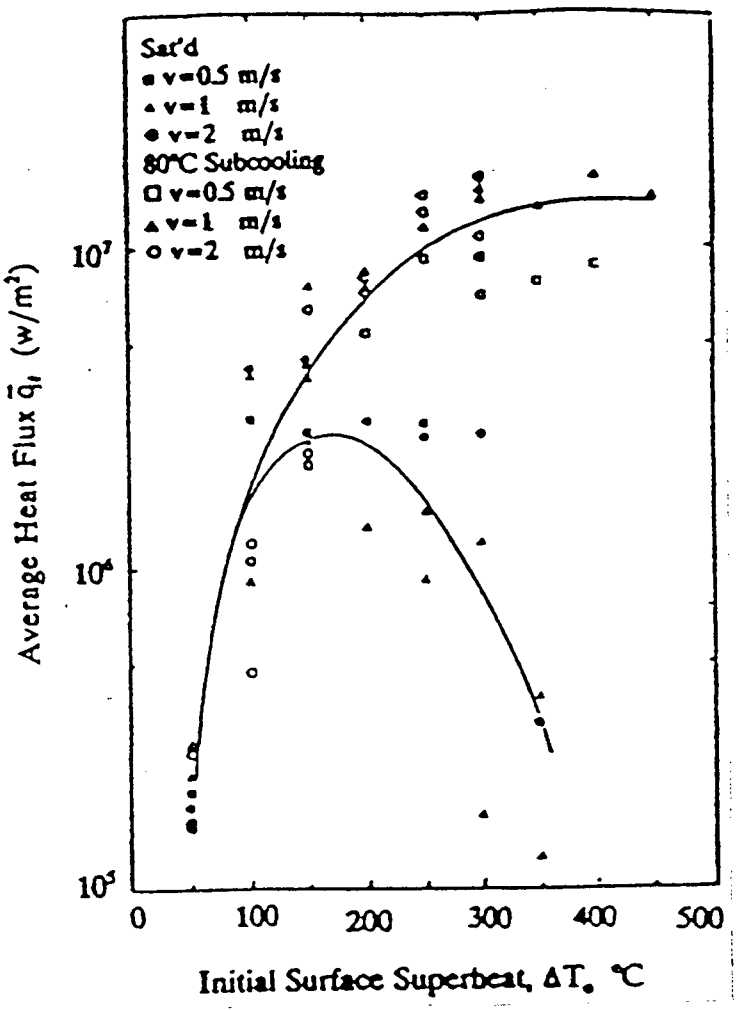

Figure 2.25: Heat Flux during Solid-Liquid Contact of a Falling Drop[50]

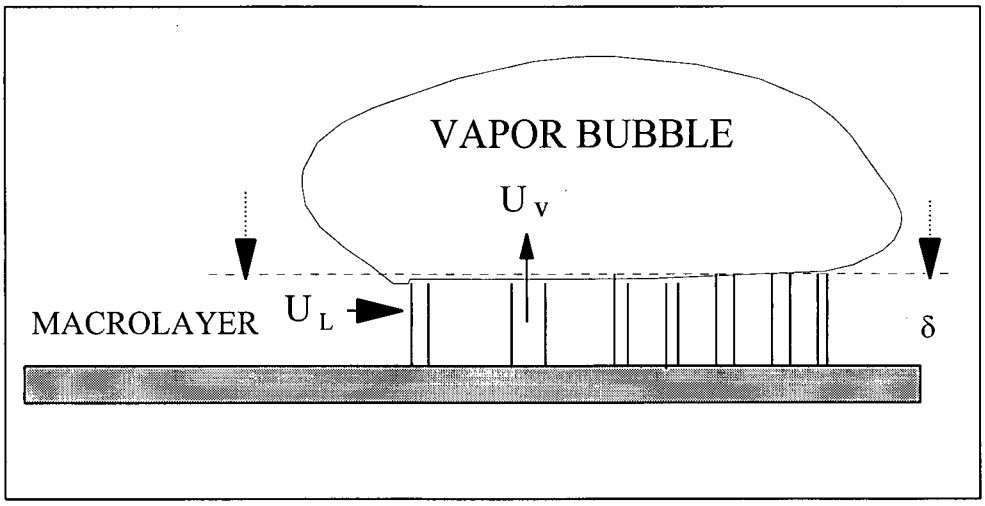

Figure 2.26:Macrolayer Evaporation Mechanism

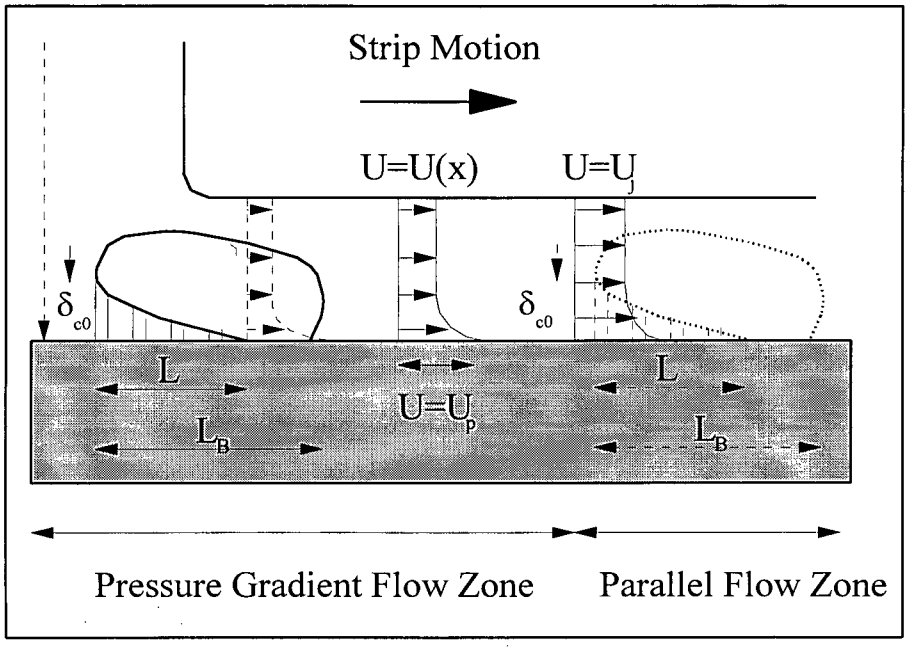

Figure 2.27:The Macrolayer Evaporation Mechanism in Jet Boiling[16]

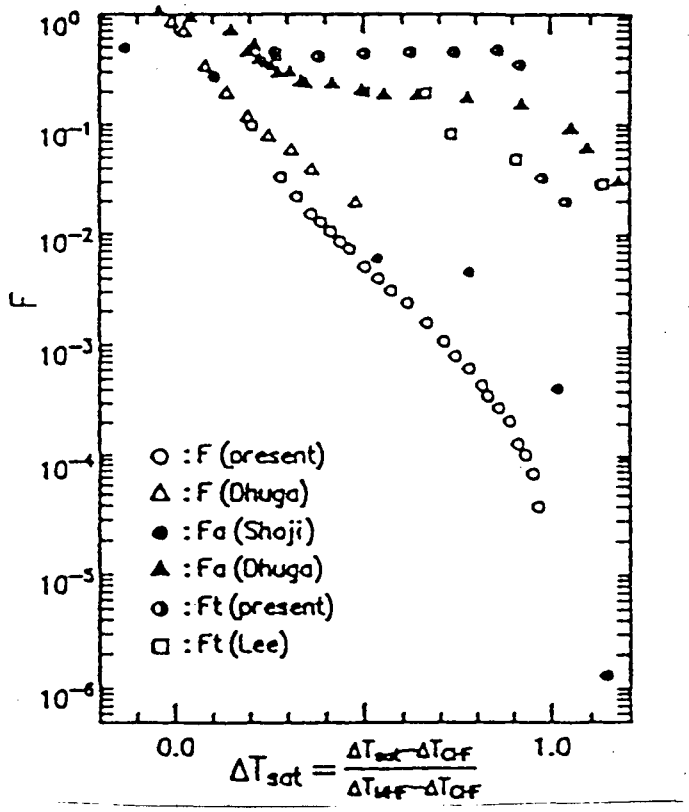

Figure 2.28: Liquid-Solid Fractional Contact Area as a Function of Superheat in Saturated Pool Boiling[59]

[a]

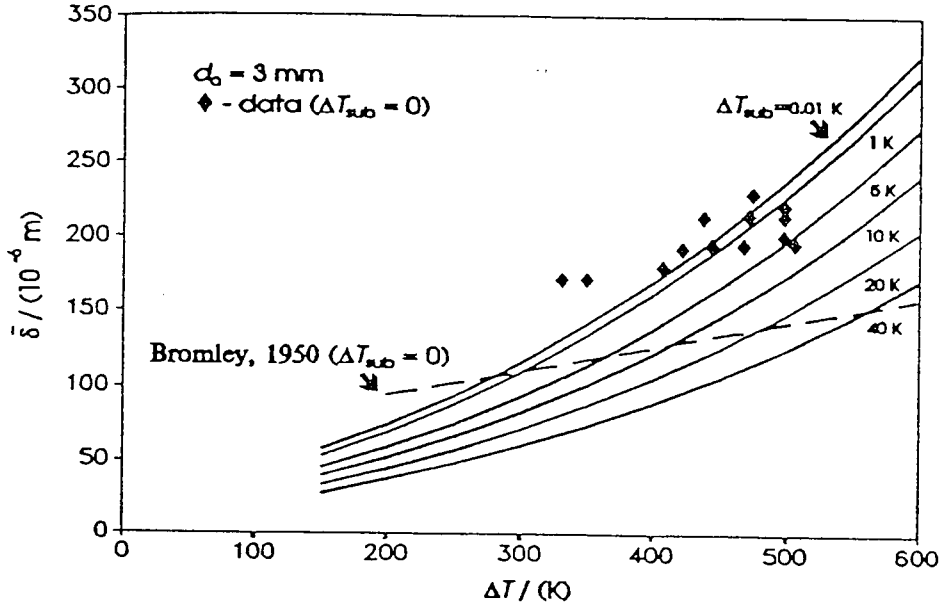

[b]

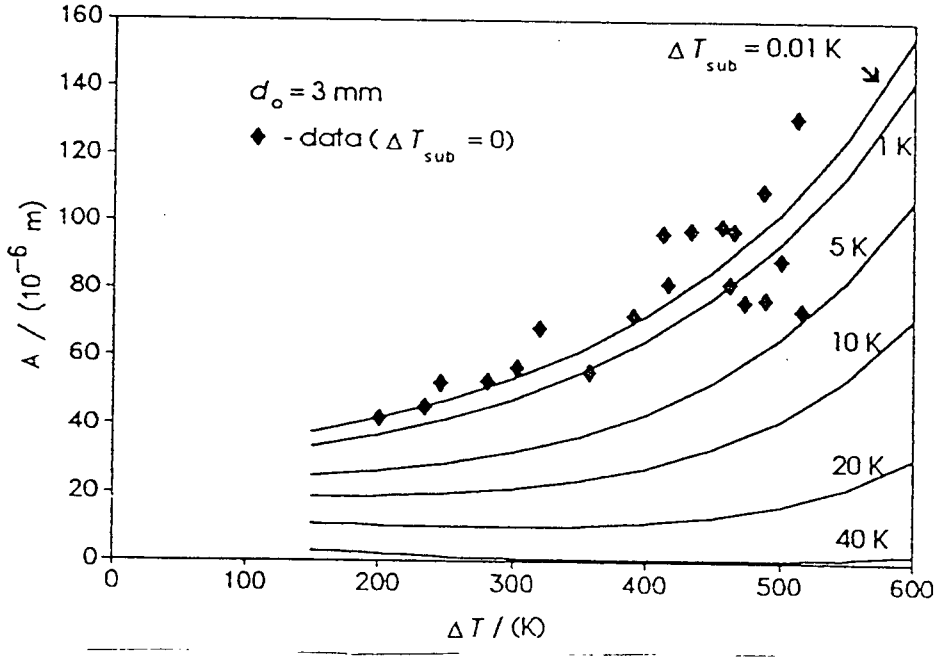

Figure 2.29: [a] Average Vapor Film Thickness, [b] Average Wave Amplitude of Vapor-Liquid Interface in Film Boiling on a Horizontal Cylinder[68]

3. OBJECTIVES AND METHODOLOGY

From the literature review it became evident the need not only for process models which describe the runout table operation better, but also of a unifying approach to link the different experimental results obtained to the actual process events. Recently, the number of published results on the heat fluxes in processes similar to laminar cooling has increased. However, mathematical relationships between the heat fluxes and the process parameters have not been reported in any of the experimental works published. Consequently, those results cannot be applied directly to a process model. It is believed that the lack of understanding of the boiling mechanisms has precluded any form of mathematical description of these results. By developing a boiling curve model, it is intended to provide an explanation of the role of the process variables on the associated heat fluxes; this model is then validated using published data. An additional reason for the development of this boiling model is to extrapolate the behaviour of these experimental results to the real process conditions, since the great majority of the experiments carried out so far are outside the limits of the typical operating conditions.

In order to adopt a realistic approach to solving the heat transfer in the runout table, careful observations of the operation were needed. Given the obvious diversity of the runout table operations, video-recording of the steel on the runout table was obtained for several mills. This data was analyzed and characterized to obtain a unified treatment of the thermal events for the mills analyzed. Even though the thermal and fluid flow conditions are visible to the naked eye, observations or analysis of this kind have never

appeared in the literature even though they are indispensable to the understanding of the operation of the runout table.

Experimental measurements of the heat fluxes during the runout table cooling for typical operating conditions are considered to be extremely difficult and complicated, and therefore beyond the scope of this work. The reason for this is the fact that in the runout table the cooling is in 2-D (across the width and along the length of the strip), and it is approaching a steady state condition (except for small variations due to differences in the initial runout table temperature) at a fixed position in space. This is due to the strip motion which cannot be reproduced completely by measurements on a static strip, or in experiments using small moving plates. Consequently, the development of the boiling curve model arises as an alternative tool to create a runout table process model and may provide the framework for the development of more explicit mathematical equations to describe future quantification of cooling on the runout table.

The main goal of this work is the development of a mathematical model to predict the thermal events taking place during a wide range of runout table cooling operations.

3.1 Objectives

To accomplish this goal, the objectives of this work can be stated as:

[1] Development of an accurate model that links the runout table layout (type of cooling system, position of the water jet lines, nozzle position and characteristics, etc.), the operating conditions (strip finishing-rolling temperature, thickness, speed, and acceleration; water flow velocity, temperature; water jetlines on/off) and the chemistry of steel with the thermal history of the steel. Specifically, the steel grades

under study are the plain carbon A36 steel (approximately AISI 1018) and DQSK (approximately AISI 1005).

[2] To make a systematic study of the characteristics of the water flow on the surfaces of the strip and to relate them to the thermal events.

[3] To establish a fundamentally based framework to analyze the results and observations obtained in laboratory, pilot-plant and full-scale experiments related to laminar cooling, and the creation of a model to predict the local boiling curves in terms of the process variables.

[4] To relate or link the thermal model to a detailed phase transformation model to predict the effect of phase transformations on the thermal history of the steel.

3.2 Methodology

To accomplish these objectives the following methodology was followed:

[1] Development of the runout table process model. This includes the finite different solution of the 1-D transient non-linear* heat conduction equation in the strip with variable boundary conditions according to each cooling zone (jet impingement, parallel flow, air cooling). The initial conditions can be those obtained from mill measurements or from an existing finishing mill process model developed at The Centre for Metallurgical Process Engineering, UBC.

* The heat conduction equation with temperature-dependent thermal properties is classified as a non-linear partial differential equation in standard books of differential equations and heat conduction books, such as the one by Ozisik, "Heat Conduction", 2nd Edition, John Wiley and Sons Inc., 1993, pp. 437.

[2] Development of the boiling curves during jet cooling. This includes the analysis of the microscopic and macroscopic mechanisms of boiling. In order to be able to understand the behaviour of the vapor-liquid interface during film and transition boiling under a wide variety of process parameters, the solutions of the fluid flow and heat transfer equations are required. The solution of Navier-Stokes equations for film boiling in the impingement region and the parallel flow zones for a moving surface was obtained by the boundary-layer integral method. A transition boiling model which allows the prediction of the full boiling curve was developed based on the adoption of the macrolayer evaporation mechanism linked to a trial and error procedure to estimate the liquid-solid contact area based on published work and the results of the film boiling model. Verification with experimental and theoretical data published in literature was carried out.

[3] Collection of mill operating data and video-recording of the runout table, coiling and coil cooling operations. Empirical analysis of the mill data was carried out to establish similarities and differences in the efficiencies of the different operations. The video-recordings were systematically studied to determine regions of more favorable heat transfer, and if possible, to determine the specific cooling mechanisms.

[4] Incorporation of the models for austenite decomposition kinetics to include the effect of the heat generated by such transformations on the thermal history of the steel. In particular, the mathematical models developed at The Centre for Metallurgical Process Engineering, UBC, to predict the austenite decomposition of the A36 and DQSK steels during non-continuous cooling conditions were included.

[5] Verification of the runout table model. Comparison of the coiling temperatures for A36 and DQSK steel strips manufactured in about ten hot strip mills was carried out to establish the range of applicability and the accuracy of the model.

4. OBSERVATIONS OF THE FLUID FLOW AND HEAT TRANSFER IN THE RUNOUT TABLE OPERATIONS

Even though in most of the mills the operation of the runout table can be observed by the naked eye, many details of the water jet interaction with neighbor jets and the moving strip have not been recognized, therefore their importance in the performance of the runout table has not been studied. It is evident in the significant differences between the plant operations, that a standard criteria or understanding of how to operate the runout table is not existent, so a wide variety of conditions are adopted based on highly empirical trial and error procedures along with computer control, which allows a steady operation of the process. Additional improvements in the optimization of the process are still needed given the rising demands in the steel properties and quality; probably the only way to attain this progress is by obtaining a better understanding of the process itself. Consequently, a systematic study to characterize the fluid flow and the heat transfer phenomena and their relationship with operation parameters and product quality is highly desirable. That kind of study can only be carried out by a careful observation of several operations, which is more favorably done by video-recording the different operations and further characterization of the video and photographic observations.

With that goal, the operations of five hot strip mills were video-recorded and photographed to characterize the fluid flow of water from the issuing nozzles to the flow on the strip during cooling. An additional goal was to determine through qualitative observation of the strip color, the relative magnitude of the local heat extraction in the different fluid flow zones. The video-recordings were obtained using a Quasar video

recorder (Zoom 8x, tape type VHS-C), with no special filters, and photographs were taken on 35mm color film.

A photographic summary of the observations is presented in Figure 4.1 to Figure 4.16. In order to systematically characterize the fluid flow phenomena, the flow was divided into several zones: [1] The pre-impingement of top jets, [2] The impingement and the jet interaction zones, [3] The downstream parallel flow region, [4] The upstream parallel flow region, [5] Bottom jets. A summary of the relevant fluid flow characteristic observed in each of these regions is presented in Table 4.1 to Table 4.5. A discussion about the similarities and differences between the runout table operations is presented.

[1] Fluid Flow characteristics of the pre-impingement top jet.

The jets prior to impingement are in many cases turbulent, and in some cases can be discontinuous because of the low jet velocity and the effect of gravity. The impingement jet diameter (or jet width for curtains) is reduced by 30-50% because of gravity acceleration, as summarized in Table 4.1. These characteristics can be better seen in Figure 4.3, Figure 4.5, Figure 4.8, Figure 4.9, and Figure 4.12, for each company.

[2] Fluid Flow in the impingement and jet interaction zones of top jets.

The impingement region of a single bar jet is rarely seen in operation, because the interaction of the neighbor jets prevents it. However, in Figure 4.4 the impingement region of single jets are seen, wherein the water flow rate was considerably reduced and the effect of neighbor jets reduced. The impingement region is confined to an area similar to the pre-impingement jet cross section, and beyond this, the water flows parallel to the moving strip surface almost immediately, without significant sputtering. This is a

remarkable difference between the fluid flow found in experimental setups on non-moving surfaces and the actual flow in the runout table.

The interaction between circular jets in a jetline is extremely complicated, and it is very much characteristic of each jet arrangement, as it is seen in Figure 4.2, Figure 4.5, Figure 4.9 and Figure 4.13 for each company. However some common characteristics are:

[i] The presence of "dark holes". The holes are formed by the pressure exerted by the jet, but these were observed to correspond to groups of jets rather than to individual jets. The dark appearance of the strip surface reveals that in this region the heat extraction is the highest (see Figure 4.5, Figure 4.9 and Figure 4.13). This feature could not be observed in company A.

[ii] Formation of water peaks. Immediately after impingement, the water forms "peaks" as a results of the strong interaction between the jets and the dragging effect of the strip motion, appearing only in the downstream direction. These are zones of high concentration of water, which later on, in the downstream parallel flow region, are transformed into water stripes. The thick appearance of these peaks is a result of some sputtering caused by the interaction of different streams. The strip surface was dark underneath these areas of high water flow density (see Figure 4.5, Figure 4.10 and Figure 4.13). Water peaks were not observed in company A.

[3] Fluid flow characteristics of the downstream parallel flow zone.

The downstream parallel flow region, which appears after the strong interaction between jets, is also strongly dependent on the bar jet configuration. This region can be

better observed in Figures 4.2, 4.6, 4.7 (curtain), 4.9, and 4.14 for each company. Common characteristics in this region are:

[i] Presence of water "stripes". Water flows for some distance near the impingement jet mainly in "stripes", coming from previous peaks (see Figure 4.2, Figure 4.4-5, Figure 4.11 and Figure 4.15). The top surface of the steel strip has "stripes" of different tonalities, suggesting that an important portion of cooling occurs on bands or stripes parallel to the strip longitudinal axis. The thickness of those stripes is variable, depending on the runout table configuration, and the tonalities vary as well with each mill. The thickness of the stripes seem to be between the diameter of the impingement jet and the jet impingement region (2.6 times the jet diameter). These stripes are regions of localized cooling, as it is evidenced by the dark-red color of the strip underneath. Interestingly, Figure 4.4 shows that water stripes can be formed without the effect of neighbor jets, and they are caused mainly by the strip motion.

[ii] Smooth boundary between the downstream flow and the upstream flow of the next jet line. No sputtering appears (see Figure 4.2 and Figure 4.16).

[4] Fluid flow characteristics of the upstream parallel flow zone.

The fluid flow in the upstream (countercurrent) parallel flow region is completely different of that found in the downstream. Characteristics of this region are seen in Figures 4.1, 4.5, 4.7, 4.10, and 4.16 for each company. The flow is almost stagnant at the top of a continuous layer, and its thickness is considerably higher than what may appear in the downstream. From Figure 4.4, it may be seen that the dragging effect of the strip motion makes the countercurrent flow decrease its velocity and even change direction,

creating a continuous water film. In this region no water stripes were observed. From the color of the strip surface, this region seems to be of higher local heat transfer than the downstream parallel flow region. However, for company H, apparently water flowing downstream from the previous jet line seemed to flow underneath the countercurrent flow, and the dark stripes prevail in this zone.

[5] Bottom jets fluid flow.

The bottom jets are turbulent, and in occasions tend to form almost a curtain. Nozzles are tilted in the direction of the strip motion, which enhances the contact of the water with the strip. The jets increase their diameter slightly because of the reduction of the jet velocity due to gravity.

As summary, these observation show that in the cooling by water bars, the highest cooling is attained at the relatively small impingement band, followed by the cooling in the parallel flow areas of higher water flow density, such as the countercurrent zone and the water stripes. Also, localized cooling was evident in the regions where sweepers interact with the parallel flow, wherein a recirculating flow is formed.

The different tonalities of the steel surface reveal differences in temperature, and the differences in color in the parallel flow region are enough to suggest substantial differences in local heat fluxes. At the typical operation temperatures, transition and film boiling are mainly present, and distinguishing between them is of great importance to understand the cooling process.

Given the close relationship between the local water flow density (or thickness of the water layer at a particular position) and the local heat fluxes, a parameter related to

the amount of water supplied locally must be determining the existence of localized cooling. This has also been recognized in several cooling systems and has led many researchers to relate global heat tranfer with global water flow densities. From the literature review and an overview of the possible parameters causing this, only two fundamental parameters of the flow appear responsible: the local water velocity and the local water temperature.

Even though water velocity measurements of the parallel flow streams on the runout table are practically impossible, from visual inspection it is clear that the water velocity seems constant across the width of the strip, so the velocity between adjacent stripes of high and low water flow density observed in the downstream parallel flow zone is for practical purposes the same. Consequently, differences in water velocity in the parallel region are very unlikely to be responsible for the localized cooling observed. Also, even in regions where the water velocity is comparatively small, such as the countercurrent parallel flow region, higher rates of heat extraction have been found as compared to its corresponding downstream flow (see Figure 4.1). Finally, if water velocity played a significant role, then the effect of nozzle height on cooling would be extremely important, since the water velocity is mainly dependent of this parameter. Figure 2.12[b] shows clearly that it is not the case.

Accordingly, the local water temperature must be responsible for the localized cooling in these areas. This results is not surprising since it is evident in the literature review the strong effect of water temperature on the heat fluxes in any region of the runout table. This is the only parameter that can explain the strong effect that flowrate has

on the cooling performance of a runout table (see Figure 2.12[a]). In regions of higher water density, the heat absorbed increases the local water temperature to a lesser extent than in regions of low water flow density. The countercurrent parallel flow region characterized by an almost stagnant thick water layer, and its local temperature is determined by a complex mixture of factors, which mainly encompasses the local water temperature of the previous jetline and the mixing with the current jetline flow. Probably in many cases this area is a relatively cool water layer, which as expected, should have a higher heat extraction, as observed in operations.

The importance of the use of sweepers relies on the same principle. Sweepers supply colder water to part of the parallel flow region, so the local water temperature is lowered and the heat extraction enhanced. Sweepers are important because they prevent the mixing of water at higher temperature with the colder water of the next cooling section, providing the next cooling sections with lower local water temperatures that increase the heat extraction.

It is important to mention that differentiation between transition and film boiling cannot be based entirely on these observations, since transition boiling of high temperature water may be comparable with film boiling of colder water, and transition boiling for different water temperatures can vary substantially.

The cooling after some distance in long parallel flow regions, mostly at the end of the runout table, seemed to be almost negligible, suggesting that after the water has reached a relatively high temperature, its cooling performance is diminished, corresponding to the presence of film boiling of almost saturated water, which in

magnitude is close to radiation in air. Consequently, it was observed that the presence of water under those circumstances is not advantageous.

One practical application of these observations would be in the proper design of the header, nozzle arrangement and the operating water flow rate and temperature to attain specific functions of the cooling system. For example, if maximum heat extraction and minimum variation across the width of the strip is required, the header must deliver water at a uniform rate to the different nozzles, so each of the nozzles receives the same water flow rate. The nozzle arrangement should be offset between jetlines, and preferably they should be close to each other within a jetline; the distance between the jetlines should be short and the water supplied at high water flow rates and low temperatures. The guiding principle should be to maintain low local water temperature and uniformity of the water flow across the width.

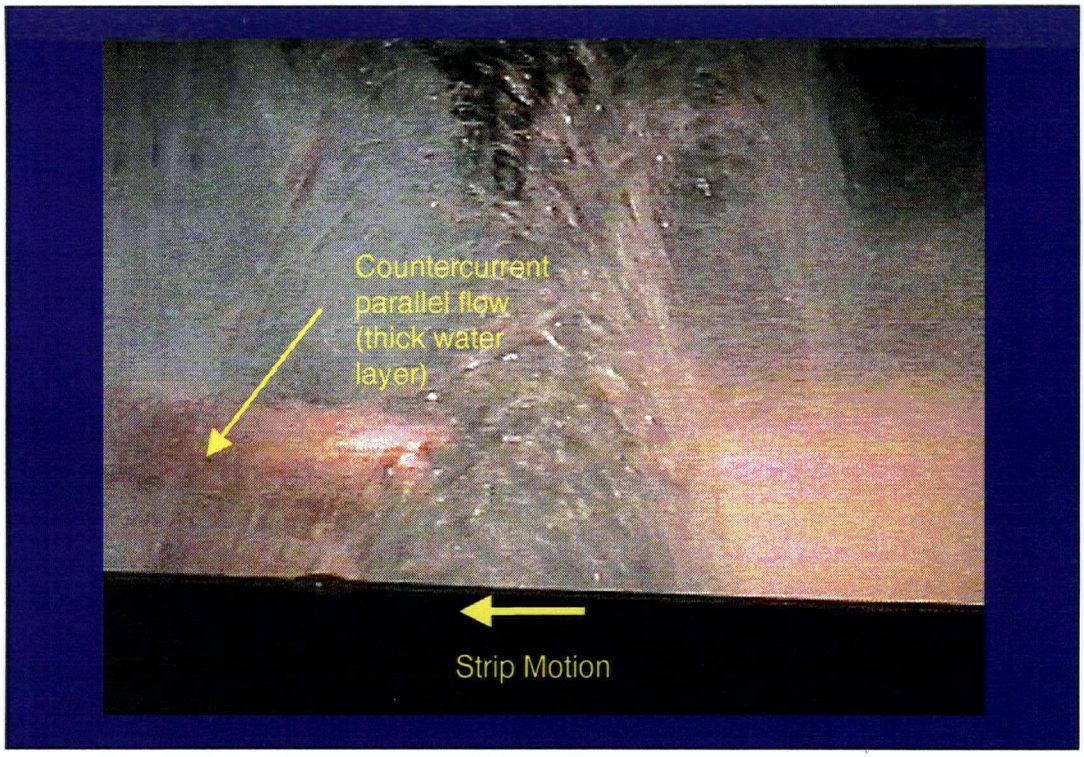

Figure 4.1: Company A: Countercurrent parallel flow region

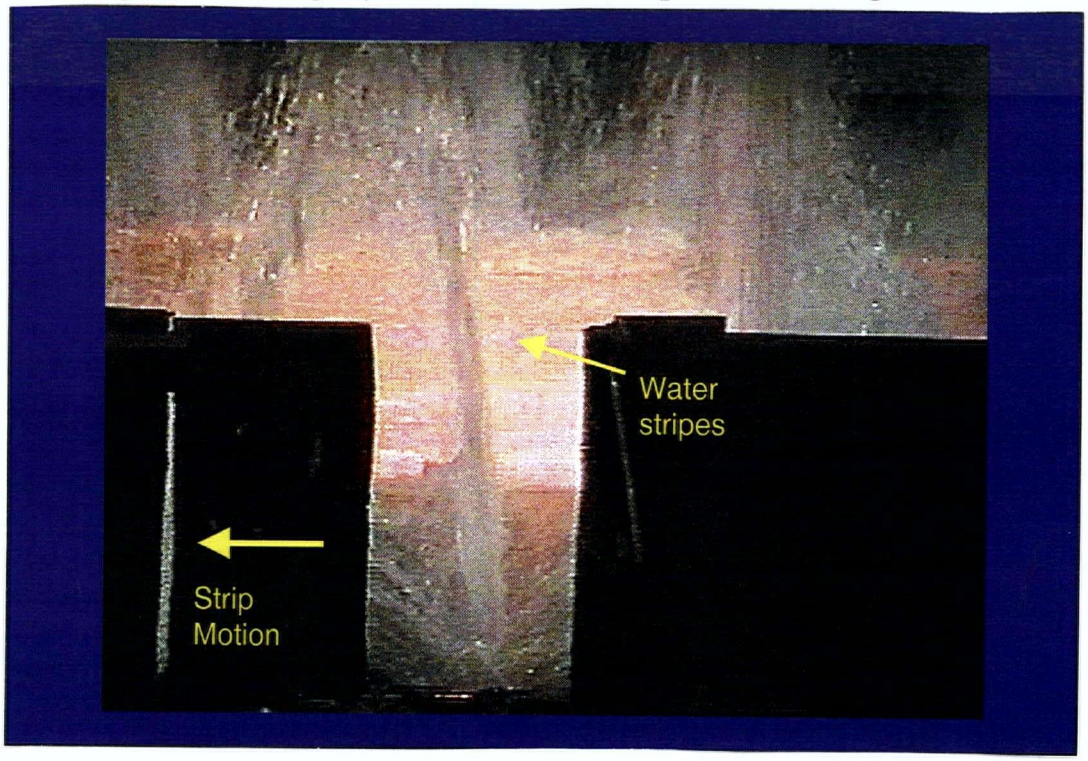

Figure 4.2: Company A: Parallel flow region

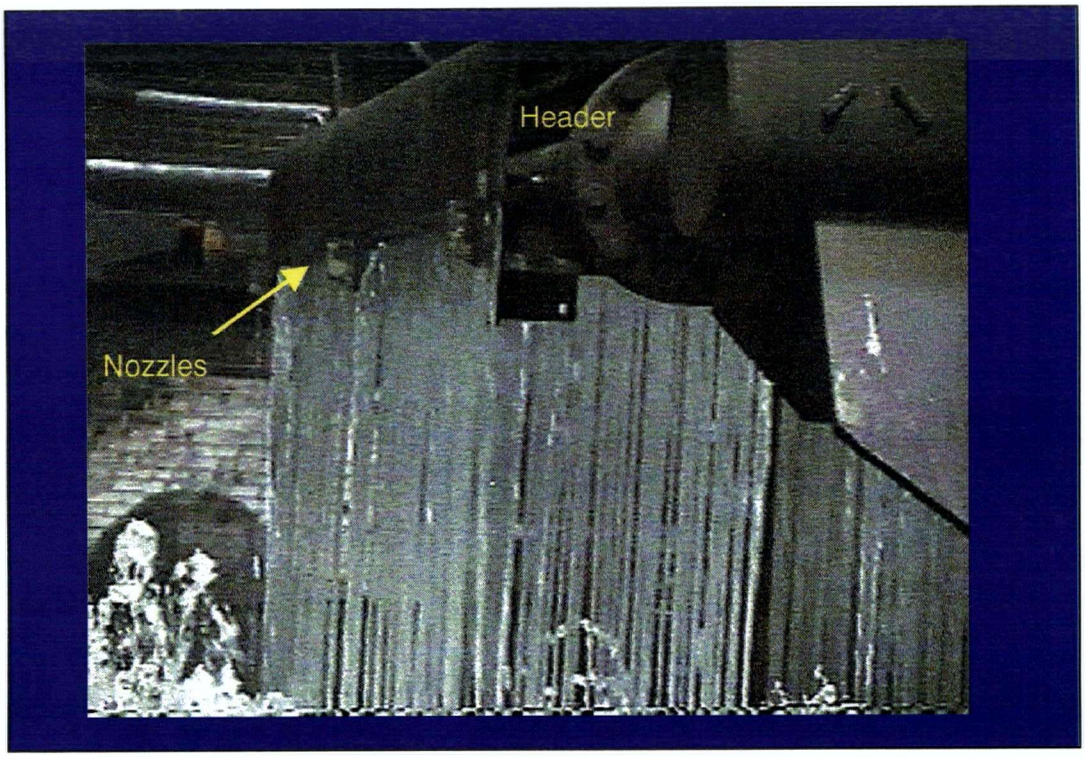

Figure 4.3: Company A: Water jet bars, header and nozzle arrangement.

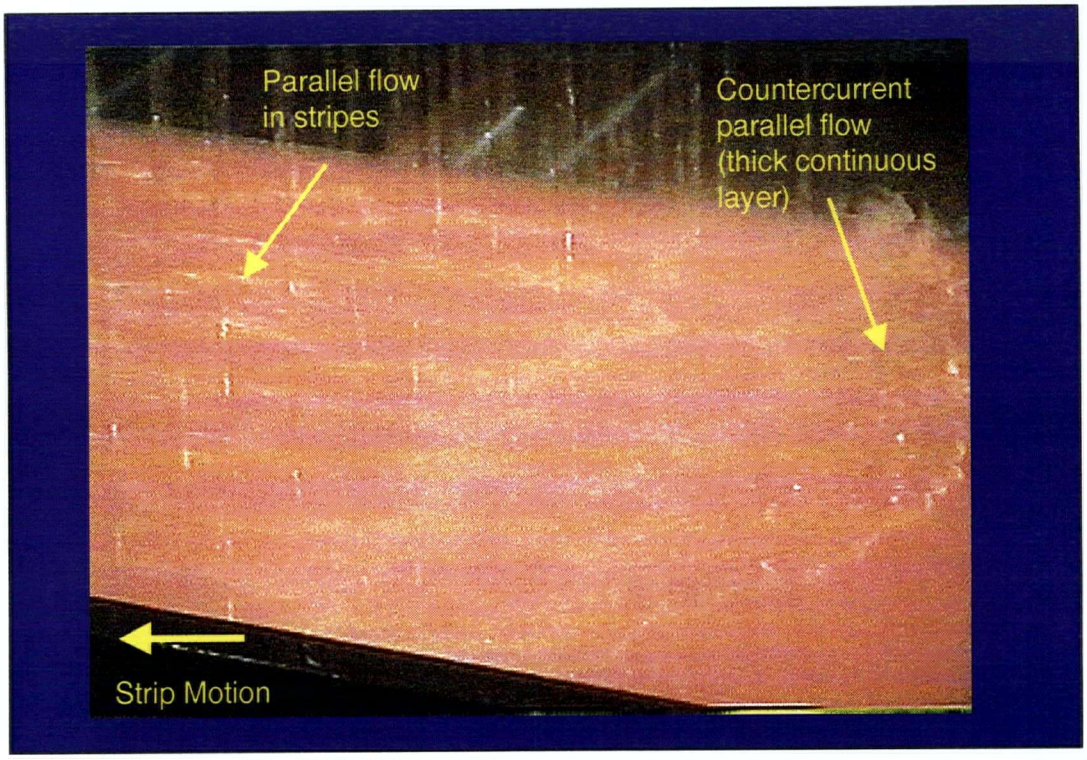

Figure 4.4: Company B: Parallel flow and countercurrent parallel flow

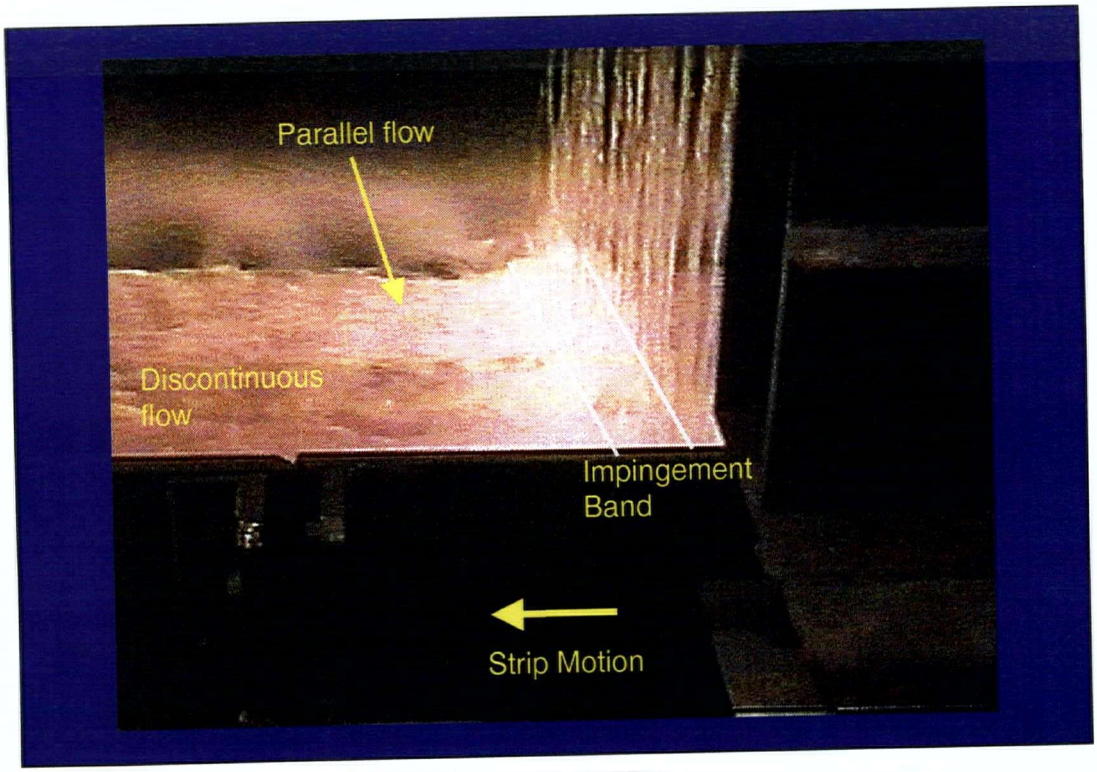

Figure 4.5: Company B: Impingement band and parallel flow region.

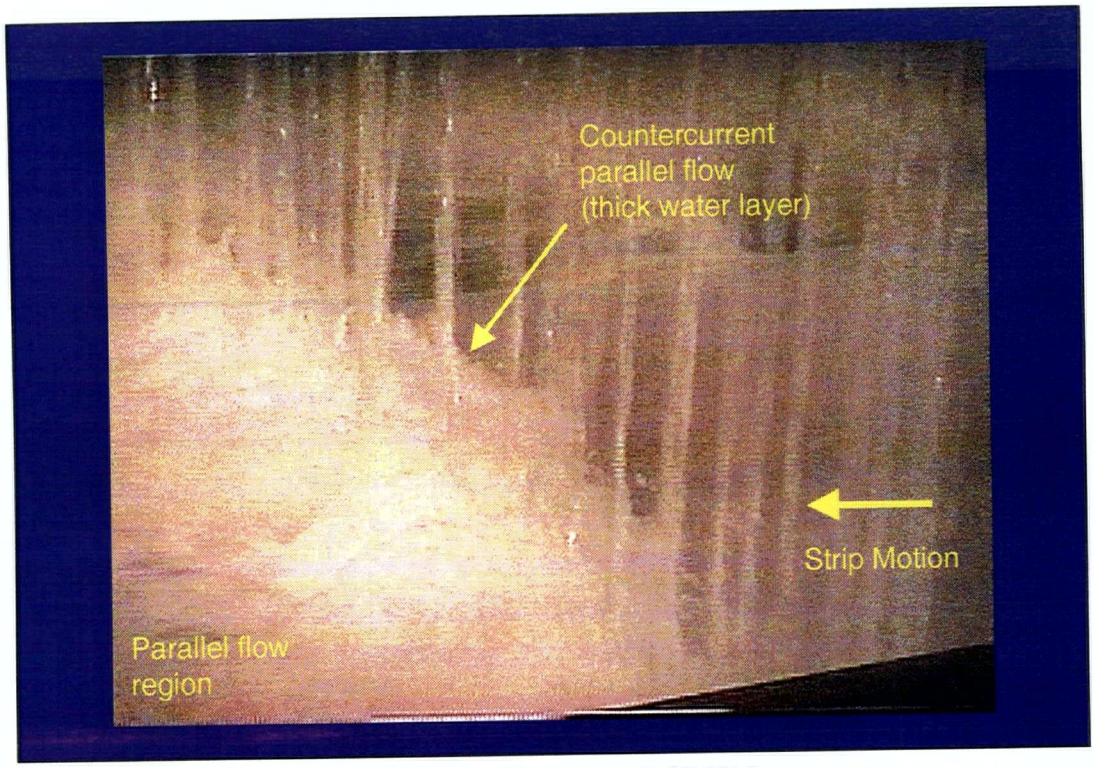

Figure 4.6: Company B: Impingement Band.

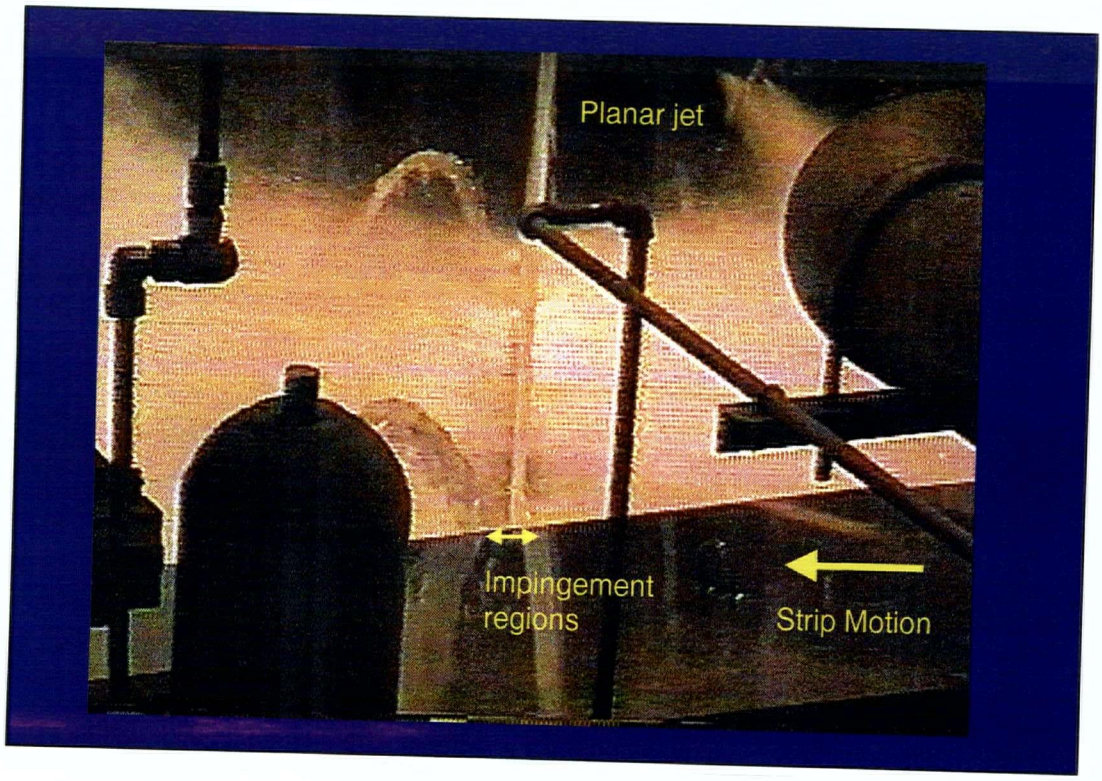

Figure 4.7: Company D: Impingement and parallel flow regions.

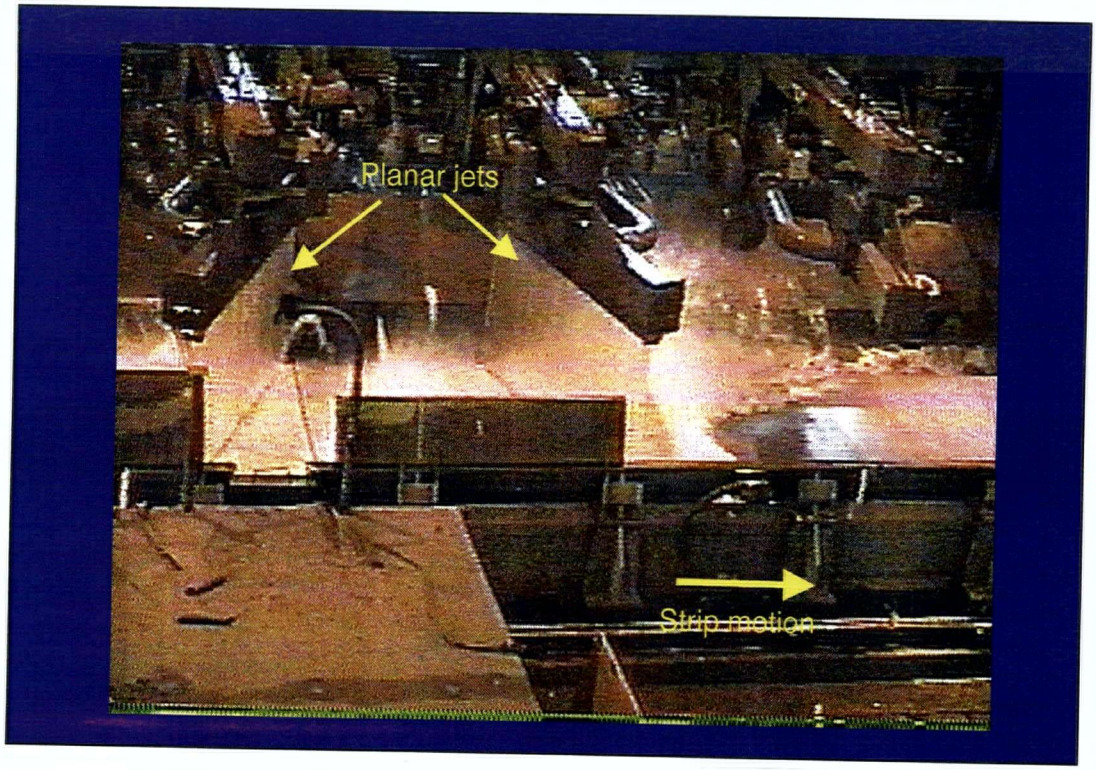

Figure 4.8: Company D: Planar jet arrangement.

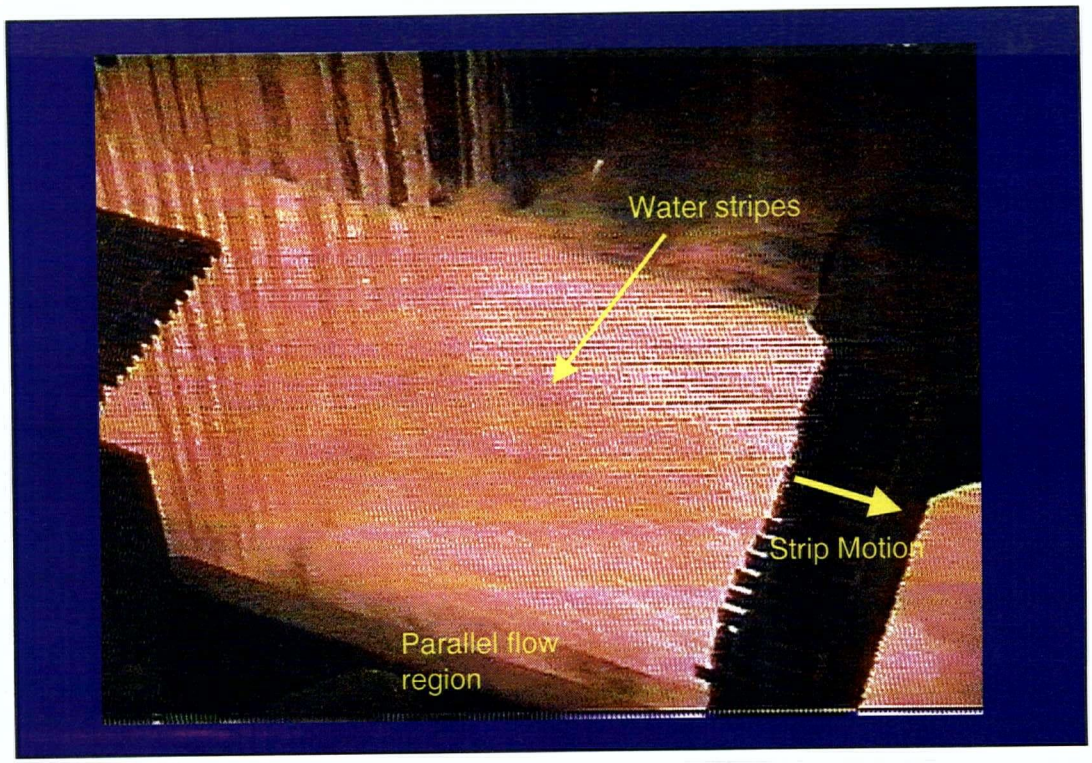

Figure 4.9: Company K: Impingement and parallel flow regions.

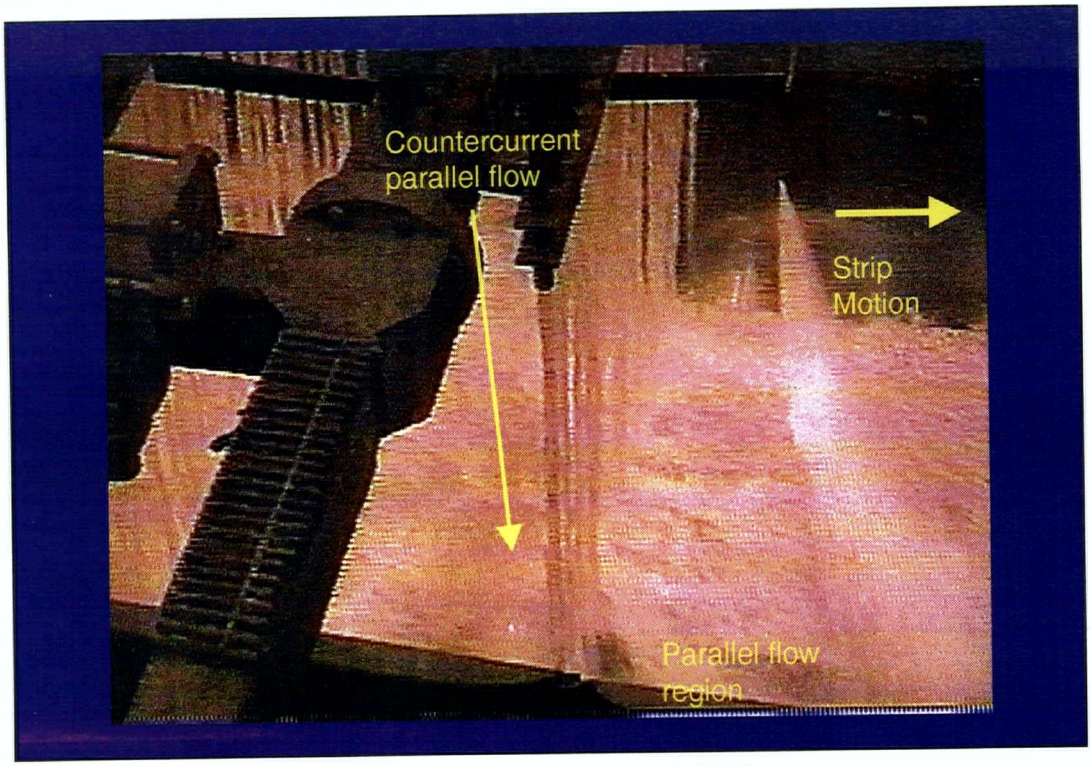

Figure 4.10: Company K: Countercurrent and downstream parallel flow regions.

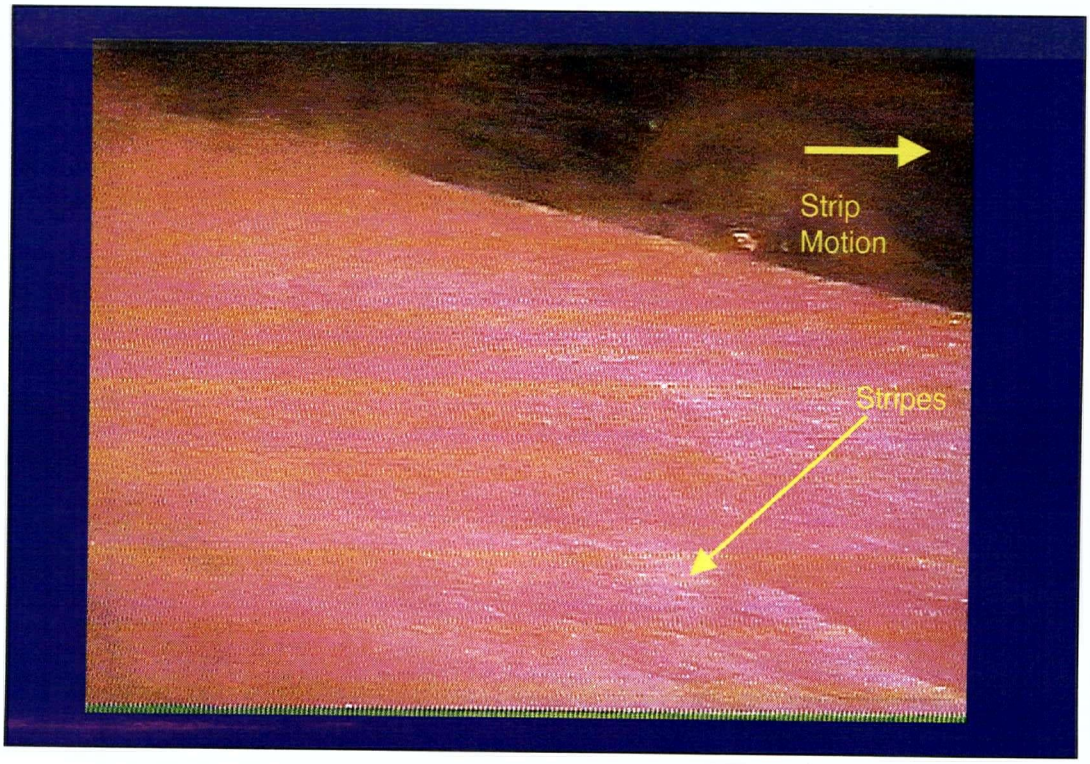

Figure 4.11: Company K: Parallel flow region.

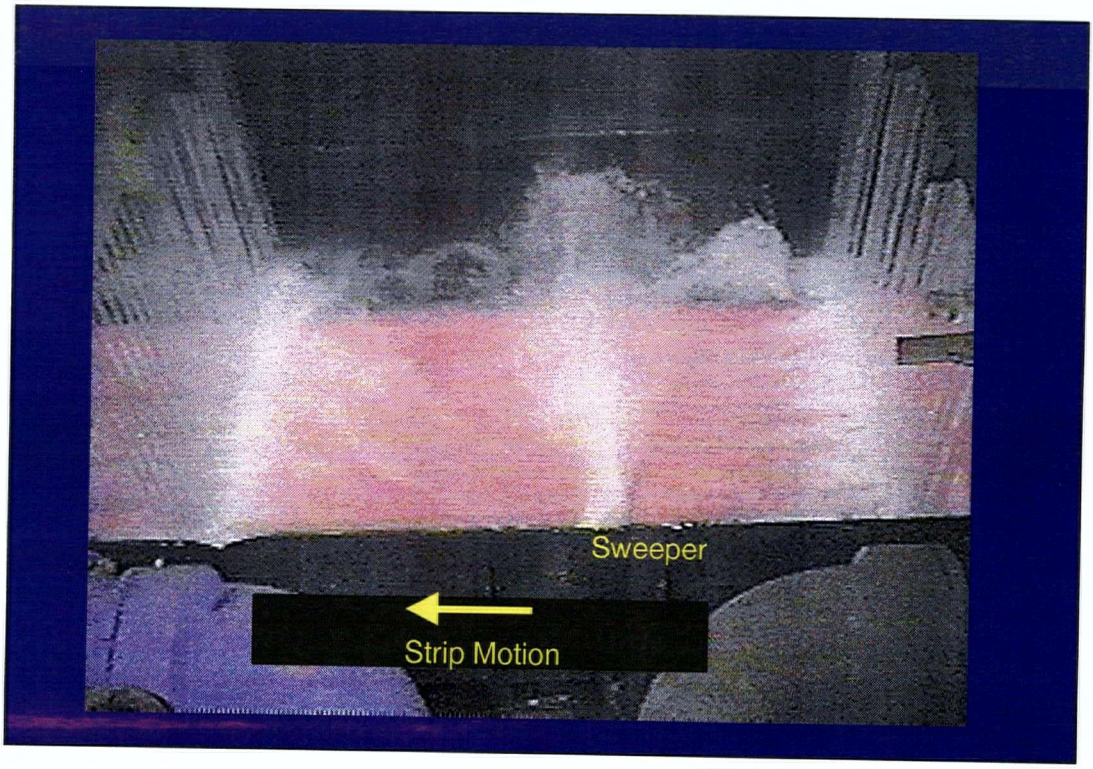

Figure 4.12: Company H: Jet cooling arrangement, parallel flow and sweeper.

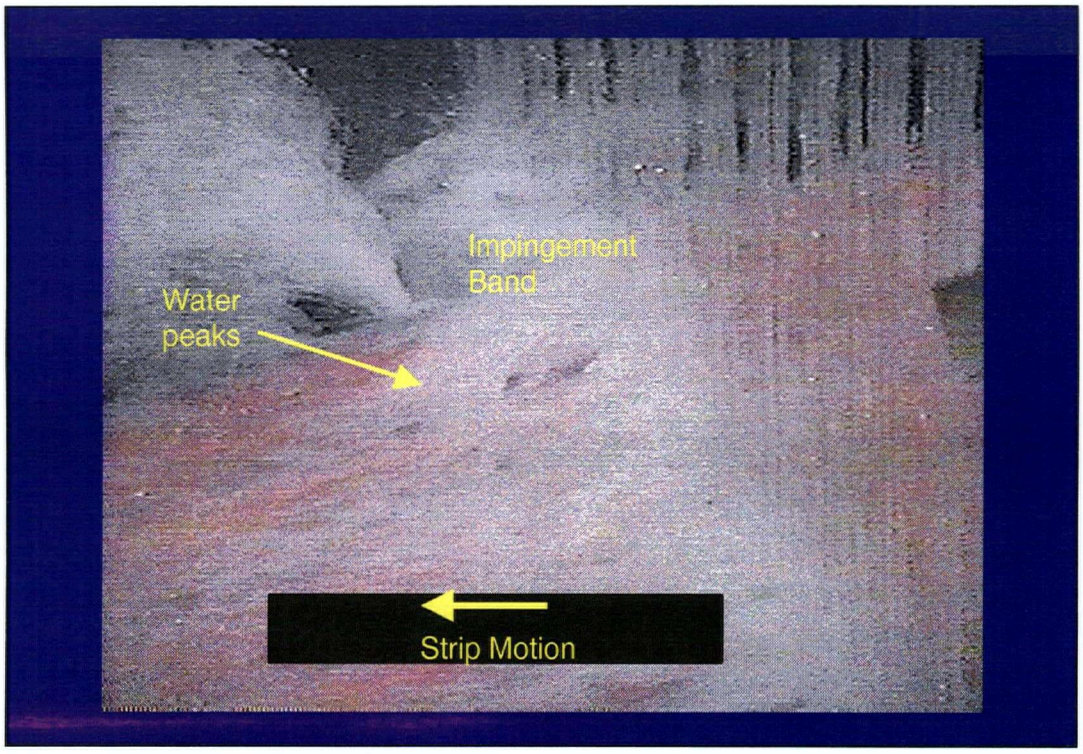

Figure 4.13: Company H: Impingement band and parallel flow region.

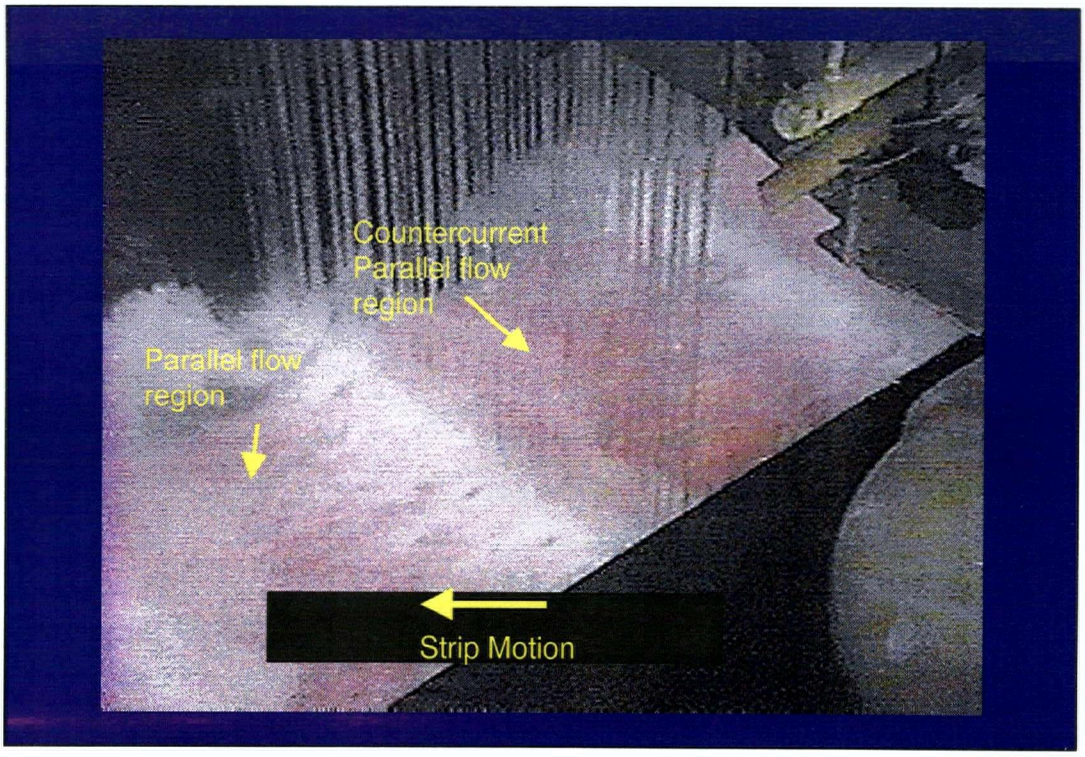

Figure 4.14: Company H. Preimpingement of jet, and fluid flow regions.

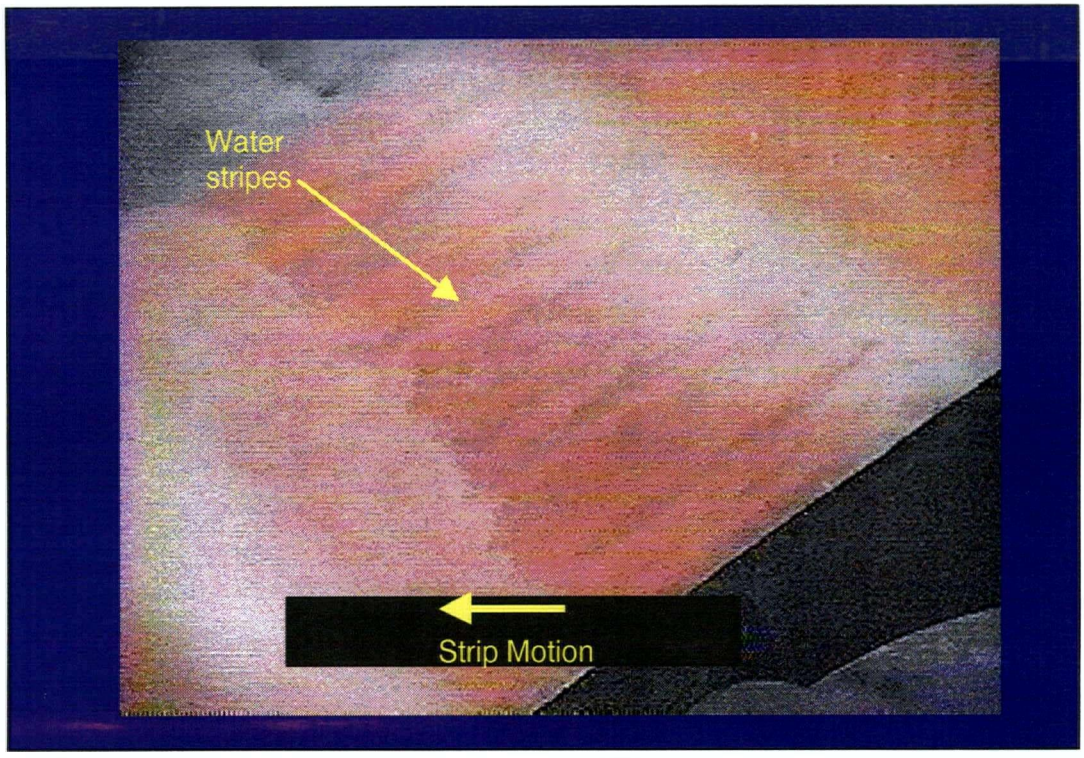

Figure 4.15: Company H. Parallel flow region.

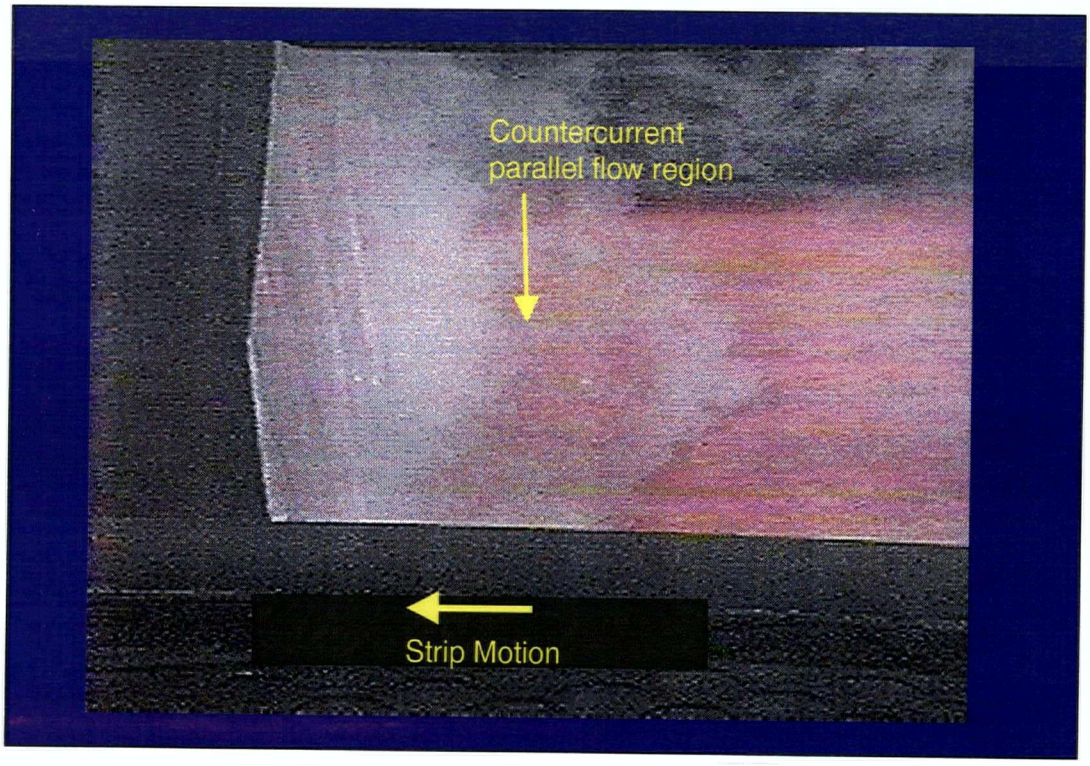

Figure 4.16: Company H. Countercurrent parallel flow region.

Table 4.1: Fluid flow characteristics of the pre-impingement top jet

Parameter	Company				
	A	B	D	K	H
Kind of flow	Turbulent, continuous, some breakdown	Turbulent, continuous, some breakdown	≈Laminar, continuous	Turbulent, continuous	Turbulent, continuous
Reduction in jet diameter	30-50%*	50%*	Unable to determine	50%** 30-50%*	Some reduction, unable to quantify

*Measurements from video-recordings

**Measurements from photographs

Table 4.2:Fluid Flow observations in the impingement and jet interaction zone of top jets

Parameter	Company				
	A	B	D	K	H
Number of jet lines in the interaction zone	1	2, spaced 0.15m	1	2	2, spaced 0.07m
Length of the direct interaction zone	≈0.05-0.10m	≈0.20m	≈ 3 times impinging jet width	≈ 3 times impinging jet diameter	≈0.15m
Length of water peaks (downstream)	Not seen	≈0.15m (in impingement region)	Not existent	≈roll diameter	≈0.30-0.40m
Length of water peaks (upstream)	Not seen	Not existent	Not existent	Not existent	Not existent
Diameter of the holes formed by the jet impingement	Not seen	Unable to measure. Hole formed by more than one jet.	Not existent	Unable to measure. Holes formed by groups of jets	≈0.02-0.03m*. Only appear in the row downstream, and not in the upstream row.
Strip surface color	Dark	Probably dark (as seen just after water coverage)	Probably dark	Apparently dark	Dark

*Measured from comparison to roll diameter, and to the distance between jet lines and nozzles across width. Same dimensions and positions were observed during impingement on rolls.

Table 4.3: Fluid Flow observations in the downstream parallel flow zone of top jets

Parameter	Company				
	A	B	D	K	H
Length	≈0.25m when d_{jetlin}=0.46, and ≈0.60 when d_{jetlin}=0.92	≈2.30m	Variable arc	≈ Distance between jet lines minus roll diameter	≈0.90m
Kind of flow	Turbulent, continuous with water stripes, and sputtering	Turbulent, continuous at center, discontinuous at edges, with stripes of ≈0.20 in parallel flow region (extension of those in the imp. region)	Parallel, turbulent, with high degree of sputtering (up to ≈0.40m high)	Turbulent, continuous, with some water stripes	Turbulent, continuous, with high density of water stripes, especially at center and diminishing to the sides
Strip surface color	Red, dark stripes with different tones, more at center.	Edges are dark. Close to the edges bright red. Slightly dark at center, and slightly brighter downstream	Completely dark	Red, stripes in the middle, sides brighter	Red. Dark stripes appear with higher density where there is a higher density of water stripes.
Interaction with sweepers	Not seen	Not seen	Sweeper clears the surface, creates an arc with high degree of sputtering	Creates a complex recirculating flow which affects the whole parallel region upstream, and cuts completely the flow to the next jet line.	Creates a distorted cone, which partially separates the flows, but water stripes cross underneath. Upstream the cone an quasi-stagnant flow appears, whereas downstream a similar region appears but also creates a recirculating flow near the sweeper nozzle. Dark stripes seem unaffected.
Interaction with next jet line	Smooth, no sputtering	Smooth, no sputtering	Not existent	Smooth, no sputtering	Smooth, no sputtering

Table 4.4: Fluid Flow observations in the upstream parallel flow zone of top jets

Parameter	Company				
	A	**B**	**D**	**K**	**H**
Length	≈0.25m when d_{jet}=0.92, ≈0.15m when d_{jet}=0.46	≈0.15m (not seen in all cases)	≈1/2 distance between jets	≈2/3 roll diameter	≈0.40m
Kind of flow	Almost stagnant, turbulent, continuous and thick, wavy, 2-D toward end of strip	Almost stagnant, turbulent, continuous and thick, wavy, 2-D toward end of strip	Parallel, turbulent, with high degree of sputtering (up to ≈0.40m high)	Close to stagnant, turbulent, continuous and thick, wavy, 2-D toward the end of strip	Almost stagnant, turbulent, wavy, 2-D toward the end of strip with interaction with a sweeper, more turbulent in some occasions with interaction with previous jet.
Strip surface color	Darker than the parallel flow of the previous jet. Clear color delimitation	Unable to determine	Darker than the parallel flow of the previous jet.	Unable to determine in normal, dark when there is a sweeper	Red and black stripes from previous jet continue
Interaction with sweepers	Upstream flow disappears	Not seen		When there is a sweeper a recirculating flow appears creating a large dark area at the center of the eddy.	
Interaction with previous jet line	Bulky	bulky	Turbulent	bulky	

Table 4.5: Fluid Flow observations of the bottom cooling configurations

Parameter	Company				
	A	B	D	K	H
Kind of flow	Turbulent, continuous at the beginning, breakdown after some distance	?	Turbulent, not as continuous as top jets	Unable to identify	Discontinuous at top, very alike that of bars
Increase in cross section	Existent, but unable to measure	?	?		Existent, but unable to determine (probably thicker than 0.01m all the time)
Estimated maximum jet height	≈0.60m from nozzle	?	Vary significantly, from 0.30 to 0. 80		≈0.15m from nozzle for 19.6l/s, the other is unknown
Interaction with top surface	Some water reach the top surface	not seen	not seen		not seen

5. MODEL OF THE BOILING CURVES DURING JET COOLING

The need of a general and accurate tool to calculate the local heat fluxes during cooling by water in the runout table, together with the lack of relevant experimental data to develop an empirical equation, has led to the development of a mathematical model to describe the boiling curves in the impingement and parallel flow regions during jet cooling.

It is important to mention that measurements of local heat transfer events in an actual mill are beyond the limits of this research, in view of the extremely difficult circumstances to perform such experiments. Consequently, in this work an alternative semi-empirical approach is presented, which is believed to be the best alternative at the present time to obtain the local heat fluxes. This semi-empirical model is based on the application of some fluid flow and boiling heat transfer fundamentals together with a fitting procedure to obtain the boiling curves, as will be discussed.

5.1 Boiling Curve Modelling and the Mechanisms of Cooling

As it was discussed in the literature review, the extent to which the various mechanisms associated with boiling water heat transfer take place in the runout table are unknown. However, detailed studies on the mechanisms of boiling during forced convective boiling are available, which may help significantly in determining the possible mechanisms of boiling taking place. It was seen in the literature review, that for any fixed position, the surface is in alternate contact with liquid and vapor, and the local heat

transfer was determined by the time averaged magnitude of the heat extraction to each of these contacts.

Also from the literature review, it was concluded that during local contact of the liquid water with the strip surface nucleate boiling takes place, and the heat transfer during this contact is very high. The mechanism of heat transfer during the liquid-solid contact is the evaporation of a layer of liquid (macrolayer) in contact with the strip surface. The vapor rises from the surface in small columns (stems) which then coalesce into larger vapor bubbles. The larger bubbles may rise to break free from the surface or be condensed depending on the local fluid conditions. The evaporation process takes place mainly at the perimeter of the stem contact with the solid surface, that is, in the perimeter where vapor, liquid and solid are in contact. When vapor-solid contact takes place, the vapor acts as an isolating layer, reducing considerably the heat transport since the heat is transferred through the low conducting vapor instead of the more efficient evaporation during liquid-solid contact. The fraction of the total area where liquid-solid contact occurs, F, is dependent on several variables, such as water velocity and temperature, strip surface temperature, etc., and except for very few pool boiling experiments, is unknown.

Detailed observations of the boiling processes and measurements of the boiling curves by Filipovic et al. [1] are probably the closest to typical runout table conditions in parallel flow. Unfortunately, the observed strong propagation of the boiling front driven by extreme variations of the surface temperature along the flow ($\approx$1000°C/m), may not be seen in the runout table because of the comparatively smaller variations (10-100°C/m) found there.

In order to obtain a first approximation of the length scale of the events described, the basic theory of the hydrodynamic instability in a two-phase flow presented elsewhere[2,3] may be adopted. Calculations were done to estimate the typical critical wavelengths in the parallel flow region of a runout table operation, adopting theory which was used by Galloway et al.[4] in the modelling of the critical heat mechanism during flow boiling. The thermophysical properties used are given by the equations shown in Table 5.1. The critical wavelength was estimated to be approximately 0.012m. However, the application of the Kelvin-Helmholtz instability theory to the prediction of the area where the liquid-solid contact occurs may be limited because of the complex evaporation processes taking place during the liquid-solid contact and the very complicated mathematical analysis required. This issue will be discussed in section 5.4.

Given the comparatively small distance between the liquid-solid contacts, the grouping of several of these contacts occurring alternatively on a larger surface to maintain transition boiling is necessary. Thus, the mechanism of transition boiling on a long surface should be similar to the one depicted in Figure 5.1. At very high temperatures (time=t1, temperature= T1), the interface is at an average position $\delta(x)$ to the strip surface, and perhaps only very limited contact with the liquid is possible. After, at a time t2, the strip has moved to another position along in the runout table; the steel temperature has decreased to T2; the interface can touch the surface, and during this contact, nucleate boiling through the macrolayer evaporation mechanism takes place. The liquid-vapor interface propagates in the direction of the flow, with a speed that is not that of the flow nor of the strip. A similar scheme was observed experimentally by

Galloway et al.[4], except for the details of the bubble, but a layer of liquid such as the macrolayer was also observed. It is noteworthy that the same basic mechanism suggested by Hernandez et al.[5], and confirmed by Filipovic et al. [1] for smaller surfaces is assumed, but it is applied only to the possible liquid-solid contacts. The main distinction is that the fraction of the total area in contact with the liquid is no longer given by the ratio of the macrolayer length over the bubble length, but it is also dependent on the characteristics of the liquid-vapor interface, which include: [1] Mean vapor layer thickness, [2] Wave length and amplitude, [3] Interface speed.

The mathematical modelling of the boiling curves, for either the impingement or the parallel flow regions in the runout table, can be based on the equation [2.4.1.2], presented previously in the literature review:

$$q_{TB} = q_{l-s}F + q_{v-s}(1-F) \qquad [2.4.1.2]$$

where q_{TB}, q_{l-s}, q_{v-s} are the transition boiling, the liquid-solid contact and the vapor-solid contact heat fluxes respectively, and F is the fractional liquid-solid contact area. This equation is the basis of most of the current studies on transition boiling heat transfer, and it is also consistent with the mechanisms of boiling proposed in this work. It is important to note that the application of this equation is very broad, so when regions of the strip are cooled under film boiling, the model simply sets itself $F \approx 0.0$.

The numerical evaluation of such parameters can be done under different assumptions, as it was discussed in section 2.4.1. In this work, the assumptions adopted to use equation [2.4.1.2] are depicted in Figure 5.2, for both the parallel flow and the impingement regions. The liquid-solid contact heat flux, $q_{l\text{-}s}$, is calculated as an

extrapolation to the transition boiling regime of the nucleate boiling behavior. Similarly, the vapor-solid contact heat flux, $q_{v\text{-}s}$, is obtained by extrapolation of the film boiling expressions to the transition boiling regime. The fractional liquid-solid contact area, F, is a function of superheat as shown in Figure 5.2, and depends on the stability of the liquid-vapor interface, as depicted in the figure, but also on the macrolayer dryout. A complete liquid-solid contact is not achieved until close to the onset of nucleate boiling.

The boiling curves for the impingement and the parallel flow regions are in general very different, so the parameters of equation [2.4.1.2] have to be obtained for each flow region.

Mathematical models for the liquid-solid and vapor-solid contact heat transfer ($q_{l\text{-}s}$, $q_{v\text{-}s}$) and the fractional liquid-solid contact area, F, for the impingement and parallel flow zones are presented.

5.2 Vapor-Solid contact heat transfer in the Impingement Zone

As it is clear in the general transition boiling equation [2.4.1.2], the heat flux during the vapor-solid contact, $q_{v\text{-}s}$, has to be calculated. Accordingly, the objectives of this section are to estimate the heat fluxes during the vapor-solid contacts and also to obtain a better understanding of how the process parameters affect the heat extraction. In this work, such a heat flux is approximated by the extrapolation to the transition boiling regime of the heat transfer during film boiling on an isothermal surface. For the impingement zone, the work of Nakayama [6] on the modeling of subcooled forced-convection film boiling in the presence of a pressure gradient, which is applicable in the

impingement of a jet, was extended in this research to account for moving strip conditions. The main assumptions of this model are:

[1] The flow is incompressible, laminar and two-dimensional, and the 2-D laminar boundary layer equations are applicable[♦] .

[2] Constant thermo-physical properties of liquid and vapor.

[3] The impingement flow is a Falker-Skan Flow (Power law flow)

[4] Isothermal surface.

[5] Constant strip speed.

[6] Smooth liquid-vapor interface.

[7] Radiation across the vapor layer has a negligible effect on the vapor layer thickness.

[8] Vapor inertia and convection terms are negligible, because $\rho << \rho_l$.

[9] Momentum transfer to the vapor is negligible compared to that to the liquid, since $\rho << \rho_l$.

Webb et al. [7] mention that for a single-phase jet, unless the preimpingement jet is characterized by extremely high turbulence, a laminar boundary layer will begin at the stagnation point and proceed outward into the radial flow zone, and also pointed out that turbulent flows behave qualitatively in the same manner as laminar flows. In the event that the jet is extremely turbulent, Webb et al. [7] stated that the velocity gradient and the

[♦] The Reynolds number of an impinging jet, given by $Re=U_{jet}d_{jet}/\nu$ is at the most $2x10^5$, which is smaller than the typically recognized for transition to turbulence on a flat plate, which is $5x10^5$. For a water flow of 6m/s on a flat plate, transition to turbulence will start at about 7cm from the leading edge. Also, the requirement of laminar flow is only for the boundary layer region, so the free stream flow can be turbulent.

free stream turbulence intensity are not easily predicted, and will not be known a priori for arbitrary nozzle and liquid supply systems. As it is manifest, an analysis of turbulence during the impingement of a jet is beyond the limits of this work. Additionally, even though the surface of a material being quenched is never isothermal, the thermal gradients along the surface in general are small compared to their possible effect on the development of the vapor layer or the boundary layer, and in most of the cases can be considered to be negligible.

The system analyzed is schematically shown in Figure 5.3. The liquid flows on the stable vapor layer formed on the solid surface, which is at an angle θ from the horizontal axis* , x, with a bulk flow velocity in the x-direction, U_e, given by the Falker-Skan power-law, and a bulk flow temperature T_e. The high temperature of the surface, T_W, creates a vapor layer of thickness δ, bounded by an interface where the fluid flows with a velocity U_i and a temperature T_i. Heat and momentum are conducted through the liquid, creating thermal and momentum boundary layers of thicknesses, Δ_T and Δ respectively. The velocities u and v are respectively the y and x components of the velocity vector, whereas the solid moves with speed U_p in the direction of the liquid flow. It is important to note that the impingement of top jets, for example, is a special case of this more general flow, where $\theta=\pi/2$ (90°).

The continuity, momentum and energy differential equations to solve for the vapor and the liquid are:

* Note that the impingement angle adopted is consistent with the scheme adopted by Webb et al.[7] showed in Figure 2.3, corresponding to one half of the wedge angle. The power-law exponent, m, is given by $m=\theta/(\pi-\theta)$, which gives the same result as the one taking the whole wedge angle[8,9], $m=2\theta/(2\pi-2\theta)$.

VAPOR:

Continuity

$$\frac{\partial u}{\partial x}+\frac{\partial v}{\partial y}=0 \qquad [5.2.1]$$

Momentum in *x*

$$\rho u\frac{\partial u}{\partial x}+\rho v\frac{\partial u}{\partial y}=-\frac{\partial P}{\partial x}+\frac{\partial \tau_{xy}}{\partial y} \qquad [5.2.2]$$

Energy

$$u\frac{\partial T}{\partial x}+v\frac{\partial T}{\partial y}=\frac{k}{\rho C_p}\frac{\partial^2 T}{\partial y^2} \qquad [5.2.3]$$

LIQUID:

Continuity

$$\frac{\partial u}{\partial x}+\frac{\partial v}{\partial y}=0 \qquad [5.2.4]$$

Momentum in *x*

$$\rho_l u\frac{\partial u}{\partial x}+\rho_l v\frac{\partial u}{\partial y}=-\frac{\partial P}{\partial x}+\frac{\partial \tau_{xy}}{\partial y} \qquad [5.2.5]$$

Momentum in *y* (from Bernoulli's equation)

$$-\frac{1}{\rho_l}\frac{\partial P}{\partial x}=u_e\frac{\partial u_e}{\partial x} \qquad [5.2.6]$$

Energy

$$u\frac{\partial T}{\partial x}+v\frac{\partial T}{\partial y}=\frac{k_l}{\rho_l C_{p_l}}\frac{\partial^2 T}{\partial y^2} \qquad [5.2.7]$$

Which are solved for Newtonian fluids, thus:

$$\frac{1}{\rho}\frac{\partial \tau_{xy}}{\partial y}=\nu\frac{\partial^2 u}{\partial y^2} \qquad [5.2.8]$$

and applying the Falkner-Skan Flow (Power-Law Flow)

$$u_e = cx^m \;\; ; \;\; m=\theta/(\pi-\theta) \qquad [5.2.9]$$

Now, under the assumption that the vapor inertia and convection terms are negligible, that is, assuming that the left sides of equations [5.2.2] and [5.2.3] are zero and applying equations [5.2.6] and [5.2.8] into equation [5.2.2], the following equations for the VAPOR are obtained:

Momentum in x

$$-\frac{\partial P}{\partial x}+\frac{\partial \tau_{xy}}{\partial y}=\frac{\rho_l}{\rho}u_e\frac{\partial u_e}{\partial x}+\nu\frac{\partial^2 u}{\partial y^2}=0 \qquad [5.2.10]$$

Energy

$$\frac{\partial^2 T}{\partial y^2}=0 \qquad [5.2.11]$$

The continuity, momentum and energy equations have to be solve with the following boundary conditions:

At $y=0$:

No slip condition:

$$u = U_p \qquad [5.2.12]$$

No transpiration condition:

$$v = 0 \qquad [5.2.13]$$

Temperature continuity:

$$T = T_w \qquad [5.2.14]$$

At the liquid-vapor interface $y = \delta$:

Velocity continuity:

$$u\big|_f = u\big|_v = u_i \qquad [5.2.15]$$

Shear-stress continuity:

$$\mu_f \left.\frac{\partial u}{\partial y}\right|_f = \mu \left.\frac{\partial u}{\partial y}\right|_v \qquad [5.2.16]$$

Mass conservation, evaporation at interface:

$$\left[\rho u \frac{\partial \delta}{\partial x} - \rho v\right]_v = \left[\rho_l u \frac{\partial \delta}{\partial x} - \rho_l v\right]_l \qquad [5.2.17]$$

Temperature continuity:

$$T\big|_f = T\big|_v = T_i \qquad [5.2.18]$$

Energy conservation (energy required for evaporation is equal to the energy across vapor layer minus energy across liquid layer):

$$\left[\rho u\frac{\partial\delta}{\partial x}-\rho v\right]_v h_{fg}=\left[k_l\frac{\partial T}{\partial y}\right]_l-\left[k\frac{\partial T}{\partial y}\right]_v \qquad [5.2.19]$$

At the bulk flow $y=\Delta+\delta$:

Free stream conditions:

$$u=U_e \qquad [5.2.20]$$

At the bulk flow $y=\Delta_l+\delta$:

Free stream conditions:

$$T=T_e \qquad [5.2.21]$$

The solution of the continuity, momentum and energy equations with their boundary conditions was obtained by the boundary layer integral technique, which is a standard procedure of widespread use, which is described elsewhere [8, 9]. The integral method has been specifically adopted to film boiling heat transfer extensively[10,11] to obtain an expression for the local Nusselt number.

This solving technique requires the assumption of velocity and temperature profiles that satisfy all the boundary conditions of the problem. The profiles obtained for this problem are:

Vapor profiles:

Velocity:

$$\frac{U}{U_i} = \Omega \frac{U_p}{U_i} + \left[1 - \Omega \frac{U_p}{U_i} + \Lambda\right]\left(\frac{y}{\delta}\right) - \Lambda\left(\frac{y}{\delta}\right)^2 \qquad [5.2.22]$$

Temperature:

$$\frac{T - T_i}{T_w - T_i} = 1 - \frac{y}{\delta} \qquad [5.2.23]$$

Liquid profiles:

Velocity:

$$\frac{U}{U_e} = U_i^* + (1 - U_i^*)(2\eta - \eta^2) \qquad [5.2.24]$$

Temperature:

$$\frac{T - T_e}{T_i - T_e} = (1 - \eta_t)^2 \qquad [5.2.25]$$

The integral equation of the momentum in x for the liquid is obtained by the substitution of the Bernoulli's equation [5.2.6], the newtonian fluid equation [5.2.8] and the continuity equation [5.2.4] in the x-momentum equation [5.2.5], integrating over the momentum boundary layer. The resulting equation is:

Momentum in x:

$$\frac{\partial}{\partial x}\int_{\delta}^{\delta+\Delta} u(U_e - u)dy + \frac{dU_e}{dx}\int_{\delta}^{\delta+\Delta}(U_e - u)dy = \nu_l \left.\frac{\partial u}{\partial y}\right|_{\delta} \qquad [5.2.26]$$

Similarly, the integral equation of the energy in the liquid is obtained from the substitution of the continuity equation [5.2.4] in the energy equation [5.2.7], integrating over the thermal boundary layer, to get:

Energy:

$$\frac{d}{dx}\int_{\delta}^{\delta+\Delta_t} u(T-T_e)dy = -\frac{\nu_l}{\mathrm{Pr}_l}\frac{\partial T}{\partial y}\bigg|_{\delta} \qquad [5.2.27]$$

The integral equation for the energy conservation at the interface is:

$$\left[\rho u\frac{\partial \delta}{\partial x}-\rho v\right]_v h_{fg} = h_{fg}\frac{d}{dx}\int_0^{\delta}\rho u dy = \left[k_l\frac{\partial T}{\partial y}\right]_l - \left[k\frac{\partial T}{\partial y}\right]_v \qquad [5.2.28]$$

Equations [5.2.26]-[5.2.28] are integrated substituting the velocity and temperature profiles already presented, to obtain ordinary differential equations, which later on are solved with the appropriate boundary conditions. The details of the solution are very lengthy, and only the solutions are presented here.

Solution of the momentum in x for the liquid (Equation [5.2.26]):

$$\left(\frac{\Delta}{x}\right)^2 Re_x = \frac{30}{\left(1+\frac{3}{2}U_i^*\right)(1+3m)+5m} \qquad [5.2.29]$$

Solution of the energy equation for the liquid(Equation [5.2.27]):

$$\left(\frac{\Delta_t}{x}\right)^2 Re_x = \frac{4}{(1+m)\,Pr_l\,D} \qquad [5.2.30]$$

Solution of the energy equation at interface (Equation [5.2.28]):

$$\left(\frac{\delta}{x}\right)^2 Re_x = \frac{\nu}{\nu_l}\frac{H}{Pr}\frac{12}{3U_p^* + 3 + \Lambda} *$$

$$\frac{\left\{1 - \frac{\Gamma U_i^*}{1-U_i^*}\sqrt{\mathrm{Pr}_l}\varsigma^*\left(1-\Lambda-U_p^*\right)\right\}\left\{1+m\left[1-\frac{3+\Lambda}{3U_p^*+3+\Lambda}\left(1-\frac{\frac{\Gamma U_i^*}{1-U_i^*}\sqrt{\mathrm{Pr}_l}\varsigma^* U_p^*}{1-\frac{\Gamma U_i^*}{1-U_i^*}\varsigma^*\sqrt{\mathrm{Pr}_l}\left(1-\Lambda-U_p^*\right)}\right)\right]\right\}}{(1+m)U_i^*}$$

[5.2.31]

Solution of the shear-stress continuity equation (Equation [5.2.16]):

$$\frac{\delta}{\Delta} = \frac{\mu}{\mu_l}\frac{U_i^*}{2}\left(\frac{1-\Lambda-U_p^*}{1-U_i^*}\right) \qquad [5.2.32]$$

For this work, the heat transfer coefficient is defined by:

$$h_{FB,imp}(T_w - T_i) = -k_v \left.\frac{\partial T}{\partial y}\right|_{y=0} \qquad [5.2.33]$$

Applying this definition of heat transfer coefficient to the linear behavior of the temperature profile in the vapor (see equation [5.2.23]), renders the following the local Nusselt number:

$$Nu_{x,imp} = \frac{x}{\delta} = \left[\frac{\mu_l}{\mu}\frac{m}{2}\frac{1}{U_i^*\Lambda}\right]^{1/2} Re_x^{1/2} \qquad [5.2.34]$$

It is noteworthy that the Nusselt number obtained contains the heat transfer coefficient during pure convective film boiling. When the heat released from the surface

reaches the interface, most of it is transported through the liquid, whereas the remaining fraction is used to evaporate and superheat the vapor. The total heat removed from the surface includes these plus a radiation component.

To evaluate the local Nusselt number it is necessary to solve equations [5.2.29] to [5.2.32] to get expressions for $U_i^*, \Lambda, \varsigma^*$ and δ. To eliminate this latter variable from the system, equations [5.2.29] to [5.2.32] are equated to get a system of three non-linear algebraic equations with 3 unknown $(U_i^*, \Lambda, \varsigma^*)$, from which equation [5.2.34] can be evaluated. The system of equations consists of:

$$\varsigma^{*2} = \frac{\dfrac{30}{\left(1+\dfrac{3}{2}U_i^*\right)(1+3m)+5m}}{\dfrac{4}{(1+m)D}} \qquad [5.2.35]$$

$$\alpha_o = \frac{\alpha_1 \alpha_2}{(1-\alpha_3\varsigma^*)\left\{1+m\left[1-\alpha_4\left(1-\dfrac{\alpha_5\varsigma^*}{1-\alpha_3\varsigma^*}\right)\right]\right\}} \qquad [5.2.36]$$

where

$$\alpha_o = \frac{H}{\mathrm{Pr}\,R}\frac{\mu}{\mu_l};\ \alpha_1 = \frac{1+m}{2m};\ \alpha_2 = U_i^{*2}\Lambda\left[U_p^* + (1+\Lambda/3)\right];\ \alpha_3 = \frac{\Gamma U_i^*}{1-U_i^*}\sqrt{\mathrm{Pr}_l}\left(1-\Lambda-U_p^*\right)$$

$$\alpha_4 = \frac{(1+\Lambda/3)}{U_p^* + (1+\Lambda/3)};\ \alpha_5 = \frac{\Gamma U_i^*}{1-U_i^*}\sqrt{\mathrm{Pr}_l}U_p^*;\ \alpha_6 = 1+m(1-\alpha_4)$$

and,

$$c_o = c_1 \Lambda \left(\frac{c_2}{c_3 - \Lambda} \right)^2 \qquad [5.2.37]$$

where

$$c_o = \frac{\mu}{\mu_l};\ c_1 = \frac{4}{15}\frac{1}{mU_i^*}\left[\left(1+\frac{3}{2}U_i^*\right)(1+3m)+5m\right];\ c_2 = 1-U_i^*;\ c_3 = 1-\frac{\Omega U_p}{U_i^* U_e}$$

$$D = \frac{\left[(5\varsigma - 1) + (10\varsigma^2 - 5\varsigma + 1)U_i^*\right]}{30\varsigma^2} \quad \text{for } \varsigma \geq 1$$

$$D = \frac{\left[(10 - 10\varsigma + 5\varsigma^2 - \varsigma^3) + (10\varsigma - 5\varsigma^2 + \varsigma^3)U_i^*\right]}{30} \quad \text{for } \varsigma \leq 1$$

The solution of the system of equations [5.2.35] to [5.2.37] has to satisfy the following conservation equation:

$$0 < \psi = \frac{\textit{Heat conducted through the liquid}}{\textit{Total heat released from the steel surface}} < 1$$

$$\psi = \Gamma U_i^* \varsigma^* \sqrt{Pr_l}\left(\frac{1}{1-U_i^*}\right) - \Gamma U_i^* \varsigma^* \sqrt{Pr_l}\left(\frac{\Lambda}{1-U_i^*}\right) - \Gamma U_i^* \varsigma^* \sqrt{Pr_l}\left(\frac{U_p^*}{1-U_i^*}\right) \qquad [5.2.38]$$

Motionless flat plate + Pressure gradient effect + Motion effect

The numerical solution of this system of equations was obtained by adding small increments to an initial value of ς^*; then the parameters λ and U_i^* were calculated and substituted in the set of equations, until the system of equations and the conservation

equation are satisfied. The convective film boiling heat transfer coefficient is calculated by:

$$h_{FB,imp} = \frac{Nu_{x,imp} k_v}{x} \qquad [5.2.39]$$

and the local convective film boiling heat flux is:

$$q_{FB,imp} = h_{FB,imp} \Delta T_{sat} \qquad [5.2.40]$$

Finally, as a verification of the solution obtained, the special case of U_p=0 was substituted in the set of equations [5.2.34] to [5.2.37], which is the problem solved by Nakayama [6], and the resulting equations were [2.4.4.2] to [2.4.4.5] obtained by Nakayama[6].

5.3 Film Boiling in the Parallel Flow Zone

This problem is a special case of the more general problem for the impingement region presented in the previous section. In parallel flow, the impingement angle θ is zero, and consequently the bulk flow velocity is constant. Accordingly, the parameters $m = 0,\ \Lambda = 0$ were substituted in equations [5.2.22] to [5.2.28], to obtain:

Solution of the momentum in *x* for the liquid(Equation [5.2.26]):

$$\left(\frac{\Delta}{x}\right)^2 Re_x = \frac{30}{\left(1+\frac{3}{2}U_i^*\right)} \qquad [5.3.1]$$

Solution of the energy equation for the liquid (Equation [5.2.27]):

$$\left(\frac{\Delta_t}{x}\right)^2 Re_x = \frac{4}{Pr_l D} \qquad [5.3.2]$$

Solution of the energy equation at interface (Equation [5.2.28]):

$$\left(\frac{\delta}{x}\right)^2 Re_x = \frac{\nu}{\nu_l}\frac{H}{Pr\,U_i^*}\frac{4}{1+U_p^*}\left\{1-\frac{\Gamma U_i^*}{1-U_i^*}\sqrt{Pr_l}\varsigma^*\left(1-U_p^*\right)\right\} \qquad [5.3.3]$$

Solution of the shear-stress continuity equation (Equation [5.2.16]):

$$\frac{\delta}{\Delta} = \frac{\mu}{\mu_l}\frac{U_i^*}{2}\left(\frac{1-U_p^*}{1-U_i^*}\right) \qquad [5.3.4]$$

The heat transfer coefficient is defined as previously (see equation [5.2.33]). The solutions of the x-momentum, energy, interface energy conservation, and the shear-stress continuity equations are equated with equation [5.2.33] to obtain:

$$\frac{Nu_{x,par}}{Re_x^{1/2}}\left(\frac{\mu}{\mu_l}\right) = \left[\frac{2}{15}\left(1+\frac{3}{2}U_i^*\right)\right]^{1/2}\frac{1-U_i^*}{U_i^*}\frac{1}{1-U_p^*} \qquad [5.3.5]$$

which is evaluated by solving the system of two non-linear algebraic equations with two unknowns (U_i^*, ς^*) that follows:

$$\frac{H}{Pr\,R} = \frac{15}{8}\frac{\dfrac{U_i^{*3}\left(1+U_p^*\right)\left(1-U_p^*\right)^2}{\left(1-U_i^*\right)^2\left(1+\dfrac{3}{2}U_i^*\right)}}{1-\dfrac{\Gamma U_i^*}{1-U_i^*}\sqrt{Pr_l}\varsigma^*\left(1-U_p^*\right)} \qquad [5.3.6]$$

$$\varsigma^{*2} = \frac{15}{2}\frac{D}{\left(1+\dfrac{3}{2}U_i^*\right)} \qquad [5.3.7]$$

In order to solve this system of equations more efficiently, equation [5.3.6] is arranged for ζ^* as follows:

$$\varsigma^* = \frac{\alpha_o - \alpha_1}{\alpha_o \alpha_2} \qquad [5.3.8]$$

where

$$\alpha_o = \frac{H}{\Pr R}; \quad \alpha_1 = \frac{15}{8}\frac{U_i^{*3}\left(1+U_p^*\right)\left(1-U_p^*\right)^2}{\left(1-U_i^*\right)^2\left(1+\frac{3}{2}U_i^*\right)}; \quad \alpha_2 = \frac{\Gamma U_i^*}{1-U_i^*}\sqrt{Pr_l}\left(1-U_p^*\right)$$

The solution of equations [5.3.7] to [5.3.8] has to satisfy the same conservation equation [5.2.38]. In the same way as for the impingement case, the solution of the system of equations is obtained by assuming a value of ς^*, then U_i^* is calculated, and both are substituted in the set of equations until the system of equations and the conservation equation are satisfied.

The convective film boiling heat transfer coefficient is calculated by:

$$h_{FB,par} = \frac{Nu_{x,par}\, k_v}{x} \qquad [5.3.9]$$

and the local convective film boiling heat flux is:

$$q_{FB,par} = h_{FB,par}\Delta T_{sat} \qquad [5.3.10]$$

The equations [5.3.6] and [5.3.7] were verified by setting the plate speed equal to zero in these equations, and comparing them with the solution obtained by Nakayama et al.[12] for subcooled forced convection film boiling on a flat non-moving plate. The same equations were obtained.

5.4 Fractional Liquid-Solid Contact Area

As it was discussed in the literature review and in section 5.1, some attempts have been done to obtain relationships for this parameter, but for the runout table cooling such relationships do not exist. It is important to recognize that in the impingement region of a jet, the contact of the liquid with the strip surface is enhanced by the pressure exerted by the impinging jet on the liquid-vapor interface. Consequently, it is expected that two different expressions for the parameter F are required, one for the impingement and another for parallel flow zone.

The fractional liquid-solid contact area, F, may be calculated, in principle, by mathematically modeling of the simple boiling mechanism shown in Figure 5.1, to calculate the mean vapor layer thickness, the wave length and amplitude, and the interface velocity, which are needed. Solutions for the mean vapor layer thickness, δ, can be directly obtained from the film boiling local Nusselt numbers calculated in sections 5.2 and 5.3 for the impingement and the parallel and regions respectively, because the mean vapor layer thickness is given by:

$$Nu_x = \frac{x}{\delta} \qquad [5.4.1]$$

and the wave length, amplitude of the disturbances of the interface, and the interface velocity could be obtained by the solution of the Kelvin-Helmholtz instability problem with evaporation at the interface. However, the solution of such problem is extremely complex mathematically, and many uncertainties with respect to the processes involved during the liquid-solid contact may limit its results. Given the complexity of the

mechanisms involved, it is unavoidable to predict the parameter, F, without some degree of empiricism.

In this research, an alternative semi-empirical solution is proposed, in view of the extreme difficulties of modelling the liquid-vapor interface. This alternative solution is based on the physical observations by Galloway et al.[4], a close observation of the film boiling behavior of the measured boiling curves presented in the literature review, the numerical results of the film boiling models presented in sections 5.2 and 5.3, the behavior of the vapor film thickness and the liquid-vapor interface amplitude with variations in superheat and subcooling during film boiling on a horizontal cylinder in a pool (see Figure 2.29), and the experimental results obtained for the parameter F in saturated pool boiling presented in Figure 2.28.

The experimental data shown in Figure 2.28 suggests that the fractional liquid-solid contact area can be approximated by an equation of the form:

$$\log F = a - b\Delta T_{sat}^{*} + c\Delta T_{sat}^{*2} \qquad [5.4.2]$$

For the impingement region of a jet, Figures 2.5, 2.10 and 2.11 show that F increases significantly with increasing subcooling, and also to a lesser extent with jet velocity. For parallel flows the same behavior was seen, as shown in Figures 2.16 and 2.18. Consequently, the parameters a, b and c are dependent on subcooling and jet velocity. It is important to recognize that the fractional liquid-solid contact area, F, must approach unity with decreasing superheat given a constant subcooling and water velocity. For this reason, the relative variations of F with variations of subcooling or jet velocity

have to be smaller at lower superheats. This situation is schematically presented in Figure 5.4. The reason for the higher liquid-solid contact at lower superheat can be explained with aid of the experimental results presented in Figure 2.29. During cooling, the vapor layer thickness decreases more than the amplitude of the liquid-vapor interface, promoting more liquid-solid contact. Accordingly, the effect of subcooling and jet velocity on the liquid-solid contact can be better explain in terms of the effect of such variables on the vapor layer thickness. The film boiling results obtained from the model presented in section 5.2, to be shown in another section, revealed that at high superheats a decrease in subcooling increases the vapor layer thickness considerably, and more so when subcooling approaches zero. However, decreasing superheat reduces this effect, and at superheats ranging from 200°C to 300°C the vapor layer thickness tends to converge to a single value, regardless of subcooling. A similar behavior was observed while decreasing jet velocity, but the effect was less pronounced.

Based on these observations, the parameters *a, b* and *c* were fitted, by a trial and error procedure, to obtain the closest agreement possible with the reported boiling curves measured (see Figures 2.5, 2.10, 2.11, 2.15, 2.16, 2.18, 2.24), which includes the impingement region of water bars, curtains and the parallel flow region, and at the same time, being able to predict the coiling temperatures of about two hundred strips cooled by ten companies within a reasonable error.

The fitting procedure started with the definition of a dimensionless superheat within the range of 100 to 1200K as follows:

$$\Delta T^*_{sat} = \frac{\Delta T_{sat} - 100}{1200 - 100} \qquad [5.4.3]$$

Values of F were adopted at three different superheats for each boiling curve to be fitted:

$$\begin{aligned} FA1 &= F(\Delta T^*_{sat} = 0) \\ FA2 &= F(\Delta T^*_{sat} = 0.5) \\ FA3 &= F(\Delta T^*_{sat} = 1.0) \end{aligned} \qquad [5.4.4]$$

from which the constants a, b, and c in equation [5.4.2] are calculated by:

$$a = \log(FA1) \qquad [5.4.5]$$

$$b = -\frac{log(FA2) - log(FA1)}{0.5} - 0.5\frac{log(FA3) - 2\{log(FA2)\} + log(FA1)}{2(0.5)^2 - 1} \qquad [5.4.6]$$

$$c = \frac{\log(FA3) - 2\{\log(FA2)\} + \log(FA1)}{2(0.5)^2 - 1} \qquad [5.4.7]$$

Two sets of values of FA's were obtained, one for the impingement and another for the parallel flow region. For the impingement region, according to the discussion presented in the literature review, it is clear that the parameter F should be a function of the water subcooling, the jet velocity and diameter, and possibly of strip speed. Since the information with regards to the jet diameter is far from sufficient to guess any behavior, and since the typical variations of this parameter for the different mills are not large, this parameter was discarded. Additionally, during the fitting procedure adopted, it was clear that the boiling curves were independent of the strip speed. Accordingly, three empirical equations for parameters *FA1*, *FA2*, and *FA3* of the form:

$$FA = a_1 + a_2\Delta T_{sub} + a_3\Delta T^2_{sub} + a_4 u_{je} + a_5 u^2_{je} \qquad [5.4.8]$$

were obtained, where all a_i's are constants given in Table 5.2.

For the parallel flow region, the parameter F is dependent only on water subcooling and velocity, given that similarly to the impingement region case, the boiling curves were independent of the strip motion. So, the same procedure was followed, except that equation [5.4.8] was not applied, but a semi-empirical equation based on a simple model of the contact between the liquid-vapor interface and the strip surface that is described below.

In an attempt to investigate further the possible relationship between the mean vapor layer thickness and the amplitude of the interface displacement, a very simple model of the contact between the interface and the surface was developed. This model consists on: [1] Wave displacement equation, [2] Liquid-solid contact criterion, [3] Mathematical equation of the fractional liquid-solid contact area. The displacement of the interface was assumed to be the typical sinuosoidal wave:

$$\eta = A\cos(\omega x) \qquad [5.4.9]$$

whereas two assumptions were considered for the liquid-solid criterion: [a] The contact of the wave with the surface does not affect the wave displacement or the frequency in any position, and symmetry is maintained; [b] The thickness of the vapor layer is determined by film boiling on a surface of constant temperature, and the effect of the wave behavior on it is negligible. Under the assumptions adopted, the liquid-vapor interface behaves during its contact with the surface as depicted in Figure 5.5. When the mean vapor thickness is $\delta 1$, the contact begins, and decreasing the vapor thickness, the higher the

contact between liquid and solid. From the system shown in the figure, the fractional liquid-solid contact area is given by:

$$F = \frac{L}{\left(\frac{2\pi}{\omega}\right)} \qquad [5.4.10]$$

where contact occurs over the length L, where $L = x_2 - x_1$, and x_2, x_1 are the contact points of the wave with the surface, that is the two points where $\eta = -\delta$ in the domain $0 \le x \le \frac{2\pi}{\omega}$. From the symmetry of the wave:

$$x_1 \le \frac{\pi}{\omega};\ x_2 \ge \frac{\pi}{\omega}$$

$$\frac{\pi}{\omega} - x_1 = x_2 - \frac{\pi}{\omega} \quad \Rightarrow \quad x_1 + x_2 = \frac{2\pi}{\omega}$$

Therefore

$$L = 2\left(\frac{\pi}{\omega} - x_1\right)$$

From this later result and equations [5.4.9] and [5.4.10], F is given by:

$$F = 1 - \frac{1}{\pi} Cos^{-1}\left(-\frac{\delta}{A}\right) \qquad [5.4.11]$$

According to Figure 2.29, the ratio δ/A should be dependent on water subcooling and it is expected to be also dependent on velocity. As a result, equation [5.4.11] can be applied to fit the parameters FA for the parallel flow region, which hereafter will be

called *FP1, FP2* and *FP3* to differentiate them from the ones of the impingement region. A modified form of equation [5.4.11] in terms of subcooling and jet velocity was used:

$$FP = 1 - \frac{1}{\pi} Cos^{-1}\left[-\left(a - b\overline{\Delta T}_{sub}^{c}\,\overline{U}_{jet}^{d}\right)\right] \qquad [5.4.12]$$

where *a, b, c,* and *d* are constants given in Table 5.3, and

$$\overline{\Delta T}_{sub} = \Delta T_{sub} / 100$$
$$\overline{U}_{jet} = U_{jet} / 20$$

Equations [5.4.11] and [5.4.12] allow an approximation of the complex relationship between film and transition boiling, and of the interface displacement with the mean vapor film thickness. Also, they open the opportunity to calculate the boiling curve by only using process parameters, or the vapor-film thickness. With regards to this latter parameter, recently Weichert et al.[13] developed an optical measuring technique for the vapor film thickness that may be very promising with respect to quantifying not only film boiling heat transfer, but the transition boiling as well.

The effect of water subcooling and jet velocity on the fraction liquid-solid contact area for a fixed superheat, *FA1, FA2,* etc., is presented in Figure 5.6. Figure 5.6[a] for the impingement region of a water bar, and Figure 5.6[c] for the parallel flow region present the different parameters *FA* and *FP* as a function of subcoooling for a constant jet velocity of 6m/s, and both show that the liquid-solid contact is enhanced significantly with increasing subcooling, and the rate of increase is higher at lower subcoolings, which is in agreement with the observations presented earlier in this section. The effect of jet velocity is presented in Figure 5.6[b] for the impingement region of a water bar

maintaining the subcooling to a typical value of 75°C. The fitted results show that increasing the water jet velocity the liquid-solid contact is enhanced, according a previous discussion.

5.5 Nucleate Boiling

In the literature review it was pointed out that the extrapolation of the presently reported nucleate boiling correlations to the transition boiling regime might overestimate in orders of magnitude the actual liquid-solid contact heat flux, $q_{l\text{-}s}$. On the other hand, experimental measurements of this parameter are confined to only one set of experiments on falling drops.

Alternatively, this author developed previously a mathematical model to predict the extrapolation of nucleate boiling to the transition boiling regime. That mathematical model was modified for this research to account for the experimentally observed decrease of the heat fluxes during liquid-solid contact at higher temperatures in the transition boiling regime of the falling drop, as shown in Figure 2.25. At low water temperatures, the heat fluxes increase with superheat, and eventually they reach a plateau, whereas at higher water temperatures, a maximum heat flux is found, and after the heat fluxes decrease dramatically.

Accordingly, the model developed previously by Hernandez[5] (equation [2.4.2.5]) was modified to obtain:

$$q_{triple-point} = \left\{15.575 m_{e,tp} H_{fg} \Delta T_{sat}\right\}^{1.333(1-DX\,\Delta T_{sat}/1200)} \qquad [5.5.1]$$

It is noteworthy to mention that the only difference between the two equations is the term $DX\Delta T_{sat}/1200$ in the exponent. The exponent DX, which accounts for the reduction of the heat flux with superheat, can be dependent on subcooling and velocity, but this later one is believed to have a negligible effect at high temperatures on nucleate boiling, since as it was discussed in the literature review, the evaporation process is dominant, and only subcooling becomes relevant. Thus, empirical formulas were obtained so as to have a reasonable agreement with results in Figure 2.25, as follows:

For the impingement region of a water bar jet:

$$DX = 0.1548 + 0.6285\, exp(-0.0444\Delta T_{sub}) \qquad [5.5.2]$$

For the impingement region of a water curtain jet and the parallel flow region:

$$DX = 0.1493 + 0.5507\, exp(-0.0825\Delta T_{sub}) \qquad [5.5.3]$$

In order to evaluate $q_{l\text{-}S}$ in the general transition boiling curve equation [2.4.1.2], adopted in section 6.1, a modified form of the nucleate boiling equation [2.4.2.4] was adopted to include the one-phase convection heat transfer taking place during nucleate boiling, which ensures that at surface temperatures below the boiling temperature of water a heat flux can also be calculated. The equation employed is:

$$q_{l-s} = q_{NB} = q_{triple-point} + q_{conv} \qquad [5.5.4]$$

where the pure convection heat transfer in the impingement region was obtained from Webb et al.[7]:

$$Nu_{x,conv} = \frac{q_{conv} d_{jet}}{\Delta T_{sub} k_f} = 0.505 Re_{jet}^{0.5} Pr^{0.376} \qquad [5.5.5]$$

where

$$Re_{jet} = \frac{U_{jet} d_{jet}}{\nu}$$

The single-phase convection heat transfer for parallel flow is calculated using the equation [2.2.3] and equation [2.2.4], adopting arbitrarily the Reynolds number at half the distance between jetlines.

$$Re_x = \frac{U_p (x_{between-jetlines} / 2)}{\nu}$$

5.6 Transition Boiling in the Impingement Zone

According to the discussion presented in section 5.1, the general transition boiling equation:

$$q_{TB} = q_{l-s} F + q_{v-s} (1 - F) \qquad [2.4.1.2]$$

was adopted. The heat-transfer coefficients used in the runout table model are defined as:

$$h_{TB} = \frac{q_{TB}}{\Delta T_{sat} + \Delta T_{sub}} \qquad [5.6.1]$$

The liquid-solid heat flux, $q_{l\text{-}s}$, is given by equation [5.5.4], where the macrolayer evaporation parameter, $m_{e,tp}$, was considered a constant, $m_{e,tp} = 6.0x10^{-5}\ Kg\ m^{-1}\ s^{-1}\ {}^{o}C^{-1}$, according to the value found by Pasamehmetoglu et al[14].

The vapor-solid contact heat transfer, $q_{v\text{-}s}$, is assumed to be given by film boiling on an isothermal surface as follows:

$$q_{v-s} = q'_{FB} \qquad [5.6.2]$$

where the contribution of radiation heat transfer through the vapor layer is accounted for by:

$$q'_{FB} = q_{FB} + q_{rad} \qquad [5.6.3]$$

During the development of the model of the boiling curves, it was observed that they were independent of the strip speed. Consequently, if the liquid-solid heat flux and the fractional liquid-solid contact area were independent of the strip motion, it is only natural to neglect the strip motion effect on the minor contributor to the transition boiling heat flux, which is the film boiling heat transport. Also, the subcooling of the water in the impingement region of all the runout table operation is high, since typically the water temperature is below 40°C. Accordingly, in order to simplify the calculations in the runout table model, the asymptotic expression obtained by Nakayama [6] was adopted (equation [2.4.4.8]):

$$Nu_x = \frac{q_{FB}x}{\Delta T_{sat}k} = \left(\frac{m(1+3m)\xi^{*3}}{10}\right)^{1/4}\left(\frac{\mu_f}{\mu}\Gamma\sqrt{Pr_f}\right)^{3/4} Re_x^{1/2} \qquad [2.4.4.8]$$

where

$$m = 1$$

$$\xi^* = \left(\frac{5}{3}\frac{1+m}{1+3m}\right)^{1/2}$$

$$\Gamma = \left(\frac{Pr}{Pr_f}\right)\left(\frac{C_{p_f}\Delta T_f}{C_p \Delta T_{sat}}\right)$$

That equation was also obtained as a special case of the general model presented in section 5.2, neglecting the effect of the strip motion and assuming large subcooling of the liquid. The assumption of negligible effect of the strip motion was also justified by the results obtained for typical runout table conditions by the model in section 5.2, which are to be presented later in this work. The Reynolds number employed during the calculations was:

$$Re_x = \frac{U_e x}{\nu}$$

where the free stream velocity for a water curtain and a water bar jet are given by equation [2.3.2] and [2.3.3], respectively, and the position was arbitrarily selected $x=0.5x^* d_{jet,}$ where $x^*=1.3$ for bars, and $x^*=1.75$ for curtains (see Figures 2.4 and 2.5). The selection of an arbitrary position in the impingement region is justified by the experimental results shown in Figure 2.7, as discussed in the literature review.

The radiation heat transfer component was given by[15]:

$$\begin{aligned} q_{rad} &= \varepsilon\sigma\left(T^4 - T_{sat}^4\right) \\ \varepsilon &= 0.85 \\ \sigma &= 0.56697x10^{-7} \end{aligned} \qquad [5.6.4]$$

The fractional liquid-solid contact area, F, was calculated from equation [5.4.2], and equations [5.4.5]-[5.4.8]. The constants in equation [5.4.8] are given in Table 5.2.

5.7 Transition Boiling in the Parallel Flow Region

The same general transition boiling equation and definition of the heat transfer coefficients as in the model for the impingement region were adopted (equations [2.4.1.2] and [5.6.1]).

The liquid-solid heat flux, $q_{l\text{-}s}$, comes similarly from equation [5.5.4], where $m_{e,tp} = 6.0x10^{-5}\ Kg\,m^{-1}\,s^{-1}\,{}^{o}C^{-1}$ [14]. The heat flux in the vapor-solid contact is also given by equation [5.6.2], but the total film boiling heat transfer coefficient was obtained by extending the analysis by Filipovic et al.[15] to the present conditions. The resulting total heat transfer coefficient is:

$$h_{FB} = \frac{1}{2}h_r + \frac{1}{2}\left[h_r^2 + 4h_c^2\right]^{1/2} \qquad [5.7.1]$$

where

$$h_r = \left(\frac{1}{\frac{1}{\varepsilon_s} + \frac{1}{\varepsilon_p} - 1}\right)\left(\frac{\sigma\left(T_p^4 - T_s^4\right)}{T_p - T_s}\right) \qquad [5.7.2]$$

where $\varepsilon_p = 0.85$, $\varepsilon_s = 1$, $\sigma = 0.56697x10^{-7}\,Wm^{-2}K^{-4}$, and the total heat flux is:

$$q'_{FB} = h_{FB}\Delta T_{sat} \qquad [5.7.3]$$

The convection film boiling heat transfer coefficient was taken from the correlation developed by Filipovic et al.[15]:

$$Nu_{x,FB} = \frac{q_{FB}x}{k_v \Delta T_{sat}} = \frac{h_c x}{k_v} = C^d(1+m)^{-a}\beta\overline{U}_l^{\,c}\frac{\mu_l}{\mu_v}\left(\frac{D_2}{\alpha}\right)^a Re_x^d\, Pr_l^{1-p} \qquad [5.7.4]$$

where

$C = 0.0228$ *(ref. 9)*

$n = 7,\ p = 1/3$

$m = 2/(n+1)$

$a = m/(m+1)$

$$\beta = \frac{Pr_v\, C_{p_l} \Delta T_{sub}}{Pr_l\, C_{p_v} \Delta T_{sat}}$$

$d = 1/(m+1)$

$\overline{U}_l = U_l / U_i$

$U_i = U_{jet}$ *if* $U_{jet} > U_p$; $U_i = U_p$ *if* $U_{jet} \le U_p$

$U_l = \left| U_{jet} - U_s \right|$

$c = (1-m)/(1+m)$

$D_2 = 2\overline{U}_s + n\overline{U}_{jet}$

$$\overline{U}_s = U_s / U_i = \frac{\overline{U}_{jet} + \beta\, Pr_l^{1-p}\, \overline{U}_p}{1 + \beta\, Pr_l^{1-p}}$$

$\overline{U}_{jet} = U_{jet} / U_i$

$\alpha = (n+1)(n+2)$

$Re_x = U_i x / \nu$

$\overline{U}_p = U_p / U_i$

In the application of this equation, the effect of strip motion was neglected for the same reasons discussed in section 5.6 for the impingement region, and the x position was arbitrarily selected as half the distance between jetlines, since it was assumed that the heat flux at that position may represent well the average over the length.

The fractional liquid-solid contact area, F, was calculated using equation [5.4.12]. The constants in this equation are shown in Table 5.3.

5.8 References

1.- J. Filipovic, F.P. Incropera, R. Viskanta, "Quenching Phenomena associated with a Water Wall Jet: I. Transient Hydrodynamic and Thermal Conditions", Experimental Heat Transfer, vol. 8, 1995, pp. 97-117.

2.- C. S. Yih, Stratified Flows, Academic Press, 1980.

3.- M. Ishii, "Wave Phenomena and Two-Phase Flow Instabilities", in the Handbook of Multiphase Systems, Hemisphere Publishing Corporation, 1982, pp. 2-95-2-96.

4.- J. E. Galloway, I. Mudawar, Int. J. Heat and Mass Transfer, Vol. 36, No. 10, 1993, pp.2511-2526.

5.- V. H. Hernandez A., "Heat Transfer Model of the Hot Rolling Runout Table-Cooling and Coil Cooling of Steel", M. A. Sc. Thesis, December, 1994.

6.- A. Nakayama, Subcooled Forced-Convection Film Boiling in the Presence of a Pressure Gradient, AIAA Journal, vol. 24, No.2, 1986, pp. 230-236.

7.- B. W. Webb, C. F. Ma, "Single-Phase Liquid Jet Impingement Heat Transfer", Advances in Heat Transfer, Vol. 26, pp. 105-217, 1995.

8.- F. M. White, Viscous Fluid Flow, 2nd Ed., McGraw Hill, 1991.

9.- L. C. Burmeister, Convective Heat Transfer, 2nd Edition, John Wiley and Sons Inc., 1993.

10.- V. S. Arpaci, P. S. Larsen, Convection Heat Transfer, Prentice Hall, Englewood Cliffs, NJ, pp. 182-187.

11.- D. A. Zumbrunnen, R. Viskanta, F. P. Incropera, "The Effect of Surface Motion on Forced Convection Film Boiling Heat Transfer", Journal of Heat Transfer, Vol. 111, August 1989, pp. 760-766.

12.- A. Nakayama, H. Koyama, "Integral Treatment of Subcooled Forced Convection Film Boiling on a Flat Plate", Wärme-und Stoffübertragung, 20, 1986, pp. 121-126.

13.- R. Weichert, et al., "A New, Optical Measuring Technique for the Determination of the Vapour Film Thickness during Film Boiling", Steel Research, 66, No. 6, 1995, pp.244-250.

14.- K. O. Pasamehmetoglu, P. R. Chappidi, C. Unal, R. A. Nelson, "Saturated Pool Nucleate Boiling Mechanisms at Heat Fluxes", Int. J. Heat Mass Transfer, Vol. 36, No. 15, 1993, pp. 3859-3868.

15.- J. Filipovic, R. Viskanta, F. P. Incropera, "An Analysis of Subcooled Turbulent Film Boiling on a Moving Isothermal Surface", Int. J. Heat Mass Transfer, Vol. 37, No. 17, 1994, pp. 2661-2673.

16.- CRC Handbook of Chemistry and Physics, 61st Ed., CRC Press Inc., 1981.

17.- Touloukian Y. S., Thermophysical Properties of Matter, Vol. 6, Washington, 1970.

18.- Touloukian Y. S., Thermophysical Properties of Matter, Vol. 11, Washington, 1970.

19.- Touloukian Y. S., Thermophysical Properties of Matter, Vol. 3, Washington, 1970.

20.- M. N. Ozisik, Basic Heat Transfer, 1st Ed. (Spanish), McGraw Hill, 1977.

Table 5.1: Thermophysical Properties of liquid water and steam.

Property	Equation	Units	Ref.
	Water		
Density	$\rho_l = 1.001x10^3 - 6.974x10^{-2}\,T - 3.588x10^{-3}\,T^2$	Kg/m^3	16
Heat Capacity	$Cp_l = 2.140 - 9.681x10^{-3}\,T_k + 2.685x10^{-5}\,T_k^{\,2} - 2.421x10^{-8}\,T_k^3$	Cal/g/K	17
Surface Tension	$\sigma_l = (75.99 - 0.1666T)x10^{-3}$	N/m	16
Viscosity	$\nu_l = 2.414x10^{-2} * 10^{247.8/T_k - 140}$	Kg/m s	18
Thermal Conductivity	$k_l = 4.183x10^{-4}\left(-1391 + 15.19T_k - 0.01904T_k^2\right)$	W/m°C	19
Heat of evaporation	$h_{fg} = 9596$	Cal/mol	20
	Steam		
Density	$\rho_v = 0.7599 - 1.871x10^{-3}\,T + 2.376x10^{-6}\,T^2 - 1.066x10^{-9}\,T^3$	Kg/m^3	20
Heat Capacity	$Cp_v = 1000\left(1.833 + 4.965x10^{-4}\,T + 1.146x10^{-7}\,T^2\right)$	J/Kg/K	20
Viscosity	$\nu_v = 1x10^{-5}\left(0.8946 + 4.065x10^{-3}\,T - 6.943x10^{-7}\,T^2\right)$	Kg/m s	20
Thermal Conductivity	$k_v = 0.01681 + 8.188x10^{-5}\,T + 2.107x10^{-8}\,T^2$	W/m°C	20

T_k is the temperature in K, T is in °C

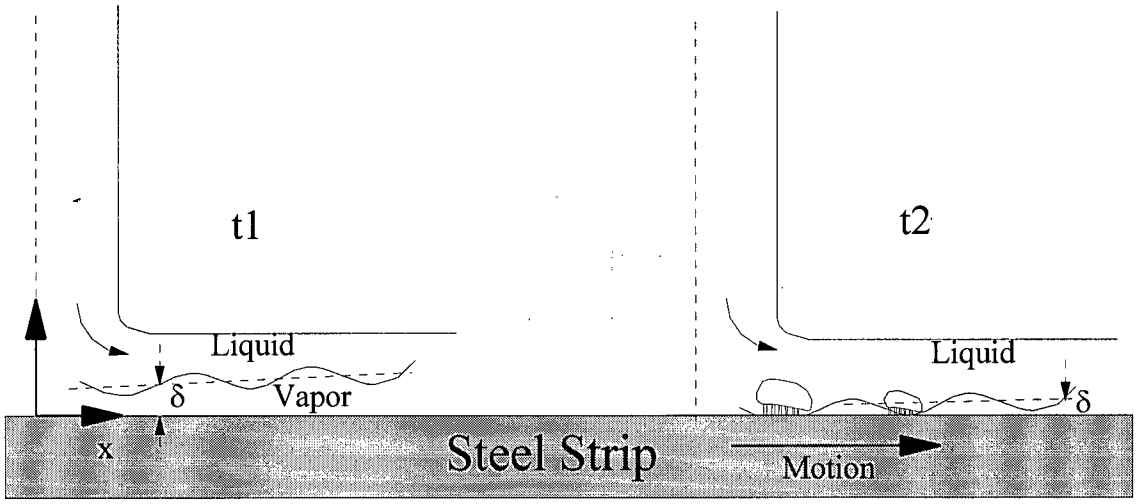

Figure 5.1: Macrolayer Evaporation Mechanism in Jet Boiling on a Long Surface.

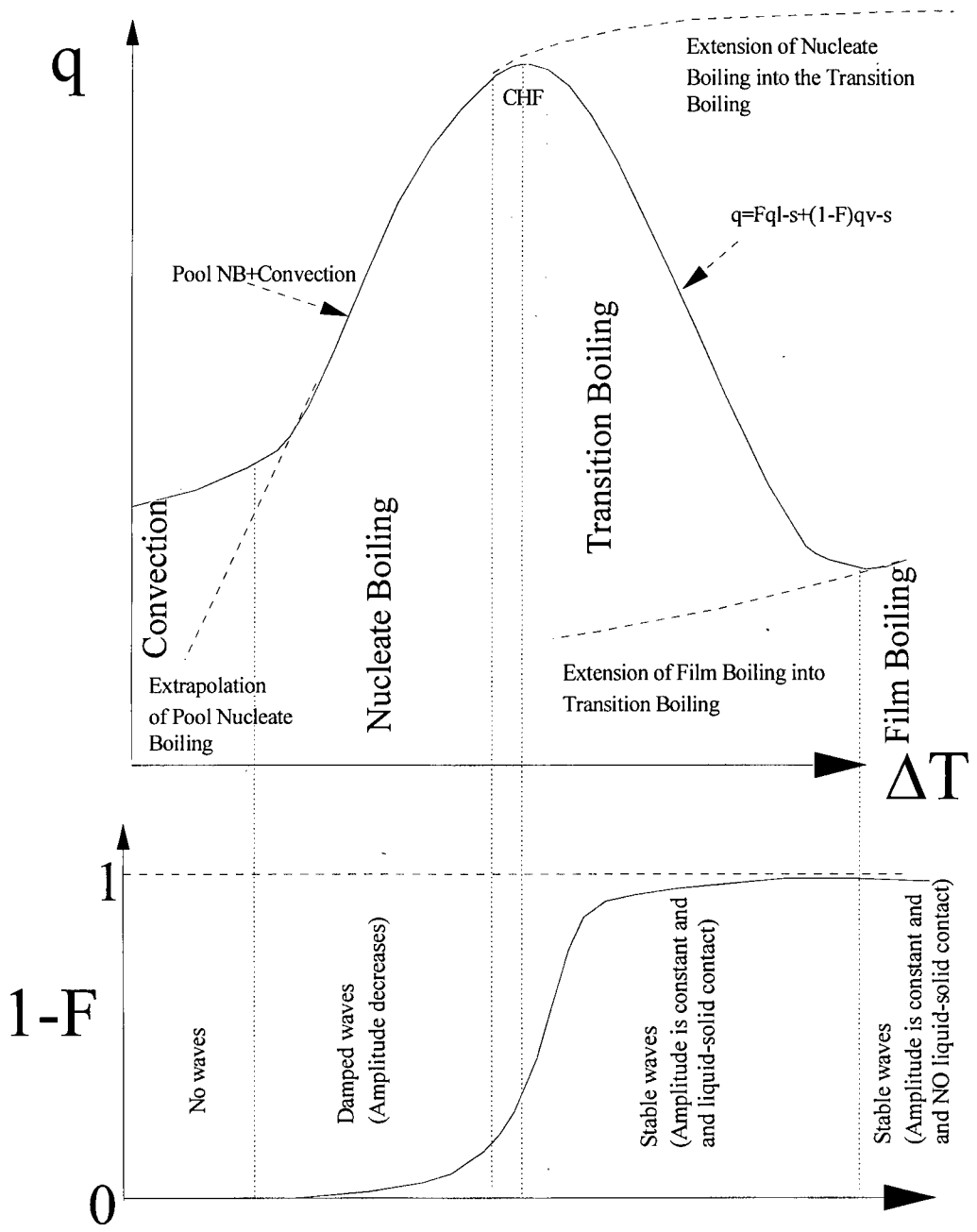

Figure 5.2: Principles of Boiling Curve Modeling and the Mechanisms of Boiling

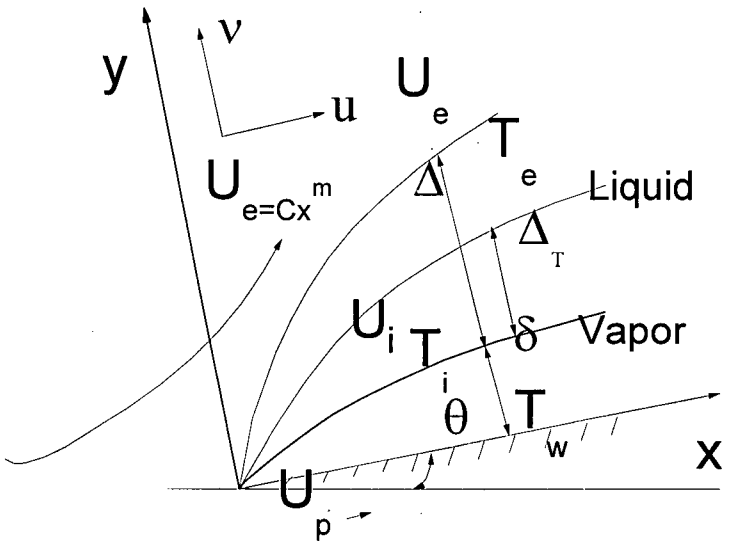

Figure 5.3: Schematic flow and coordinates for the film boiling model in the impingement region

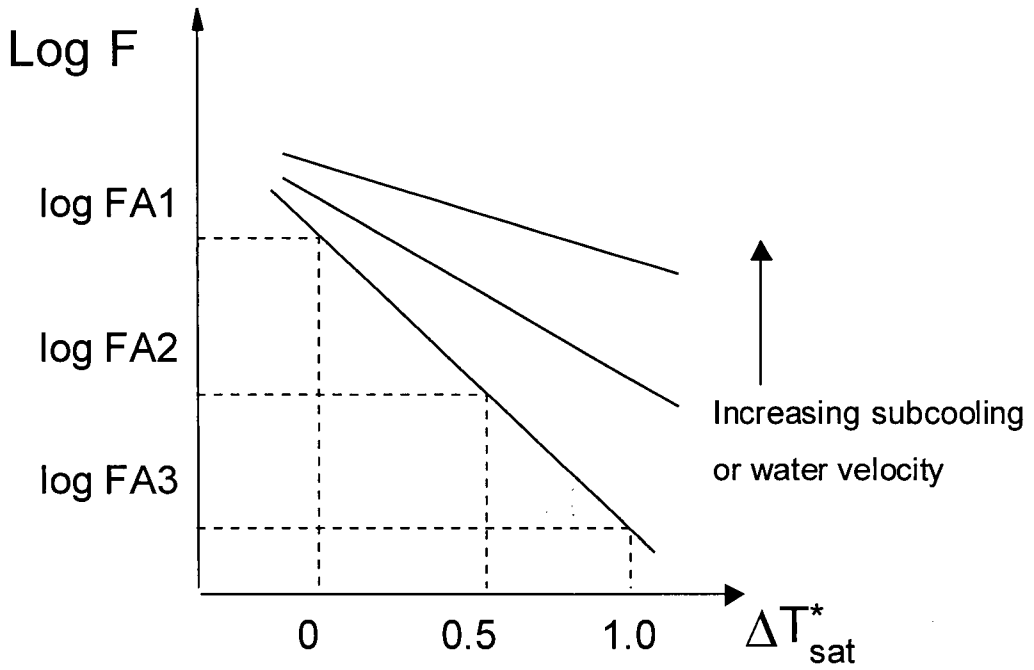

Figure 5.4: Schematic effect of water subcooling and velocity on the fractional liquid-solid contact area.

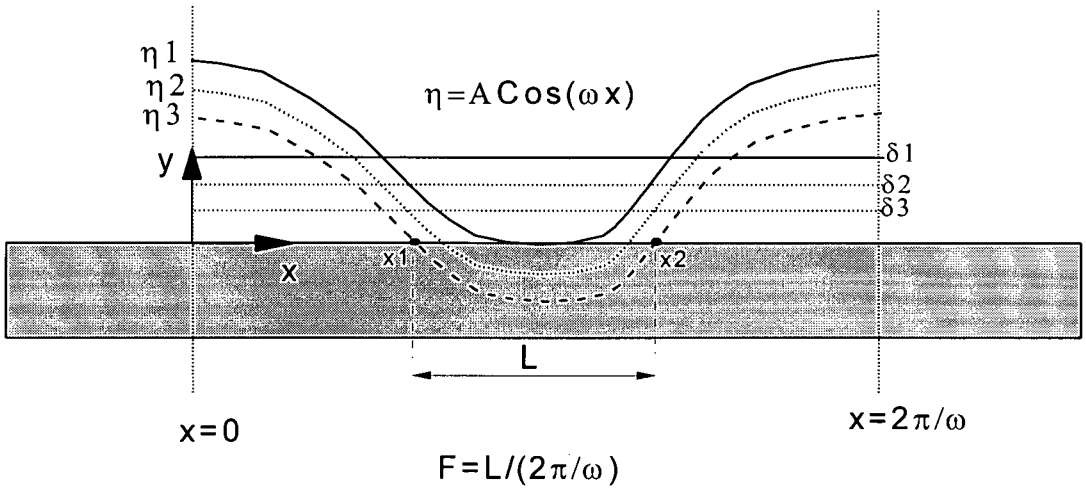

Figure 5.5: Schematic liquid-vapor interface and the fractional liquid-solid contact in transition boiling

Table 5.2 Constants of the equation for the fractional liquid-solid contact area in the impingement region

Parameter	a_1	a_2	a_3	a_4	a_5
FA1	0.2034	2.1464e-3	6.30e-13	6.23e-9	1.01e-9
FA2	2.0581e-9	1.6103e-3	2.41e-13	4.9148e-3	1.3185e-3
FA3	1.8633e-9	8.0542e-4	9.8e-14	5.08e-12	2.1739e-3

Table 5.3: Constants of the equation for the fractional liquid-solid contact area in the parallel flow region

Parameter	*a*	*b*	*c*	*d*
FP1	0.8443	0.1830	0.6422	0.0808
FP2	0.9999	0.2928	3.1755	1.4432
FP3	1.0	0.1910	5.6670	3.6361

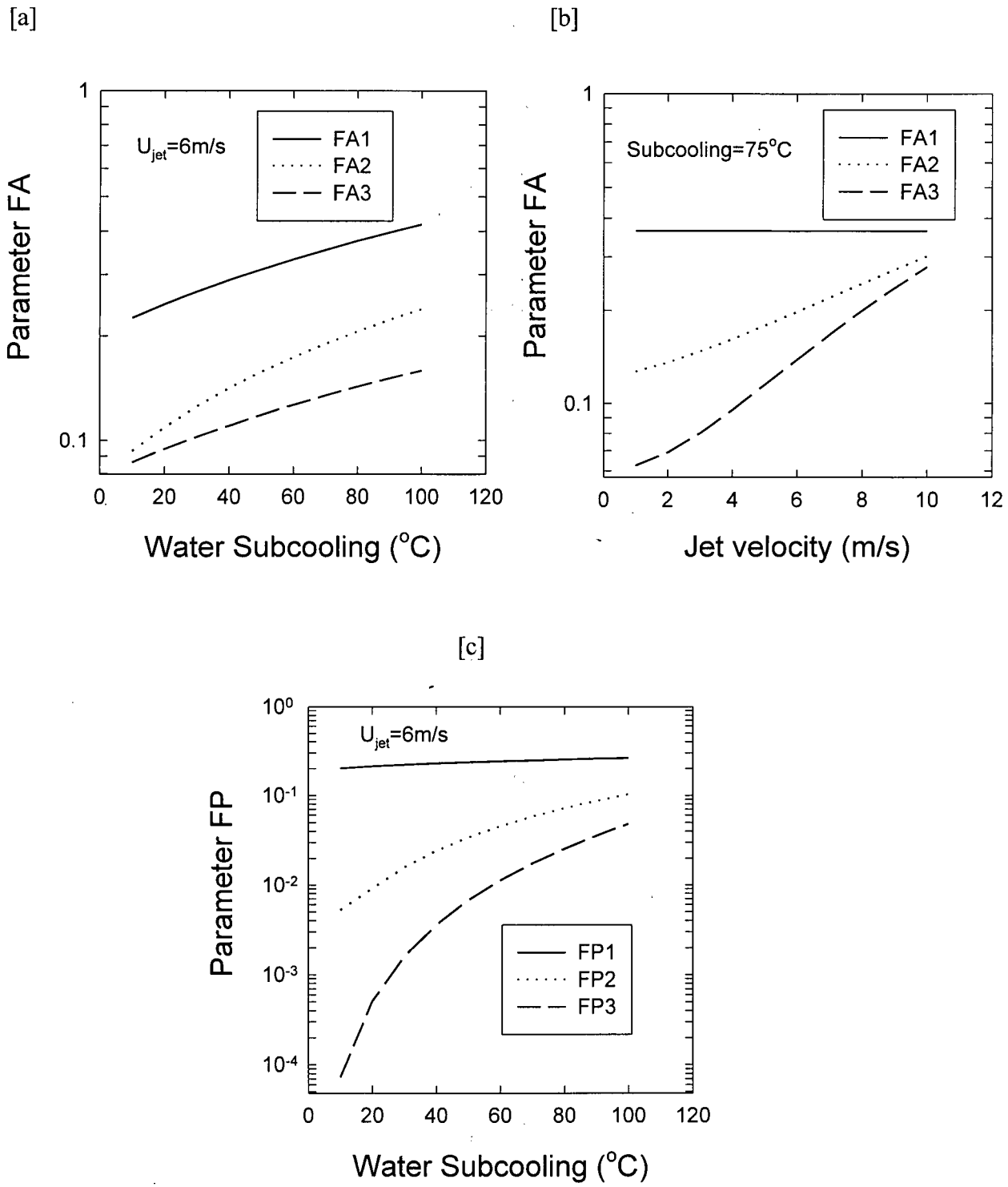

Figure 5.6: Fractional liquid-solid contact area at different superheats. [a] Effect of water subcooling for an impinging bar jet, [b] Effect of jet velocity for an impinging jet, and [c] Effect of water subcooling in the parallel flow. FA1=F(ΔT^*_{sat}=0), FA2=F(ΔT^*_{sat}=0.5), FA3=F(ΔT^*_{sat}=1.0) for bar jets, FP1=F(ΔT^*_{sat}=0), FP2=F(ΔT^*_{sat}=0.5), FP3=F(ΔT^*_{sat}=1.0) for parallel flow.

6. RUNOUT TABLE MODEL

The mathematical formulation of the runout table is presented in this chapter. This formulation includes the boiling curve model developed in the previous chapter and a simple mathematical description of the water flow on the top and bottom surfaces based on the observations presented in Chapter 4.

6.1 Runout Table Model

A flowchart of the runout table model is presented in Figure 6.1. The general layout of the runout table is introduced along with the operating and initial conditions, and some other model parameters. The heat conduction in the strip is calculated by solving the differential equations for a moving volume element such as the one shown in Figure 6.2, by the finite difference method for each time step while moving through the different cooling zones present in the runout table. At each position a cooling zone is defined for both surfaces and the heat transfer coefficients are calculated accordingly. In the case of water cooling areas, the local water temperature is calculated, which is used to determine the local heat transfer coefficients. For each time step, the thermal properties and the phase transformation kinetics are calculated through the thickness of the strip. The mathematical description of each of the model components is presented.

6.1.1 Heat Conduction in the Steel Strip

The general heat-conduction equation for a moving solid is given by [1]:

$$\rho_s C_{p_s} \frac{DT}{Dt} = \nabla \cdot (k_s \nabla T) + g \qquad [6.1.1]$$

where $\rho_s = \rho_s(T)$; $C_{p_s} = C_{p_s}(T)$; $T = T(\mathbf{r},t)$; $g = g(\mathbf{r},t)$, are the steel density, heat capacity, temperature and the volumetric heat source respectively. The differential operators for a rectangular coordinate system (Figure 6.2) are defined as:

$$\frac{D}{Dt} \equiv \frac{\partial}{\partial t} + u_x \frac{\partial}{\partial x} + u_y \frac{\partial}{\partial y} + u_z \frac{\partial}{\partial z} \quad ; \quad \nabla \equiv \hat{i} \frac{\partial}{\partial x} + \hat{j} \frac{\partial}{\partial y} + \hat{k} \frac{\partial}{\partial z}$$

where $\hat{i}$, $\hat{j}$, $\hat{k}$, are the unit direction vectors along the x, y and z directions, and $\mathbf{r}$ is the position with respect to a fixed coordinate system.

A particular heat conduction equation for the runout table model was obtained from equation [6.1.1] under the following assumptions:

(1) The temperature field is in steady state,

$$\frac{\partial T}{\partial t} = 0 \qquad [6.1.2]$$

(2) The heat flux in the direction of the width of the strip is negligible, and the thermal profile in this direction is not required.

$$\frac{\partial T}{\partial z} = 0 \qquad [6.1.3]$$

(3) Strip speed condition

$$u_x = u_p; \; u_y = u_z = 0 \qquad [6.1.4]$$

(4) Heat transfer due to bulk motion is much larger than the heat conduction in the same direction. In order to compare the magnitude of these two terms, the equation [6.1.1] was put in a dimensionless form by neglecting the heat generation term, which is not necessary for this comparison. The resulting equation is, under the assumptions (1)-(3), as follows:

$$\frac{\partial T^+}{\partial x^+} = \frac{1}{Pe}\left\{\frac{\partial^2 T^+}{\partial^2 x^+} + \left(\frac{l_c}{l}\right)^2 \frac{\partial^2 T^+}{\partial^2 y^+}\right\}$$

$$y^+ = y/l;\ \ x^+ = x/l_c;\ \ T^+ = T - T_{ref}\,/\Delta T_{ref};\ \ Pe = u_x/(\alpha / l_c)$$

where

$$Pe_{min} = \frac{Convection}{Diffusion} = 6x10^7;\ \ (l_c/l)^2{}_{min} = 1x10^7$$

for the typical hot strip mill conditions. Therefore,

$$\frac{\partial}{\partial x}\left(k\frac{\partial T}{\partial x}\right) = 0 \qquad [6.1.5]$$

(5) Constant strip velocity within the time interval of each calculation. Thus, the coordinate transformation

$$x = u_p t$$

can be applied.

Consequently, under these assumptions the runout table heat conduction differential equation is:

$$\rho C_p \frac{\partial T}{\partial t} = \frac{\partial}{\partial y}\left(k\frac{\partial T}{\partial y}\right) + g \qquad [6.1.6]$$

subject to the initial condition:

$$t = 0,\ 0 \le y \le L_s,\ T = T_0(y) \qquad [6.1.7]$$

and boundary conditions:

$$y = 0;\ \ -k\frac{\partial T}{\partial y} + h_0 T = h_0 T_{\infty,0} \qquad [6.1.8]$$

$$y = L_s;\ \ k\frac{\partial T}{\partial y} + h_{L_s} T = h_{L_s} T_{\infty,L_s} \qquad [6.1.9]$$

Equation [6.1.6] with initial and boundary conditions was solved by the Crank-Nicholson finite difference scheme [1] (see Appendix A). The local heat-transfer coefficients were calculated according to the cooling zone. The model was run with 100 through-thickness nodes and a variable time step depending on the cooling zone (approximately 4000).

6.1.1.1 Initial Conditions

The initial through-thickness condition to solve Equation [6.1.6], $T_0(y)$, was obtained from regression analysis of the predictions of a Finishing Rolling Mill model developed at UBC [2]:

$$\theta = \frac{T_0(y) - T_0(0)}{T_0(L_s/2) - T_0(0)} \qquad [6.1.1.1.1]$$

where

$$\theta = \theta_{ref} + \frac{\Delta\theta}{\Delta y}\Delta y_c$$

$$\theta_{ref} = 1.5988y^* - 0.5988(y^*)^2$$

$$\frac{\Delta\theta}{\Delta y} = -0.01869y^* + 0.01869(y^*)^2$$

$$y^* = \frac{y}{L_c};\ \Delta y = y - y_{ref};\ y_{ref} = 5mm$$

$$T_0(L_c/2) = 0.9989T_0(0) + 1700.0L_c$$

and L_C and $T_O(0)$ are the measured thickness and initial top surface temperature respectively.

6.1.1.2 Thermophysical Properties of steel

The thermophysical properties of austenite, ferrite and pearlite were obtained by regression analysis of the measurements by BISRA [3]. Calculation of thermophysical properties in the model in the multi-constituent regions is performed by the application of a linear law of mixtures such as:

$$X = \sum_{i=1}^{C} F_i x_i \qquad [6.1.1.2.1]$$

where X is the property of the mixture, F_i is the volume fraction of the microconstituent, x_i is the property of the microconstituent i, and C is the total number of microconstituents.

- Thermophysical properties of austenite

The closest chemistry of steel to the A36 reported by BISRA was %C=0.23, %Mn=0.635 (as compared to the nominal A36 %C=0.17, %Mn=0.74), whereas the closest to the DQSK was a %C=0.06, %Mn=0.38 steel. The chemistry differences are considered to be negligible according to an inspection of the variations in thermal properties with chemistry around these values. Regression analysis was performed to obtain the density, the thermal conductivity, and the heat capacity as a function of temperature. It is noteworthy to mention that the change of behavior of the heat capacity at lower temperatures was considered by the researchers of BISRA [3] to also be part of the behavior of austenite. In order to verify the set of equations obtained, calculation of the thermal diffusivity was carried out and compared to the measured values from the same source. Very consistent results were obtained as shown in Figure 6.3 and Figure 6.4, even

considering the apparent deviation of austenite thermal conductivity at lower temperatures.

• Thermophysical properties of ferrite

The ferrite properties were obtained for the ferritic part of a %C=0.06, %Mn=0.38 steel. It is assumed that the thermal properties of the ferrite in this steel are the same as the ferrite formed in the A36 and DQSK steels. Similarly to the previous case, the density and the thermal conductivity were obtained by regression analysis, whereas the heat capacity was obtained from an equation published elsewhere[4]. Figure 6.5 shows the regression lines obtained, as well as the verification of these equations by the comparison of the thermal diffusivity calculated with the one measured. Agreement is very good.

• Thermophysical properties of pearlite

Pearlite properties were obtained for a %C=0.80, %Mn=0.32 steel (eutectoid). Again regression equations were obtained and verified by the calculation of the thermal diffusivity, as shown in Figure 6.6 .

A summary of the thermophysical properties and the specific enthalpy of transformation is presented in Table 6.1.

6.1.2 Cooling in Air

Cooling in air occurs by radiation and convection to the surrounding air. Mixed convection always takes place at typical runout table conditions, since the high temperature of the steel promotes a density driven flow (natural convection) and the always moving strip encourages forced convection.

Radiation heat transfer is calculated by Equation [2.2.1]:

$$q_{rad} = \varepsilon\sigma(T_{surface}^4 - T_{ambient}^4) \qquad [2.2.1]$$

$$\varepsilon = 1.1 + \frac{(T-273)}{1000}\left[1.25x10^{-4}(T-273) - 0.38\right];\ T \text{ in } K$$

Since mixed convection takes place, appropriate equations are needed to calculate the heat transfer coefficients for this kind of cooling. Estimation of natural, forced and mixed convection was carried out for top and bottom surfaces. In order to calculate the mixed convection heat transfer, the natural and forced convection contributions to the total mixed convection heat transfer were considered by equation [2.2.5] assuming an exponent n=3.75. In the study of mixed convection, results are often presented by plots of Nu/Re^a *vs.* Gr/Re^b, which are of widespread use [5]. The exponents a and b depend on whether the flow is turbulent or laminar. One important advantage of such a plot is that the pure natural or the pure forced convection heat transfer are obtained as limiting cases of the mixed convection curve. Consequently, only one equation is necessary to predict natural, forced or mixed convection, and the transition between them by changing the conditions is continuous. Such heat transfer plots were obtained for the top and bottom surfaces based on Equations [2.2.2] to [2.2.5]. Results for the top surface are presented in Figure 6.7. The air thermal properties were calculated at $T=0.5(T_{surface} - T_{surroundings})$, using equations obtained from regression analysis of published data [5], as shown in Table 6.2. Accordingly, the equations employed in the model are:

For laminar convection on top surface ($Gr_L\ Pr \le 2x10^7$, $Re_L < 5x10^5$):

$$\frac{Nu_{mix_L}}{Re_L^{0.5}} = \frac{2\,Pr^{0.5}}{\left(\frac{10}{3}\right)^{0.5} + \frac{20r}{27\,Pr^{0.5}\,A_l^{0.5}}} *$$

$$\left\{1+0.00737\left[\left(\frac{10}{3}\right)^{0.5}+\frac{20r}{27\,Pr^{0.5}\,A_1^{0.5}}\right]^{3.75}\left(\frac{Gr_L}{Re_L^2}\right)^{0.9375}Pr^{-0.9375}\right\}^{0.2667} \qquad [6.1.2.1]$$

For turbulent convection on top surface:

$$\frac{Nu_{mix_L}}{Re_L^{0.5}}=1.25*0.019(9-7r)^{0.2}\,Pr^{0.333}\left\{1+0.000272\left[0.019(9-7r)^{0.2}\right]^{-3.75}\left(\frac{Gr_L}{Re_L^{2.4}}\right)^{1.25}\right\}^{0.2667} \qquad [6.1.2.2]$$

For laminar convection at bottom surface:

$$\frac{Nu_{mix_L}}{Re_L^{0.5}}=\frac{2\,Pr^{0.5}}{\left(\frac{10}{3}\right)^{0.5}+\frac{20r}{27\,Pr^{0.5}\,A_1^{0.5}}}*$$

$$\left\{1+0.000548\left[\left(\frac{10}{3}\right)^{0.5}+\frac{20r}{27\,Pr^{0.5}\,A_1^{0.5}}\right]^{3.75}\left(\frac{Gr_L}{Re_L^2}\right)^{0.9375}Pr^{-0.9375}\right\}^{0.2667} \qquad [6.1.2.3]$$

where $r=1-u_{air}/u_p$; $A_1=1/(0.3-0.1174r)$.

6.1.3 Runout Table Roll Cooling

An analysis of roll cooling in the runout table is presented. The assumptions for this analysis are:

[1] The strip-roll contact is described as the contact of two parallel plates.

[2] During the contact, the thermophysical properties of the roll and the strip are constant.

[3] The contact resistance is described by a constant heat transfer coefficient.

[4] Friction dissipation is negligible.

[5] Constant strip speed.

[6] No slip between roll and strip.

[7] The strip behaves elastically only.

[8] The contact length is similar to the continuously loaded beam with two pointwise supports at its ends.

[9] Vibration due to strip motion is neglected

Under these assumptions, the length of the contact is given by[6]:

$$f = \frac{2\psi R L_R}{\psi^2 + L_R^2} \qquad [6.1.3.1]$$

where

$$\psi = \frac{1}{2}\frac{g L_R^4 (t_p \rho_p + t_{wat}\rho_{wat})}{E(T) t_p^3}$$

Schematically, the roll cooling is shown in Figure 6.8. The heat transfer problem is described by:

$$\frac{\partial T_1}{\partial t} = \alpha_1 \frac{\partial^2 T_1}{\partial x^2}; \quad 0 < x < L_1, \; t > 0 \qquad [6.1.3.2]$$

$$T_1 = T_{roll}; \quad x = 0, \; t > 0$$

$$-k_1 \frac{\partial T_1}{\partial x} = h\left(T_{1(x=L_1,t)} - T_{2(x=L_1,t)}\right); \quad x = L_1, \; t > 0$$

$$T_1 = T_{roll}; \quad 0 \le x \le L_1, \; t = 0$$

$$\frac{\partial T_2}{\partial t} = \alpha_2 \frac{\partial^2 T_2}{\partial x^2}; \quad L_1 < x < L_2, \; t > 0$$

$$T_2 = T_{strip}; \quad x = L_2, \; t > 0$$

$$-k_2 \frac{\partial T_2}{\partial x} = h\left(T_{1(x=L_1,t)} - T_{2(x=L_1,t)}\right); \quad x = L_1, \; t > 0$$

$$T_2 = T_{strip}; \quad L_1 \le x \le L_2, \; t = 0$$

The solution of this system of differential equations is by the Explicit Finite Differences method.

The modulus of elasticity for carbon steels was obtained from regression analysis of data published elsewhere[7]:

$$E = 214.8 - 0.1414T \qquad [6.1.3.3]$$

where E is in GPa, T in °C, valid for $20<T<700$°C ($r^2=0.984$). Due to lack of data for higher temperatures, the modulus of elasticity was extrapolated at higher temperatures by this equation. The Poisson ratio was set to 0.30.

6.1.4 Water Flow and Temperature Distributions on the Top Surface

From the runout table observations made, it is clear that the cooling by water bars in the runout table is two-dimensional in nature. Since the proposed model does not account for variations in conditions across the width of the strip, reasonable approximations to the 2-D nature of the water flow have to be introduced in the model. Consequently, a jet impingement band is defined, which is the area where one array of jets, on a jet line, impinges, as seen in Figure 6.9. Within this band (length=header length, width=$x_{imp}=2x^*d_{jet}$), jet impingement and parallel flow areas coexist. In this way, the 2-D characteristics of the water flow, and hence of the heat transfer, can be introduced into the runout table model by an interaction factor, w, defined as: (the distance between nozzle centers-distance between impingement regions)/distance between nozzle centers. The closer to the unity is the interaction factor, the more one-dimensional the arrangement behaves. As it will be discussed in the next section, this parameter is a weighting function that allows the calculation of the heat fluxes in the impingement band.

The impingement jet velocity and width are estimated by Appendix equations [B.1.1] and [B.1.2].

On the other hand, the flow in the parallel region is in many cases, and specially near the impingement band, constituted of water stripes along the strip length. Again, the simplification required for the application of this model is the assumption of a uniform film thickness. Hence, the film thickness of the parallel flow stream is obtained by performing a mass balance on a control volume, such as the one shown in Figure 6.10. The film thickness is given by:

$$h_l = \frac{x_{water} \pi/4 d_{jet}^2}{x_{noz}} \qquad [6.1.4.1]$$

where x_{water} is the fraction of the water flowing in the direction of the strip motion, x_{noz} is the distance between nozzle centers across the width of the strip, and d_{jet} is the impinging jet diameter. Similarly, the water film thickness of a curtain is

$$h_l = x_{wat} w_{jet} \qquad [6.1.4.2]$$

The amount of water flowing with the strip was observed to be dependent on the strip speed. In agreement with the video observations, the following relationships are suggested:

For water bar jets:

$$\begin{aligned} x_{wat} &= 0.75 \qquad U_p > 2.0 m/s \\ x_{wat} &= 0.5 \qquad U_p \leq 2.0 m/s \end{aligned} \qquad [6.1.4.3]$$

For water curtain jets:

$$x_{wat} = 0.5 \qquad [6.1.4.4]$$

The length of the countercurrent parallel flow region (countercurrent with strip motion) is considered to be given by:

$$\begin{aligned} x_{p,counter} &= 0.10 \qquad U_p < 11.0 m/s \\ x_{p,counter} &= 0.05 \qquad U_p \geq 11.0 m/s \end{aligned} \qquad [6.1.4.5]$$

The water temperature along the runout table in the countercurrent parallel flow region is approximated by:

$$T_{local} = \overline{T} - (\overline{T} - T_{jet}) \frac{x}{x_{p,counter}} \qquad [6.1.4.6]$$

where x is the position from the impingement region, $x_{p,counter}$ is the length of the parallel flow region and $\overline{T} = (T_{jet} + T_{previous,parallel})/2$.

Since the heat used for vapor generation and superheating in transition boiling is much less than the maximum 20% found in film boiling, given that at subcooled conditions practically all the bubbles and vapor formed are condensed by the colder water stream, the temperature of the water moving along the strip is obtained by performing a heat balance assuming that all the heat released from the strip is absorbed by the flowing water.

$$T_{local}^{i+1} = T_{local}^{i} + \frac{q}{\rho U_{jet} h_l C_p} \Delta x \qquad [6.1.4.7]$$

where

T_{local}^{i+1} = Actual water temperature
T_{local}^{i} = Previous water temperature
q = Local Heat flux
ρ = Water density
U_{jet} = Impinging jet velocity
h_l = Water film thickness
C_p = Heat capacity
Δx = Position increment (finite differences)

6.1.5 Heat Flux Model during Jet Cooling

The boiling curves during jet cooling are calculated by the procedure described in sections 5.6 and 5.7 for the impingement and parallel flow zones respectively. It is important to mention that the heat fluxes are assigned according to the local water temperature and steel surface temperature, which are calculated for each jet line along the length of the runout table. The heat fluxes in the impingement band are calculated by:

$$q_{band} = wq_{imp} + (1-w)q_{parallel} \qquad [6.1.5.1]$$

where q_{imp} is the heat flux in the impingement region of a jet, $q_{parallel}$ is the heat flux in the parallel flow region of the impingement band, and w is the interaction factor defined as previously, w=(the distance between nozzle centers-distance between impingement regions)/distance between nozzle centers. The interaction factor is dependent mainly on the geometry of the cooling system.

6.1.6 Austenite Decomposition Kinetics

The mathematical model of the austenite decomposition kinetics adopted in this work was developed by researchers of The Centre for Metallurgical Process Engineering.

The details of this model have been published elsewhere [8, 9,10,11,12], and only the equations relevant to this work are presented in Appendix C.

6.2 References

1.- M. N. Ozisik, Heat Conduction, Second Edition, John Wiley and Sons Inc., New York, 1993.

2.- C. A. Muojekwu, private communication, August, 1994.

3.- The British Iron and Steel Research Association, Physical Constants of Some Commercial Steels at Elevated Temperatures, Butterworths Scientific Publications, London, 1953.

4.- F. Medina, "Thermal and Microstructural Evolution of a Hot Strip Mill on a Runout Table", M. Eng. Essay, UBC, 1992.

5.- M. N. Ozisik, Basic Heat Transfer, McGraw Hill, 1st Spanish Edition, 1977.

6.- J. Filipovic, R. Viskanta, F. P. Incropera, T. A. Veslocki, "Thermal Behaviour of a Moving Steel Strip Cooled by an Array of Planar Water Jets", Steel Research, Vol. 63, No. 10, 1992, pp. 438-446.

7.- ASM, Metals Handbook, 9th Edition, Vol. 8 Mechanical Testing, pp.23.

8.- M. Militzer, R. Pandi, E. B. Hawbolt, "Ferrite Nucleation and Growth During Continuous Cooling", Metallurgical and Materials Transactions A, Vol. 27A, June 1996, pp.1547-1555.

9.- M. Militzer, E. B. Hawbolt, T. R. Meadowcroft, "Ferrite Nucleation during Continuous Cooling", Proceedings of the International Symposium on Phase Transformations During the Thermal/Mechanical Processing of Steel, CIM, Vancouver, B. C., Canada, 1995, pp. 445-458.

10.- M. Militzer, R. Pandi, E. B. Hawbolt, T. R. Meadowcroft, "Modelling the Phase Transformation Kinetics in Low-Carbon Steels", Proceedings of the International Symposium on Hot Workability of Steels and Light Alloys-Composites, CIM, Montreal, Quebec, Canada, August 24-28, 1996.

11.- R. Pandi, M. Militzer, E. B. Hawbolt, T. R. Meadowcroft, "Modelling of Austenite Decomposition Kinetics in Steels during Run-out Table Cooling", Proceedings of the International Symposium on Phase Transformations During the Thermal/Mechanical Processing of Steel, CIM, Vancouver, B. C., Canada, 1995, pp. 459-471.

12.- R. Pandi, M. Militzer, E. B. Hawbolt, T. R. Meadowcroft, "Effect of Cooling and Deformation on the Austenite Decomposition Kinetics", 37th MWSP Conference, ISS, Hamilton, Ontario, October 1995, Warrendale, PA, Vol. XXXIII, pp. 635-643.

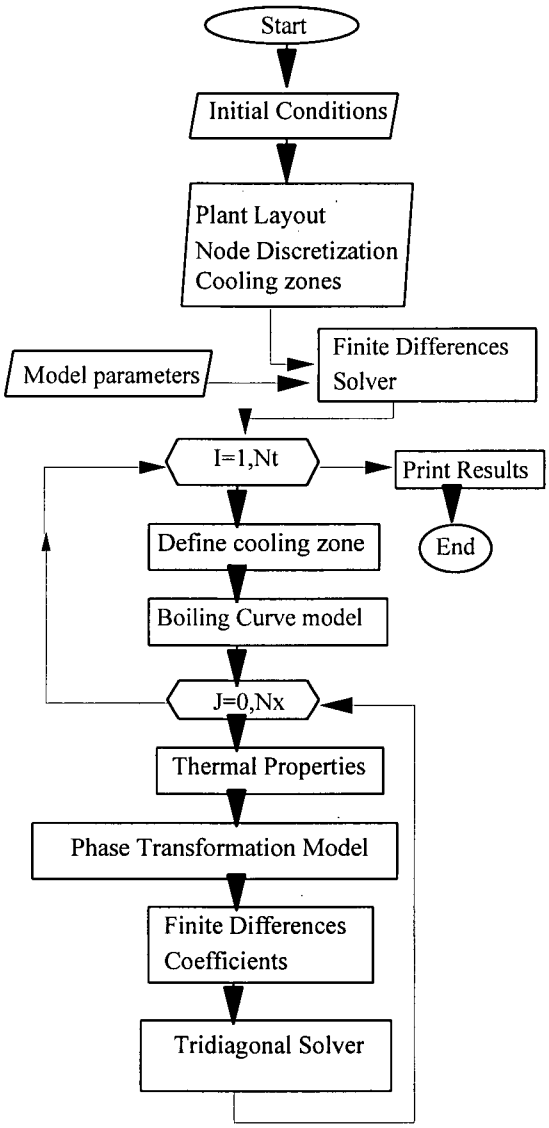

Figure 6.1: Runout Table Model Flowchart

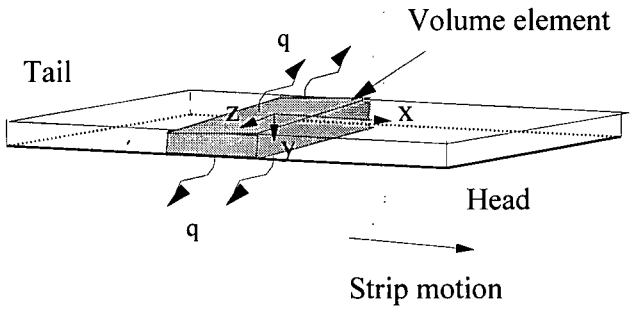

Figure 6.2: Runout table model reference system

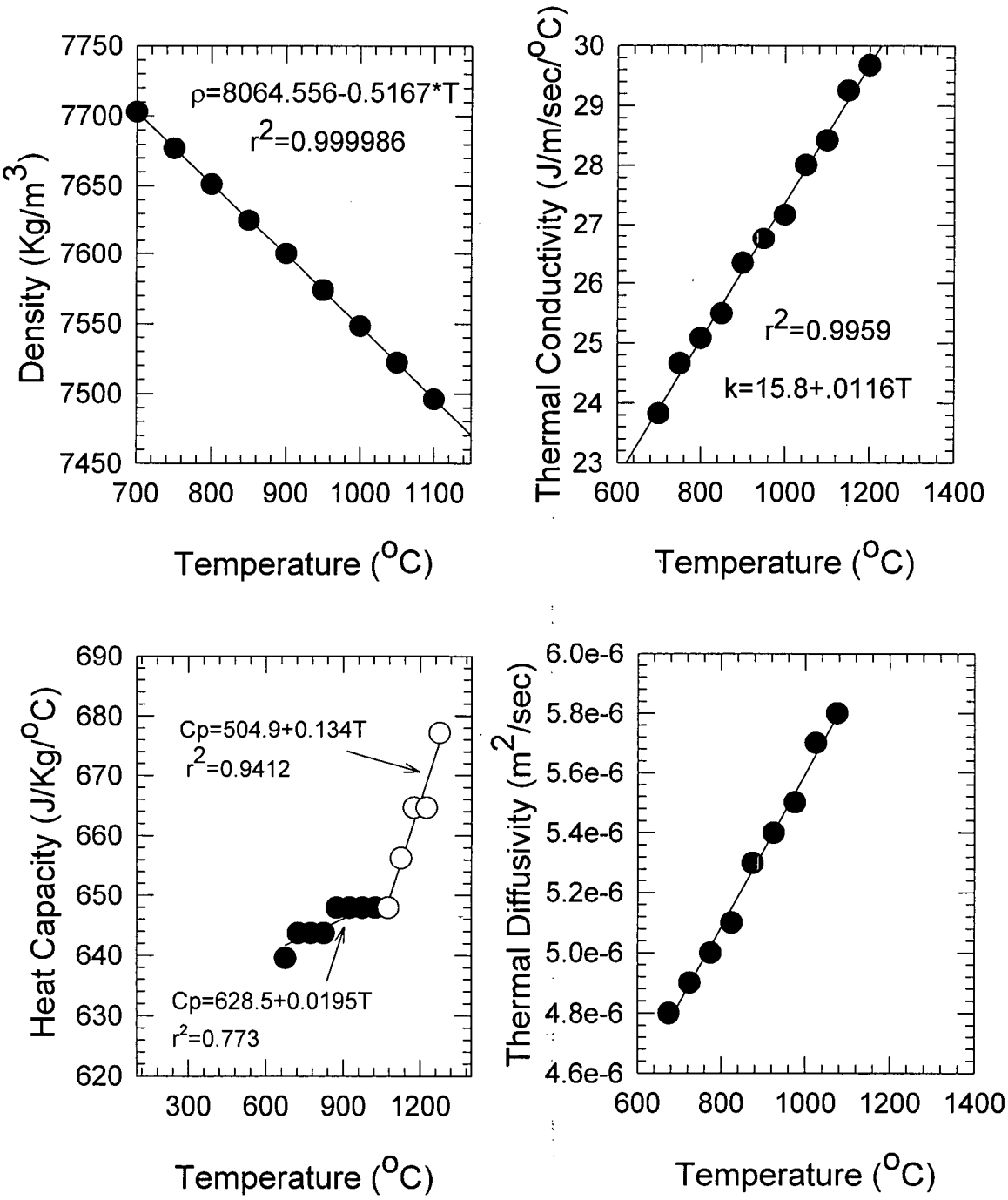

Figure 6.3:Thermophysical Properties of A36 austenite. Measured data by BISRA [3]

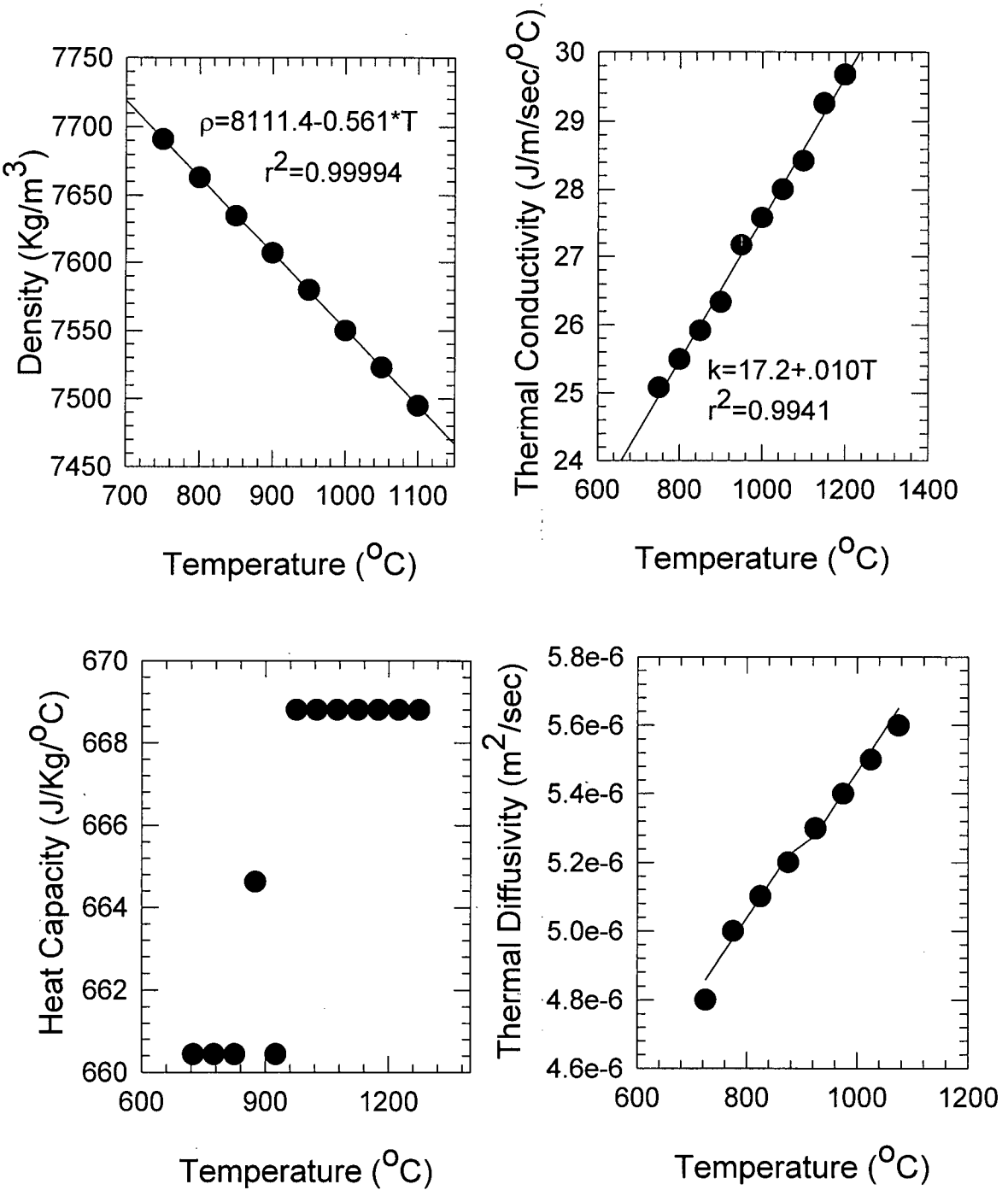

Figure 6.4: Thermophysical Properties of DQSK austenite. Measured data by BISRA[3]

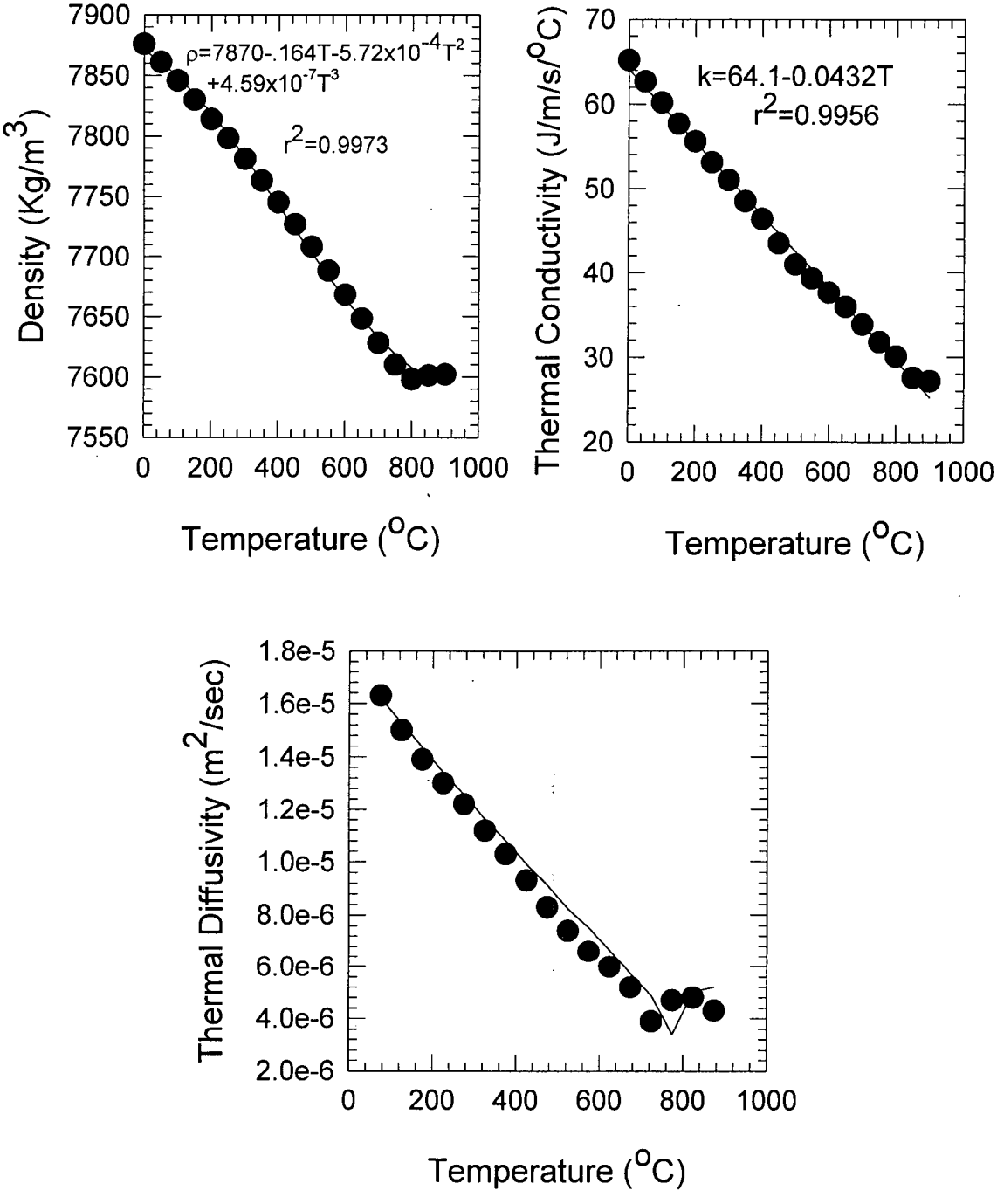

Figure 6.5: Thermophysical Properties of Ferrite. Measured data by BISRA [3]

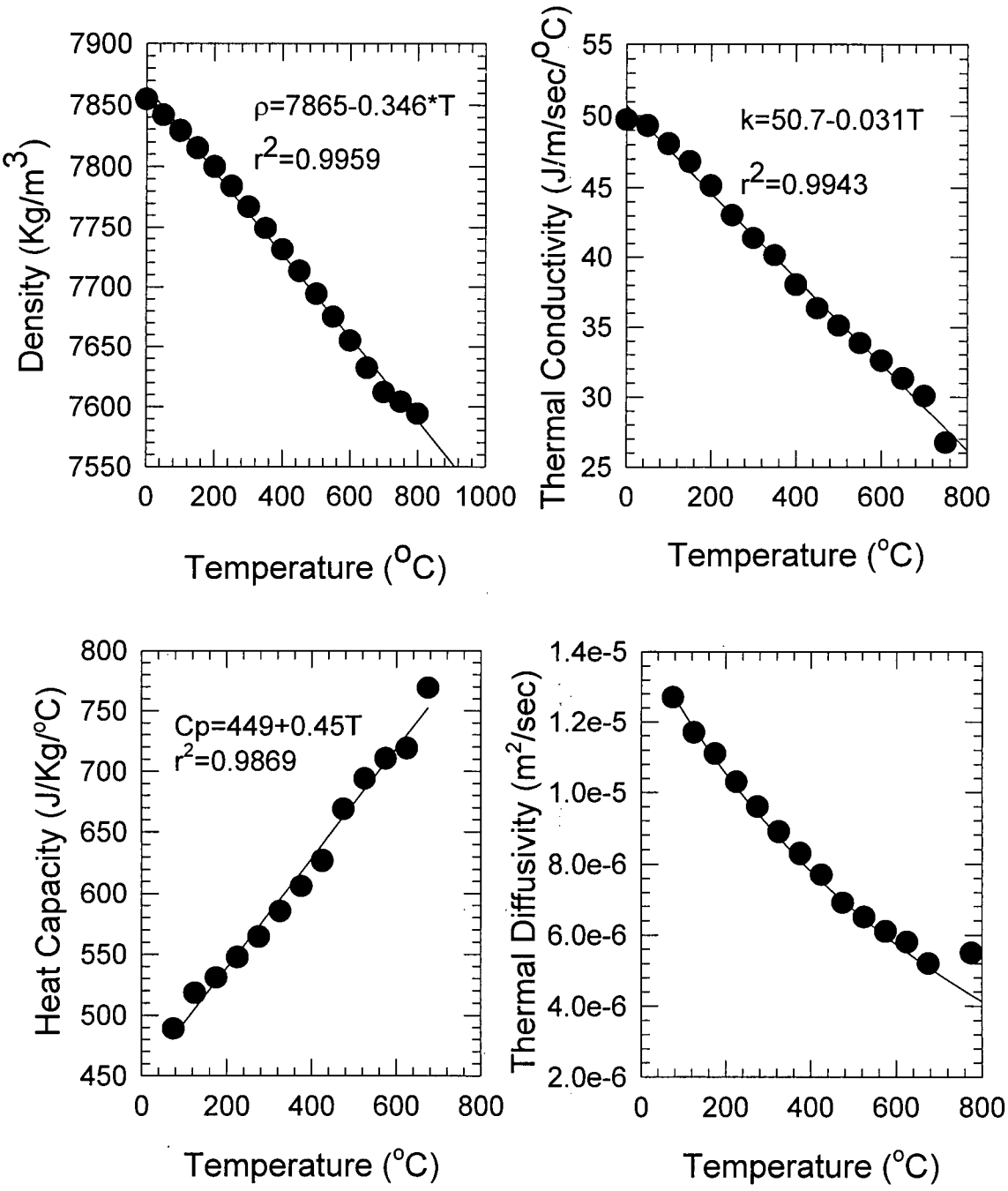

Figure 6.6: Thermophysical Properties of Pearlite. Measured data by BISRA[3]

Table 6.1: Summary of Thermophysical Properties of Steel Microconstituents

Constituent	Equation	Range (°C)
Density (Kg/m^3)		
Austenite A36	$\rho_\gamma = 8064.56 - 0.517T$	700-1100
Austenite DQSK	$\rho_\gamma = 8111.4 - 0.561T$	750-100
Ferrite	$\rho_\alpha = 7870 - 01644T - 5.722x10^{-4}T^2 + 4.590x10^{-7}T^3$	0-900
Pearlite	$\rho_p = 7865.0 - 0.3461T$	0-800
Heat Capacity (J/Kg/°C)		
Austenite A36	$Cp_\gamma = 628.51 + 0.0195T$	$T \leq 1075$
	$Cp_\gamma = 504.9 + 0.134T$	$T > 1075$
Austenite DQSK	$Cp_\gamma = 668$	$T > 925$
	$Cp_\gamma = 660$	$T \leq 925$
Ferrite	$Cp_\alpha = -10034.5 + 5.9668T_* + 5.2002x10^9 T_*^{-2}$	$T > 787$
	$Cp_\alpha = 34754.5 - 31.9196T_*$	$769 < T < 787$
	$Cp_\alpha = -11462.6 + 12.4346T_*$	$727 < T \leq 769$
	$Cp_\alpha = -4704.5 + 4.568T_* + 1.10577x10^9 T_*^{-2}$	$527 < T \leq 727$
		$T \leq 527$
Pearlite	$Cp_p = 449.04 + 0.450T$	0-700
Thermal Conductivity (J/m/sec/°C)		
Austenite A36	$k_\gamma = 15.82 + 1.156x10^{-2}T$	700-1200
Austenite DQSK	$k_\gamma = 17.17 + 1.04x10^{-2}T$	750-1200
Ferrite	$k_\alpha = 64.07 - 4.32x10^{-2}T$	0-900
Pearlite	$k_\alpha = 50.74 - 3.07x10^{-2}T$	0-800
Enthalpy of Transformation[4] (J/Kg)		
γ-α	$H_{\gamma\to\alpha} = 221656.4 - 864.4T + 1.9795T^2 - 0.001478T^3$	$T \leq 720$
	$H_{\gamma\to\alpha} = -2.917x10^7 + 114590T - 148.8T^2 + 0.06399T^3$	$720 < T \leq 780$
	$H_{\gamma\to\alpha} = 3277373 - 10575T + 11.545T^2 - 0.00424T^3$	$T > 780$
γ-p	$H_{\gamma\to per} = 70651 + 225.23T - 0.3469T^2 + 6.755x10^{-5}T^3$	

$T*$ is in K

[a]

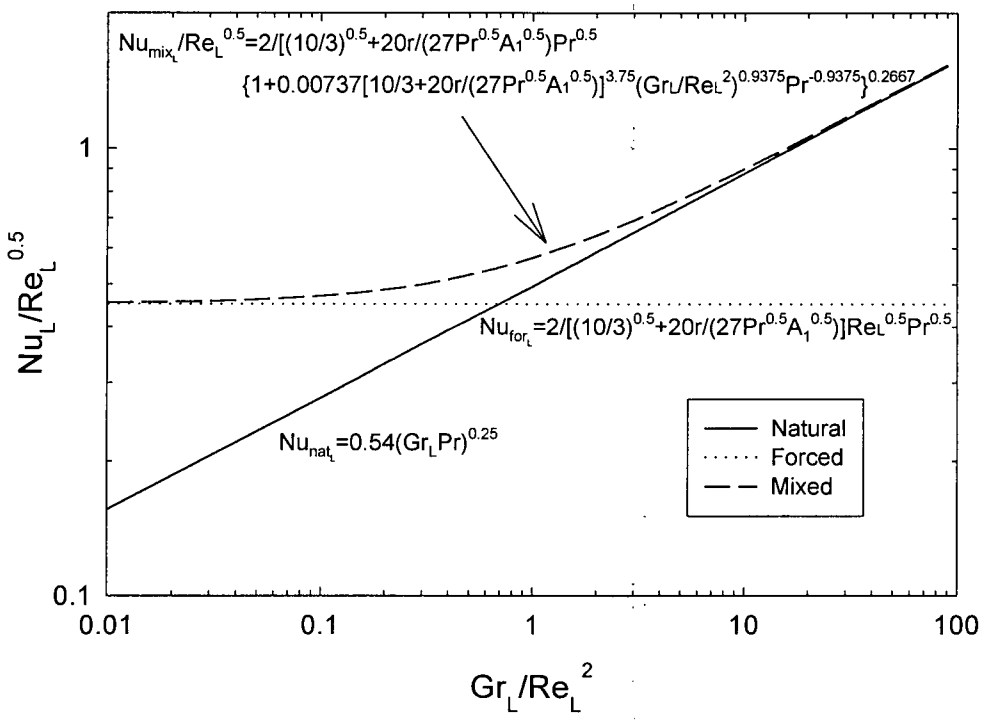

[b]

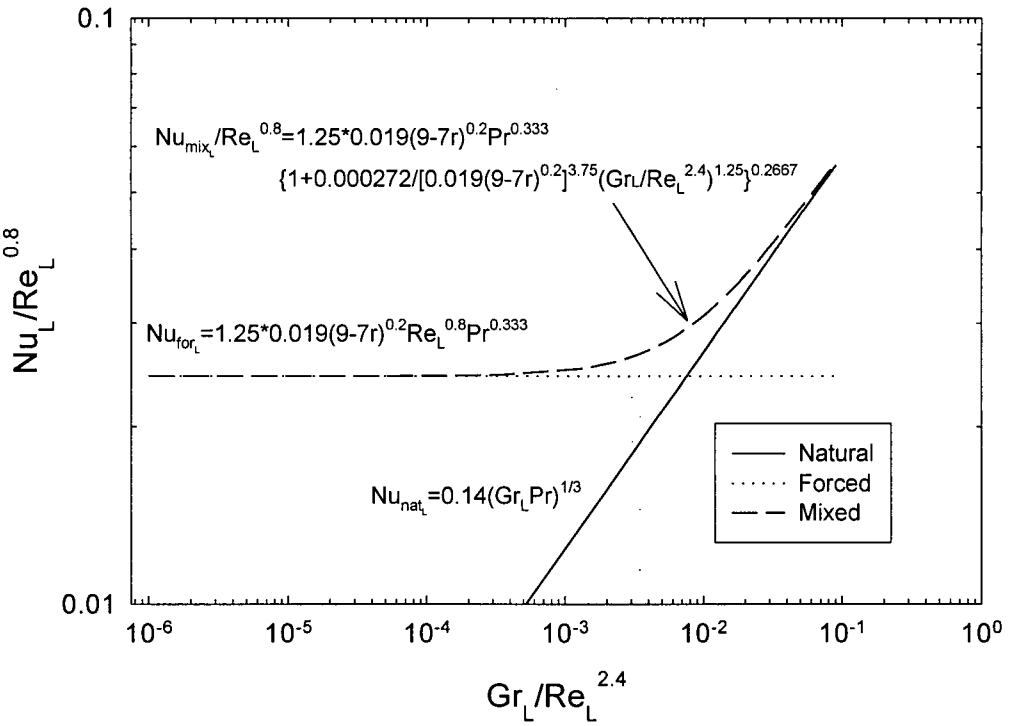

Figure 6.7: Air Convection Heat Transfer Maps for the Top Surface: [a] Laminar flow, [b] Turbulent flow

Table 6.2: Thermophysical Properties of Air

Property	Range (°C)	Equation	Units	r^2	Ref.
Conductivity	75-780	$k = 0.02526 + 6.9834x10^{-5}T - 1.8419x10^{-8}T^2$	W/m/°C	0.999	5
Density	75-780	$\rho = 1.2744 - 2.778x10^{-3}T + 2.1185x10^{-6}T^2$	Kg/m^3	0.981	5
Heat capacity	75-780	$Cp = 1.00268 + 1.13076x10^{-4}T + 1.1716x10^{-7}T^2$	J/Kg/°C	0.996	5
Kinematic viscosity	75-780	$\nu = 1.3425x10^{-5} + 9.1179x10^{-8}T + 7.5913x10^{-11}T^2$	m^2/s	0.999	5

T in °C

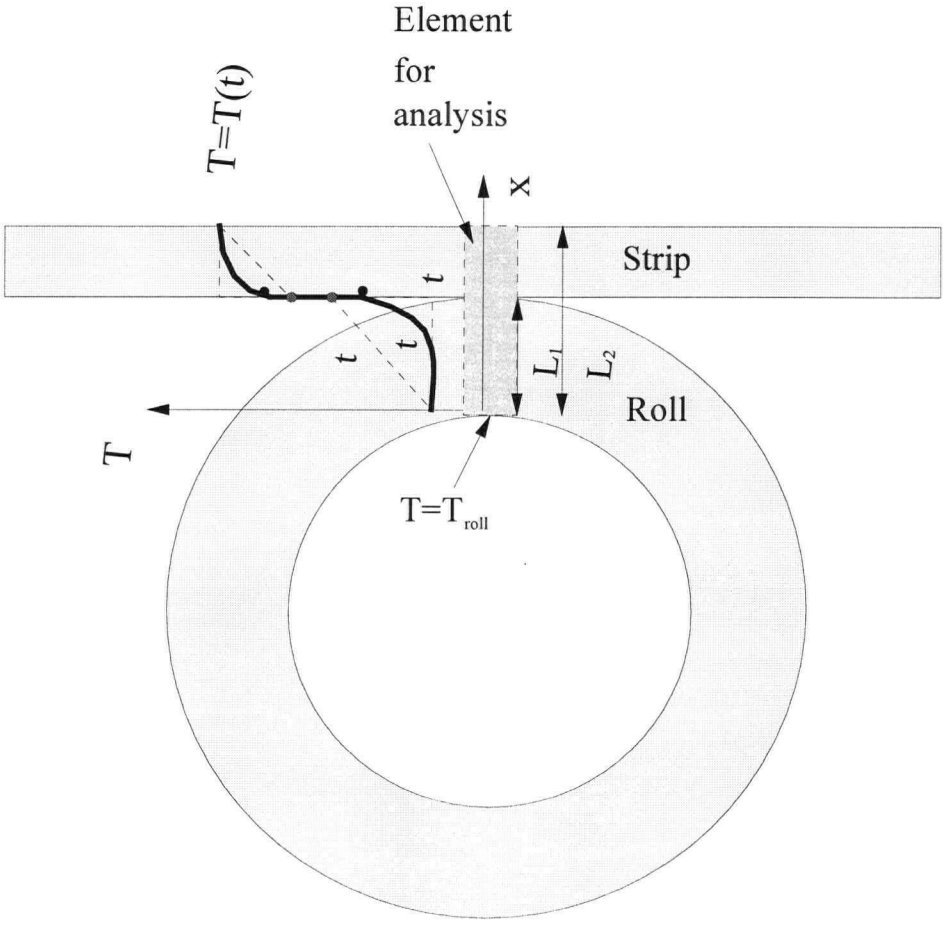

Figure 6.8: Schematic runout table rolls cooling

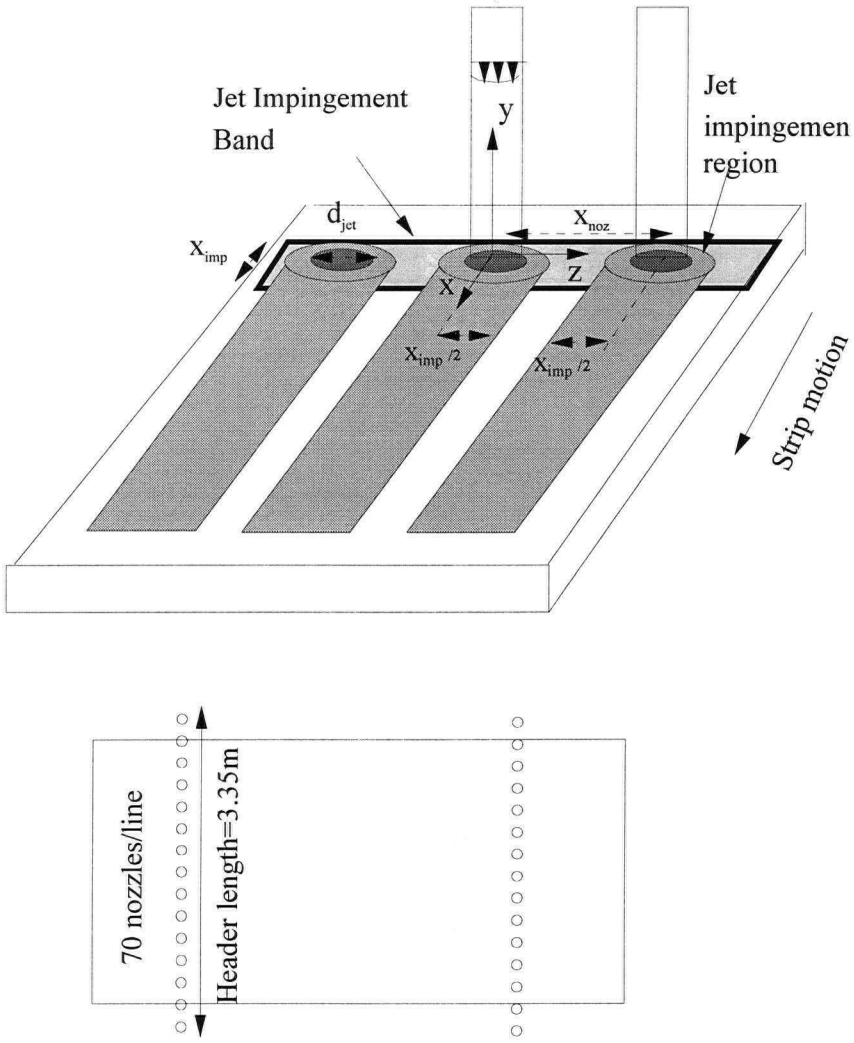

Figure 6.9: Jet Impingement Band

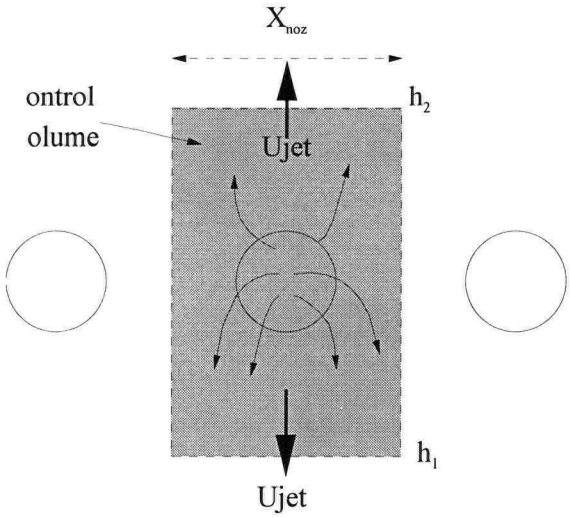

Figure 6.10: Control volume to calculate water film thickness

7. MODEL VALIDATION, RESULTS AND DISCUSSION

This chapter deals with the validation of the predictions of the different models that are part of the runout table model. Comparison of the results of these models with the experimental measurements published in the literature and with measurements done during the development of this work is presented.

As previously discussed, the calculation of the local heat-transfer coefficients during water cooling in the runout table is an important part of this work. This is done by the application of the boiling curve model during jet cooling presented in Chapter 5 to the runout table model described in Chapter 6. Hereafter, In order to define the regime in the boiling curve where discussions are being focused, each of the components of the boiling curve model will be referred to either as the film boiling model, the nucleate boiling model or the transition boiling model. In particular, since the film boiling model is very important to the development of the transition boiling model, it is highly desirable to discuss in detail its results.

The discussion starts with the boiling curve model and its components. Verification of the film boiling model is presented by comparison with measurements in this boiling regime, and also by the analysis of the effect of the process variables on the film boiling phenomena. Then, the validation of the other components of the boiling curves is carried out by comparison of the model predictions with experimental measurements published in the literature.

The runout table model is verified by comparison of its predictions with measurements conducted during the processing of strips under air cooling only, then with measurements using different laminar cooling configurations. Predictions of the thermal history are compared with the measurements shown in Appendix B.

7.1 Boiling Curve Model

One of the most important components of the runout table model, and an important contribution to explain how the heat is extracted during laminar cooling, is the boiling curve model.

Firstly, the results of the film boiling model developed in section 5.2 are presented, providing the background into the behavior of the transition boiling regime which is the region of main interest in this work. After, the heat transfer during transition boiling is explained in terms of the local heat transfer during the liquid-solid and vapor-solid contacts. Comparison between the boiling curve model results with many of the experimental results shown in the literature review is presented.

7.1.1 Film Boiling

As it was discussed earlier, the analysis of the film boiling phenomena is very important to understand the experimental results obtained by the different researchers. In this section, it will be shown that the effect of the different process parameters on the boiling curves, and more specifically on the transition boiling, can be explained by understanding the behavior of the vapor layer thickness. The analysis is focused on the heat transfer in the impingement region of water bars and curtains, because the behavior of the parallel flow region is only a special case (no pressure gradient) of the general

problem solved. The film boiling model presented in section 5.2 was run for a constant position downstream.

Comparison of the model predictions with the measurements in the film boiling region carried out by Ochi et al. [1] during the impingement of a water bar jet on a non-moving surface (see Figure 2.5) are presented in Figure 7.1. Figure 2.5 shows that for relatively high water temperatures it is possible to observe an extensive the film boiling regime, which is the section of the boiling curve that is almost flat; in this region the heat fluxes increase with decreasing water temperature. In Figure 7.1, the total heat flux, that is, the convective plus the radiative components of the heat transfer, was calculated adopting the empirical equation [2.4.4.9] by Nakanishi et al. [2], and the agreement found was good.

Predictions of the film boiling model are compared also with the measurements by Ishigai et al. [3] in the film boiling region during the impingement of a water curtain on a non-moving surface (see Figure 2.10). The total heat flux was calculated by equation [2.4.4.9]. The results are shown in Figure 7.2, and as it can be seen, a reasonable agreement was found. Similarly with the film boiling for water bars, the heat fluxes vary slightly with superheat and decrease slightly with water temperature.

Comparison of the model predictions adopting a more common expression for the total heat flux (Equation [5.6.3]) with the same experimental data of Figure 7.1 is presented in Figure 7.3. The curves predicted are about 50% below the measurements, but the trend predicted is in reasonable agreement with the measurements.

The typical operating conditions of company C were adopted (u_{jet}=6.78m/s, h=2.17m, d_{nozzle}=0.0186m) to analyze the effect of water temperature and strip speed on the film boiling phenomena. Prediction of the convective heat fluxes and heat-transfer coefficients appear in Figure 7.4. The effect of the strip motion is very small at high water temperatures, but it increases while decreasing the water temperature. Quantitatively, within the range of conditions of interests in the runout table operations where film boiling might be present (T_{water}<40°C, and ΔT_{sat}>800°C), the effect of the strip motion on the heat fluxes is relatively independent of superheat, and the heat fluxes might increase up to 20-30% with increasing the strip speed (0-8m/s). For the sake of comparison, the same conditions were analyzed for a planar water jet (u_{jet}=6.78m/s, h=2.17m, w_{nozzle}=0.0186m). The results shown in Figure 7.5 indicate clearly that the same effects of water temperature and strip speed are seen. However, the heat fluxes are slightly higher in the case of the bar jet because of the higher pressure gradient for the bar jet than for the planar jet.

Figure 7.6 shows the pure convective heat transfer results obtained for the planar jet, and compares them with the total heat flux calculated by the Equations [2.4.4.9] and [5.6.3]. Even though equation [2.4.4.9] gives good agreement with the experimental measurements presented for high water temperatures and low jet velocities, it is clear that for the moving strip case and low water temperatures, the heat fluxes are higher than expected for film boiling, even being higher than those measured in transition boiling under similar circumstances. Therefore, it is believed that the conventional equation [5.6.3] gives better results in the range of the runout table operations.

An important factor to consider during boiling is the surface condition of the substrate. Generally, the effect of roughness during cooling on the runout table is acknowledged, but its quantification has not been done. In this respect, the calculation of the vapor layer thickness during quenching may help as a good first approximation of the effect of the strip roughness. The vapor layer thickness during the typical operation of the water bars of company C were calculated, as shown in Figure 7.7[a]. From this figure, it is expected that in the runout table the vapor layer should lie within 2-20μm, and consequently, the roughness of the substrate should be higher than those values to produce a contact of the liquid-vapor interface with the substrate, which would have an appreciable effect on the heat transfer. On the other hand, micro roughness may also have an effect on the nucleation rate of bubbles. The momentum boundary layer in the water, which gives a measure of the depth of the effect of the strip motion and vapor motion on the water flow, is shown in Figure 7.7[b]. It is approximately 30μm, and almost independent of operation conditions. Similar calculations were carried out for the equivalent planar jet, as shown in Figure 7.8. The vapor layer thickness and the momentum boundary layer thickness are seen to be slightly higher than those for bars, but their behavior is very similar. Figure 7.9 shows that the thermal boundary layer thickness in the water is of the same order as the momentum, which is expected for Prandtl numbers of the order of unity, being approximately 28μm for typical conditions of water bars, and 32μm for water curtains.

It is also important to determine what fraction of the heat released during film boiling goes into the formation of vapor. Figure 7.10 shows that for water bars or curtains

more than 80% of the convective component of the heat reaches the liquid-vapor interface and is further conducted through the liquid layer. Therefore, less than 20% of the total heat flux helps in the formation and superheating of vapor.

The effect of the impinging jet velocity of a water curtain and a water bar on the heat flux is shown in Figure 7.11 and Figure 7.12 respectively. Figure 7.11 shows a comparison between the measurements for planar water jets done by Ishigai et al. [3] (only taking the film boiling part of Figure 2.11) and the model predictions of the total heat flux using Equation [2.4.4.9]. Although the agreement is good for lower jet speeds, the theoretical model is not capable to reproduce the measurements at higher jet speeds. However, given the specific experimental conditions and the assumptions of the model, the behavior of the heat fluxes with variations in the jet velocity is reasonably predicted. In Figure 7.12 predictions for conditions closer to those typical of the runout table operations are presented. In this figure, the darker lines correspond to the total heat flux while the lighter represent the convective heat flux. Increasing the jet velocity within the expected range in a runout table enhances slightly the rate of heat extraction in film boiling (≈10%), which is in good qualitative agreement with the experimental data shown in Figure 2.11.

The impinging jet diameter has a stronger effect than jet velocity on the local film boiling heat transfer, as shown in Figure 7.13 and Figure 7.14. Figure 7.13 shows a comparison of the model predictions of the total heat flux using Equation [2.4.4.9] with the measurements for water bar jets by Ochi et al. [1] (see Figure 2.6). The agreement found was good, specially at larger jet diameters. Decreasing the impinging jet diameter within

the typical range of many runout table operations (0.0075-0.015m) produces an increase of up to 50% in the local heat fluxes, as shown in Figure 7.14. These results are in good qualitative agreement with the experimental data shown in Figure 2.6.

Figure 7.15 shows the effect of the impinging jet angle on the heat fluxes during film boiling. Increasing the angle from the vertical by 30° reduces the heat fluxes approximately by 25%. These results are in good agreement with the discussion in the literature review (section 2.3.4[c]). Consequently, for bottom jet cooling, the local heat fluxes during film boiling for the same jet conditions will be in most of the operations smaller than for top jets, because at the bottom the jets are slightly inclined. However, the main reason for the lower heat fluxes encountered in bottom cooling is the direction of gravity.

All of the heat transfer results presented during film boiling can be explained exclusively by the effect of the different process variables on the vapor layer thickness, because the heat transfer coefficients are inversely proportional to the vapor layer thickness. Under the assumption that the vapor inertia and convection terms in the vapor are negligible because of the much higher liquid density, the temperature profile in the vapor layer is linear, according to Equation [5.2.11]. Consequently, the Nusselt number is given by Equation [5.4.1]:

$$Nu_x = \frac{hx}{k_v} = \frac{x}{\delta} \qquad [7.1.1]$$

It is important to mention that equation [7.1.1] is valid whether the jet flow is laminar or turbulent. The vapor layer thickness is defined by the energy equation at the

liquid-vapor interface, Equation [5.2.31], and the shear-stress continuity equation, Equation [5.2.32].

Qualitatively, the trends of the behavior of the film boiling heat transfer coefficients with operating parameters is similar to those found in transition boiling for the operating parameters studied experimentally, as shown in the literature review. These parameters include superheat (strip temperature), water jet temperature, velocity, diameter, and impingement angle. These observations are of significant importance to understanding the behavior of the boiling curve during the runout table cooling, and are consistent with the boiling mechanism suggested in section 5.1.

7.1.2 Heat fluxes and fractional contact area during Liquid-Solid contact

The procedure to calculate these parameters was explained in section 5.5. Verification of the model predictions with measurements is presented here. However, the heat fluxes and the area of contact of the liquid-vapor interface with the substrate have not been measured during jet cooling, so comparison is possible only between the model predictions with measurements in other systems.

Comparison between the model predictions during the impingement of a planar water jet at different water temperatures with measurements during the falling of a water drop on an Inconel surface [4] (see Figure 2.25) is presented in Figure 7.16. The experimental data for a falling drop reveals no dependence of the heat transfer with water velocity, which is not surprising since it is well established that fully developed nucleate boiling is not affected by the water velocity. Equation [5.5.4] expresses the liquid-solid contact heat transfer in terms of the pure boiling component plus the convective term.

However, it was verified that the second component is negligible except at superheats close to zero. Consequently, the heat transfer calculated through equations [5.5.1] and [5.5.4] shows no dependence on water velocity. The exponent *DX* in equation [5.5.1], accounts for the observed decrease of heat transport at higher superheats in the experimental data. The exponent *DX* is dependent on water subcooling according to the experimental data. The calculations for the planar jet are higher than the measurements for the falling drop, but the measured boiling curve for the bar jet by Hall et al. [5] (see curve for 0mm in Figure 2.8) plotted in Figure 7.16 shows that these heat fluxes are close to the values that would be expected.

Predictions of the fractional liquid-solid contact area, *F*, in the impingement and the parallel flow regions of a planar jet are compared with measurements [6] during saturated pool boiling in the transition boiling region in Figure 7.17. This comparison is valid only in a qualitative sense, since the actual values for subcooled flow boiling must be different to those for saturated pool boiling. Nevertheless, the comparison is very useful since it shows that the behavior of this parameter within the operational conditions of the runout table is similar to that found in saturated pool boiling. The experimental data shows that very different results can be obtained according to the differences in the experimental setup and the definition of this parameter. The contact decreases by increasing the surface temperature and the water temperature, in agreement with the discussion presented in section 5.4. Higher liquid-solid contact occurs in the impingement region as compared to the parallel flow region because of the pressure exerted by the jet. The calculated lines reflect the same behavior as the measurements. It is interesting to

note that the liquid-solid contact does not cover the entire surface in the transition region nor at some part of the nucleate boiling regime. In this work, the values of F obtained are lower than the measurements reported close to the critical heat flux in accordance with more recent photographic evidence obtained by Galloway et al. [7] and the mechanism of boiling proposed, as discussed in section 5.1.

The vapor layer thickness during turbulent parallel flow was calculated for a typical water velocity of 6.5m/s and different water temperatures (neglecting the strip motion) using the equation developed by Filipovic et al. [8]. This equation was used in the transition boiling model (see Equation [5.7.4]). Results appear in Figure 7.18 together with predictions of the amplitude of the liquid-vapor interface and the corresponding fractional liquid-solid contact areas. It is clear that the behavior of the vapor layer with variations of water temperature is similar to that found in the impingement region. The vapor layer is thicker in the parallel flow region as expected (compare with Figure 7.7[a]). The calculated amplitude of the interface behaves similarly to the measurements by Nigmatulin et al. [9] for quasi-stationary film boiling in external flow on a horizontal cylinder in a pool of water, as shown in Figure 2.29. The liquid-solid contact is enhanced considerably by decreasing the water temperature, as discussed in Chapter 5. Calculations for the vapor layer thickness were carried out for conditions similar to those of Weichert et al.[10], who measured the vapor film thickness at the equator of a sphere immersed in a pool of water at 55°C during film boiling. Weichert et al. [10] measured vapor film thicknesses of 0.2 and 0.11mm for surface temperatures of 690°C and 420°C respectively. Using the equation adopted in this work, which was developed by Filipovic et al. [8] for

turbulent forced flow on a flat plate, the vapor film thicknesses are 0.204 and 0.078mm respectively, assuming bulk flow of 1.0m/s. These results are in good agreement with the measurements by Weichert et al[10].

The magnitude of the vapor layer thickness presented in this work can be applied to estimate the effect of surface roughness on the transition boiling regime, as previously discussed. According to the predictions, the vapor layer thickness is in the range of 2-20μm in the impingement zone, whereas it is 2-100μm in the parallel flow region. The effect of roughness within these ranges should be important. These predictions are in excellent agreement with industrial findings. Shimizu et al.[11] found that during the cooling in the runout table, a 21μm-thick scale generated on one steel (two or three times greater than that generated on other steels) was responsible, due to the increased roughness of the surface, for a substantial increase in the heat fluxes. The higher heat fluxes were reflected in a drop in coiling temperature of more than 50°C.

7.1.3 Boiling Curves for Non-Moving Surfaces

In this section, comparison between the predictions of the transition model described in sections 5.6 and 5.7 with some of the experimental data available is presented.

It is important to highlight that the models developed in this work were created to reproduce the thermal histories expected in the runout table, where the strip motion promotes thermal gradients along the longitudinal axis of the strip of only 10-100°C/m, whereas during the measurements reported in the literature on non-moving surfaces these thermal gradients are of the order of 1000°C/m. This implies that the runout table operates

nearly in steady state for a fixed position in space, and significant segments of the strips are nearly isothermal. These fundamental differences should have an effect on the development of the liquid-vapor interface and in the heat fluxes expected in the transition boiling regime. Consequently, the runout table cooling can be considered under steady state and sections of the steel are nearly isothermal in the parallel flow region, whereas the experimental data published corresponds to transient non-isothermal cooling.

Another important difference between the runout table operations and experiments in the laboratory is the quality of the water employed. Most of the laboratory measurements employ relatively pure water, with low-gas entrapment and hardness, whereas during the runout table operations frequently the water used has significant hardness levels and air absorbed. The recent findings by Jeschar et al.[12] show that the temperature at the minimum heat flux (Leidenfrost temperature) during the cooling of a sphere always increases with the additions of salts, especially with salts such as $CaCl_2$ and $MgCl_2$. Those salts are found in water with higher hardness. The Leidenfrost temperature can increase up to 100°C at concentrations of Cl^- of about 300 mg/l. The same authors also showed that the dissolved gases in the water coolant can have a higher effect on the Leidenfrost temperature. Therefore, since the Leidenfrost temperature may give a measure of the stability of the vapor-liquid interface during film boiling, it may be inferred that variations in water hardness and gas entrapment between operations can have a substantial effect on the boiling characteristics, and consequently on the heat fluxes expected in the transition boiling region.

7.1.3.1 Impingement region

The effect of water temperature on the boiling curves in the impingement region of a water bar is shown in Figure 7.19. Predictions of the transition boiling model are in good agreement with the measurements carried out by Ochi et al. [1] (see Figure 2.5). The boiling curves, especially in the film and transition boiling regimes, are displaced to higher heat fluxes and superheats by lowering water temperature. This behavior can be explained by the effect of water temperature on the vapor layer thickness (see Figure 7.7[a]). The vapor layer thickness decreases significantly with decreasing the substrate temperature when superheat is high, and when water temperature is also high. However, this effect is less pronounced at lower water temperatures and superheats. A lower water temperature produces a thinner vapor layer, promoting more liquid-solid contact and increasing the heat fluxes during the contact. The high heat fluxes found during the liquid-solid contact magnify the effect that the process variables have on the interface, as compared to the film boiling regime, promoting large variations of heat fluxes in the transition boiling regime.

The impinging jet velocity has a relatively smaller effect, as shown in Figure 7.20. Comparison between the model predictions with the experimental data for the planar jets [3] shown in Figure 2.10 and 2.11, shows good agreement, but the effect of velocity is smaller in the model than in the measurements. If the effect of jet velocity on the transition boiling is explained in terms of its effect on the vapor layer thickness (or the convective heat fluxes in the film boiling regime), Figure 7.11 reveals that jet velocity has a small effect on the heat fluxes in the film boiling regime, and consequently the

vapor layer thickness. The transition boiling model is consistent with this. Perhaps, the larger magnitude of the effect of jet velocity observed in the measurements is a result of the differences in the impingement jet widths (4.8 and 5.7 mm for u_{nozzle} equal to 2.1 and 1.0 m/s respectively). These variations in jet width imply a difference of about 18% in the pressure gradients, which is inversely proportional to the jet diameter or width. As it was shown in Figure 7.13 and in section 2.3.3[b], variations in jet diameter can create considerable differences in the heat fluxes not only in the film boiling, but also in the transition boiling regime.

Figure 7.21 shows the effect of water temperature on the boiling curves in the impingement region of a planar jet. Given that the transition boiling model was tuned to reflect the real runout table conditions, its application to laboratory conditions is in reasonable agreement with the measurements[3] shown in Figure 2.10.

7.1.3.2 Parallel Flow

In this section, comparison between the transition boiling model predictions with the measurements carried out by Filipovic et al.[13] (see Figure 2.16) during the cooling of a non-moving flat plate by water parallel flow, and with the measurements done by Hernandez-Morales et al.[14] (Figure 2.18) during the forced convection quenching of a steel rod in a pipe.

Comparison of the model predictions with the measurements by Filipovic et al. [13] for a water temperature of 25°C and u=2m/s is shown in Figure 7.22. Predictions are in good agreement with measurements in the range of runout table applications taking into consideration the differences between the experimental setup and the runout table

conditions. The measurements correspond to two different boiling curves obtained at two different locations. The lower heat fluxes found at a position further downstream are the result of higher local water temperatures.

In order to estimate the capabilities of the model for different water velocities, comparison between model predictions and measurements[14] during the quenching of a steel bar in a pipe (T_{water}=25°C) is presented in Figure 7.23. Comparison between the velocities in an internal flow with the parallel flow on a flat plate can be done by assuming that the maximum velocity in the internal flow is equivalent to the free stream velocity on the flat plate flow. This approximation has been used extensively to compare flows[15]. The maximum velocities obtained under laminar flow conditions were obtained applying a laminar flow solution[16] for this configuration. Results are presented in Table 7.1. If the flow was turbulent, the equivalent free stream velocities have to be between the bulk flow velocity and the maximum velocity for laminar flow. The model results compare very well with the measurements for the flat plate velocities of 10 and 6.8 m/s.

Figure 7.24 shows a comparison between the model predictions and measurements[13] for parallel flow on a flat plate using water temperature at 55°C. Even though the CHF's are underpredicted, the agreement is also good in the typical range of the runout table temperatures (superheat above 300°C), and the effect of water velocity is predicted satisfactorily. It is important to note that the measurements at 2 m/s correspond to an initial water temperature of 25°C, but as it was discussed in the literature review, the local water temperature at this position can be close to 55°C. Figure 7.25 shows that in

the case of the quenching in a pipe[14], the predicted curves are lower, but still within reasonable values.

Model predictions for a water temperature of 75°C compare favorably with measurements[14] in the quenching of a bar, as shown in Figure 7.26. The agreement is very good at superheat above 500°C, which is typically the range in the runout table operations.

7.1.3.3 Boiling curves for typical jet temperatures and velocities in the runout table

Predictions of the boiling curves in the impingement zone of a water bar for jet velocities of 5.5-6.5m/s and water temperatures of 25 and 35°C are presented in Figure 7.27. These are typical operation conditions in full-scale operations. The heat fluxes are within 4-10MW/m^2, and the transition boiling regime is extended down to a strip surface temperature of 450°C. The effect of jet velocity within industrial operations is relatively small compared to the more common variations in water temperature, which have a more pronounced effect.

In the parallel flow region, the heat fluxes are smaller than in the impingement region, and the effect of the water velocity is small, as it is seen in Figure 7.28. Transition boiling is present in practically all operations, but as the water flows on the strip, the water stream warms up to the point where film boiling appears. Heat fluxes typical of film boiling appear at water temperatures close to 75°C. This, as it will be discussed later, has a very important effect on the performance of a cooling system.

7.1.4 Boiling curves for a moving surface

The measurements carried out by Hernandez et al.[17] described in the literature review were re-analyzed in order to obtain the boiling curves for the impingement and the parallel flow zones. The plate surface temperatures measured by two thermocouples attached to the cooling surface are presented in Figure 7.29[a]. The temperatures measured by the two thermocouples indicate that some differences, especially in the heat fluxes in the impingement region are to be expected because of the differences in the depths of the "peaks" measured. This figure shows that once the plate reaches the countercurrent parallel flow region, the cooling commences immediately with a steep temperature drop, followed by a steeper cooling in the impingement region. After leaving the impingement region, the heat fluxes at the surface decrease and cannot maintain that low temperature, so the heat conduction from the interior of the plate increases the surface temperature. Finally, during air cooling the temperature recovers.

The heat fluxes calculated from the temperature measurements by thermocouple TC1 are presented in Figure 7.29[b]. Neglecting the "noise" in the heat fluxes, it can be seen that the heat fluxes increase monotonically in the countercurrent parallel region, until the plate reaches the impingement region, where the heat fluxes reach a maximum. After, in the following parallel flow region, which in the case of this experiments is much shorter, the heat transfer also decreases monotonically.

By means of the application of an analysis technique that will be discussed in section 7.2,3, the boiling curves in the cooling of a moving plate for the initial water temperature can be obtained from the heat flux distributions, such as the one in Figure

7.29[b]. The measured boiling curves for the impingement region of a planar jet impinging on a moving surface (u_{jet}=4.6m/s, T_{water}=24°C, u_p=1.45m/s) are compared with reported measurements [1 3] on non-moving surfaces for conditions close to those of the moving plate experiments in Figure 7.30. Predictions by the transition boiling model are also presented. The heat fluxes measured for the moving plate vary considerably for the different jets, even though they operate almost under the same conditions. Due to the extremely short time that the plate resides in the impingement region (0.0024-0.0043sec), it would be expected that the thermal response of the thermocouples is not fast enough to generate very accurate temperature measurements in this region. However, the measurements for the moving plate compare favorably with the measurements for both bars and curtains. The transition boiling model predicts a boiling curve which is in reasonable agreement with some of the heat fluxes measured for the moving plate, whereas in some other cases the model results are above the measurements. Given the wide range of measurements reported in the literature, and the uncertainties present in the measurements for the moving plate, it may be concluded that the model predictions are in good agreement.

The measured boiling curves for the parallel flow regions of the planar jets impinging on the moving plate are compared with some reported measurements[13,14] for non-moving surfaces, and with predictions by the transition boiling model in Figure 7.31. The measured boiling curve for the moving plate is in excellent agreement with the measurements in both, the parallel flow and pipe flow. It is evident that the effect of the strip motion within this experimental setup is negligible. The transition boiling model

predictions for the moving plate experiments are in excellent agreement with all these measurements.

With respect to the effect of the strip motion on the boiling curves, the results of the film boiling model presented here and those reported by other researchers for laminar film boiling[18,19] reveal that the strip motion increases the heat transfer. In turbulent flow conditions, the opposite effect has been predicted[8].

It is important to mention that during a previous research work by this author[17] and at the beginning of the development of the present transition boiling model, the strip speed was believed to have a strong effect on the boiling curves. However, during the trial and error procedure adopted to obtain the parameter F in the transition boiling model, it was seen that to obtain good predictions for the boiling curves measured and the coiling temperatures, a dependence of the boiling curves on the strip speed was not necessary. Neglecting the effect of the strip motion on the local boiling curves was possible without diminishing the accuracy of the model predictions. Consequently, the boiling curves predicted by the transition boiling model are not dependent on strip speed. Perhaps, the effect of the strip motion on the boiling curves exists, but is probably small enough to be masked by other processes that are also dependent on the strip motion, such as the mixing of water, which affects the local subcooling very significantly, and also the length of the different cooling zones.

7.2 Runout Table Model

In this section the runout table model predictions are compared with the measurements presented in Appendix B. These comparisons serve as verification of the

performance of the different components of the runout table. In the previous section, verification of the boiling curves used in the runout table model was presented, and explanation of the mechanisms of cooling was also included.

This chapter deals first with predictions for strips cooled in air, which helps to verify the model predictions without water cooling. Analysis of the contribution of the different components to the total heat transfer is presented, including the runout table rolls. After, a thermal analysis of some measurements during laminar cooling operations is presented to verify the consistency of the mill data obtained. An analysis of the effect of water flow distribution at the top surface of the strip on the thermal histories is presented. This analysis was done to identify the conditions where the cooling by the flows presented in Chapter 4 can be approximated by 1-D models. The development of a heat transfer map that explains the performance of a cooling setup is presented. Then, verification of the predicted coiling temperatures with the measurements shown in Appendix B is presented. Finally, a sensitivity analysis of the effect of some design and operating parameters is presented to identify their effects on the coiling temperature.

7.2.1 Air cooling

In order to establish which is the main cooling mechanism during cooling in air, a sensitivity analysis of the relative importance of the different parameters and mechanisms within the typical runout table conditions was done. Results are summarized as follows:

(a) Radiation heat transfer is the major contributor to cooling in air, and convection heat transfer in any case is below 20%.

(b) Air velocity has an important effect on forced convection, but the real effect at the typical runout table conditions (where natural convection contribution is also important) is approximately 5%. Therefore variations in air velocity may be assumed negligible in the overall cooling.

(c) Air temperature variations have negligible effects on radiation and mixed convection heat transfer, and their contribution can be neglected.

(d) Lower strip speeds reduce significantly forced convection, but the effect in the mixed convection regime is very small. Strip speed variations are also negligible for the overall local heat flux.

(e) The surface length where air cooling applies (characteristic length in convection equations) has an important effect on the average forced convection heat transfer, which increases with decreasing length. A similar effect is found in natural convection, but the effect is smaller. In mixed convection this effect is also small.

The importance of radiation heat transfer in comparison with the convective air cooling mechanisms is clearly seen in Figure 7.32. The possible variations in emissivity may represent as much as 10% of the total heat flux, which in many cases is higher than the contribution of convection heat transfer to the overall cooling.

The runout table model was run for the operating conditions of the strips cooled by air exclusively (see Table B.17). The chemical composition of the steel analyzed was: %C=0.062, %Mn=0.95, %Si=0.198, %Cu=0.439, %Ni=0.134, %Cr=0.090, %V=0.003, %Nb=0.014, %Mo=0.036, %Al=0.034, %N=0.0092, for which a carbon equivalent of

$\%C_{eq}$=0.22 was calculated. A corresponding T_{AE3}=856°C was obtained. This chemical composition is intermediate between the nominal A36 and DQSK compositions shown in Table B.1, for which the calculated percentage of carbon equivalent, $\%C_{eq}$, were 0.29 and 0.088 and the equilibrium temperatures T_{AE3} were 824°C and 883°C respectively. The predicted coiling temperatures for the coils with gages of 9.53 and 12.7 mm are compared with the measurements in Figure 7.33. The linear behavior of the experimental data and the model predictions reveals that at those coiling temperatures no austenite decomposition took place. The model predictions are in good agreement with the measurements, but they are consistently higher by approximately 10°C. The error in the pyrometer reading during these measurements is usually of the order of 1%, which represent uncertainties of 8-9°C. Also, the chilling caused by the runout table rolls contact to the strip may be also responsible for the discrepancies. An analysis of the effect of roll chilling will be presented later.

The coiling temperatures calculated for the nominal A36 and DQSK chemistries are compared with the measurements for the 4.72mm gage strips in Figure 7.34. The measurements in this case, present a deviation from the linear behavior observed at higher temperatures in this figure and in the cooling of the higher gages. The measured coiling temperatures do not decrease linearly with the finishing temperature when the entry temperatures to the runout table are below 840°C. This is consistent with the value of T_{AE3} calculated for this chemistry. The coiling temperatures are higher because of the heat generated by the austenite decomposition during cooling. The contribution of the heat of transformation during these measurements promotes an increase of approximately 30-

40°C in the coiling temperature. Predictions adopting the nominal A36 steel chemistry show good agreement with the linear behavior present at higher coiling temperatures. For the lower coiling temperatures, there are differences in the transformation start temperature due to differences in chemical composition. It is clear that the transformation starts for the predictions at about 810°C, which implies an undercooling for the transformation to start of about 14°C, which compares well with the approximately 16°C found in the measurements. Therefore, the deviations in behavior can be attributed to the chemistry differences between the two steels. Predictions assuming the nominal DQSK chemistry show that the austenite decomposition would start at higher temperatures, and for the whole range of coiling temperatures presented in the Figure, at least some fraction of the steel would have transformed, causing a significant increase of the coiling temperature. These predictions show that the effect of chemistry is extremely important for the control of the coiling temperatures, especially when only partial decomposition of the austenite occurs in the runout table.

In order to estimate the chilling effect of the rolls on the strip, the mathematical model for the runout table rolls cooling presented in section 6.1.3 was run to calculate the maximum possible effect of roll cooling. Since the heat-transfer coefficients during the roll to strip contact are unknown, a maximum expected value of 5000W/m^{2o}C was adopted for the present calculations[20]. The roll parameters were taken from the operation of company G and are summarized in Table 7.2.

Predictions of the maximum effect of roll cooling for different strip initial temperatures, gages, and speeds within the typical operations of companies G and C are

presented in Table 7.3. From the calculations of the temperature drop in the steel during passing on a single roll, ΔT in strip, it can be seen that for the air cooling measurements analyzed in Figure 7.33 and Figure 7.34, the maximum total temperature drops expected by the 91 rolls are 8.7-13.1°C, 6.6-8.2°C, and 8.2-9.8°C, for gages 4.72, 9.53 and 12.70 mm, respectively. However, Table 7.3 shows that the heat fluxes during the strip-roll contact may seem higher than expected in an operation. Accordingly, the real effect of roll cooling should be smaller than what these predictions show. It is noteworthy that extremely high values of the temperature drop per roll were obtained at a gage of 2mm. The reason for this was an unrealistic prediction of the strip-roll contact length. Based on these results, it is believed that the effect of roll chilling on the coiling temperature is negligible for gages above 4mm. Perhaps, the effect may be more observable for thin strips, but the uncertainties with respect to the actual heat transfer coefficients and the contact length are so significant, that calculations by means of the procedure followed in this simple model are not meaningful. Probably, a better description of the roll chilling effect requires measurements of the roll to strip interface heat transfer coefficients and consideration of the non-elastic behavior of the strip. Accordingly, the roll cooling effect was neglected for the rest of the calculations presented in this chapter.

7.2.2 Experimental correlation between process variables and water cooling performance

Experience in the development of process control systems has shown that the cooling performance of each individual jet line in the runout table is as a first approximation constant, provided that the laminar cooling conditions (water temperature, flow rate and quality, jet lines pattern) and the steel grade are the same.

Experimental correlations between process parameters and the cooling performance of a jet line can be obtained from the application of such findings. In order to obtain a first approximation of the temperature drop in the strip per jet line, it is assumed that: [1] the heat extracted per jet line is approximately constant, [2] the thermal gradients in the steel strip have a small effect on the total temperature drop, and [3] the strip thermal properties are approximately constant within the range of water cooling. Under these assumptions, a heat balance was performed on a lumped element to give the following expression for the temperature drop:

$$\Delta T_{drop} = \frac{\left(q_{top} + q_{bottom}\right)}{\rho Cp} \frac{t}{th} \qquad [7.2.2.1]$$

This relationship gives a linear relation between the temperature drop in the steel and time, t. This is a good first approximation of the thermal histories obtained by the present runout table model for a substantial part of the strip. It is evident that the time under water cooling, t, is given by:

$$t = \frac{(No.\,Jet\ lines\ at\ top)\ (d_{jet\ lines\ at\ top})}{U_p} \qquad [7.2.2.2]$$

which substituted in equation [7.2.2.1] to obtain the following equation:

$$\Delta T_{drop,tot} = m\frac{(No.\,Jet\ lines\ at\ top)\ (d_{jet\ lines\ at\ top})}{(U_p)(th)} \qquad [7.2.2.3]$$

where $m=(q_{top}+q_{bottom})/\rho Cp$ must be a constant.

This equation was adopted to correlate the temperature drop in the strip by water cooling exclusively with the process parameters. The constant, m, was determined by

regression analysis. Figure 7.35 shows the results for company C while processing two different grades, DQSK and A36 respectively (data from Appendix Table B.13 and Table B.14). As it is seen in Figure 7.35, good correlation was found for both steels. Interestingly, the constant *m* is dependent on steel chemistry, but it is independent of strip speed and thickness even for wide ranges of operation. Results indicate that a jet line removes more heat while cooling a steel with a higher carbon content. Thus, the amount of jet lines working necessary to cool a DQSK strip to a fixed coiling temperature is 0.4965/0.399*100=24% more than for an A36. This is in excellent agreement with the findings by Hurkmans et al.[21], who found that going from a steel (%C=0.11, %Mn=1.070, %Si=0.24, %Al=0.060) with a $\%C_{eq}$=0.288 (compare to 0.299 of nominal A36) to a lower carbon steel (%C=0.04, %Mn=0.220, %Si=0.01, %Al=0.050) with a $\%C_{eq}$=0.077 (compare to 0.088 of nominal DQSK), required an increase of 24% in the number of jet lines used to attain the same coiling temperature. It is important to mention that this effect is a result of the differences in the austenite decomposition process, which generates heat and also phases with different thermophysical properties at different stages of the processing.

The cooling performance of a laminar system can be estimated relative to that of another system. Figure 7.36 shows the correlation found for two other companies (data from Appendix Table B.11 and Table B.15), which include a system using jet bars (company A) and one using jet curtains (company E) for two different steels. Also good results were obtained. These results together with those shown in Figure 7.35 can be used to estimate the relative performance of the different cooling systems. Given that the

parameter m gives a measure of cooling performance per unit area, comparison is only possible in terms of a parameter $m'=m*d_{jetlines}$, because the distance between jet lines is quite different between the companies. The parameter m' gives a measure of cooling performance per unit length across the width. Such a comparison is summarized in Table 7.4.

Comparison of the cooling performance parameter, m', between companies C and A (see Table 7.4) reveals that the cooling system of this latter company removes only 0.160/0.228*100=70% of the heat removed per jet line by company C, even though the distance between jet lines for company A is 0.69/0.46=1.5 times that of company C. These results can be expected, since the water density supplied (water flow rate/length across width) was $3.63x10^{-3}$ $m^3/(s\ m)$ in the case of company A compared to $7.4x10^{-3}$ $m^3/(s\ m)$ in company C (obtained from data in Appendix Table B.2 and B.4). Similarly, comparison between water curtains (company E) and bars (company C) for the DQSK steel shows that the bar system cools the strip only 0.184/0.235*100=78% compared to the curtain system. The water density used in the operation of company C was $7.4x10^{-3}$ compared to $17.0x10^{-3}$ $m^3/(s\ m)$ used in company E, which explains these results. It should be noted that the parameter m is dependent on the initial water temperature.

All these results indicate that the chemistry of the steel has an important effect on the amount of water needed to attain a specified coiling temperature. Also, the cooling performance of a laminar system depends strongly on the flow density of the water supplied.

The number of top jets calculated by equation [7.2.2.3] is compared with the actual number used in operation, as shown in Figure 7.37 and Figure 7.38. Even though equation [7.2.2.3] was developed under apparently very restrictive assumptions, its capabilities to predict a first approximation of the number of top jets used in operation are significant. Figure 7.37 and Figure 7.38 show that in most of the cases the errors are within ±5 jet lines.

Among the many possible applications of equation [7.2.2.3], an important for this work is the detection of inconsistent measured data. The mill data for the different companies can be analyzed by plots such as the ones shown in Figure 7.39 and Figure 7.40. The line at zero in these figures represents the average behavior of the data set. When the error is positive, the predicted coiling temperatures should be higher than the measured coiling temperatures and vice versa. It is assumed that within a variability of ±5 jet lines the data is consistent. When variations are more significant, it may indicate that the mill data is not consistent with the whole data set.

7.2.3 Heat transfer analysis of the actual flows observed during industrial and pilot-plant operations

The objective of this section is to analyze numerically some of the photographic observations presented in Chapter 4 by means of the application of the runout table model to the different water flow distributions observed across the width of the strip during operation.

Thus, the objective of this 2-D (thickness and width of the strip) analysis was primarily to establish the conditions where a 1-D model (thickness) is applicable.

Additionally, this study was pursued to delineate the thermal conditions for localized cooling to take place on the runout table. Finally, a behavior diagram was created to define where and when transition or film boiling occurs.

In Chapter 4, localized cooling was shown to occur in basically the following regions: [a] The impingement band, and [b] Regions in the parallel flow zones where high concentration of water exists. That is, regions where thick water stripes appear, or in the countercurrent parallel flow region when the film of water is thick. Additionally, whenever sweepers are used, a recirculating flow is created that increases the local heat transfer.

The video recordings and also the pictures in Chapter 4 show that in many cases where water bars are used, in some degree the top surface of the steel strip has "stripes" of different tonalities, suggesting that the cooling in the downstream parallel flow zone occurs mainly in bands or stripes parallel to the longitudinal axis of the strip at least close to the impingement band. The thickness of those stripes is variable, depending on the runout table configuration, and the tonalities that the strip surface shows vary with each mill. The thickness of the stripes seems to be between the jet diameter and the impingement region diameter.

In harmony with these observations, an analysis was carried out to identify the conditions where: [a] Thermal gradients (through the thickness) appear, and [b] The heat transfer across the width of the strip is significant.

[a] Estimation of the conditions where thermal gradients exist.

A non-negligible thermal gradient appears when the through-thickness Biot number is greater than 0.1, that is when

$$Bi = \frac{hL}{k} > 0.1$$

For typical runout table operations the parameters of this equation are:

$$0.1x10^6 W/m^{2o}C \le h \le 10x10^6 W/m^{2o}C$$
$$0.002m \le L \le 0.015m$$
$$25J/m\,s\,^oC \le k \le 64J/m\,s\,^oC$$

which give a minimum Biot number of:

$$Bi_{min} = \frac{0.1x10^6 * 0.002}{64} = 3.1 > 0.1$$

and therefore, during water cooling the steel thermal resistance is always important, and there will always be thermal gradients.

[b] The heat transfer along the axis and across the width of the strip.

Performing a heat balance on a differential element (Eulerian approach with no heat generation) on the configuration shown in Figure 6.9, renders the equation:

$$\frac{\partial}{\partial x}\left(k\frac{\partial T}{\partial x}\right) + \frac{\partial}{\partial y}\left(k\frac{\partial T}{\partial y}\right) + \frac{\partial}{\partial z}\left(k\frac{\partial T}{\partial z}\right) = \rho Cp\left(U_p\frac{\partial T}{\partial x} + \frac{\partial T}{\partial t}\right)$$

which can be put in a dimensionless form

$$(Fo_x)\frac{\partial^2 T^*}{\partial x^{*2}} + (Fo_y)\frac{\partial^2 T^*}{\partial y^{*2}} + (Fo_z)\frac{\partial^2 T^*}{\partial z^{*2}} = \frac{U_p t_{ref}}{L_x}\frac{\partial T^*}{\partial x^*} + \frac{\partial T^*}{\partial t^*}$$

by defining the following dimensionless variables:

$$T^* = \frac{T - T_{ref}}{\Delta T_{ref}};\ x^* = \frac{x}{L_x};\ y^* = \frac{y}{L_y};\ z^* = \frac{z}{L_z};\ t^* = \frac{t}{t_{ref}};\ \alpha = \frac{k}{\rho Cp} = constant$$

$L_x = Distance\ between\ jet\ lines;\ L_y = Strip\ Thickness;\ L_z = Distance\ between\ nozzles/2$

$U_p = 2 - 20 m/s;\ \alpha = 4x10^{-6} - 12x10^{-6}$

where $Fo = Fourier\ number = \frac{\alpha t}{L^2} \equiv \frac{Rate\ of\ heat\ conduction\ across\ L}{Rate\ of\ heat\ storage\ in\ volume\ L^3}$. Note that $0 \le x^*, y^*, z^*, T^*, t^* \le 1$, and given that all the differential terms are of order 1, the relative values of the Fourier numbers dictate which terms are more important. Since it is well known that most of the heat extracted comes from the top and bottom surfaces, the Fourier number in the y direction will be taken as a standard for comparison.

- Heat Transfer in the x-direction.

$$\text{Diffusion: } \frac{Diffusion\ in\ the\ x\text{-}direction}{Diffusion\ in\ the\ y\text{-}direction} = \frac{Fo_x}{Fo_y} = \left(\frac{L_y}{L_x}\right)^2$$

The maximum value for this ratio was found to be approximately 0.01, and therefore it is always negligible. The minimum Peclet number (ratio of the convective heat transfer over the diffusion heat transfer) is approximately $Pe_{min}=1.6x10^5 L_x$. which again establishes that the diffusive term is negligible.

$$\text{Convection: } \frac{Convection\ in\ the\ x\text{-}direction}{Diffusion\ in\ the\ y\text{-}direction} = \frac{\left(\frac{U_p t_{ref}}{L_x}\right)}{Fo_y} = \frac{U_p L_y^2}{\alpha L_x}$$

this ratio is always higher than 0.2, and therefore is never negligible.

- Heat Transfer in the z-direction.

$$\text{Diffusion: } \frac{\textit{Diffusion in the z - direction}}{\textit{Diffusion in the y - direction}} = \frac{Fo_x}{Fo_y} = \left(\frac{L_y}{L_z}\right)^2$$

The values of this ratio range from 0.0027 to 0.19, but for most conditions it is less than 0.1. Since the thermal gradients in the z-direction are slightly smaller, the heat transfer in the z-direction is negligible.

An important result of this analysis is that a 1-D (through the thickness) heat transfer model, as the one presented in this work, is applicable to any position across the width of the strip if the proper boundary conditions are adopted. Consequently, a 2-D analysis of the cooling in the runout table can be accomplished by running the runout table model for the different water flow conditions across the width.

In order to analyze the effect of position across the width of the strip, the runout table model was run for different water flow density distributions on the surface, whose thermal histories may correspond to what would be seen by a thermocouple installed at a certain position across the width. Since the best observations of the water flowing on the strip were obtained for company H, a 6.55mm coil (CNZ) from that company was selected for analysis. Two water flow densities were considered, the high, corresponding to the water flow rate from a nozzle flowing on a band of width equal to one half of the distance between nozzle centers, whereas the low corresponds to the same flow rate flowing on a band of a width twice the distance between nozzles. According to the video-recorded observations these may be good approximations of the extreme cases. In the case of company H, the jet lines are alternated at distances of 0.067 and 1.37m, and the nozzle arrangement between jet lines is offset by one half of the nozzle-nozzle distance

within one jet line to ensure that the water distribution is as homogeneous as possible. It is important to observe that due to the offsetting of the nozzles, for some fixed positions across the width of the strip, the thermal history would reveal that the jet impingement zone of an individual jet appears once each two jet lines. The cooling patterns analyzed are presented in Table 7.5. In the cooling pattern, the term "short" is given to the jet lines with a distance of 0.067m. to the next jet line downstream, in which the impingement of a jet is seen. The term "long" corresponds to jet lines with a distance of 1.37m. to the next jet line downstream, wherein the impingement of a jet is not seen because of the alternate arrangement of the nozzles. The characters H and L correspond to high and low water flow densities respectively.

Details of the thermal histories such as the top surface temperature, heat flux and water temperature are presented in Figure 7.41 to Figure 7.45. For run 1, shown in Figure 7.41, the water is concentrated only in the impingement band, whereas it is assumed that in the parallel flow downstream the water flow density is lower than actual. The predicted coiling temperature of 724°C for this cooling pattern is 43°C higher than the actual measured temperature of 681°C. The cooling pattern of run 1 represents an extreme case of low water flow density, that is perhaps only possible at the edges of the strip. However, it is interesting to note that when the water flow density is low, after the impingement band has been passed, the steel surface temperature immediately rises due to the heat conducted from the interior. The heat flux history shows that even though transition boiling occurs in the parallel flow region, the heat flux decreases with position because of the "buffering" effect of water heating, which decreases very significantly the

effectiveness of cooling. That is clearly shown in the shape of the water temperature history, where the water can reach temperatures even higher than 80°C. Thus, in the parallel flow region downstream, the transition from transition boiling to film boiling is smooth and caused by an increase of the local water temperature. Peak heat fluxes at the impingement region increase according to the transition boiling curve in that zone, but for this case, the heat fluxes vary only within 5-6MW/m^2.

In the case of run 2, the cooling pattern is very similar to the previous, except that the water flow density in the long parallel flow regions was alternated high-low-high-high and so on. Figure 7.42 shows a similar temperature history, except that when high water density was present in long parallel flow regions, the surface temperature does not recover, but decreases sharply at the beginning; after about 0.5m, the temperature reaches a local minimum. This water flow distribution is believed, according to the video observations, to be representative of the most common flows during the operation. The predicted coiling temperature is 689°C, which is very closed to the 681°C measured. As a consequence of a higher water density, the water temperature increases only up to 60-70°C, compared to 80-90°C in the low density areas. The transition from transition boiling to film boiling is not clearly seen, and the heat fluxes are always above 0.8MW/m^2.

Runs 3 and 4 are believed to represent the two most extreme cases that can be seen in the operation of company H. Run 3 represents the cooling of the strip with the highest water flow density possible, whereas Run 4 with the lowest water flow density. Figure 7.43 shows that with high water flow density everywhere, the coiling temperature

would be as low as 617°C (64°C lower than measured under normal conditions). The top surface temperature behaves very similar to the high density case of run 2, and after a sharp temperature drop, the temperature recovers slightly when the water temperature is above 50°C. Run 4, is a very similar case to run 1, except for the low water flow density in the short parallel flow zone. Figure 7.44 shows that the predicted thermal histories and coiling temperature are almost identical for runs 1 and 4. Run 7 represents the case where a piece of steel for some reason does not reach the impingement region of any jet, but it is subjected to the most common water flow densities found. The predicted coiling temperature was 695°C, which is in good agreement with the 681°C measured and with predictions for cases such as run 2. Interestingly, the results shown in Figure 7.45 are almost identical to those of case 2, except for the existence of the typical peaks in the temperature and heat flux histories corresponding to the impingement of a jet.

In order to determine if the 1-D representation of the cooling can be as accurate without establishing a specific pattern such as the ones used in this analysis, but only taking into consideration the jet lines working, the logical assumption of a homogenous water distribution in the parallel flow region was adopted. It is important to mention that this happens often in the actual operation. As Table 7.5 shows (see standard case) the predicted coiling temperature is in very good agreement with the 681°C measured and with the numerical results already discussed.

The generality of these results was tested for several coils, and companies. In particular, results for a similar 2-D analysis for a 9.4mm strip from company A ($CT_{measured}$=683°C) are summarized in Table 7.6 . Runs 1-3 and 6 represents the typical

water flow densities observed, and as it is shown in the table, variation among them are insignificant. In the standard case, where the water flow density was assumed constant and intermediate between H and L, the predicted coiling temperature is in excellent agreement with those runs. In general the predicted coiling temperatures are less than 10°C from the actual temperature. Results from the extreme cases 4, 5 and 7 reveal that for thicker strips, variations in water distribution can have a much more important effect on the coiling temperature, and consequently, during rolling of higher gages, more attention needs to be paid to ensure homogenous distribution of water.

From these results, it is seen that the actual effect of the local heat extraction in the impingement zone of a jet on the final coiling temperature is small. However, the impingement region of a jet is extremely important because it supplies the fresh, colder water to the surface. As seen in the literature review, the video recordings and the experience shows that the single most important parameter to control in a cooling system is the local water temperature on the strip. In practice, the local water temperature is a function of the design of headers, the design of the nozzle arrangement and the flow rate and temperature of the water supplied. From a modeling point of view, these results show that a 1-D runout table model assuming homogenous water flow distribution can be as accurate as a 2-D model for prediction of the coiling temperature, without sacrificing any physical significance of the results.

Finally, in order to verify these conclusions with real operation results, measurements of the water temperature at a specific location in the parallel flow region of a top jet were performed during the runout table cooling of two coils of a DQSK steel[22].

Measurements were carried out by setting a thermocouple connected to a data acquisition system to the water stream falling off the top surface. These measurements were done for coils c140751 and c140753 of company I, with the operating conditions shown in Appendix Table B.12. The runout table model was run assuming a homogenous water flow distribution across the width. Comparison between predictions and measurements is shown in Figure 7.46 and Figure 7.47, for coils c140751 and c140753 respectively. In Figure 7.46 the agreement between measurements for the coiling temperature and water temperature is exceptionally good. Given that the residence time in each jet line is short for small gages, the thermal gradients are small and the temperature peaks are short. Heat fluxes increase in the countercurrent parallel flow region while approaching the jet impingement zone, where heat fluxes of the order of 4-5 MW/m^2 are seen, and after, in the downstream parallel flow region, the heat flux decreases smoothly according to the local temperature variations. As it is shown in this figure, water temperature variations in the parallel flow region, of about 35°C/m, are quite significant. Differences in the maximum water temperature reached are related to the differences in length between the parallel flow regions. Figure 7.47 shows a similar agreement, and gives evidence of the consistency of the model predictions.

7.2.4 Heat Transfer maps and the cooling performance of a jet

In order to establish a simple method to characterize the effect of variables such as strip thickness, speed and surface temperature, residence time under cooling, jet diameter, height, velocity and temperature, and their effect on the performance of a cooling jet, a heat transfer map is proposed. This map is a useful tool to explain the local

heat transfer events during cooling and in helpful in optimizing the operating parameters of a laminar cooling system.

The proposed heat transfer map consists on a plot of the local heat fluxes found at different position in the runout table versus the local top surface superheat. This map is similar to the standard boiling curve, but its meaning is quite different.

Heat transfer maps were developed for the cooling patterns corresponding to runs 1 and 2 of company H in the previous section (see Table 7.5, Figure 7.41, Figure 7.42), and they are shown in Figure 7.48. Along with the maps, the boiling curves for the impingement at the initial water jet temperature, $T_{initial}$, and parallel flow regions, for different water temperatures, ranging from the initial temperature up to 95°C were plotted. The first graph of Figure 7.48[a] shows that at the countercurrent parallel flow region (position increases downstream from the countercurrent region as defined by the arrows) the local water temperature decreases while approaching the impingement region until it reaches a maximum heat flux in this region, which correspond to the initial water temperature of the jet. When the impingement region is reached, the heat flux increases significantly to reach the boiling curve for that region, and since the water temperature is virtually the same, the heat flux increases following that particular boiling curve. After, in the short downstream parallel flow region (approximately 0.07m) the heat fluxes follow the boiling curve for the parallel flow region at the initial water velocity, because of the high water flow density and short length of this zone. Once the next jet line is reached, the heat fluxes follow the same boiling curve because the water temperature is practically the same. After, when the long downstream parallel flow region is reached, the local

water temperature increases significantly, and the local heat fluxes decrease accordingly, until values typical of film boiling are reached. These results are obtained because the water flow density assumed in this region was low. The transition through the different boiling curves and boiling regimes (transition to film boiling) is completely smooth and determined by the local water temperature. The second graph of Figure 7.48[a], shows similar features, but a major difference is found in the long parallel flow zone, where the assumed higher flow density makes the system follow the boiling curve for the initial temperature for some time, and then a gradual decrease of cooling until a "nose" is seen when the water temperature is slightly above 50°C; the strip temperature recovers afterwards because the heat fluxes are small. Results for run 1 shown in Figure 7.48[b] exhibit a similar behavior as the first graph of Figure 7.48[a]. Because all the long parallel flow regions are assumed to have a low water flow density, the strip top surface temperature recovers throughout the cooling in this region.

A similar heat transfer map was obtained for a jet line adopting the cooling configuration of run1 of company A (see Table 7.6), which is found more typically in runout table operations. Results are shown in Figure 7.49. The map has been divided into several sections (A-G) with the purpose of explaining the effect of the different process variables on the shape of this map. Region A corresponds to the cooling in the upstream parallel flow region, for which the water temperature decreases while approaching the impingement region, and the heat fluxes are accordingly increased. This part of the map is almost linear, and its length increases with increasing the water temperature of the downstream parallel flow of the previous jet line. Increasing the water flow density in this

region moves this line around the pivotal point B in the direction of the curved arrow shown in the figure, until a maximum is obtained, when this line reaches the boiling curve for water at the initial temperature. The boiling curves for the initial water temperature are the thicker lines shown in this figure. Point B consequently, represents the intersection between the boiling curve at the parallel flow region for water at the initial temperature, the upstream parallel flow region section of the map, and section C. Section C is a region of transition between impingement region and parallel flow region, and it corresponds to those positions where the pressure gradient is small but not zero, which according to Figure 2.4, can be extended a measurable distance. Evidently, the sudden increase in heat flux depends on the difference between the boiling curves in the impingement and parallel flow regions, whereas the slope of the curve depends on the heat conduction characteristics of the substrate. The difference between the boiling curves for both regions is dependent exclusively on the jet characteristics. Region D, the impingement region, lies mainly on the boiling curve for water at $T_{initial}$, and decreases slightly at the end because of a small temperature raise of the water in this region. The top surface temperature drop in this region increases with increasing the substrate thickness and the jet diameter or width, and also with decreasing the strip speed (increasing the residence time). Region E is similar to region C, but the temperature of the surface increases instead of decreases because of the heat conducted from the interior of the substrate. Point F corresponds to the intersection of section E, the boiling curve for the parallel flow region at $T_{initial}$ and section G, the downstream parallel flow region. It is noteworthy that the section of the boiling curve that applies for this range of surface temperatures is defined approximately by the line drawn by the points F and B. This is

extremely important in analyzing the experimental measurements on the moving plate. Finally, section G is characterized by a small thermal recovery immediately after point F, which is more evident increasing the thickness of the substrate or increasing the difference between the boiling curves in the impingement and parallel flow zones. This curve tends to move in the direction of the curved arrow shown in the figure with increasing the water flow density (compare with the second graph of Figure 7.48[a]).

Among the various applications of this heat transfer map, one is in the optimization of the process variables to attain the maximum cooling possible from a jet. Evidently, increasing the water flow rate per nozzle would increase the cooling performance of the jet, but as it is seen in this heat transfer map, the maximum cooling is bounded by the boiling curves. When the water flow rate per nozzle is increased, the water flow density, the jet width and velocity increase. However, the impingement jet velocity is mainly controlled by the height of the nozzle (see Table B.10), and the slightly higher jet velocity would have an insignificant effect on the boiling curves. On the other hand, the increased jet diameter increases the impingement area, but as it was discussed in the literature review and in section 7.1.1, the increased jet diameter also decreases the boiling curve. Consequently, the variation produced on the jet diameter should be small. Therefore, the enhancement of cooling with increasing the water flow rate per nozzle is mainly due to the augmented water flow density, and disappears when the local water temperature reaches $T_{initial}$. Another obvious way to increase the cooling performance of the jet would be to decrease the supplied water temperature. This has been found to be a very practical solution in some runout table operations. In the construction of new

laminar cooling facilities, special attention is paid on the design of the cooling towers to be used to maintain the low water temperature, such as one recently built by company K.

Another important application of this map is in the analysis of the heat transfer data from experiments on moving surfaces. In order to verify the analysis presented, the measurements during the cooling of a moving plate carried out by Hernandez et al.[17] were plotted in the form of these heat transfer maps. Results are shown for four different planar water jets in Figure 7.50. The obvious similarity of these measurements with predictions such as those shown in Figure 7.49, confirm that the analysis presented is reliable. The corresponding points B and F in each of the graphs were obtained (see dotted lines in Figure 7.50), which define the boiling curve for the parallel flow region of jet cooling a moving surface. The black points corresponding to the impingement region also are part of the boiling curve for the impingement region. All the points obtained were plotted in Figure 7.30 and Figure 7.31, for the impingement and the parallel flow regions, respectively.

From Figure 7.50 it can be seen that the water flow rate employed during the pilot-plant cooling was relatively small, and the heat absorbed by the water increased its temperature significantly. Interestingly, these experiments were carried out with the lowest water flow rate possible while maintaining the stability of the jet.

7.2.5 Thermal evolution during laminar cooling

One of the most important problems to be solved nowadays during the hot rolling of a strip is to find the operating conditions during laminar cooling that enable to produce

consistently and uniformly a specific microstructure and mechanical properties. For that purpose, the coiling temperature is controlled usually in a range of ±20°C from the target.

In this section, the runout table model predictions for the thermal history of some strips are presented. In a subsequent section, the relationships between some individual laminar cooling parameters and coiling temperature are explained.

The thermal history during the cooling by company C of a 9.5mm A36 strip is shown in Figure 7.51. The temperature predictions reveal that the top surface cools at a much faster rate than the bottom surface, which is mainly caused by three effects of gravity: [1] The extended contact of the strip with the water flow on the top surface (longer parallel flow regions), and [2] The lower local heat fluxes due to higher stability of the vapor-liquid interface of the bottom cooling configuration, and [3] Water jet velocities are much smaller for the bottom jets than for those at the top, even for the same velocity at the nozzle, because gravity accelerates the jet at the top, increasing its velocity, whereas the opposite happens at the bottom . The temperature differences between both surfaces increase during laminar cooling, and may be higher than 400°C, but they rapidly decrease during cooling in air. Interestingly, the bottom surface cools slower than the center, which again highlights the importance of the top cooling, but also demonstrate that the thermal gradients between the center and the bottom surface are small. This implies that most of the cooling is localized in a region close to the top surface, whereas in the rest of the strip the thermal gradients are comparatively small. Another important observation is that in the region of water cooling, the thermal history

at the center is almost linear (cooling rate is nearly constant). This is also supported by the experimental correlation (equation [7.2.2.3]) obtained in section 7.2.2.

The effect of the strip thickness on the thermal evolution of the steel is seen in Figure 7.52 and Figure 7.53 for strip thicknesses of 6.0 and a 4.8mm, respectively. The thermal histories shown in Figure 7.52 and Figure 7.53 are similar to the one for 9.5mm, but the temperature differences between both surfaces are considerably reduced with decreasing thickness. These differences are approximately 300 °C and 200°C for the 6 and 4mm strips respectively. It is important to mention that the temperature differences between the top and bottom surfaces are not only dependent on the steel thermal resistance, but also on the residence time during each jet line. The residence time is dependent on the strip speed, which is adjusted according to thickness.

Results were obtained for a 2.5mm DQSK steel, as it is shown in Figure 7.54. The thermal history is slightly different, especially in the shape of the curve at the center, where the cooling rate is not nearly as constant as in the previous cases. The temperature differences between surfaces are approximately 100°C and are not higher at the end of the main water cooling zone.

7.2.6 Comparison between model predictions and measurements in full-scale operations of the coiling temperature

This section deals with the verification of the runout table model predictions of one of the most important quality control parameters, the coiling temperature. Comparison between the model predictions with measurements from different companies

and processing conditions was carried out. The operating conditions and measurements are presented in Appendix B.

Usually, during the runout table operation, the control systems that are placed in the process are based on off-line and on-line models. The off-line models are useful to estimate the initial cooling conditions and to analyze the process more in detail. The on-line models may be simplified versions of off-line models that enable a rapid setup of the process and corrections to the original settings while processing. Control is aimed to restrict variations in the coiling temperature in many cases within ±20°C. Strict control of the coiling temperature is necessary to maintain a uniform microstructure and mechanical properties in the whole strip. One of the main applications of the present runout table model is in the prediction of the coiling temperature.

The model was run for the strips whose operating conditions are shown in Appendix Tables B.11 to B.18. The coiling temperatures predicted by the model are compared with the measured coiling temperatures in Figure 7.55. Results indicate that the coiling temperature is predicted for most of the cases within ±20°C. The error in the coiling temperature predictions is relatively small, and it gives confidence on its application as an off-line model to setup the cooling conditions for an operation. It is extremely important to note that the model was applied to two different chemistries, and a very wide range of operating conditions. The strip speed ranged from 2 to 18 m/s, the gages from 1.8 to 16mm, the finishing mill temperatures from 850 to 950°C, and the coiling temperatures from 540 to 740°C. The laminar cooling systems analyzed ranged

from low-flow bar cooling systems to the high-flow curtain systems. For the wide variety of conditions, the results are remarkably good.

7.2.7 Effect of some laminar cooling parameters on the coiling temperature

The need for relationships between individual laminar cooling parameters and the coiling temperature was emphasized in section 7.2.5. In this section, relationships between the top and bottom flow rate, nozzle height and diameter, number of nozzles per jet line and initial water temperature and the coiling temperature are presented.

With this purpose, three coils from the operation of company C were selected: Coils c907619m (DQSK) with a measured coiling temperature of 566°C, c907272m (A36) with a measured coiling temperature of 665°C, and c907968m (DQSK) steel with a measured coiling temperature of 671°C, which will be called DQSK* hereafter.

The effect of top water flow rate on the coiling temperature is shown in Figure 7.56. The coiling temperature decreases linearly with increasing the top water flow rate. These results are in very good agreement with the findings by Wilmotte et al.[23], and are also consistent with the measurements of the effect of water flow rate on the average heat fluxes (see Figure 2.12[a]). It is important to note that the effect of chemistry is small, but the effect of the target coiling temperature is comparatively strong. This is because the cooling is well within the transition boiling regime even for high local water temperatures. It is seen that variations in water flow rate of ±40% from the nominal 931 l/min/jetline can cause variations in coiling temperature of about 90°C for target coiling temperatures close to 550°C, whereas for coiling temperatures around 650°C variations are 35 and 50°C for A36 and DQSK respectively. These results indicate that during

processing of low coiling temperature steels, which sometimes is the case for the DQSK grade, variations in water distribution and flow rate should have an important effect, and control of the coiling temperature should be more difficult. In fact, controlling the cooling to attain a low target temperature has been observed to be more difficult in the operation of several mills[11]. It is important to note that the strong effect of water flow rate is caused mainly by the increased amount of water available for cooling, and to a lesser extent by the increase in the impinging jet velocity and diameter.

The effect of variations in the bottom water flow rate is presented in Figure 7.57. As this figure shows, the coiling temperature decreases with increasing flow rate but in a lesser extent, simply because most of the cooling takes place at the top surface and the bottom surface is a small contributor. It is important to note that these calculations assume that the length of the contact of the bottom water stream with the under surface of the strip surface remains constant, since the effect of jet velocity on the that length is unknown.

One important design parameter is the height of the top nozzles. The effect of nozzle height on the coiling temperature is shown in Figure 7.58. The coiling temperature decreases with increasing the nozzle height until a minimum is found, and then the coiling temperature increases again, the effect being more pronounced at lower target coiling temperatures. The effect of chemistry is small and slightly more noticeable at low heights. Within the operating conditions analyzed, the total variations in coiling temperature are 52, 15 and 32°C for the coils DQSK, A36 and DQSK* respectively. The reason for the existence of such an effect is that the impinging jet velocity in most

operations is mainly determined by this design parameter, and the boiling curves are directly dependent of the jet velocity. Then, increasing the nozzle height results in a higher jet velocity and higher local heat fluxes because of the higher boiling curves. However, this effect is counteracted by the decrease in the impinging jet diameter, and consequently in the impingement region area. Since jet velocity affects slightly the boiling curves in the parallel flow region, these two counteracting effects produce an optimum height for a given water flow rate and nozzle diameter. In this case, the optimum height for maximum cooling was found to be 2.4m, which is very close to the 2.17m adopted in operation. These results are consistent with the results shown in Figure 2.12[b], where it is seen that the effect of nozzle height is relatively small at high temperatures but increases with decreasing temperature. Also that figure shows that the average heat flux can be increased or decreased with nozzle height. It is important to mention that other important factors may contribute to the behavior of the coiling temperature during the changing of the nozzle height, such as the air entrapment, the instability of the jet, turbulence, etc.

Another design parameter analyzed was the number of nozzles used in the top jet lines. The effect of the number of top nozzles used per jet line while maintaining the total water flow rate per jet line constant is seen in Figure 7.59. Within the operating conditions analyzed, the effect of the number of nozzles is negligible in the coiling temperature. Although a larger number of nozzles may seem to increase the total impingement area within a jet line, the diameter of each jet is also decreased, compensating for the larger number of them. However, in operation, significant

variations in the number of nozzles may have an effect, reflected perhaps on variations of temperature across the width of the strip, which are not analyzed in this work. On the other hand, changing the number of top nozzles while maintaining the water flow rate per nozzle constant, and consequently increasing the water flow rate per jet line give different results. Such calculations are presented in Figure 7.60. The results show that the effect of increasing the top nozzles is very similar to that seen for increasing exclusively the water flow rate (compare with Figure 7.56). The number of nozzles used for cooling within reasonable variations has a negligible effect on the coiling temperature, provided that the flow rate per jet line remains constant.

The effect of the diameter of the top nozzles was studied, and results are shown in Figure 7.61. For target coiling temperatures around 650°C, the effect is small and almost independent of chemistry. The coiling temperature decreases 9°C changing the nozzle diameter from 0.01 to 0.019m, whereas above that range the coiling temperature remains constant. For a lower target coiling temperature a more pronounced behavior was observed, and variations in coiling temperature may be higher than 40°C.

Whereas design parameters are mainly fixed, process parameter such as water temperature are critical in the operation of the runout table. The effect of water temperature variations from 20 to 35°C were considered. Results are presented in Figure 7.62. The coiling temperature increases linearly with water temperature by about 47 and 73°C in the A36 and DQSK* strips respectively, which have similar target coiling temperatures; whereas, in the case of the lower target coiling temperature, the coiling temperature varies linearly with water temperature and the increment was 147°C. In this

case, it is seen that the effect of water temperature is dependent on chemistry and the target coiling temperature. Very strict control in the supplied water temperature is necessary to maintain a good control of the coiling temperature, and this is more so at lower coiling temperatures. At lower coiling temperatures the critical heat flux is nearly reached and the heat fluxes are very high for almost any water temperature (see Figure 7.27 and Figure 7.28).

In order to verify the performance of the model with variations of some of these variables, comparison between model predictions with plant observations of the effect of water temperature, water flow rate and nozzle diameter, and chemistry is presented in Table 7.7.

According to some observations in a plant[24], the number of jet lines working necessary to attain a specific coiling temperature has to be increased by approximately 1% when the supplied water temperature is increased by 1°F in the range of 25-35°C. The runout table model predicts for the strips DQSK, A36 and DQSK* a value of 1.6%/1°F, 1.6%/1°F, and 1.5%/1°F, respectively, which results in excellent agreement with those observations, taking into consideration that these results correspond to very different cooling conditions. Interestingly, the model predicts that the magnitude of this effect is independent of chemistry and target coiling temperature, as observed in the plant operations.

In the same plant, trials were conducted increasing the water flow rate and the nozzle diameter by 50% to enhance the cooling capabilities of the system. However, the number of jet lines working to attain a specific coiling temperature were reduced only by

approximately ¼ (25%). The exact water flow rate conditions and nozzle diameter were not specified. However, this result indicates that not only the total amount of water supplied determines the coiling temperature, but also its distribution along the runout table. In this case, the model predicts a reduction of 18%, 17% and 15% for the DQSK, A36 and DQSK* strips respectively.

On the other hand, as it was previously mentioned, the trend in runout table operations is to produce steel with specialty properties using normal carbon grades by cooling with different patterns and coiling temperatures. One example is found in the tests carried out by Auzinger et al.[25]. Such specialty properties were obtained by cooling the strip to 250°C along a pre-defined special cooling curve. They are currently investigating the way to reduce considerably the large number of different chemical compositions of the steel normally required to produce strip with defined mechanical properties simply by adapting the cooling strategy. The chemistry effect on coiling temperature is well established. Hurkmans et al.[21] reported that the number of cooling units used to reach a certain coiling temperature has to increase by 24% from processing a steel with a similar chemistry to the A36 to one close to the DQSK. Very similar experimental findings in this work were presented in section 7.2.2. The runout table model predicts an increase of 13%, 17% and 18% for the DQSK, A36 and DQSK* strips, which results in good agreement with plant observations.

An important issue is where to focus the efforts to improve the cooling capabilities of a system. Figure 7.63 shows the relative percent of heat extraction of each cooling zone during the processing of the coil c162331 (A36) from company C. Figure

7.63[a] shows that 86% of the total heat removed from the strip is carried out at the top surface, whereas the remaining 14% takes place at the bottom. This is consistent with the observed microstructure. At the top surface, 62% of the heat is removed in the downstream parallel flow region, whereas 23% is removed in the upstream (counter current) parallel flow region. The contribution of the impingement band is of only 10%, and air cooling represents only 5%, as shown in Figure 7.63[b]. Figure 7.63[c] shows that at the bottom surface, most of the heat is extracted in air cooling (46%), followed by the impingement region that totals 36%, and a small contribution of the parallel flow region of 18%. It is important to note that these percentages were similar for different coils analyzed, and the results can be considered as general for this particular plant. Consequently, given the nature of the cooling system and geometry, most of the efforts to increase the cooling power of the system should be focused on the parallel flow regions on the top surface. As it was stressed, this is possible mainly by decreasing the local water temperature at any position, which can be accomplished by either increasing the water flow rate per nozzle or by decreasing the supplied water temperature. An increase in the actual length of the parallel flow region does not necessarily increase the cooling capabilities of the system, since after the local water temperature has reached a certain value, the cooling is basically carried out under film boiling of almost a saturated liquid, which is close to radiation heat transfer in air. This also implies that the distribution of the water flow in the parallel flow regions is extremely important to attain uniform microstructure and mechanical properties.

Finally, a sensitivity analysis of the effect of ± 20% variations in the boiling curve parameters $q_{l\text{-}s}$, $q_{v\text{-}s}$, F and $H_{transformation}$ was carried out for conditions of coil c162331. It is evident that an increase of 20% in the liquid-solid heat flux or contact area has an important effect on the coiling temperature, reducing it by around 50°C, whereas a decrease in the same percentage increases the coiling temperature about 30°C. Variations in the vapor-solid contact heat flux are comparatively less important. Finally, an increase in the heat of transformation of 20% increases the coiling temperature by 15°C, while a decrease of 20% decreases the coiling temperature by 23°C. Therefore, the heat of transformation cannot be ignored in the solution of the thermal problem.

7.3 References

1.- T. Ochi, S. Nakanishi, M. Kaji, S. Ishigai, "Cooling of a Hot Plate with an Impinging Circular Water Jet", Multi-Phase Flow and Heat Transfer III. Part A: Fundamentals, Elsevier Science Publishers B. V., Amsterdam , pp. 671-681, 1984.

2.- S. Nakanishi, S. Ishigai, T. Ochi, I. Morita, "Film Boiling Heat Transfer of Impinging Plane Water Jet", Trans. JSME, 46B, 1980, pp. 955-961.

3.- S. Ishigai, S. Nakanishi, T. Ochi, "Boiling Heat Transfer for a Plane Water Jet Impinging on a Hot Surface", Proceedings of the 6th International Heat Transfer Conference, Vol. 1, 1978.

4.- J. C. Chen, K. K. Hsu, "Heat Transfer During Liquid Contact on Superheated Surface", Proceedings of the Pool and External Flow Boiling Conference, ASME, pp. 257-261, 1992.

5.- D. E. Hall, F. P. Incropera, R. Viskanta, "Jet Impingement Boiling from Circular Free-Surface Jets during Quenching Experiments", Proceedings of the ASME Heat Transfer Division, HTD-Vol. 333, Volume 2, ASME, 1996, pp. 131-141.

6.- M. Shoji, L. C. Witte, S. Yokoya, M. Ohshima, "Liquid-Solid Contact and Effects of Surface Roughness and Wettability in Film and Transition Boiling on a Horizontal Large Surface", Proceedings of the Ninth International Heat Transfer Conference, Vol. 2, 1-BO-23, pp.135-140, Jerusalem, Israel, 1990.

7.- J. E. Galloway, I. Mudawar, Int. J. Heat and Mass Transfer, Vol. 36, No. 10, 1993, pp.2511-2526.

8.- J. Filipovic, R. Viskanta, F. P. Incropera, "An Analysis of Subcooled Turbulent Film Boiling on a Moving Isothermal Surface", International Journal of Heat and Mass Transfer, vol. 37, No. 17, 1994, pp. 2661-2673.

9.- B. I. Nigmatulin, A. S. Moloshnikov, D. V. Sidenkov, "Interface Oscillations and Heat Transfer Mechanism at Film Boiling", Proceedings of the 10th International Heat Transfer Conference, 1994, paper 10-PB-19A, pp.123-128.

10.- R. Weichert, et al., "A New, Optical Measuring Technique for the Determination of the Vapor Film Thickness during Film Boiling", Steel Research, Vol. 66, No. 6, 1995, pp.244-250.

11.- H. Shimizu, H. Kimura, H Tachibana, "Development of a Runout Table Cooling System for a Hot Strip Mill", La Revue de Metallurgie CIT, Vol. 92, July-August, 1995, pp.893-898.

12.- R. Jeschar, et al., "Influence of Gases Dissolved in Cooling Water on Heat Transfer During Stable Film Boiling", Steel Research, Vol. 67, No.6, 1996.

13.- J. Filipovic, F.P. Incropera, R. Viskanta, "Quenching Phenomena associated with a Water Wall Jet: I. Transient Hydrodynamic and Thermal Conditions", Experimental Heat Transfer, vol. 8, 1995, pp. 97-117.

14.- B. Hernandez-Morales, Ph.D. Thesis, UBC, February, 1996.

15.- L. C. Burmeister, Convective Heat Transfer, 2nd Edition, John Wiley and Sons Inc., 1993, pp. 280.

16.- R. B. Bird, W. E. Stewart, E. N. Lightfoot, Transport Phenomena, John Wiley and Sons Inc., 1960, pp. 53.

17.- V. H. Hernandez A., "Heat Transfer Model of the Hot Rolling Runout Table-Cooling and Coil Cooling of Steel", M.A.Sc. Thesis, UBC, December, 1994.

18.-D. A. Zumbrunnen, R. Viskanta, F. P. Incropera, "The Effect of Surface Motion on Forced Convection Film Boiling Heat Transfer", Journal of Heat Transfer, vol. 111, 1989, pp. 760-766.

19.- J. Filipovic, R. Viskanta, F. P. Incropera, "Similarity Solution for Laminar Film Boiling Over a Moving Isothermal Surface", International Journal of Heat and Mass Transfer, vol. 36, 1993, pp. 2957-2964.

20.- M. N. Ozisik, Heat Conduction, 2nd Edition, John Wiley and Sons Inc., New York, 1993.

21.- A. Hurkmans, G. A. Duit, Th M. Hoogendoom, F. Hollander, "Accelerated Cooling and the Transformation of Steel", Proc. of the Accelerated Cooling of Steel, AIME, 1985, pp. 481-499.

22.- Muojekwu, C. A., "Modelling of Thermomechanical and Metallurgical Phenomena in Steel Strip during Hot Direct Rolling and Runout Table Cooling of Thin-Cast Slabs", Ph.D. Thesis, University of British Columbia, June, 1997.

23.-S. Wilmotte, J. F. Noville, "Multi-Purpose Interrupted Cooling Process in Operation at Clabecq Plate Mill", Proc. of the Accelerated Cooling of Steel, AIME, 1985, pp. 181-194.

24.- J. E. Hartmann, private communication, August 1996.

25.- D. Auzinger et al., "Process Optimization for Laminar Cooling", Metallurgical Plant and Technology International, v.19, No. 5, Oct 1996, pp. 68-75.

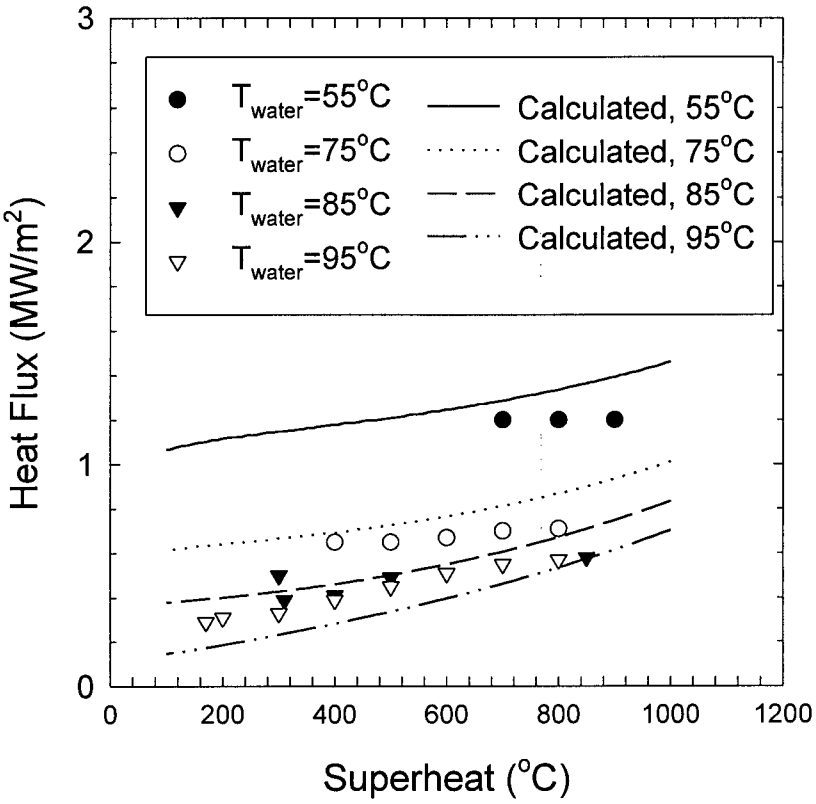

Figure 7.1: Comparison between the film boiling model predictions and measurements [1] for a water bar jet shown in Figure 2.5, (u_{jet}=3.0m/s, d_{jet}=0.020m, U_p=0m/s). $q_{tot}=1.74q_{conv}+0.75q_{rad.}$

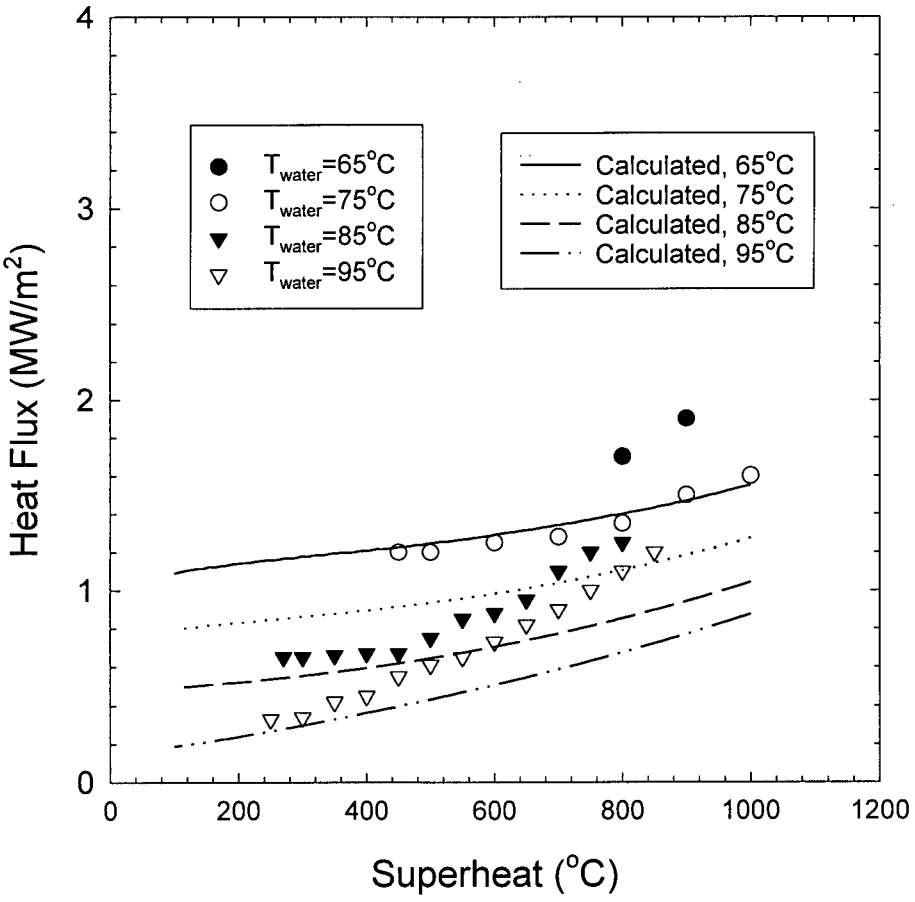

Figure 7.2: Comparison between the film boiling model predictions and measurements[3] for a planar jet shown in Figure 2.10, (u_{jet}=2.1m/s, w_{jet}=0.0062m, U_p=0m/s). $q_{tot}=1.74q_{conv}+0.75q_{rad.}$

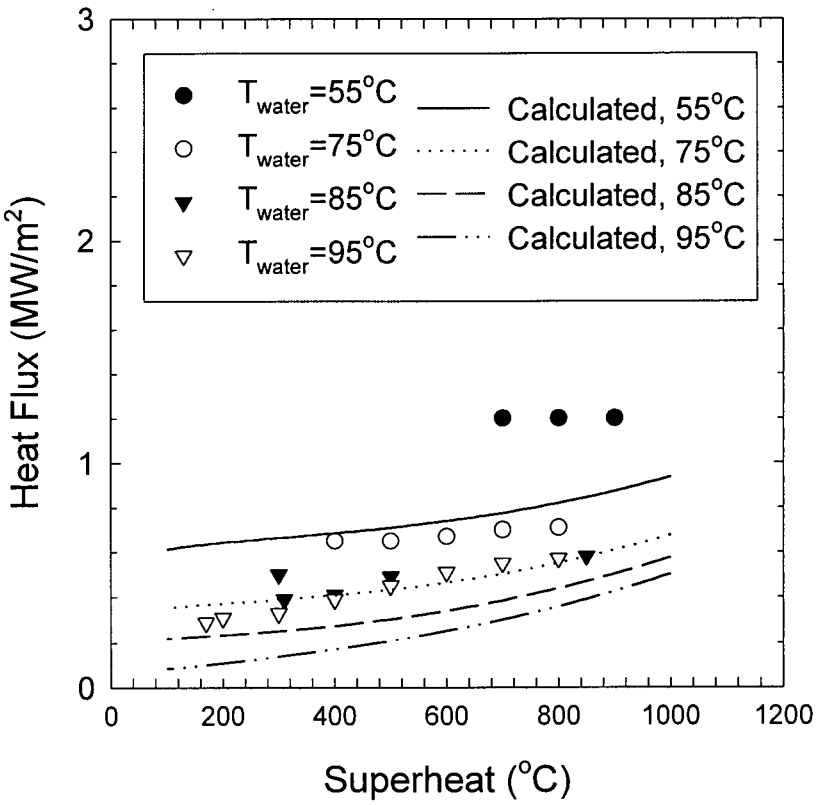

Figure 7.3: Film Boiling Predictions for the conditions of the water jet bars of Figure 7.1 using $q_{tot}=q_{rad}+q_{convection}$.

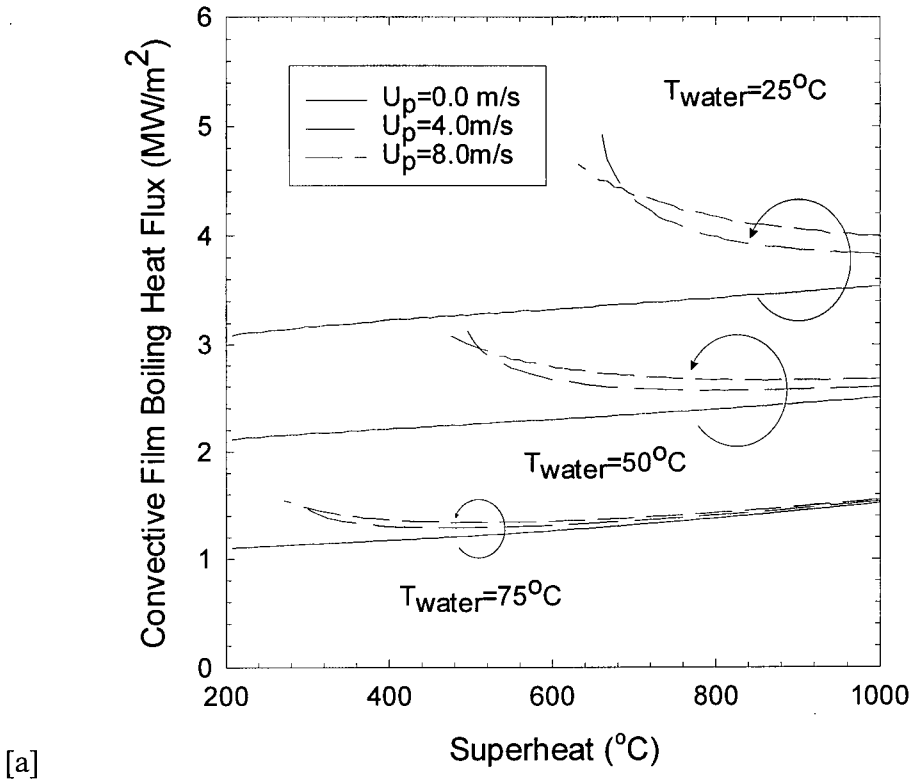

[a]

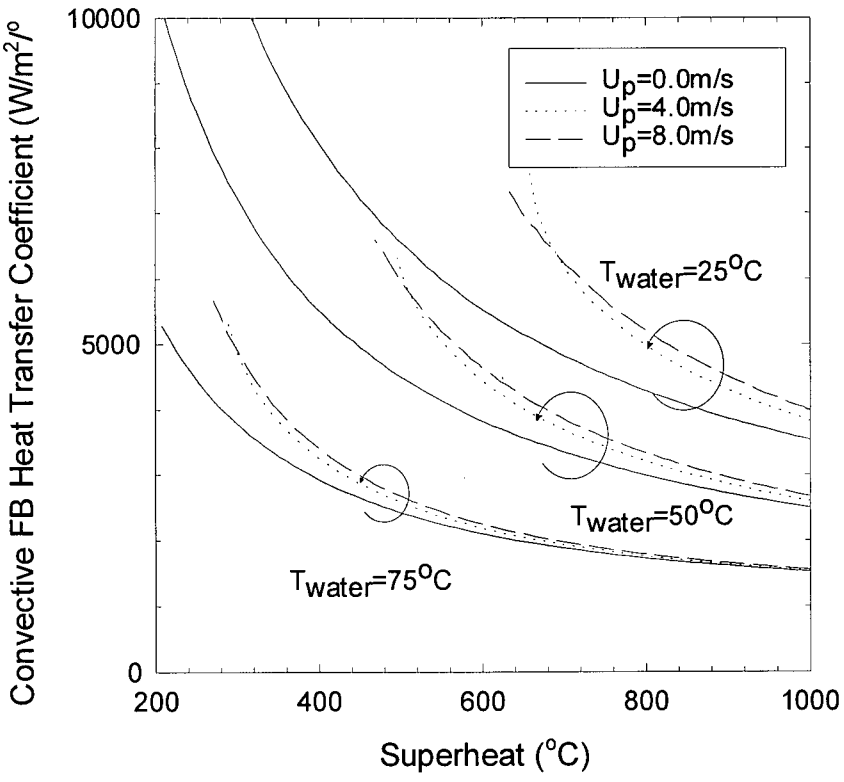

[b]

Figure 7.4: Effect of water temperature and strip speed in the typical operation of water bars of Company C on the pure convective: [a] Heat Flux, [b] Heat transfer coefficients. (d_{nozzle}=0.0186m, U_{jet}=6.78m/s).

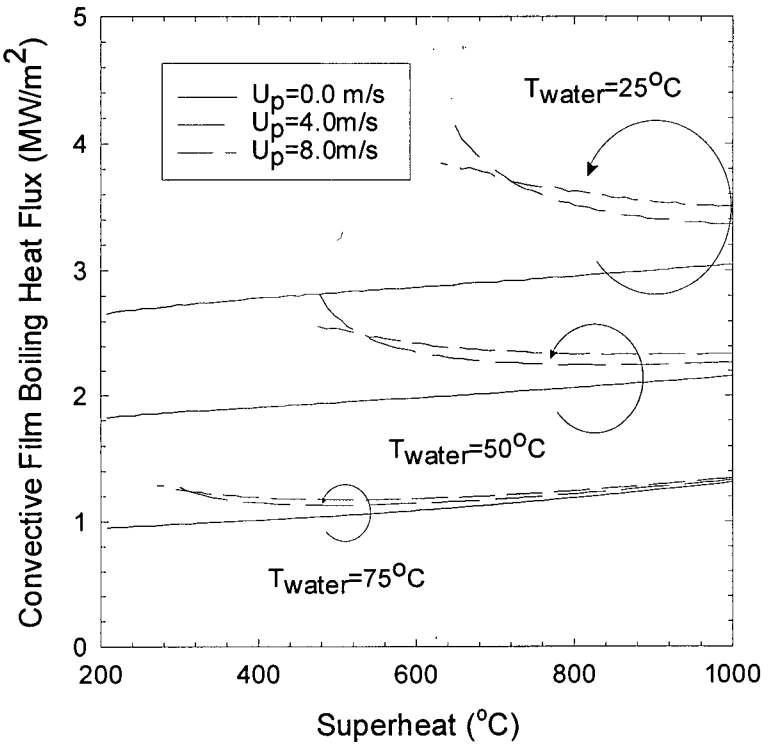

[a]

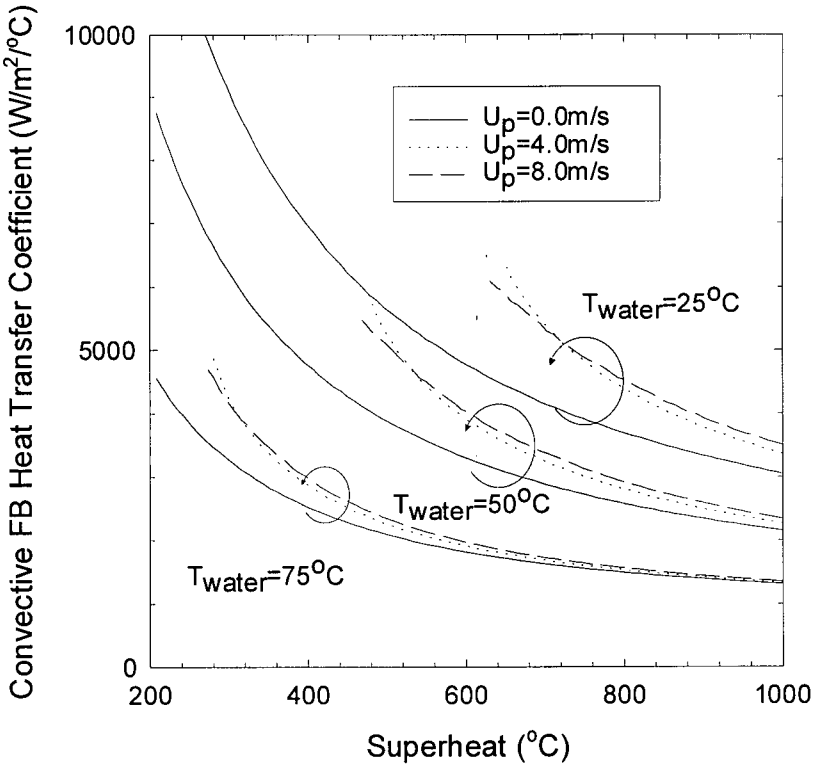

[b]

Figure 7.5: Effect of water temperature and strip speed during the operation of a planar water jet on: [a] Heat Flux, [b] Heat transfer coefficients. (w_{nozzle}=0.0186m, U_{jet}=6.78m/s).

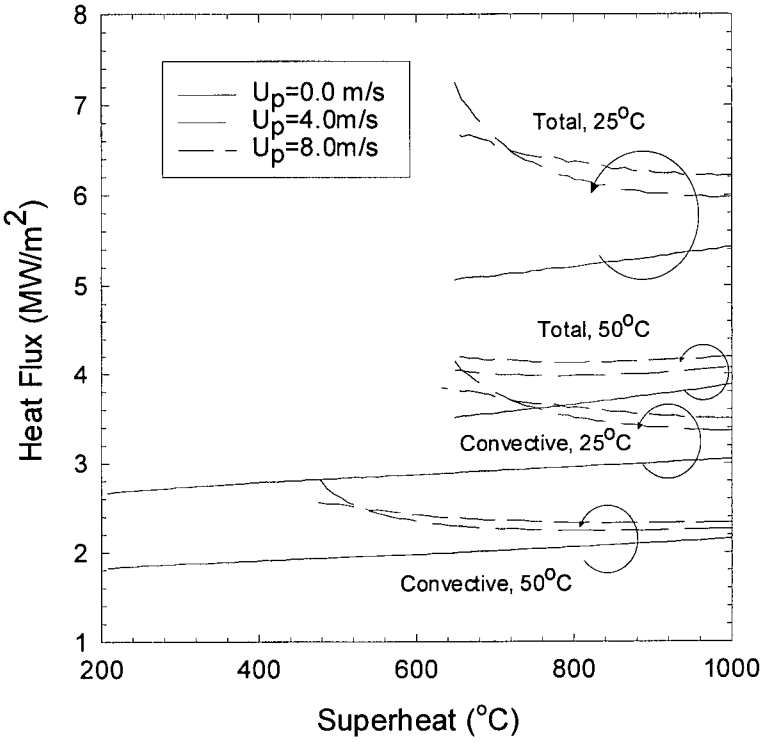

[a]

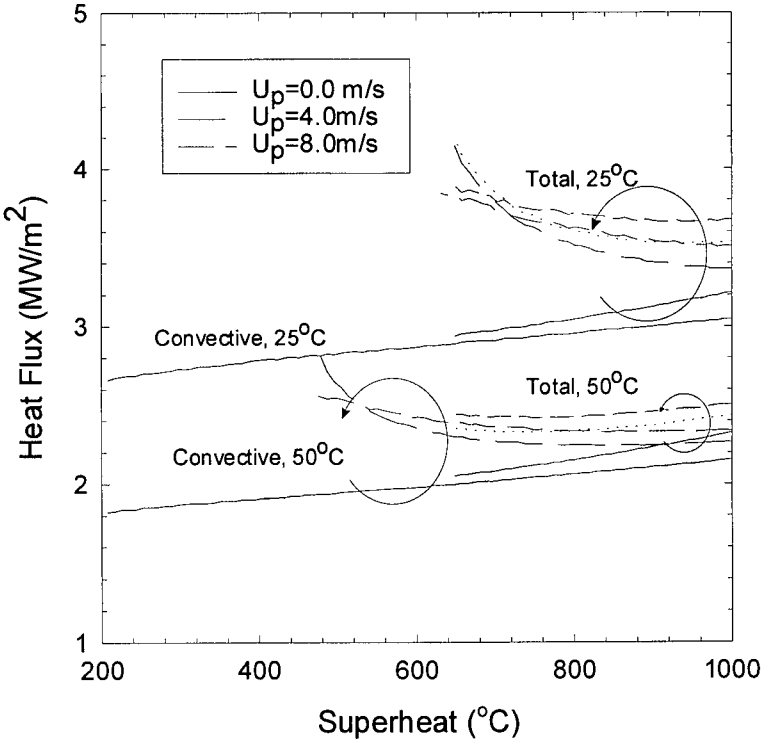

[b]

Figure 7.6: Comparison between the predicted total and pure convective heat fluxes for the conditions of the planar jet of Figure 7.5, using: [a] $q_{tot}=1.74q_{conv}+0.75q_{rad}$, [b] $q_{tot}=q_{conv}+q_{rad}$.

[a]

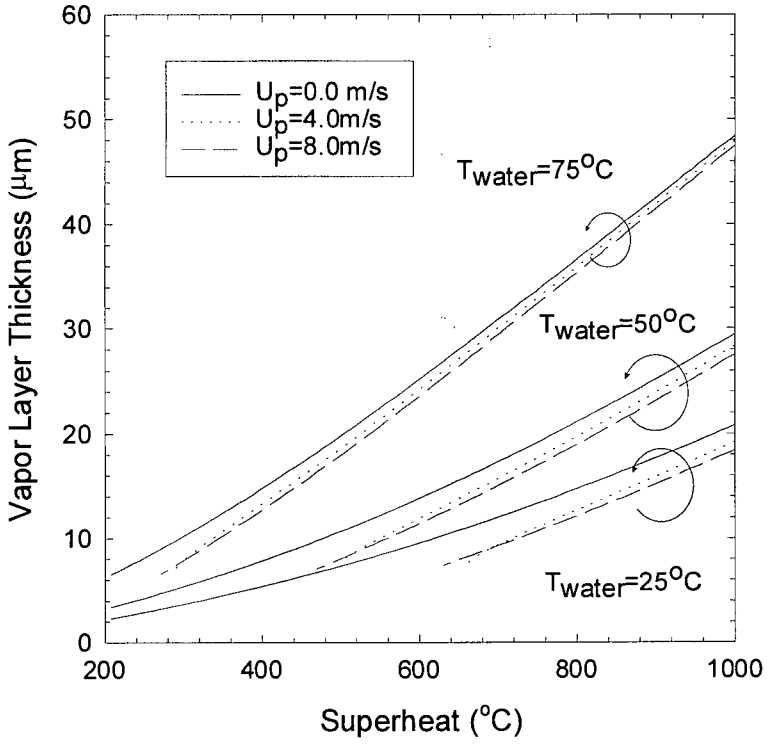

[b]

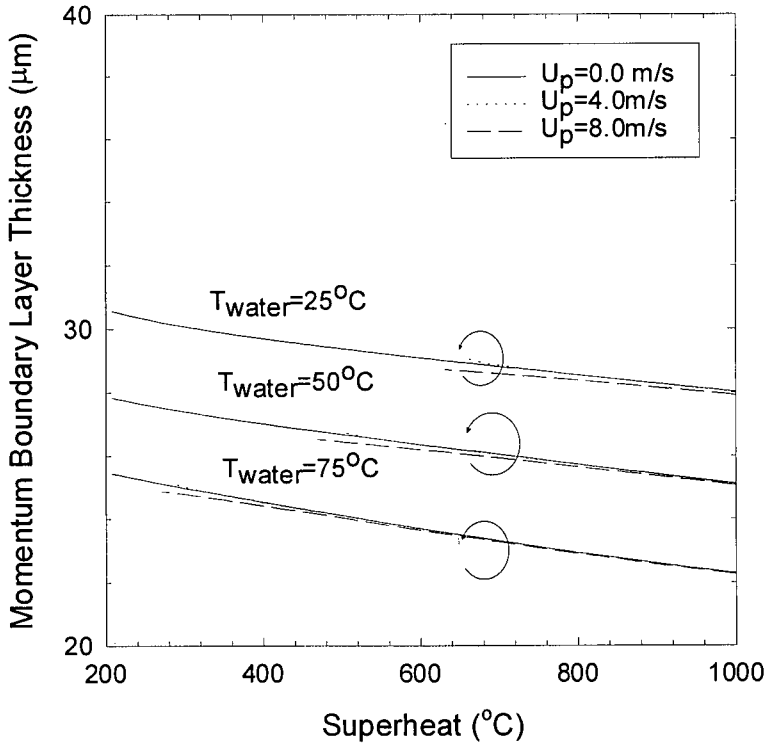

Figure 7.7: Model predictions during the typical operation of Company C of: [a] Vapor layer thickness, [b] Momentum boundary layer thickness.

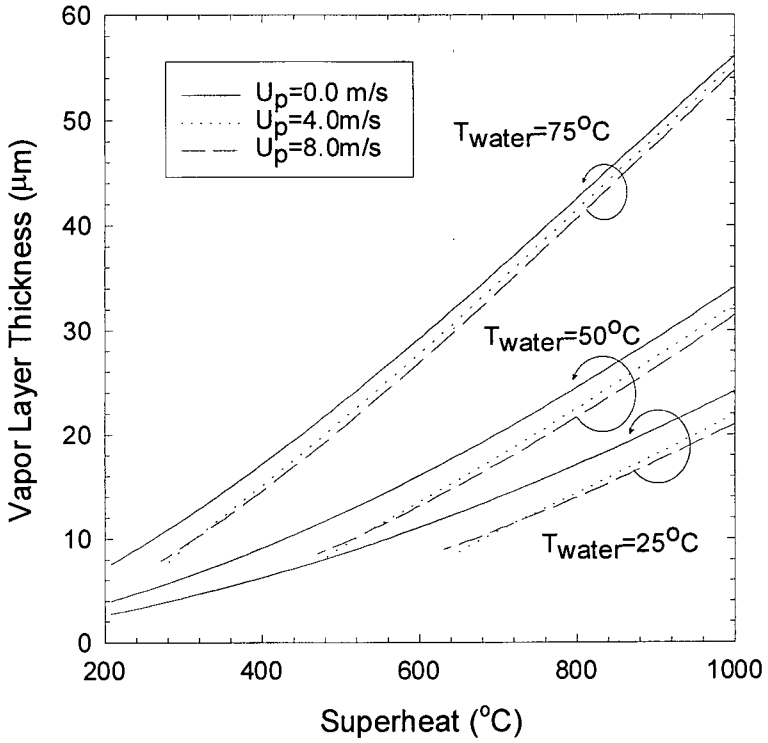

[a]

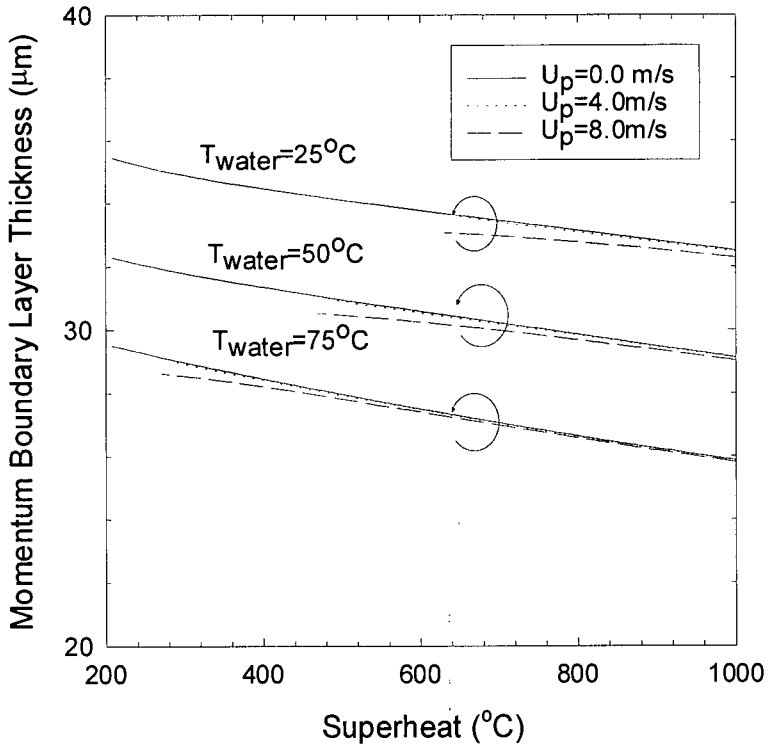

[b]

Figure 7.8: Model predictions for a planar water jet of: [a] Vapor layer thickness, [b] Momentum boundary layer thickness.

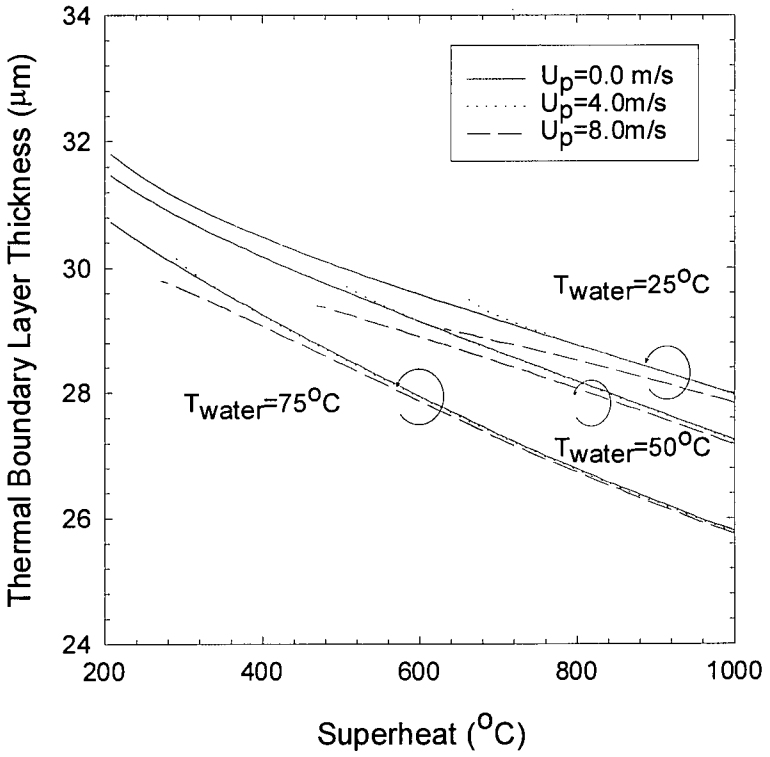

[a]

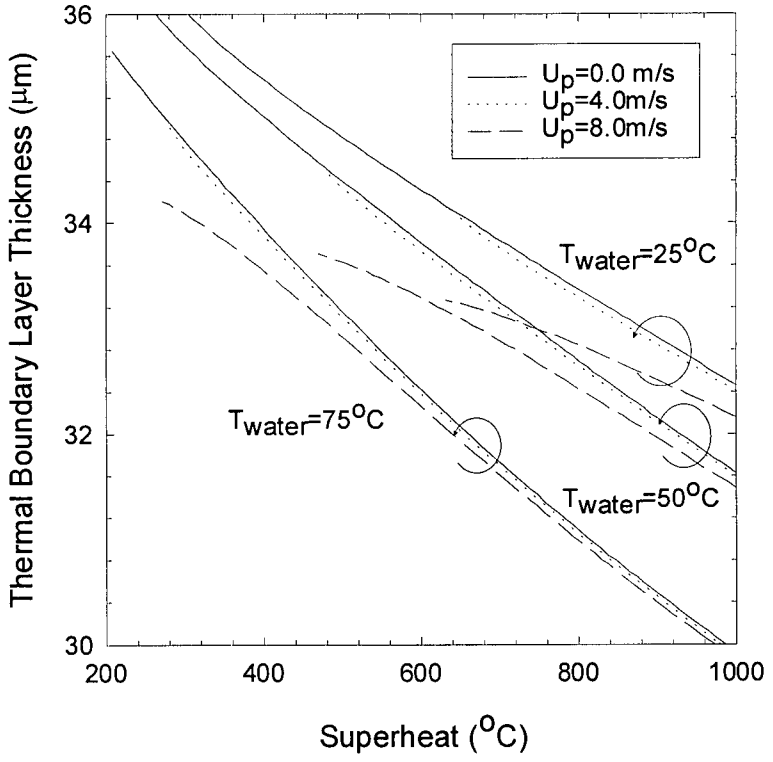

[b]

Figure 7.9: Model predictions of the thermal boundary layer thickness: [a] For water bars of Company C, [b] For a planar water jet

[a]

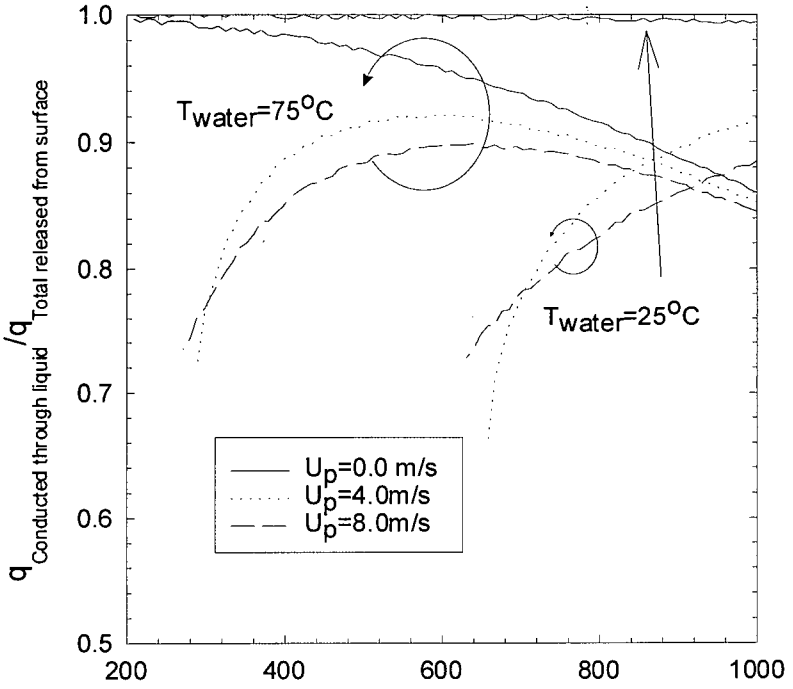

[b]

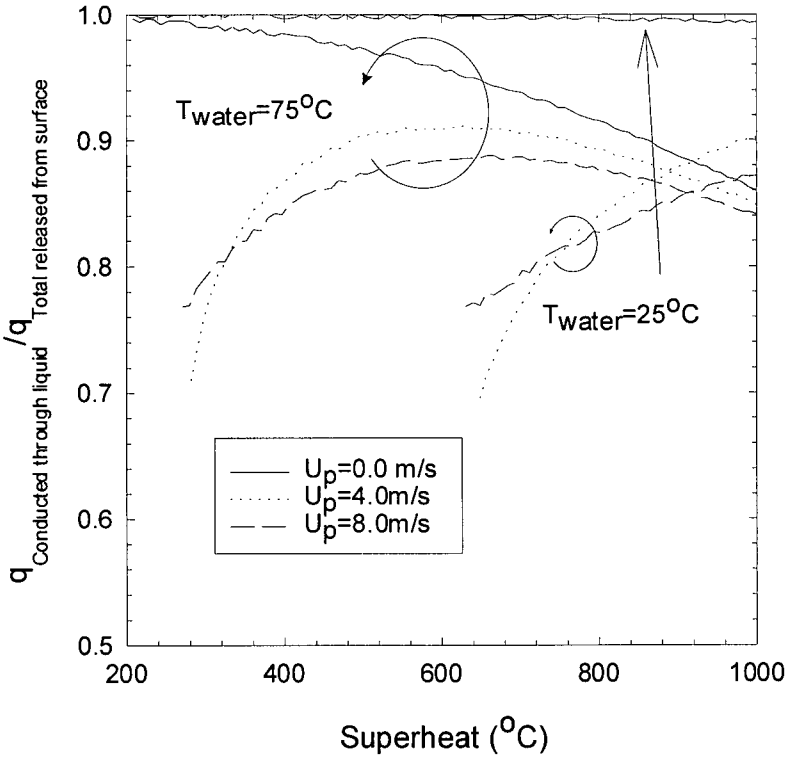

Figure 7.10: Model predictions of the fraction of the total heat released by the surface conducted through the liquid layer, for: [a] Water bars of Company C, [b] Planar water jet.

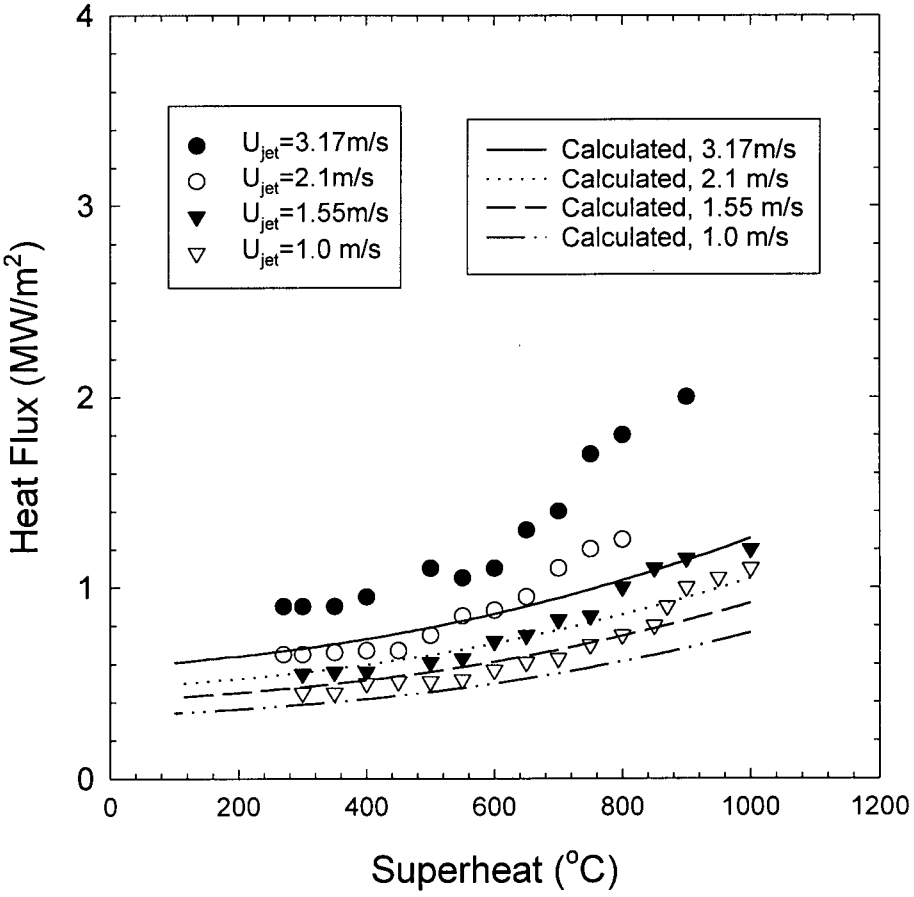

Figure 7.11: Comparison between model predictions and measurements for a planar jet shown in Figure 2.11[3], (T_{water}=85°C, w_{jet}=0.0062m)

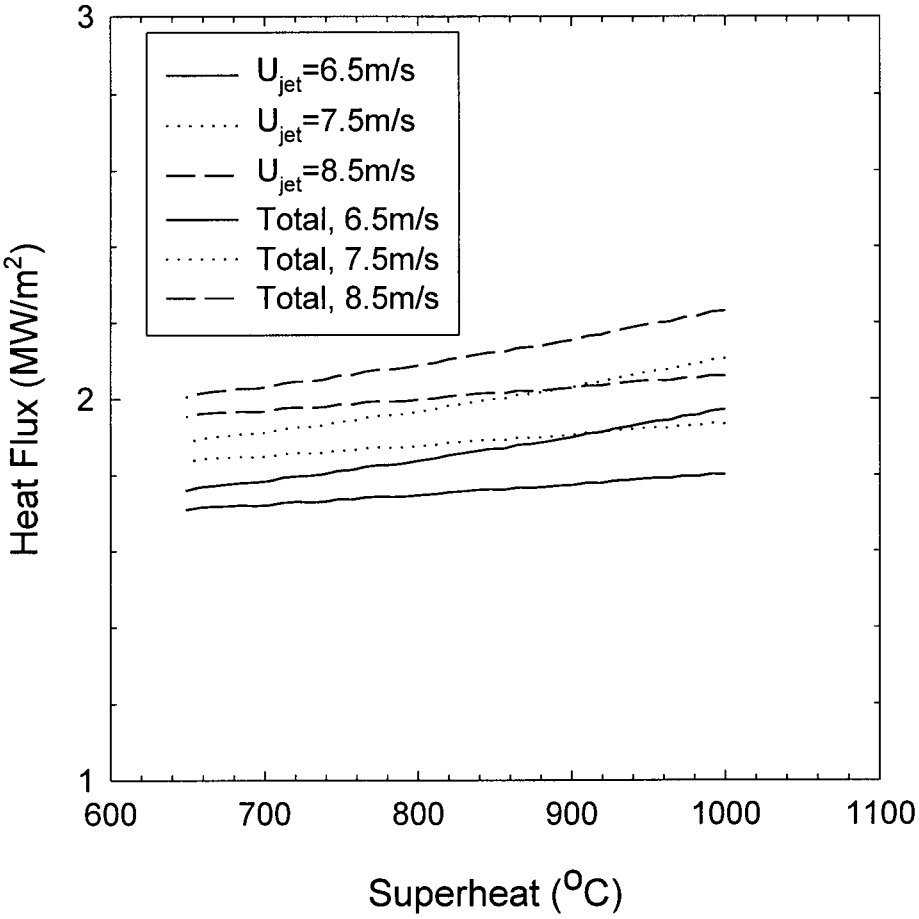

Figure 7.12: Effect of the impinging jet velocity of a water bar on the film boiling heat flux. (T_{water}=25°C, U_p=0m/s, d_{jet}=0.0186m).

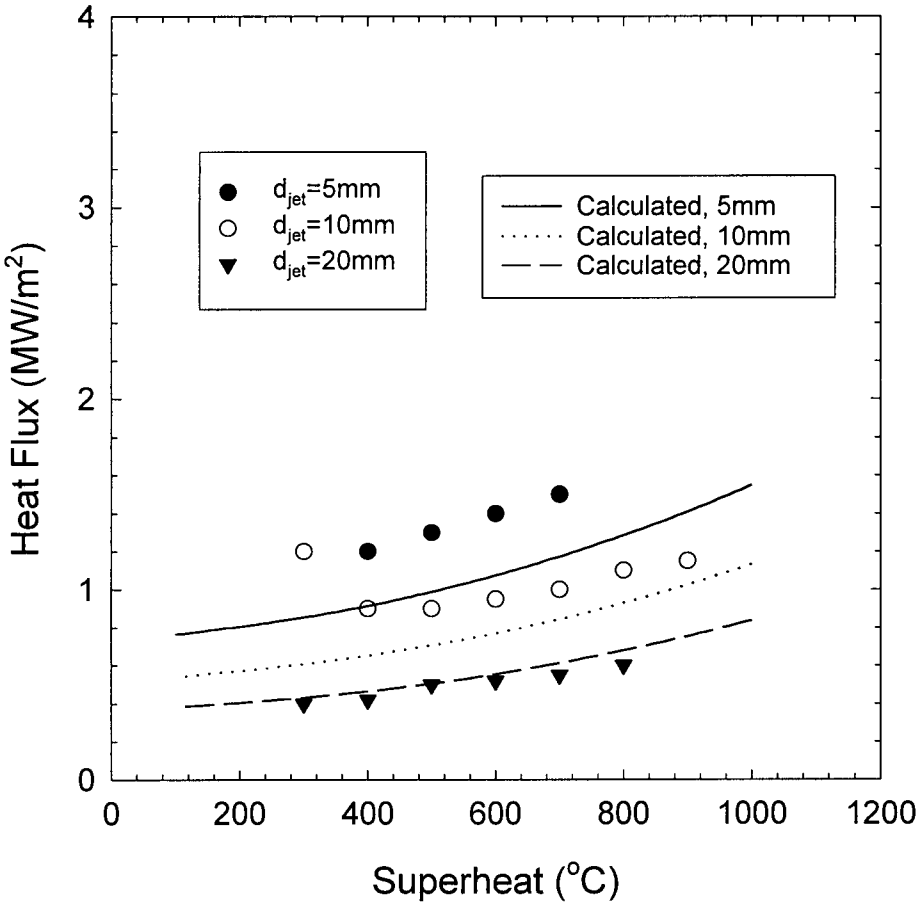

Figure 7.13: Comparison between the film boiling model predictions and measurements [1] for a water bar jet shown in Figure 2.6, (u_{jet}=3.0m/s, T_{water}=85°C).

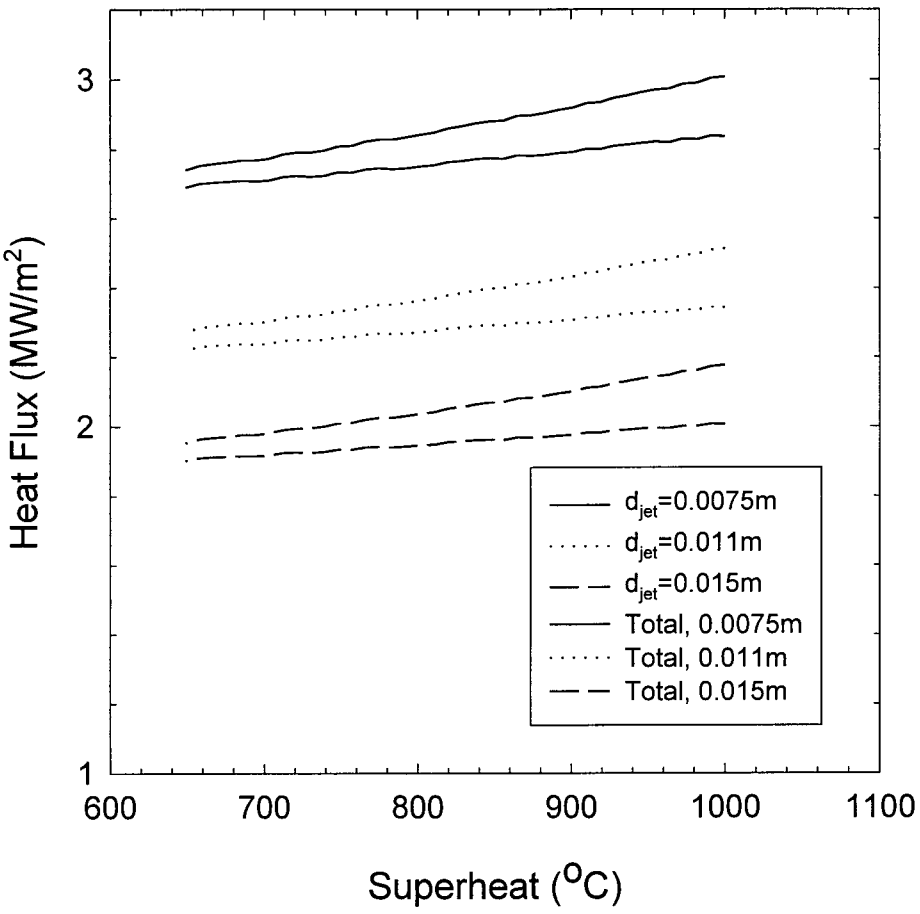

Figure 7.14: Effect of the impinging jet diameter of a water bar on the heat fluxes during film boiling, (T_{water}=25°C, U_p=0m/s, U_{jet}=6.5m/s).

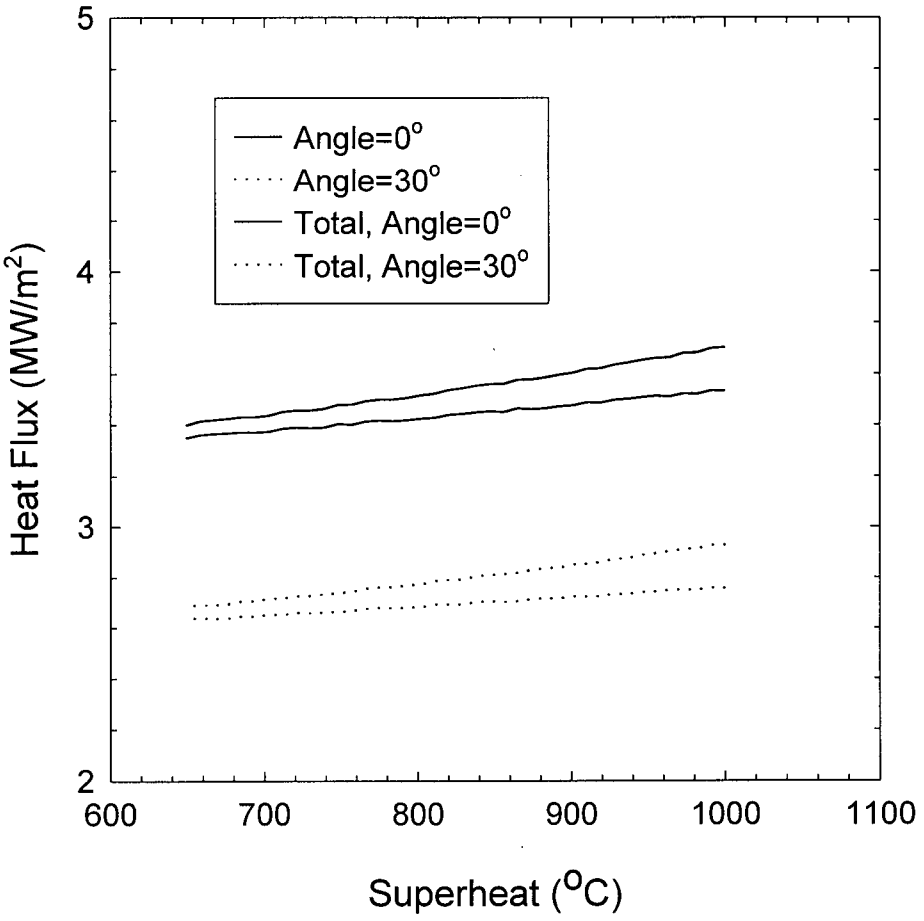

Figure 7.15: Effect of the impinging angle of a water planar jet on the heat fluxes during film boiling, (T_{water}=25°C, U_p=0m/s, d_{nozzle}=0.0186m, U_{jet}=6.78m/s).

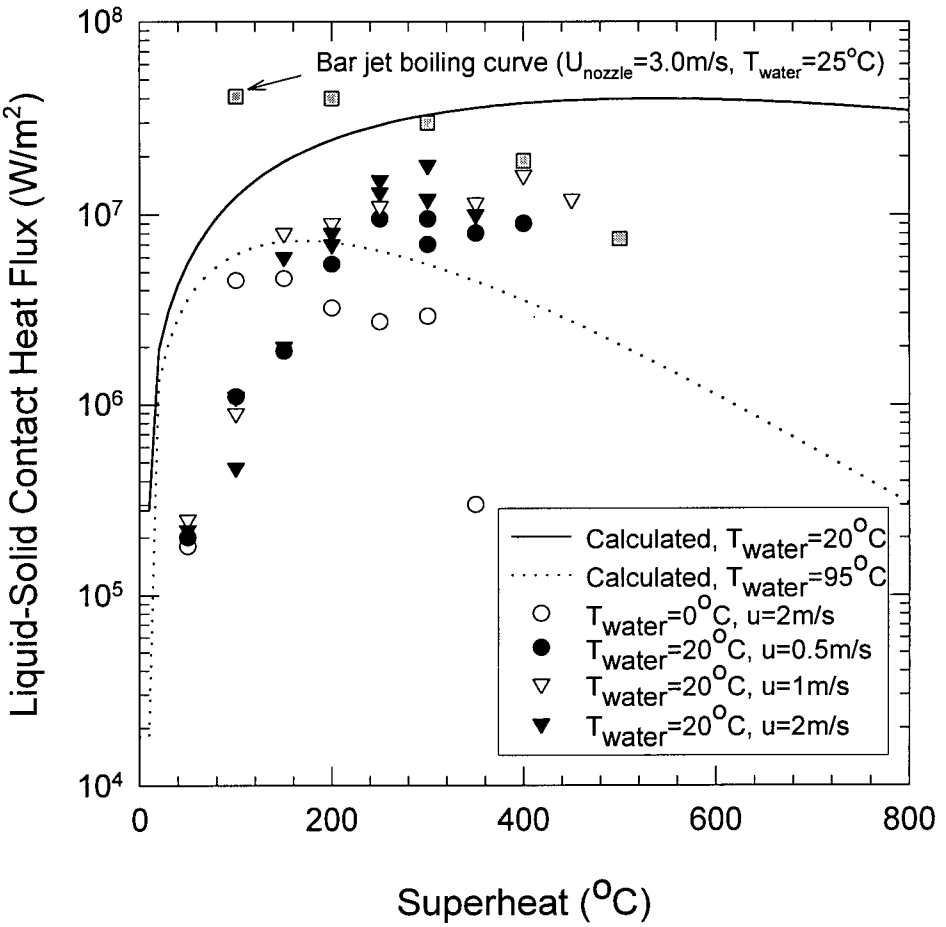

Figure 7.16: Comparison between the liquid-solid contact heat flux predicted for a planar jet with measurements for a falling drop[4] and a boiling curve of a bar jet.

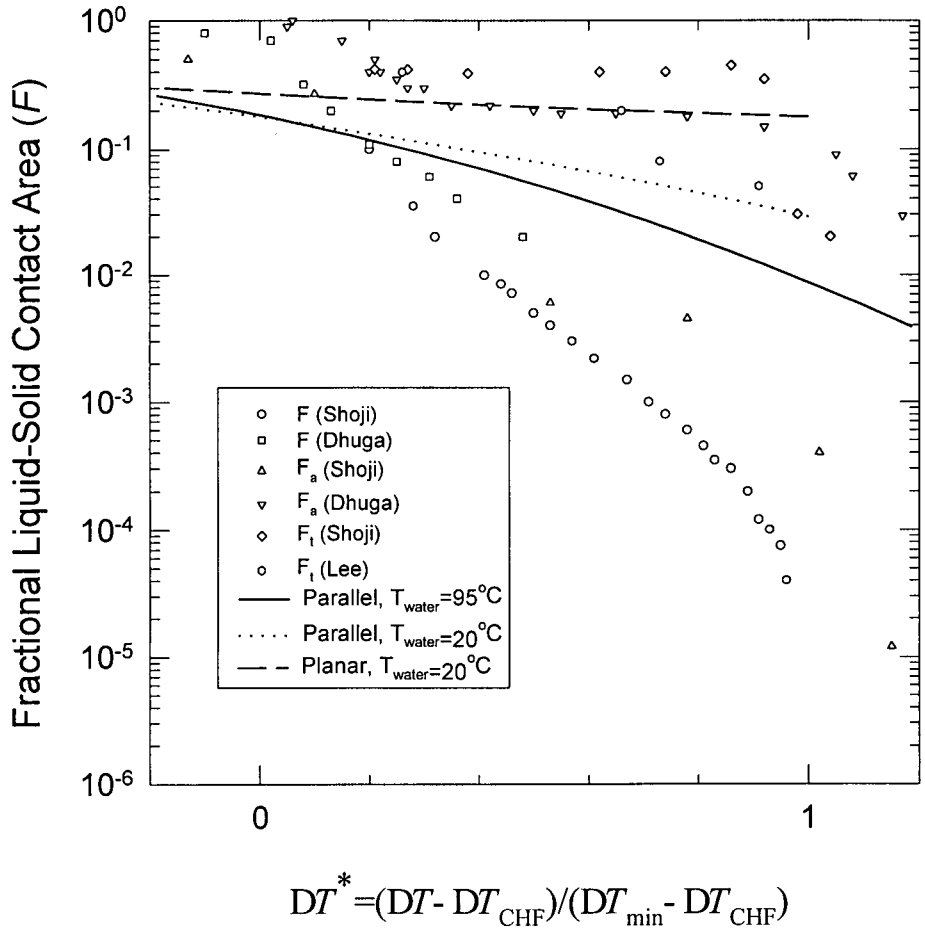

Figure 7.17: Comparison between the fractional liquid-solid contact area for the parallel and the impingement zones of a planar jet with saturated pool boiling measurements [6].

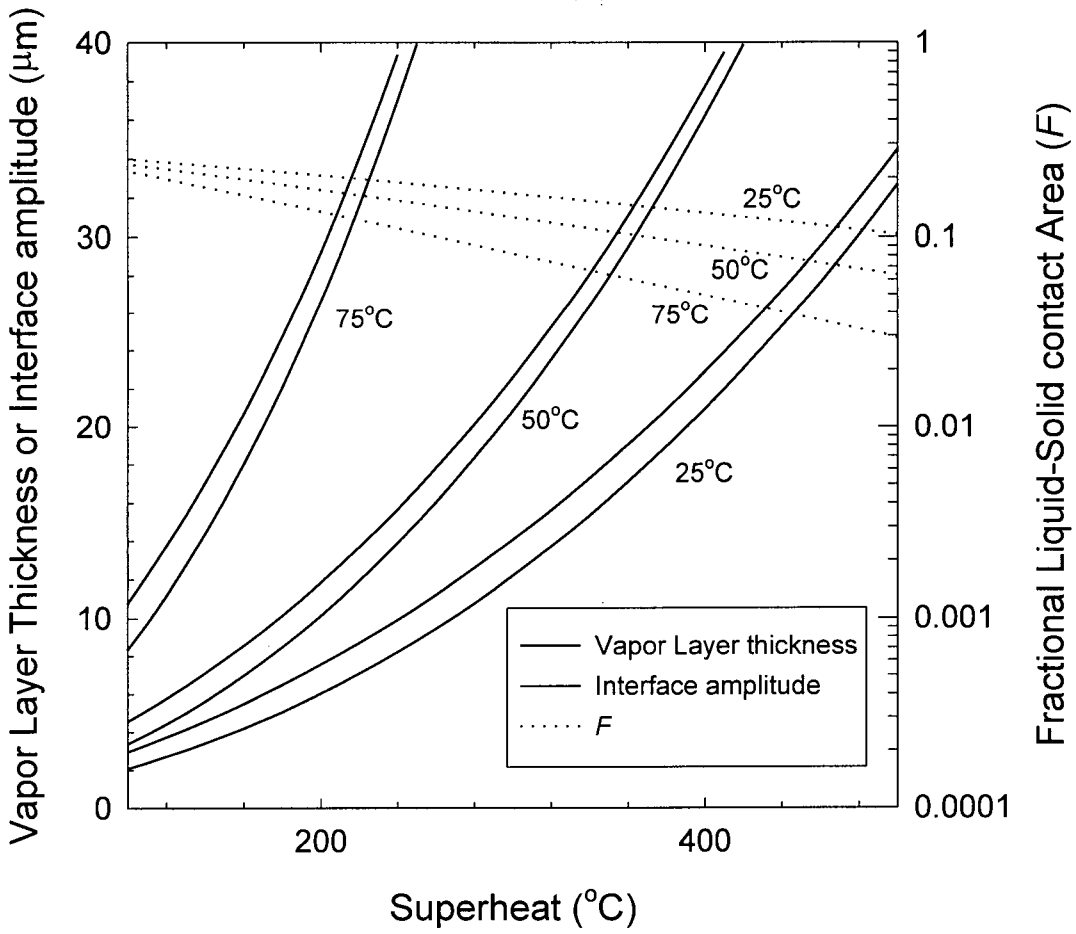

Figure 7.18: Predictions of the vapor layer thickness, interface amplitude and the fractional liquid-solid contact area for different water temperatures. Conditions: u_{water}=6.5m/s, u_p=0m/s

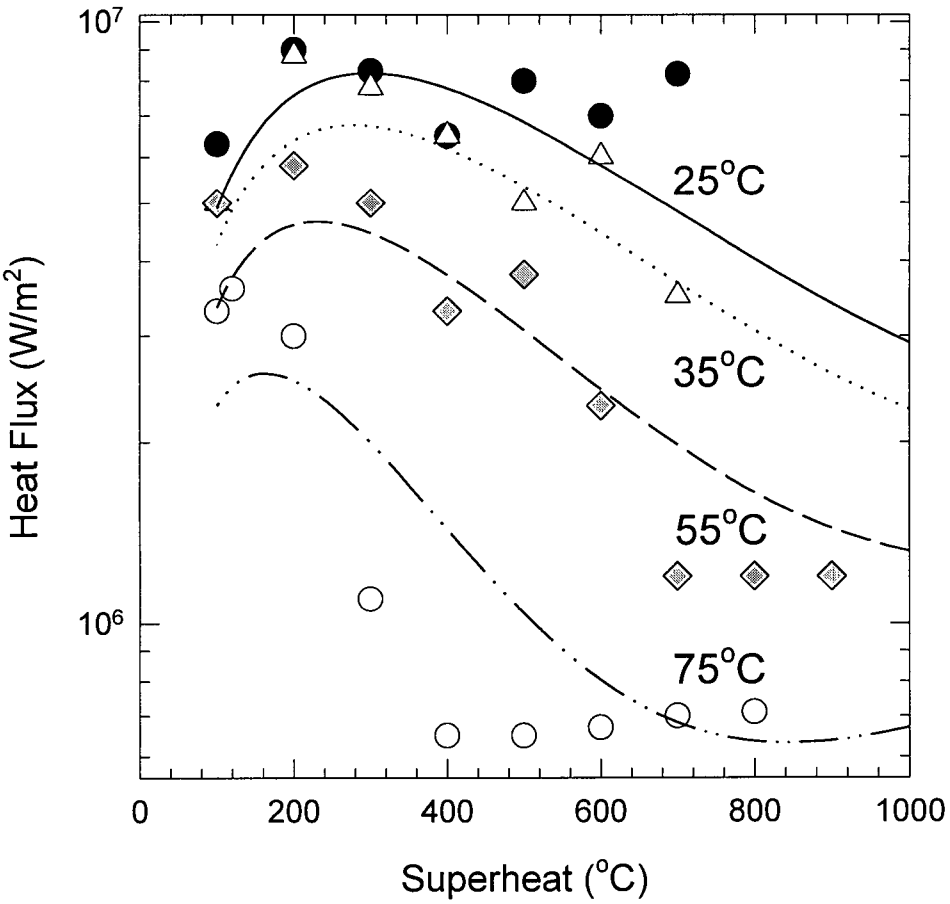

Figure 7.19: Effect of water temperature. Comparison between the transition boiling model predictions with the measurements [1] during the cooling with a water jet bar shown in Figure 2.5. Conditions: U_{jet}=3.0m/s, d_{nozzle}=0.020m, h_{nozzle}=0.025m.

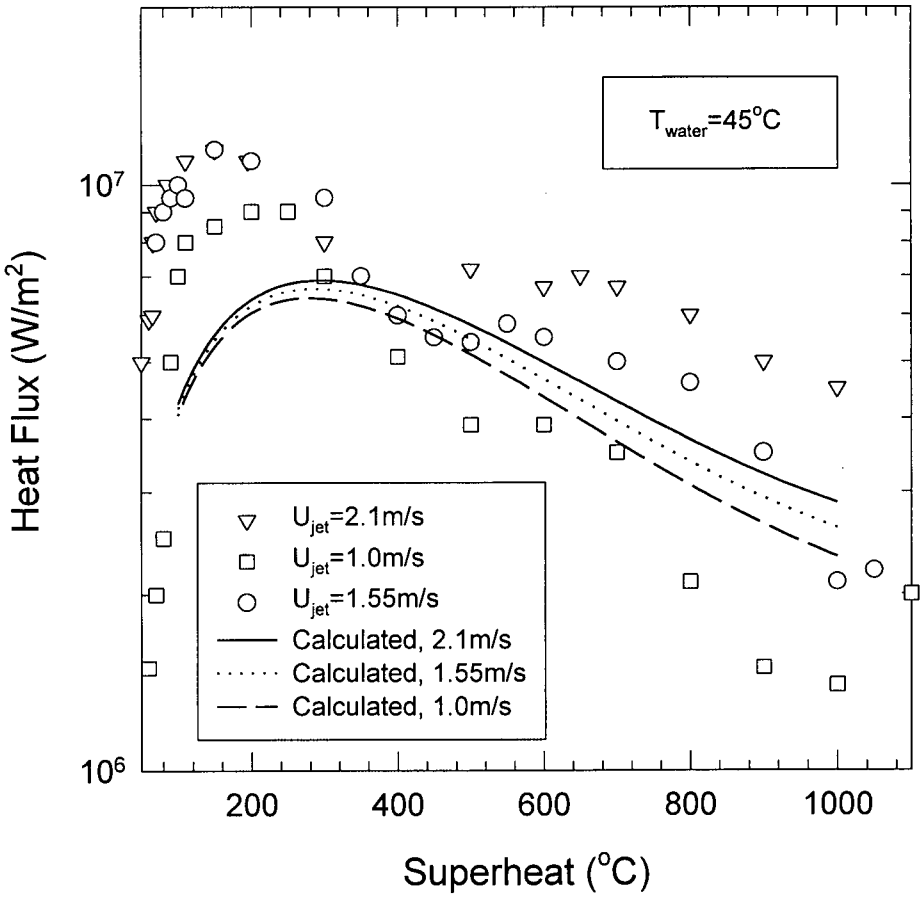

Figure 7.20: Effect of jet velocity. Comparison between the transition boiling model predictions with the measurements[3] during the cooling with a water planar jet shown in Figures 2.10 and 2.11. Conditions: T_{water}=45°C, w_{nozzle}=0.0062m.

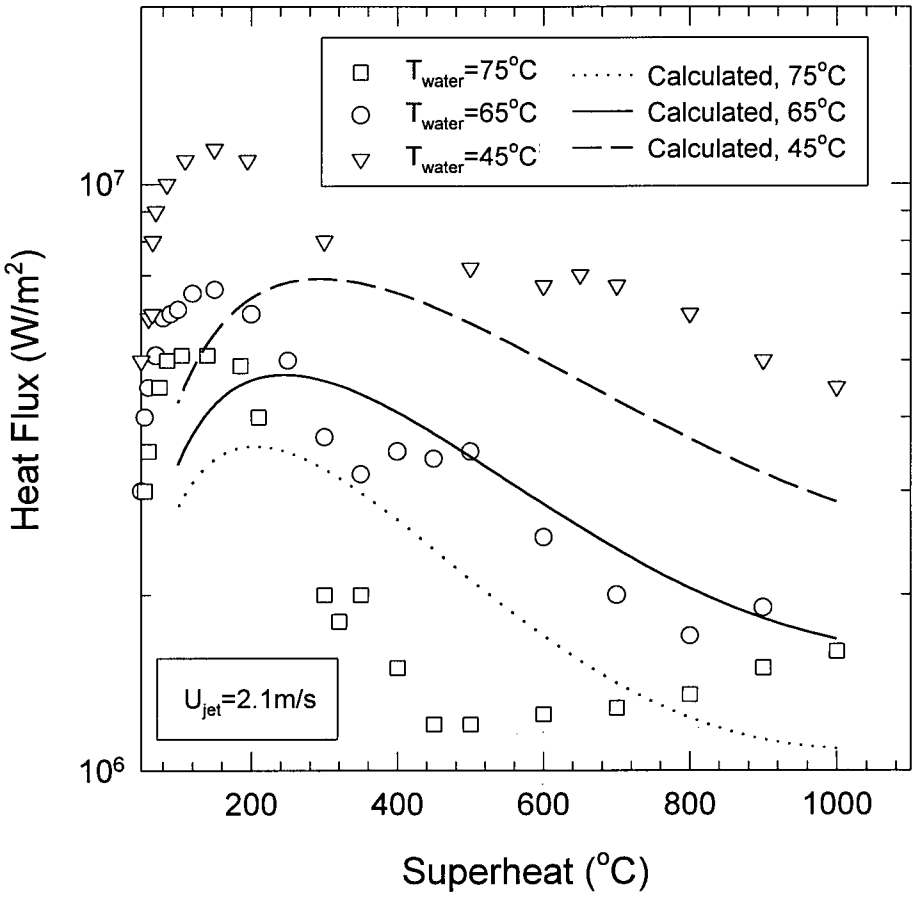

Figure 7.21: Effect of jet water temperature. Comparison between the transition boiling model predictions with the measurements during the cooling with a water planar jet shown in Figures 2.10. Conditions: U_{jet}=2.1m/s, w_{nozzle}=0.0062m.

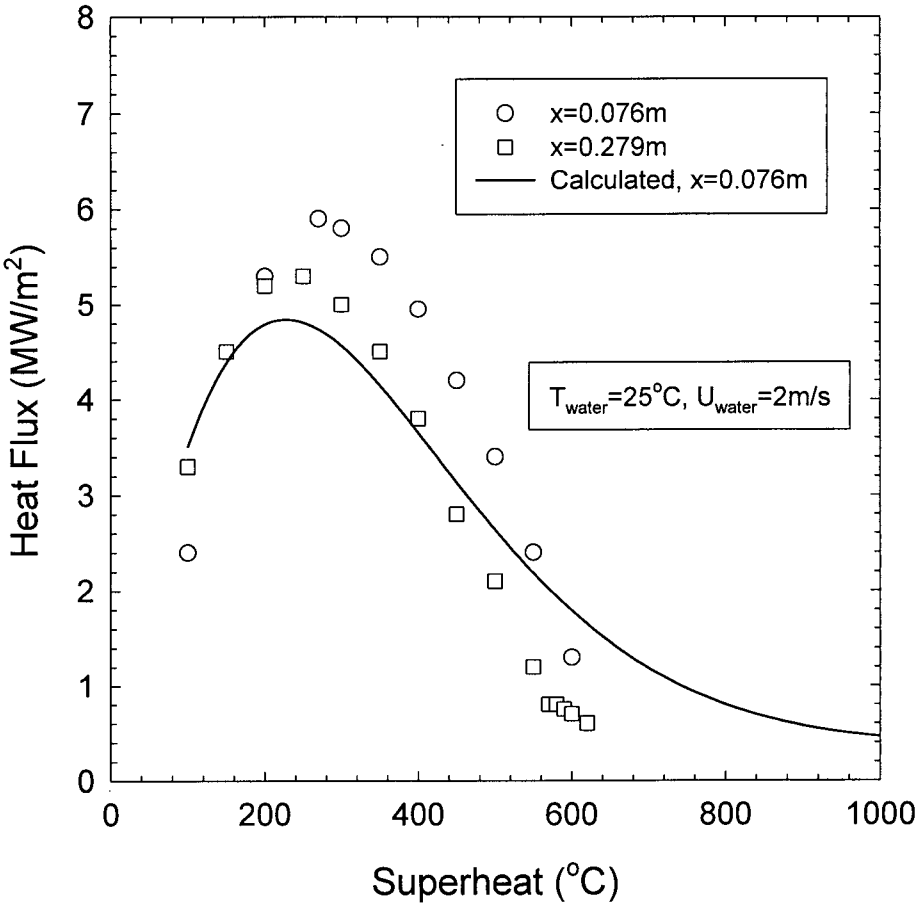

Figure 7.22: Comparison between model predictions and the measurements[13] during cooling in the parallel flow zone shown in Figure 2.16. Conditions: T_{water}=25°C, U_{water}=2m/s.

Table 7.1: Flow velocities during the experiments in pipe flow

Bulk Flow velocity (m/s)	Maximum velocity (m/s)
6.8	10.2
4.8	7.2
2.8	4.2

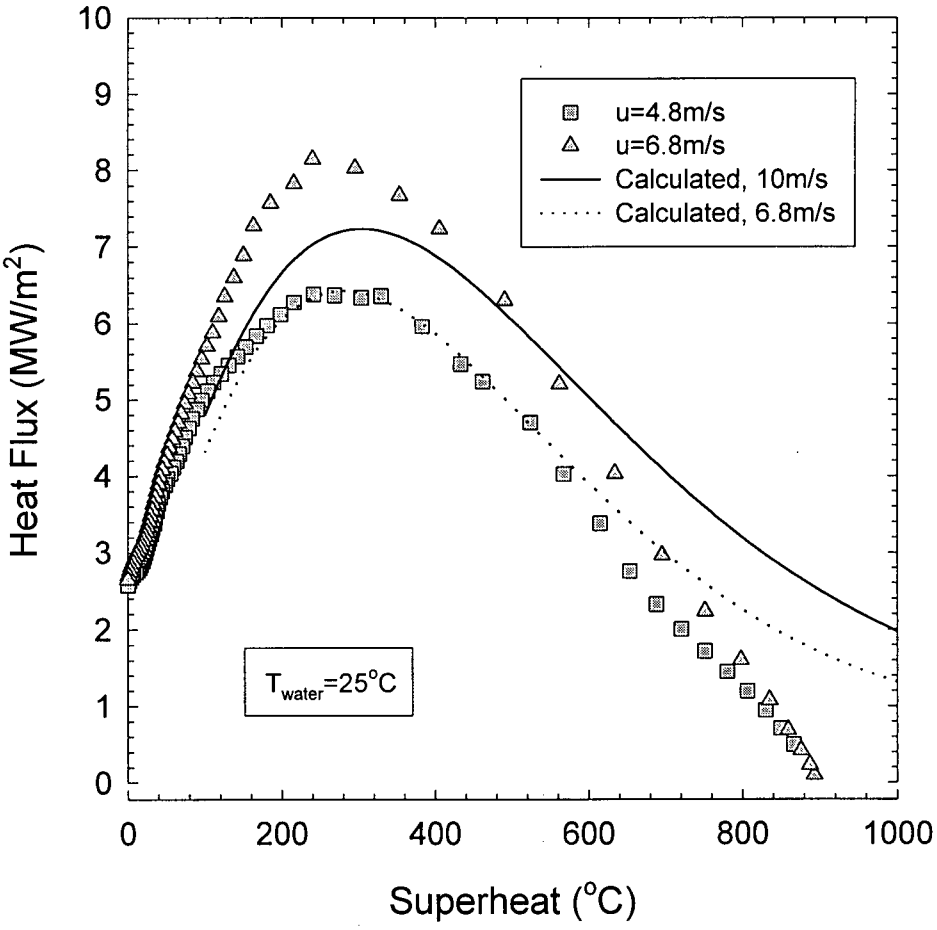

Figure 7.23: Comparison between model predictions for parallel flow and the measurements[14] during forced convective boiling on a steel bar in a pipe shown in Figure 2.18. T_{water}=25°C.

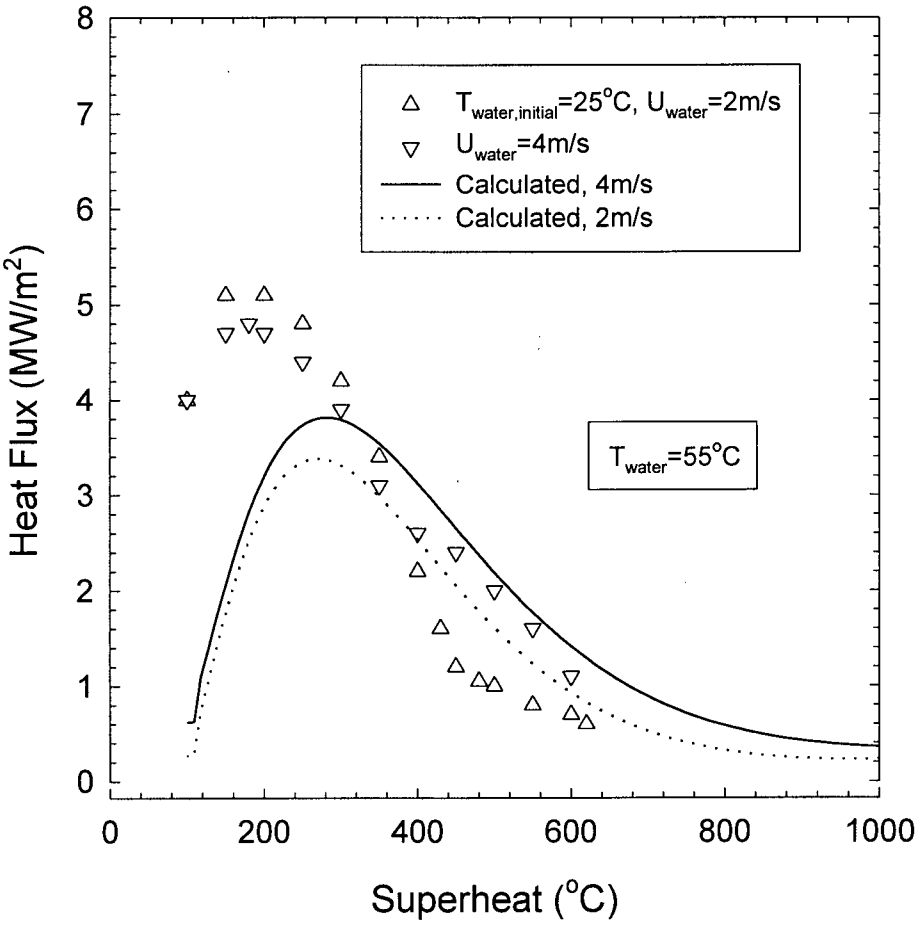

Figure 7.24: Comparison between model predictions and the measurements[13] during cooling in the parallel flow zone shown in Figure 2.16. Conditions: T_{water}=55°C.

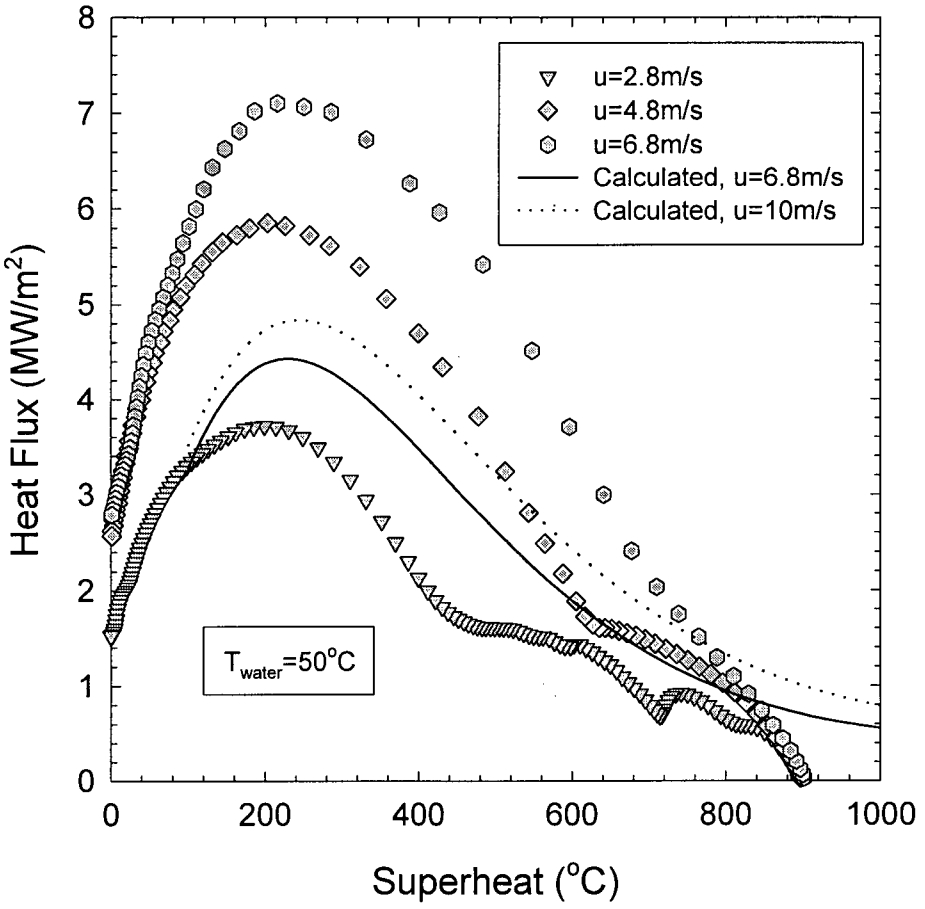

Figure 7.25: Comparison between model predictions for parallel flow and the measurements[14] during forced convective boiling on a steel bar in a pipe shown in Figure 2.18. T_{water}=50°C.

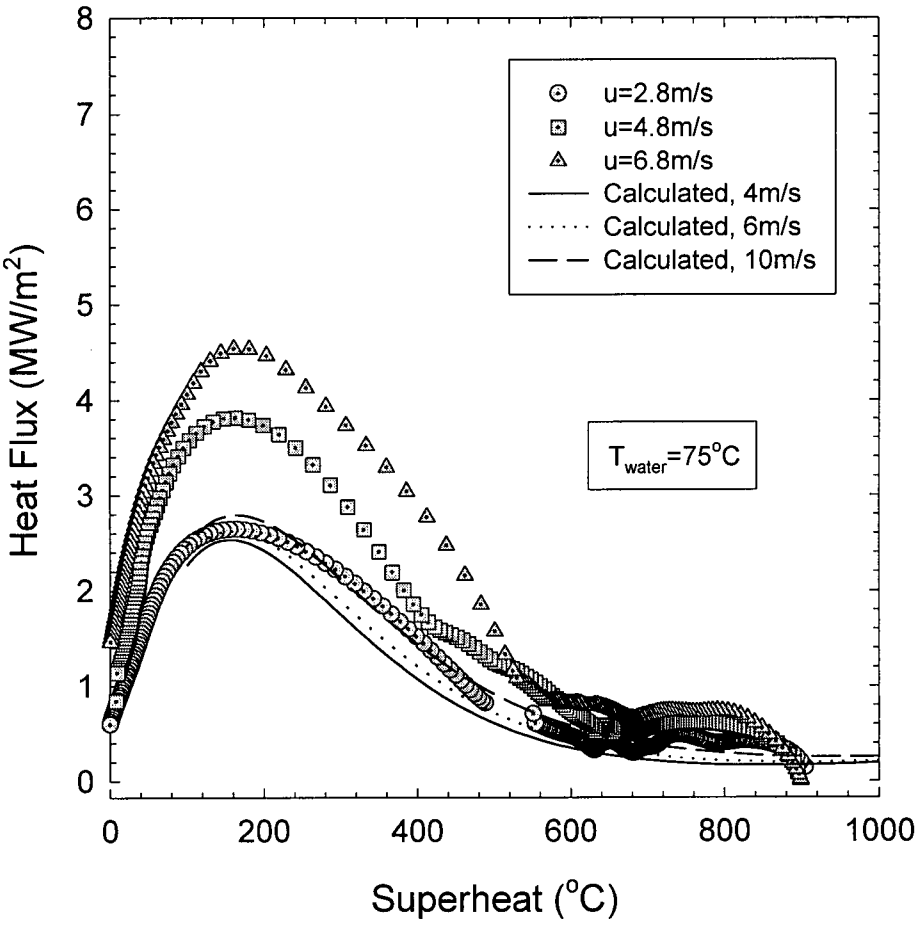

Figure 7.26: Comparison between model predictions for parallel flow and the measurements[14] during forced convective boiling on a steel bar in a pipe shown in Figure 2.18. T_{water}=75°C.

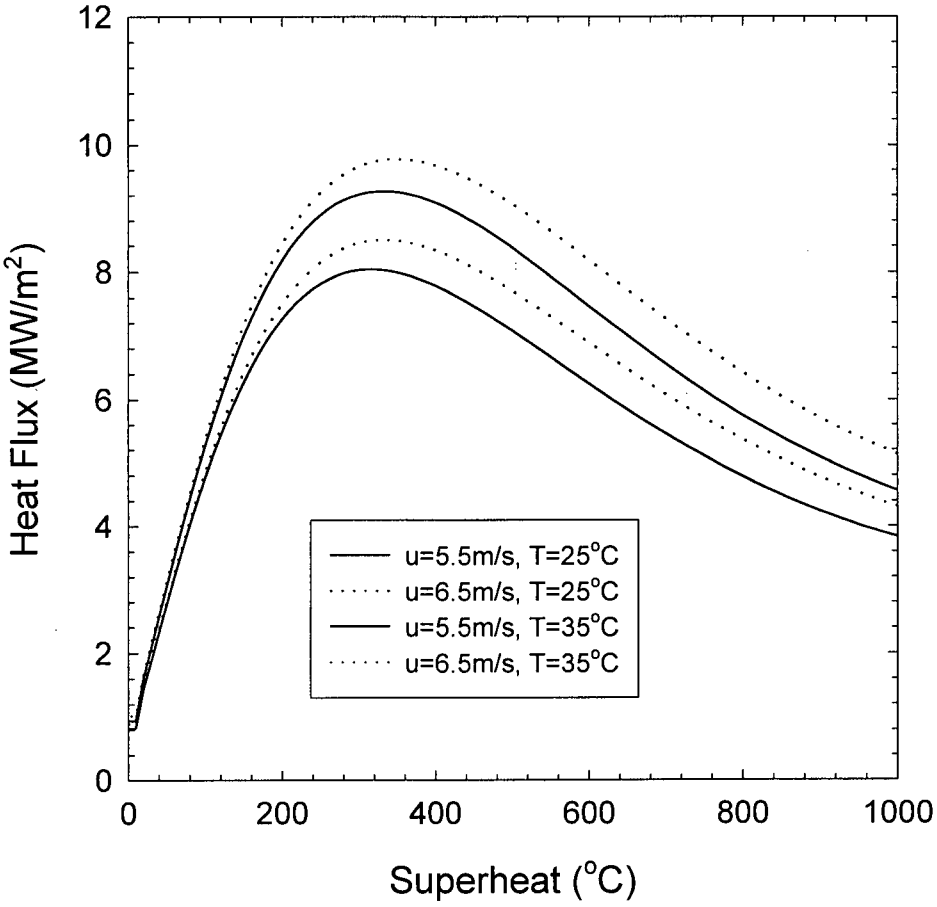

Figure 7.27: Model predictions of the boiling curves in the impingement region of water bars under typical operating conditions of the full scale runout table.

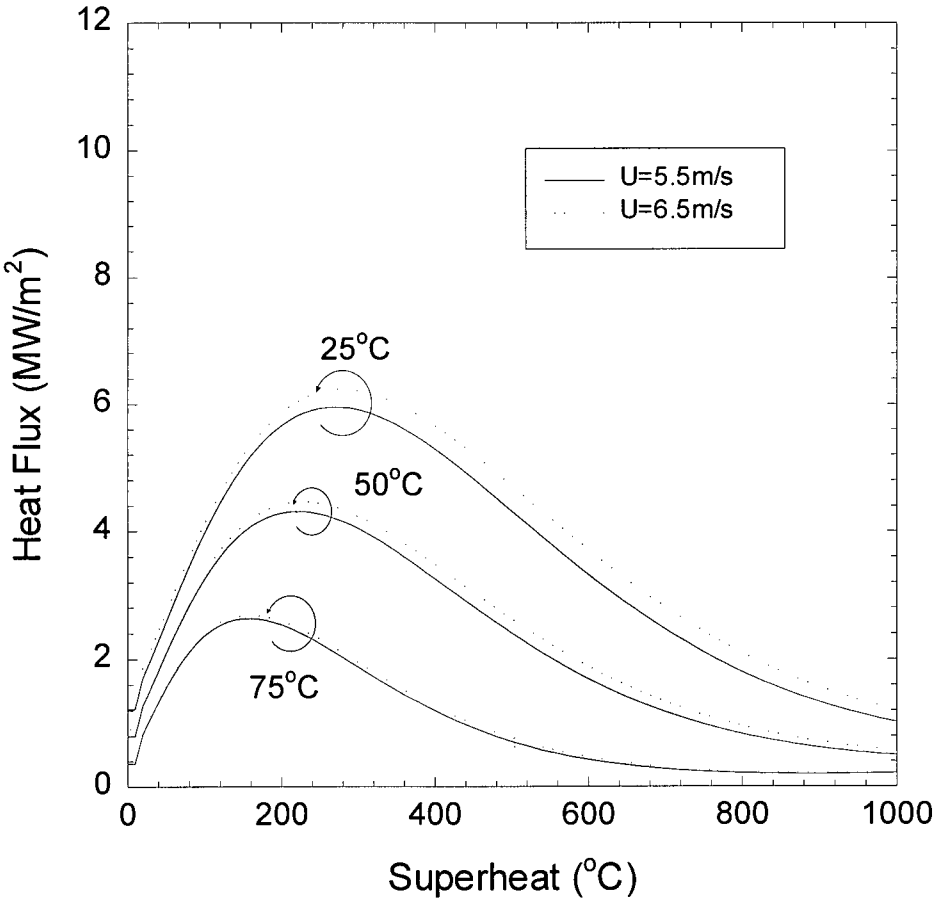

Figure 7.28: Predictions of the boiling curves for the parallel flow region under typical conditions of the runout table.

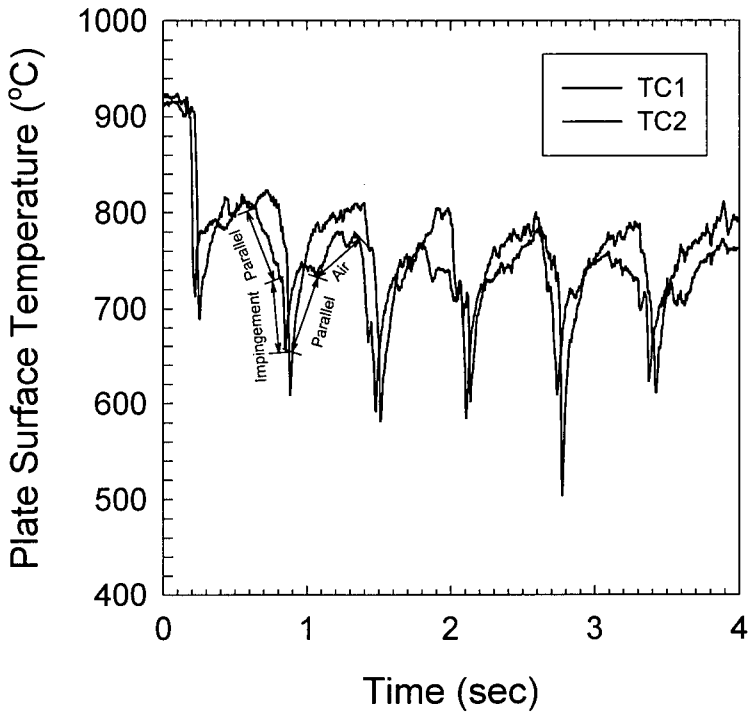

[a]

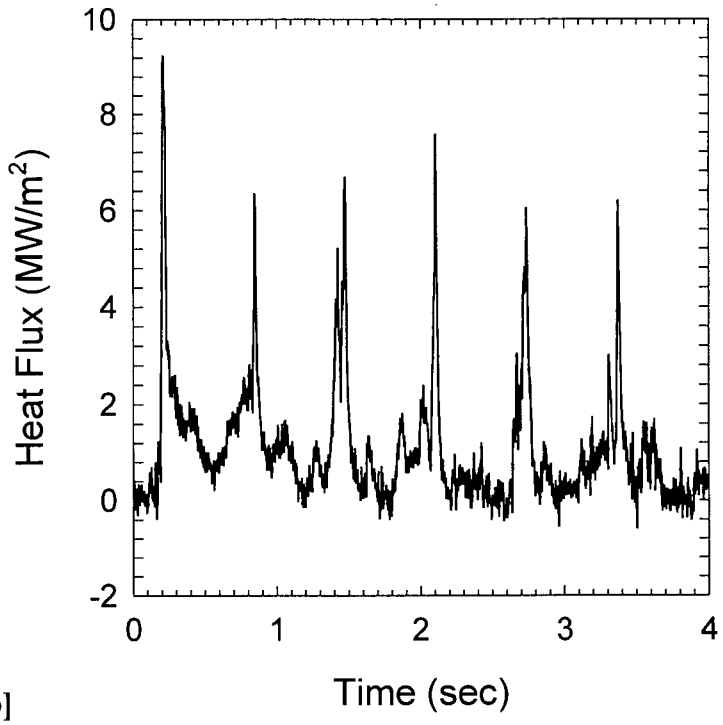

[b]

Figure 7.29: Measurements during cooling of a moving plate of: [a] Surface temperature, [b] Heat flux.

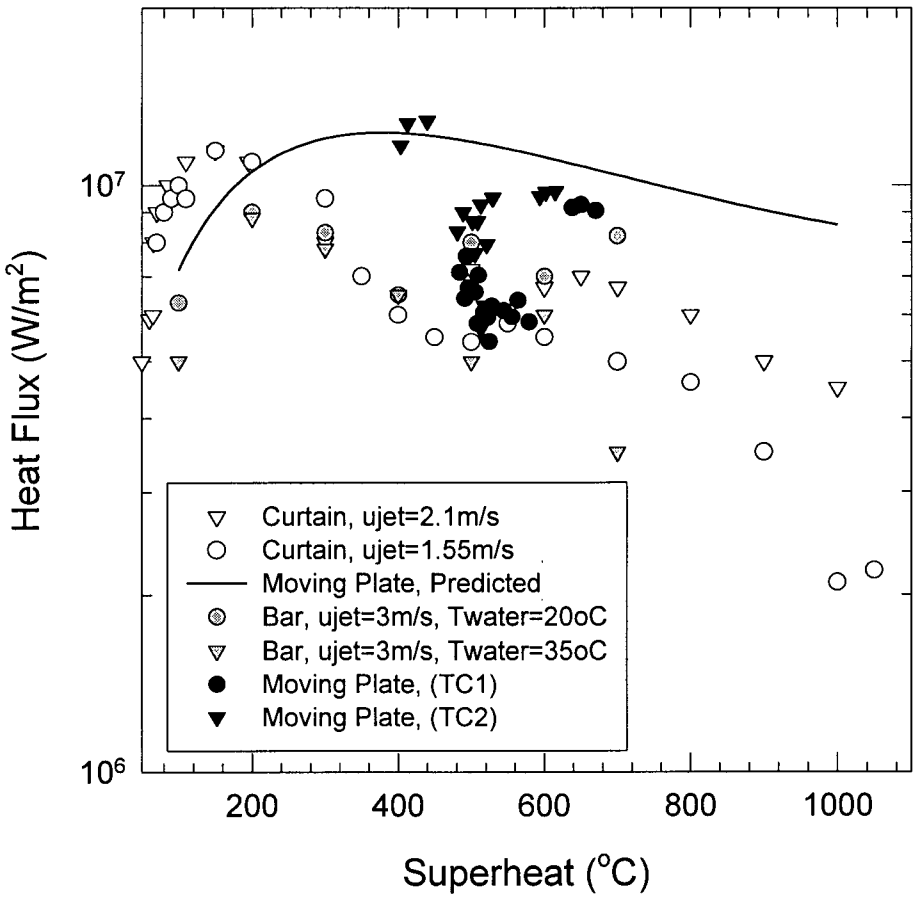

Figure 7.30: Comparison between the measured boiling curve for the impingement region of a planar jet impinging on a moving plate with measurements in other systems [13] and the transition boiling model predictions. Moving plate conditions (u_{jet}=4.6m/s, T_{water}=24°C, u_p=1.45m/s)

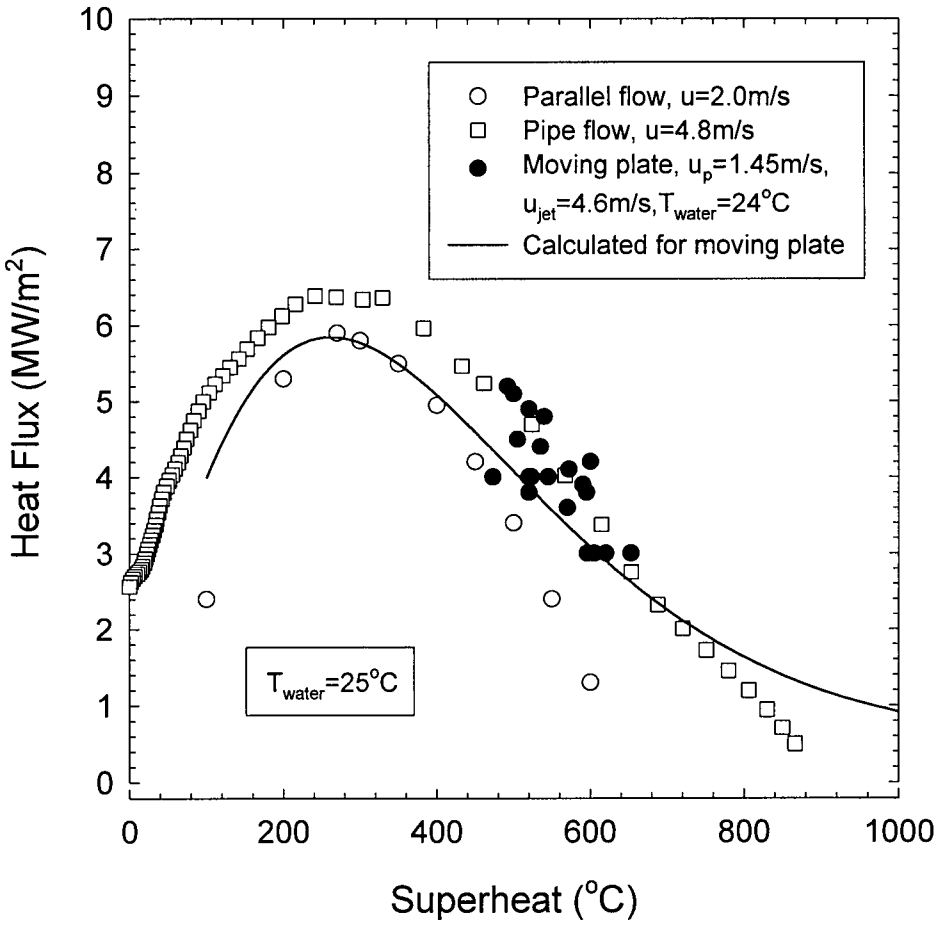

Figure 7.31: Comparison between the measured boiling curve for the parallel flow region of a moving plate with measurements[13,14] in other systems and the transition boiling model predictions. Moving plate conditions (u_{jet}=4.6m/s, T_{water}=24°C, u_p=1.45m/s)

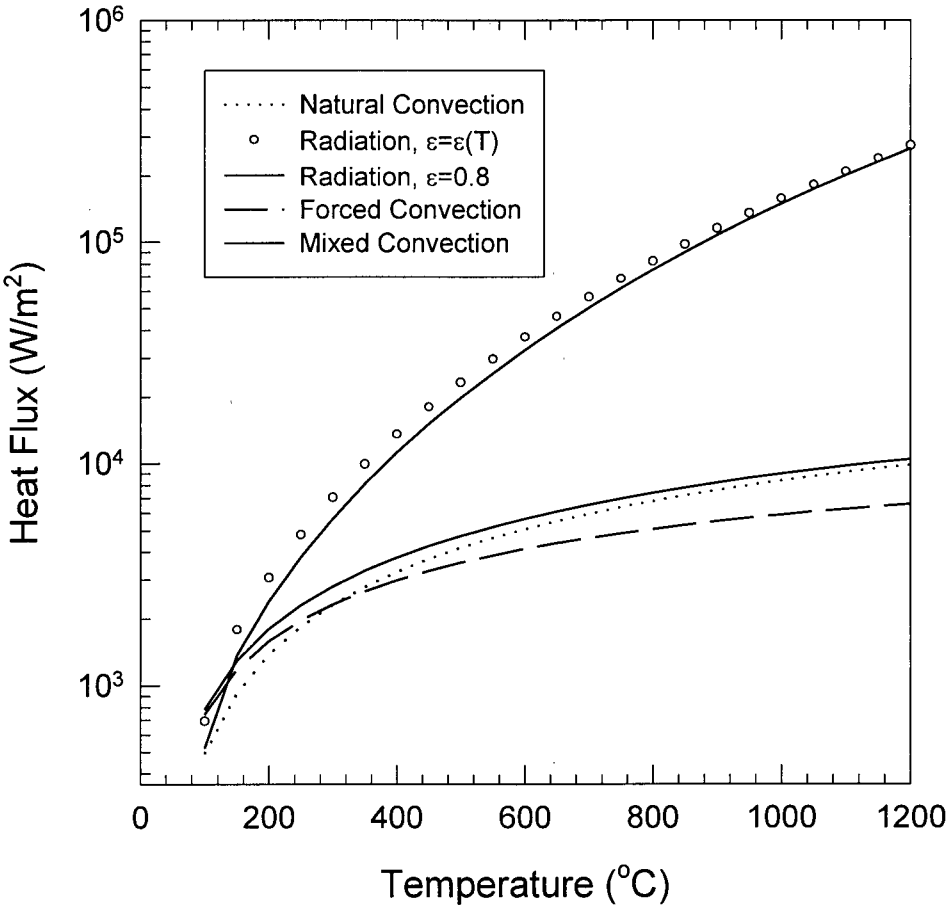

Figure 7.32: Contribution of the different cooling mechanisms during cooling in air. Conditions: u_{air}=2.0m/s, T_{air}=25°C, u_{strip}=4.0m/s, L=10.0m.

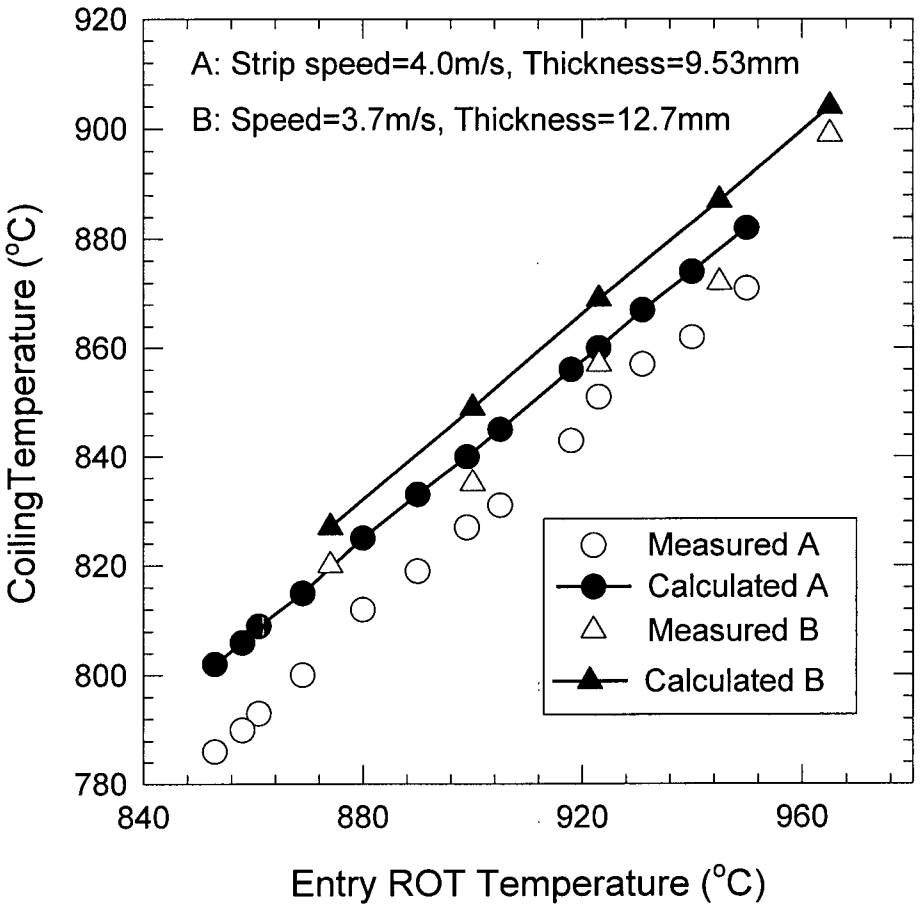

Figure 7.33: Comparison between the runout table model predictions with measurements of the coiling temperature for the air cooled A36 strips of 9.53 and 12.7mm thickness.

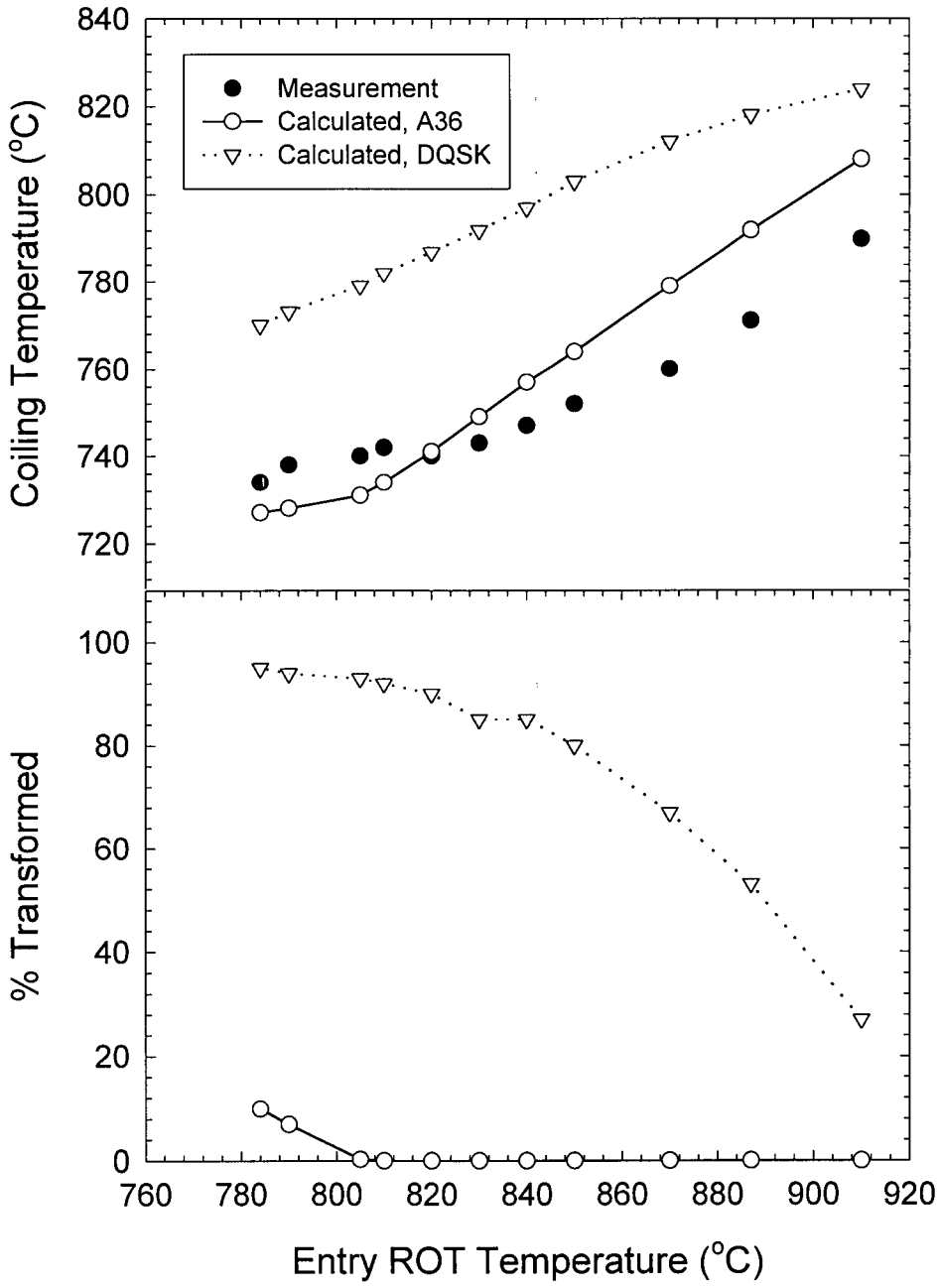

Figure 7.34: Comparison between the runout table model predictions assuming nominal A36 and DQSK chemistries with measurements of the coiling temperature for the air cooled A36 strips (4.72mm thickness), and the corresponding austenite percent transformed.

Table 7.2: Roll parameters for roll cooling calculations

Parameter	Value	Units
Distance between rolls	0.61	m
Diameter of the rolls	14	in
Thickness of the rolls	0.03175	m
Temperature of the rolls	25	°C
Heat Transfer coefficient	5000	$W/m^2°C$
Number of rolls	91	unit

Table 7.3: Predictions of the maximum effect of the runout table rolls chilling on the steel strip for different operating conditions

		Strip Temperature					
		760°C		860°C		960°C	
Thickness	**Speed**	**ΔT in strip**	**Heat flux**	**ΔT in strip**	**Heat flux**	**ΔT in strip**	**Heat flux**
mm	m/s	°C/roll	MW/m^2	°C/roll	MW/m^2	°C/roll	MW/m^2
Company G conditions							
4.72	4.2	0.096	3.40	0.117	3.87	0.144	4.35
9.53	4.0	0.073	3.39	0.081	3.86	0.090	4.34
12.70	3.7	0.090	3.37	0.099	3.84	0.108	4.32
Estimated for Company G conditions							
2.00	5.0	0.869	3.35	1.128	3.80	1.482	4.26
Estimated for Company C conditions							
2.00	11.0	0.412	3.38	0.535	3.85	0.698	4.32
4.72	9.0	0.063	3.41	0.075	3.89	0.090	4.36
9.53	4.5	0.072	3.39	0.080	3.86	0.089	4.34
12.7	4.0	0.090	3.37	0.099	3.84	0.107	4.32

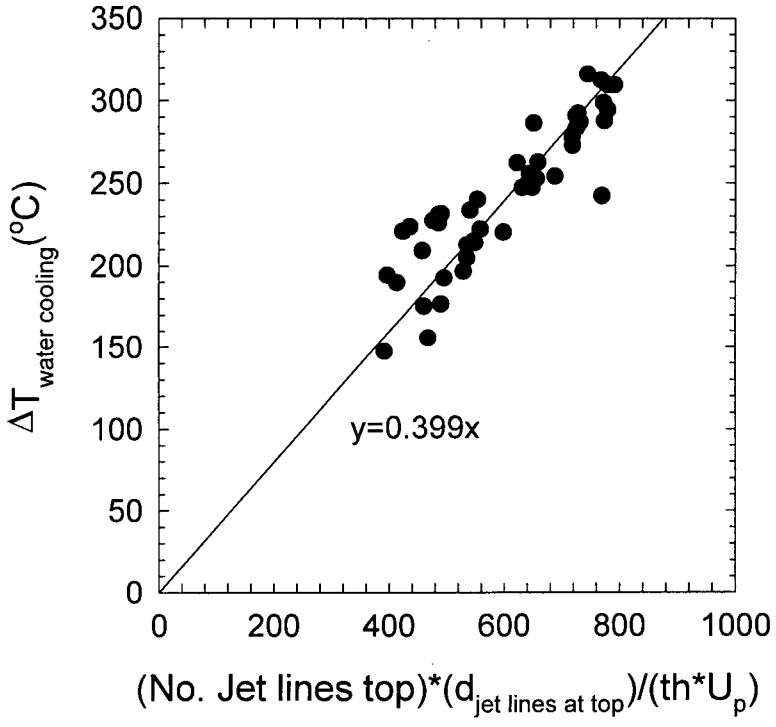

[a]

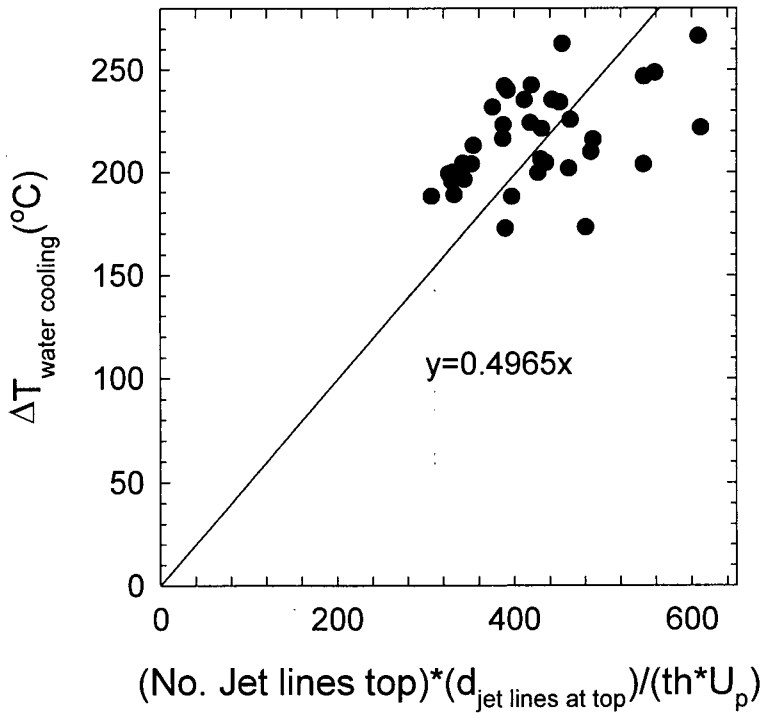

[b]

Figure 7.35: Correlation for the temperature drop in the strip during water cooling. Effect of steel chemistry for Company C: [a] DQSK, [b] A36.

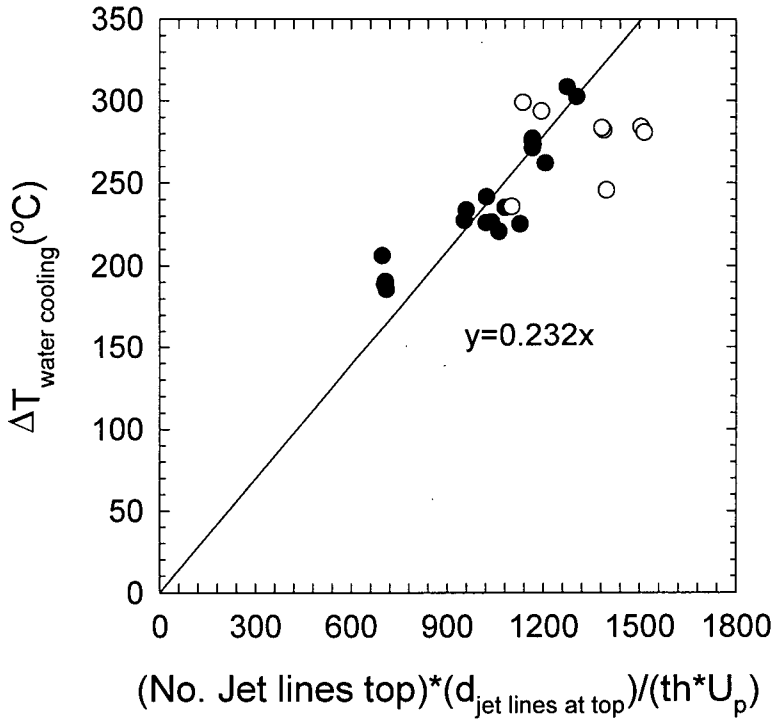

[a]

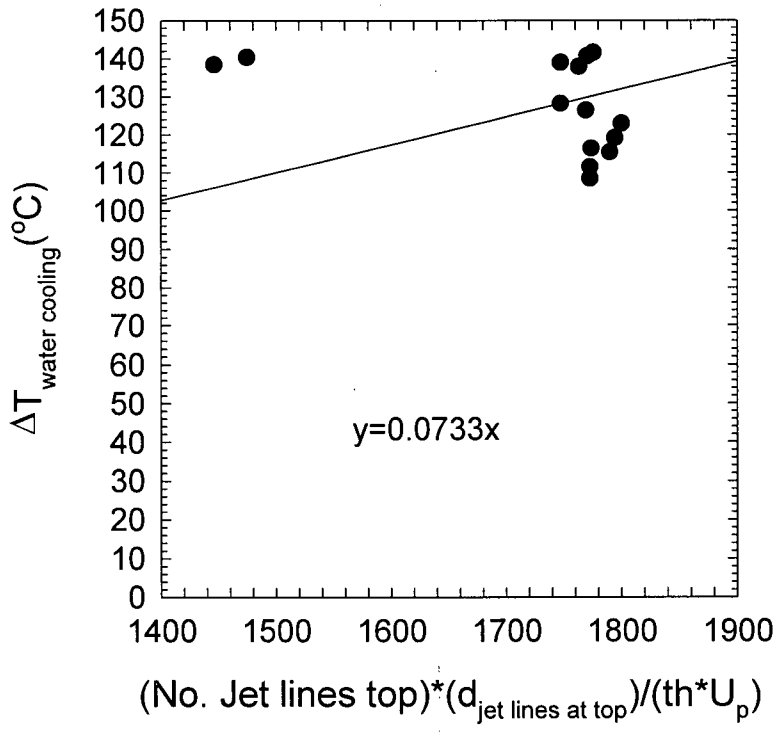

[b]

Figure 7.36: Correlation for the temperature drop in the strip during water cooling. Effect of laminar cooling configuration: [a] Company A (A36), [b] Company E (DQSK).

Table 7.4: Summary of the performance of different cooling systems

Company	Cooling system	Steel Grade	$d_{jetlines}$(m)	m (°Cm/s)	m'(°Cm^2/s)
C	Bars	A36	0.46	0.4965	0.228
C	Bars	DQSK	0.46	0.399	0.184
A	Bars	A36	0.69	0.232	0.160
E	Curtains	DQSK	3.20	0.0733	0.235

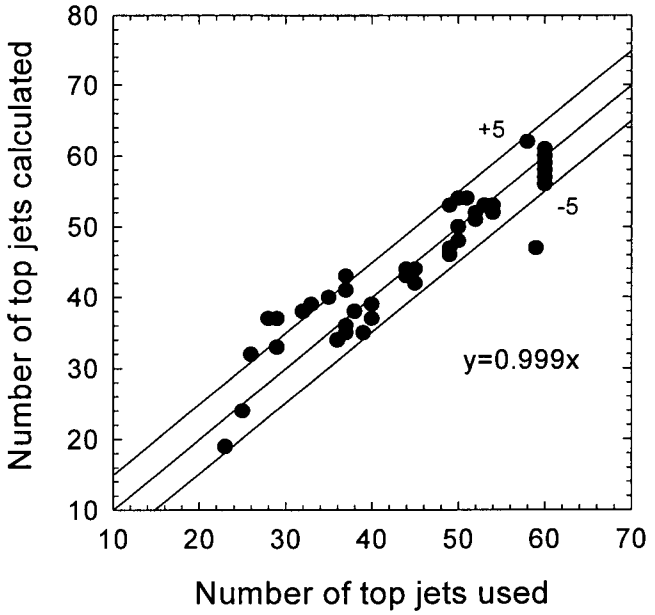

[a]

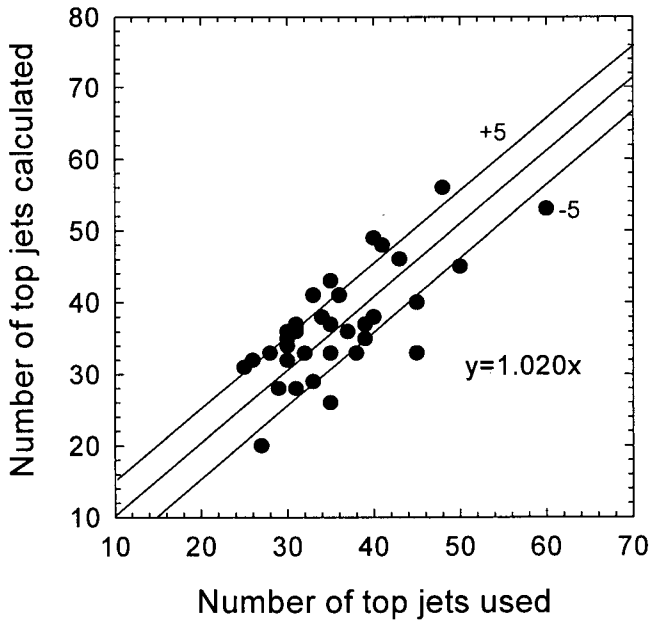

[b]

Figure 7.37: Comparison between the calculated number of top jets by Equation [7.2.2.3] and the actual used. Effect of chemistry for Company C: [a] DQSK, [b] A36.

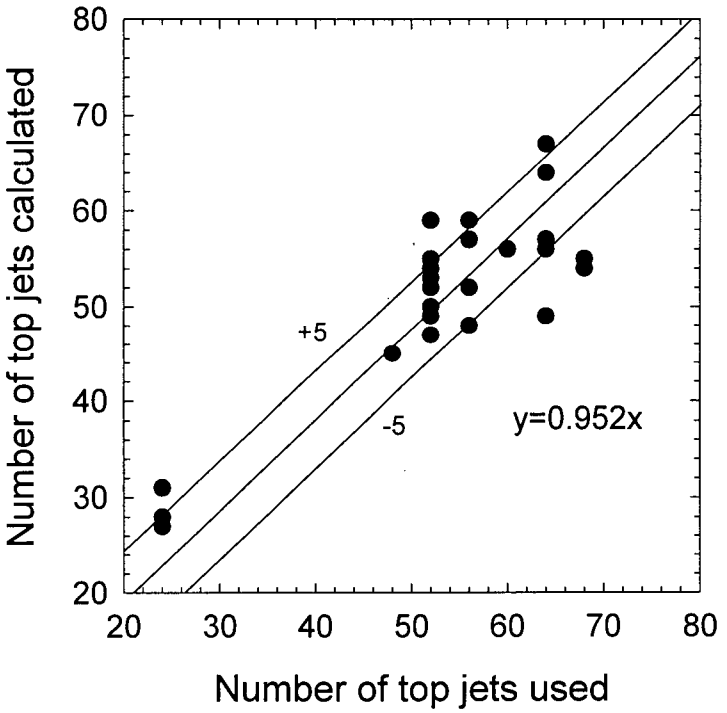

[a]

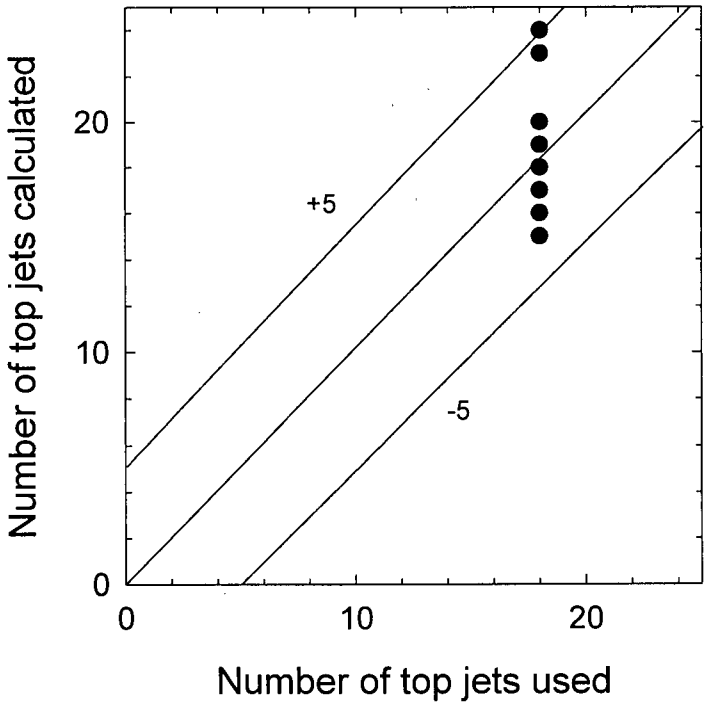

[b]

Figure 7.38: Comparison between the calculated number of top jets by Equation [7.2.2.3] and the actual used. Effect of laminar cooling configuration: [a] Company A (A36), [b] Company E (DQSK).

[a]

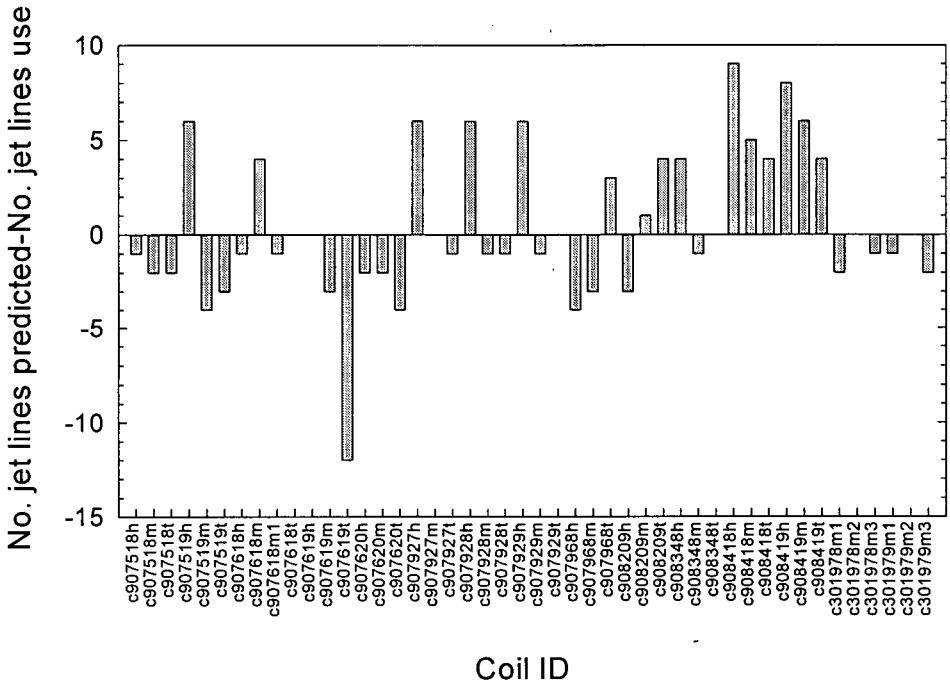

[b]

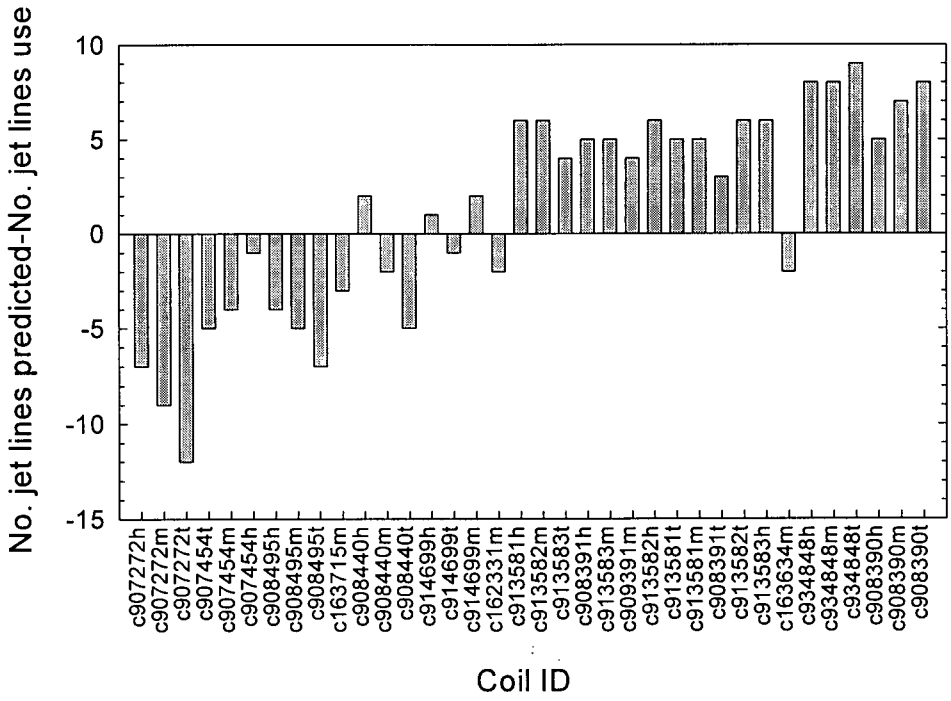

Figure 7.39: Error in the prediction of the number of top jet lines used by Company C for steels, using the empirical equation [7.2.2.3]: [a] DQSK, [b] A36.

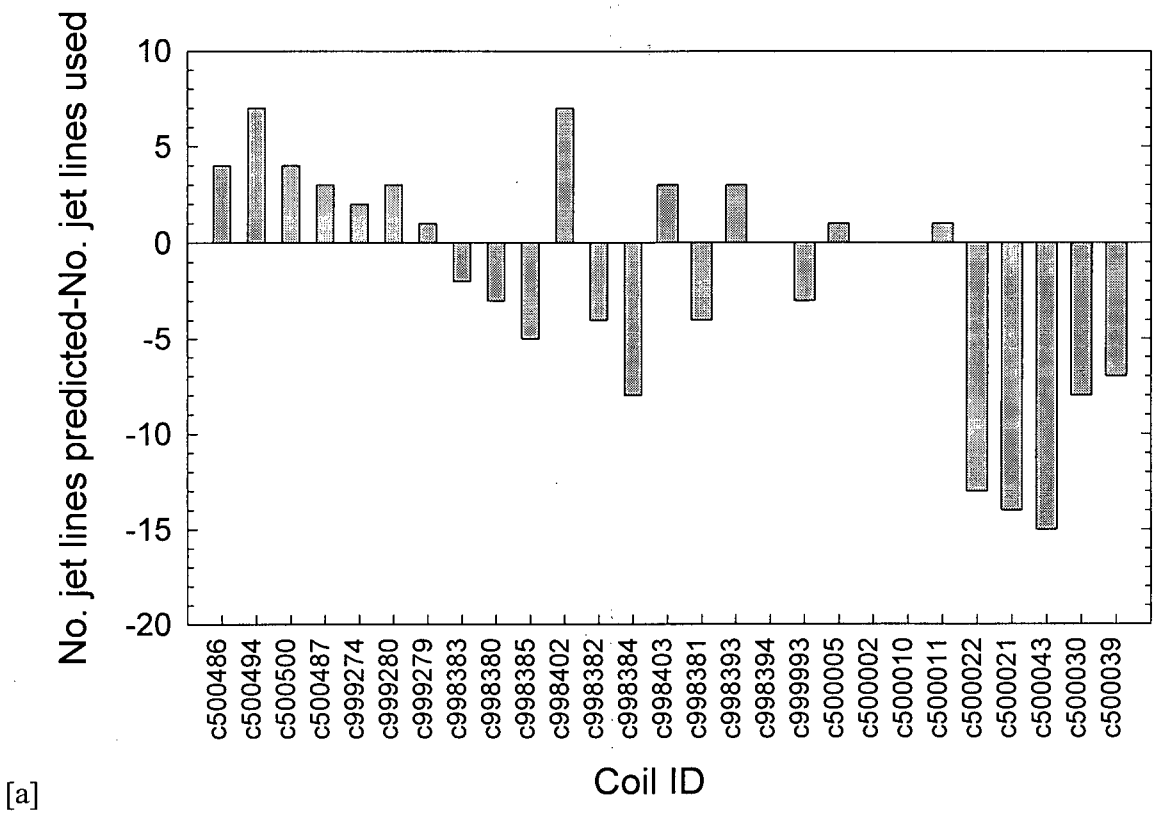

[a]

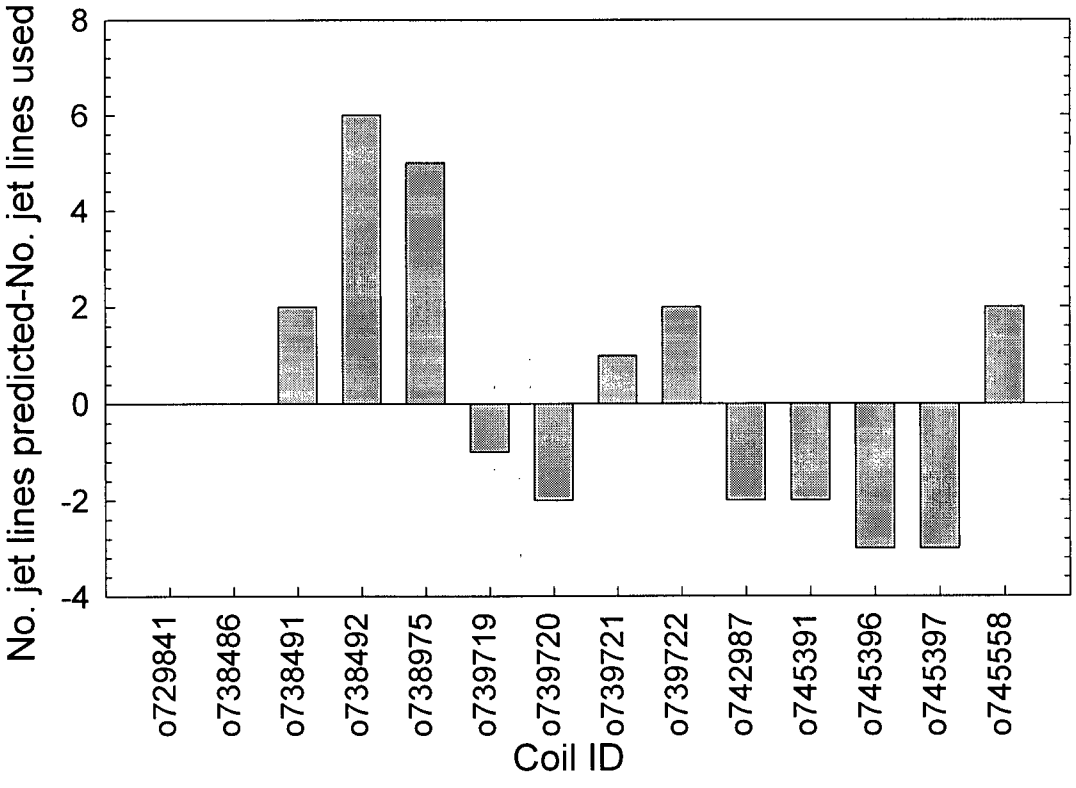

[b]

Figure 7.40: Error in the prediction of the number of top jet lines used by: [a] Company A (A36), [b] Company E (DQSK). Predictions from empirical equation [7.2.2.3]

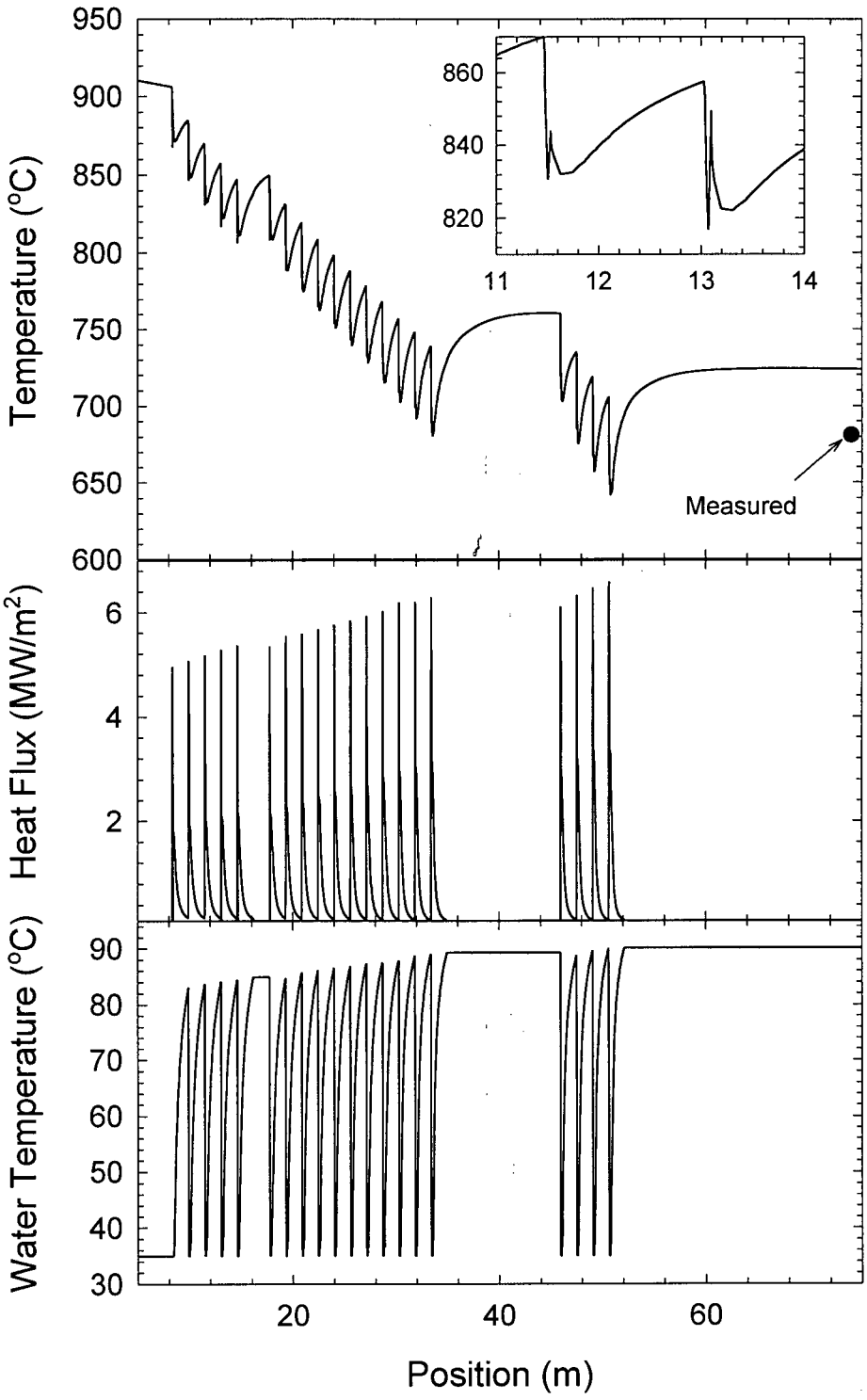

Figure 7.41: Top surface temperature, heat flux and water temperature histories for Run 1 of company H. Cooling patterns as shown in Table 7.5.

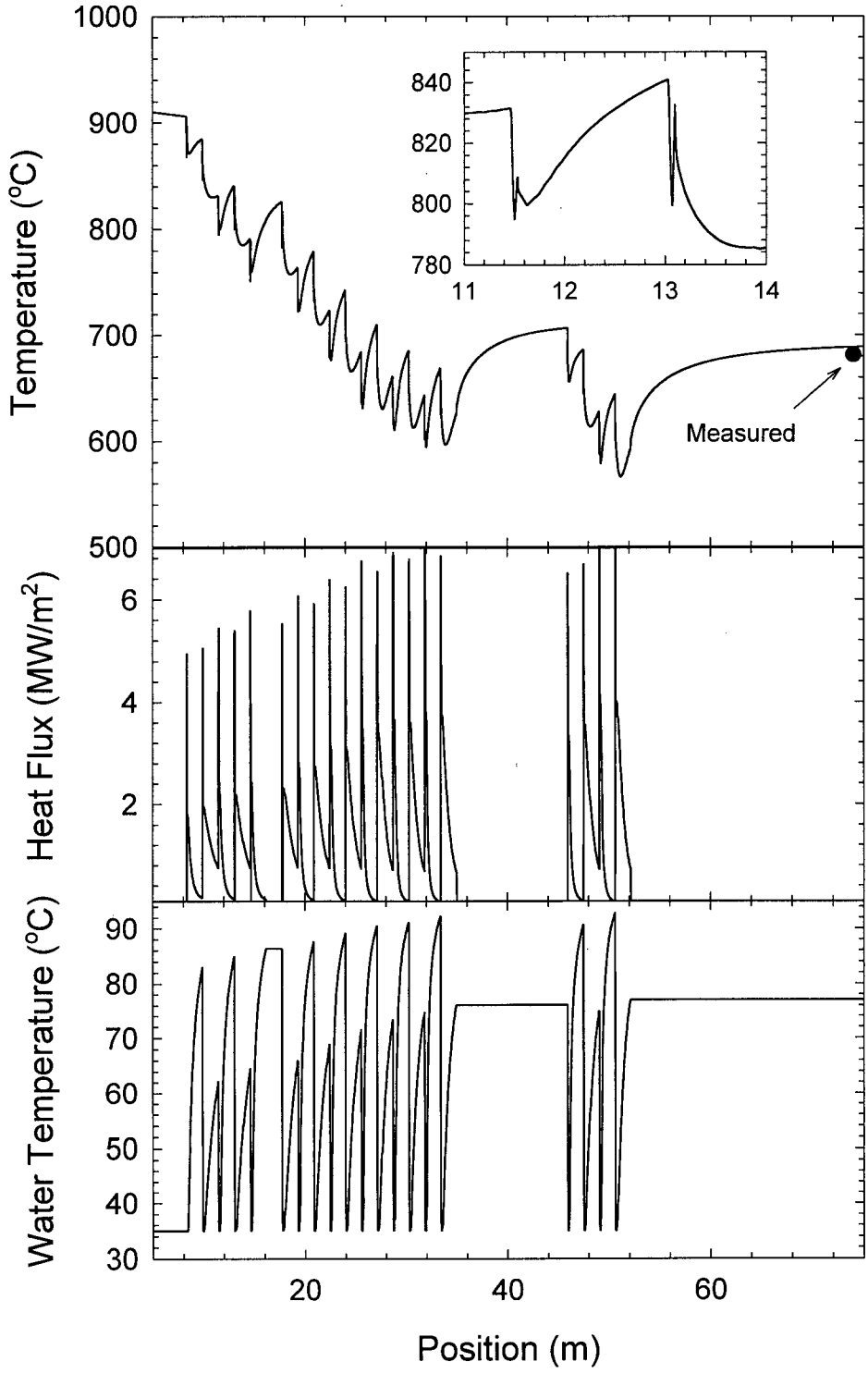

Figure 7.42: Top surface temperature, heat flux and water temperature histories for Run 2 of company H. Cooling patterns as shown in Table 7.5.

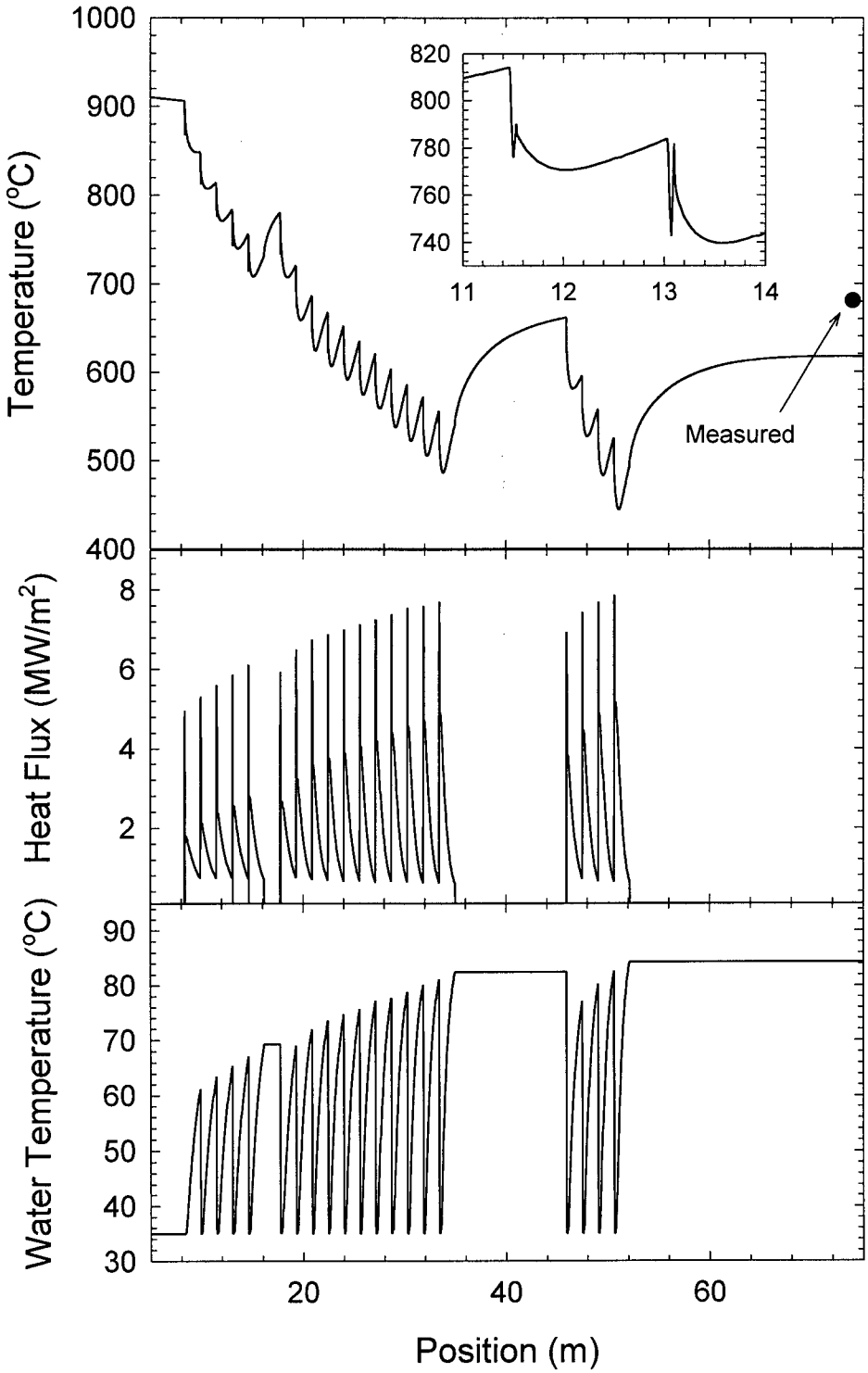

Figure 7.43: Top surface temperature, heat flux and water temperature histories for Run 3 of company H. Cooling patterns as shown in Table 7.5.

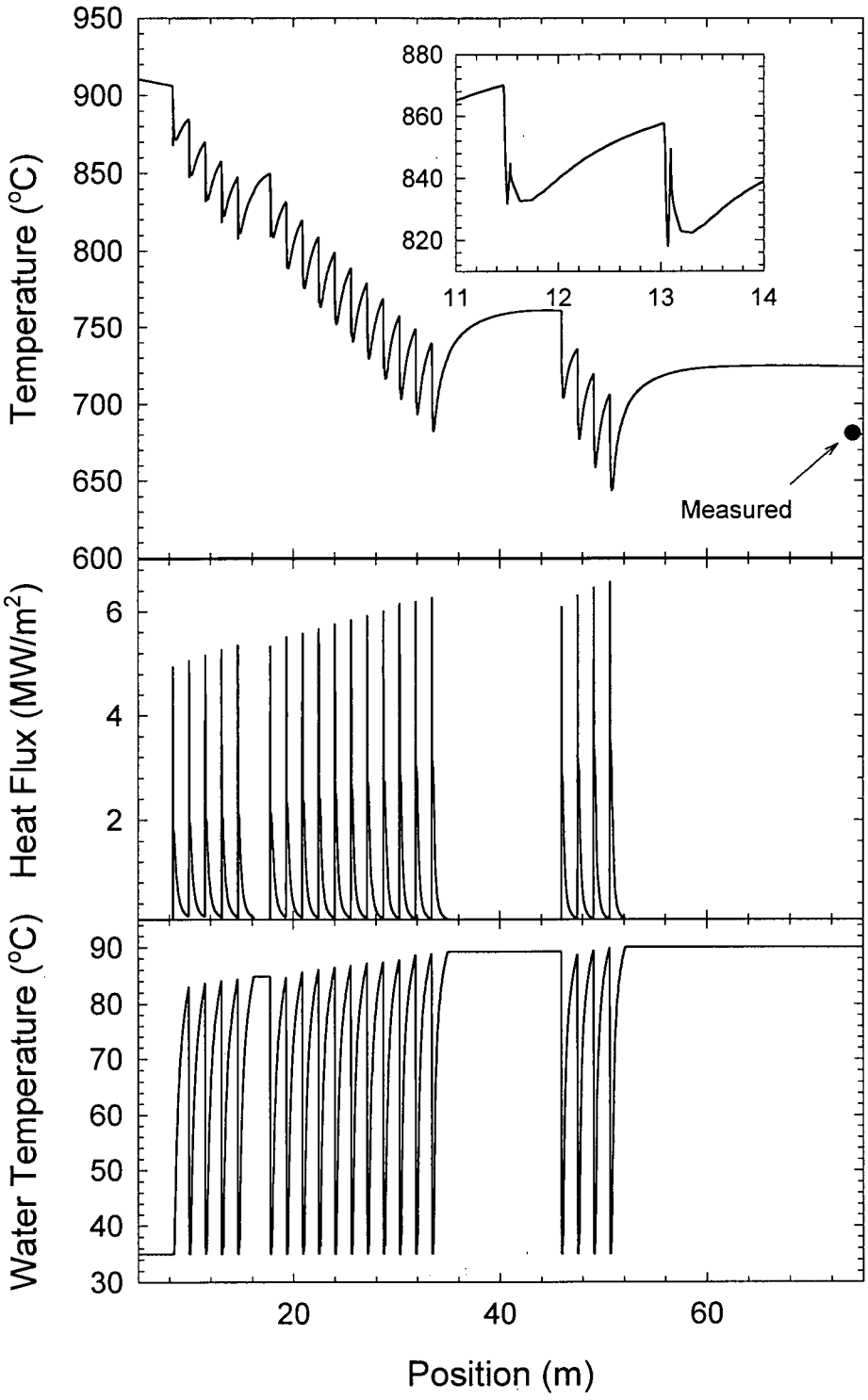

Figure 7.44: Top surface temperature, heat flux and water temperature histories for Run 4 of company H. Cooling patterns as shown in Table 7.5.

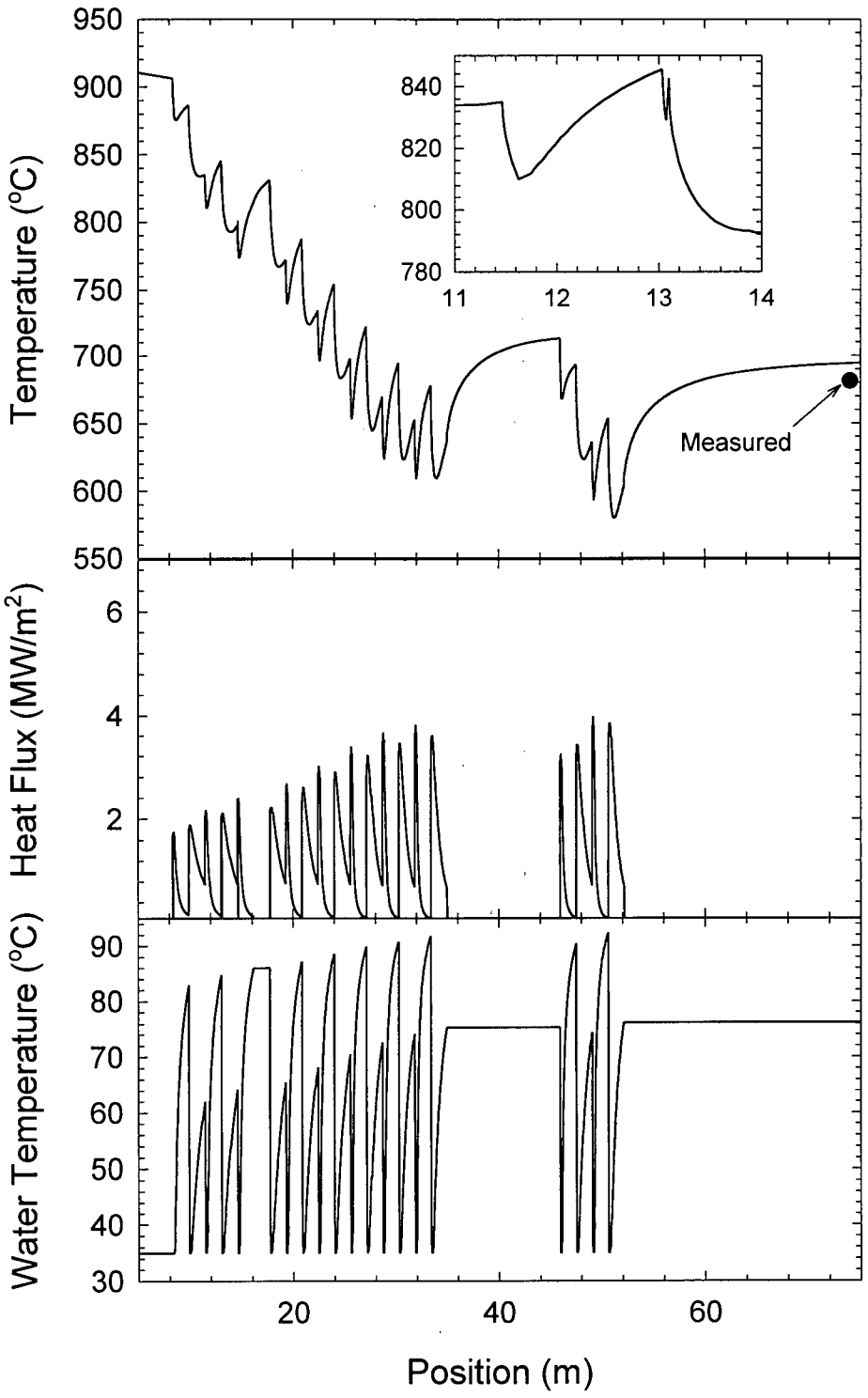

Figure 7.45: Top surface temperature, heat flux and water temperature histories for Run 7 of company H. Cooling patterns as shown in Table 7.5.

Table 7.5: Cooling patterns and predicted coiling temperature for the 2-D analysis of a 6.6 mm strip from company H. Measured coiling temperature=681°C.

Run	Cooling Pattern	Predicted Coiling Temperature (°C)
	Short -Long-Short-Long	
1	H-L-H-L	723.6
2	H-L-H-H	689.2
3	H-H-H-H	616.7
4	L-L-L-L	723.8
5	L-L-L-H	689.4
6	Standard	696.7
7	H-L-H-H (all parallel flow)	694.8

Table 7.6: Cooling patterns and predicted coiling temperature for the 2-D analysis of a 9.4 mm strip from company A.

Run	Cooling Pattern	Predicted Coiling Temperature (°C)
	Impingement -Parallel-Impingement-Parallel	
1	H-L-H-L	673.7
2	L-H-L-H	675.4
3	L-L-H-H	675.3
4	H-H-H-H	531.2
5	L-L-L-L	714.9
6	H-L-H-L (all parallel flow)	679.7
7	H-H-H-H (all parallel flow)	548
8	Standard	675.8

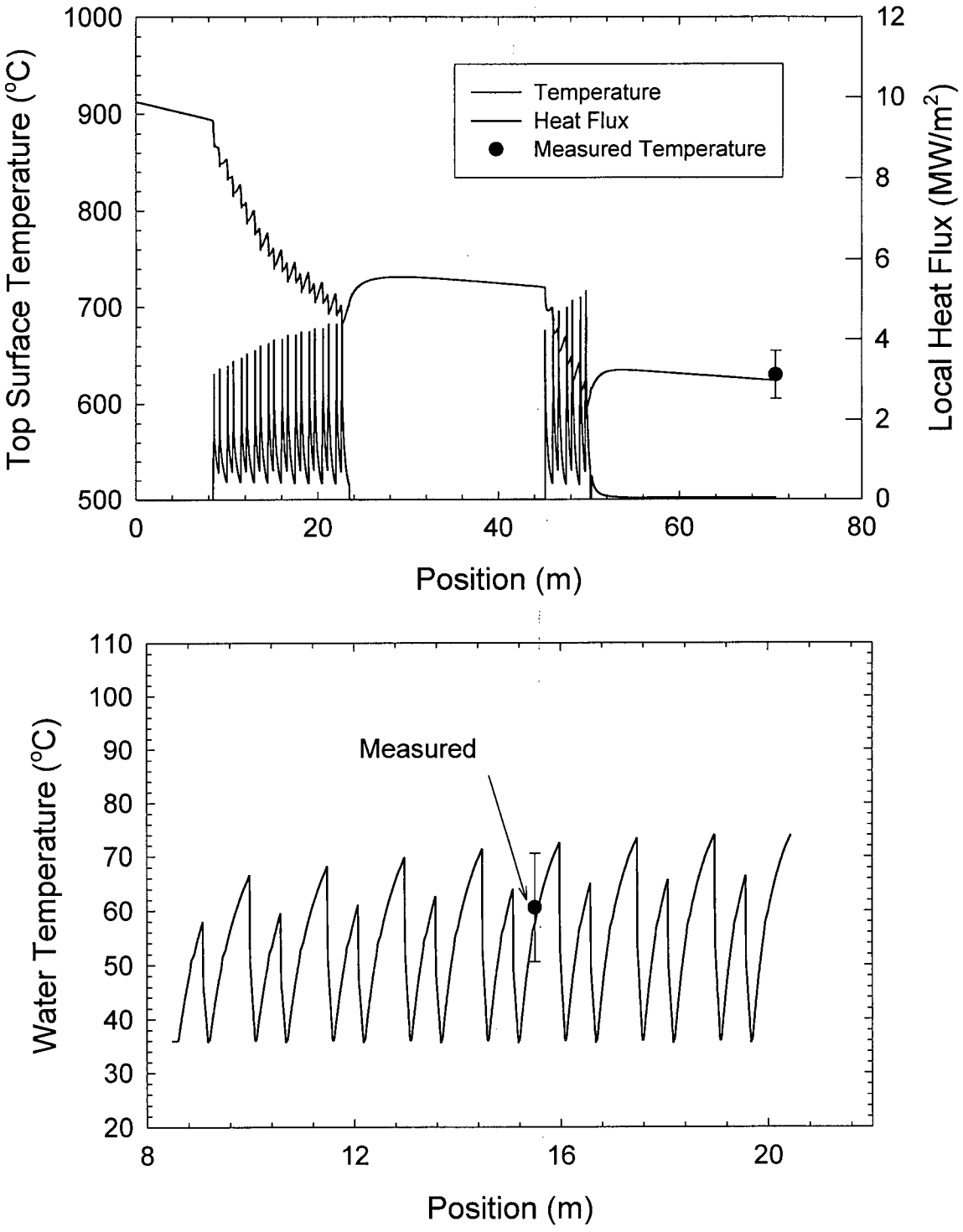

Figure 7.46: Comparison between predictions and measurements[22] during the processing of coil c140751 of company I, for: [a] Coiling temperature, [b] Local water temperature on the top surface.

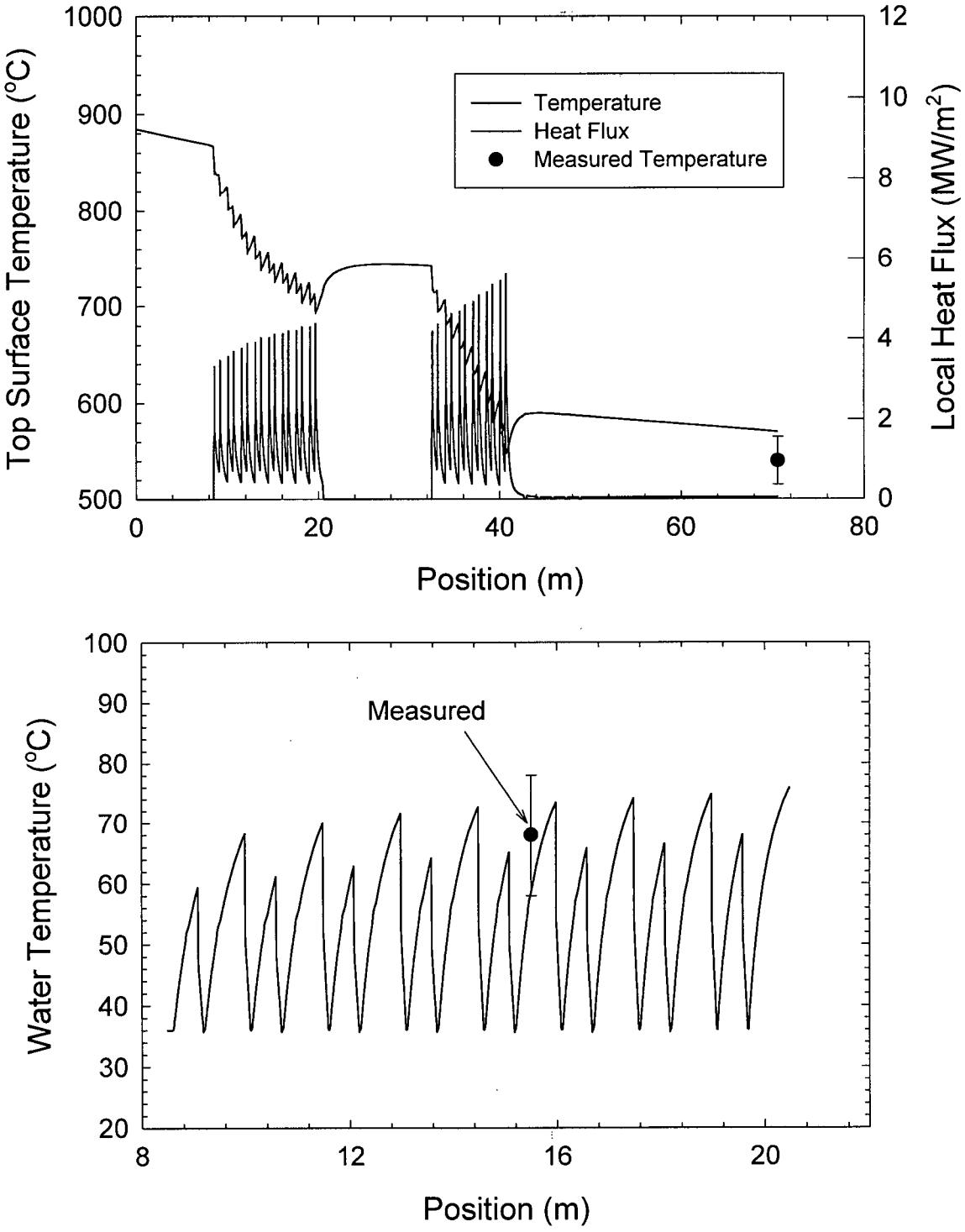

Figure 7.47: Comparison between predictions and measurements[22] during the processing of coil c140753 of company I, for: [a] Coiling temperature, [b] Local water temperature on the top surface.

[a]

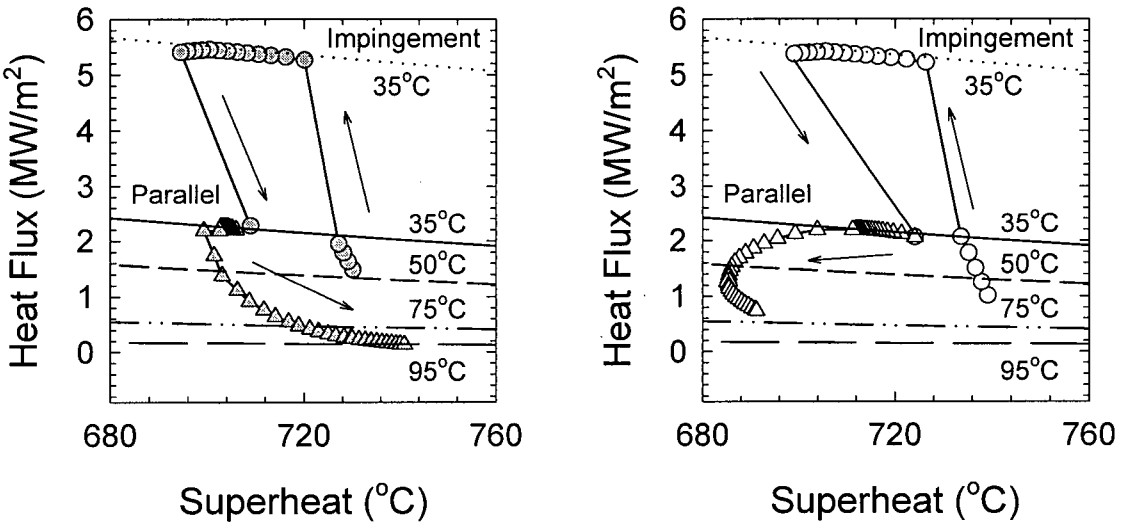

[b]

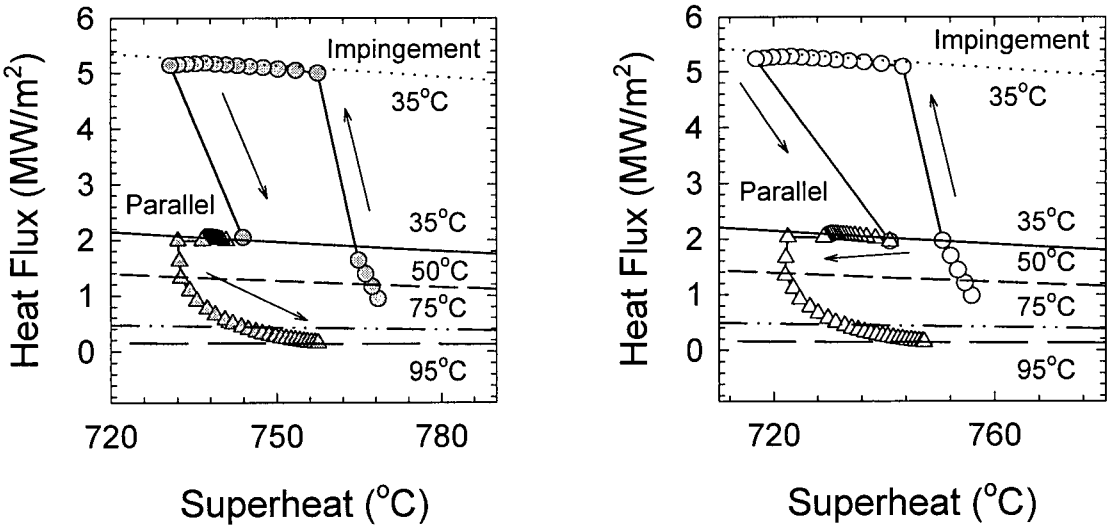

Figure 7.48: Heat Transfer Map for Company H during: [a] Run 2, [b] Run 1. Cooling patterns as shown in Table 7.5

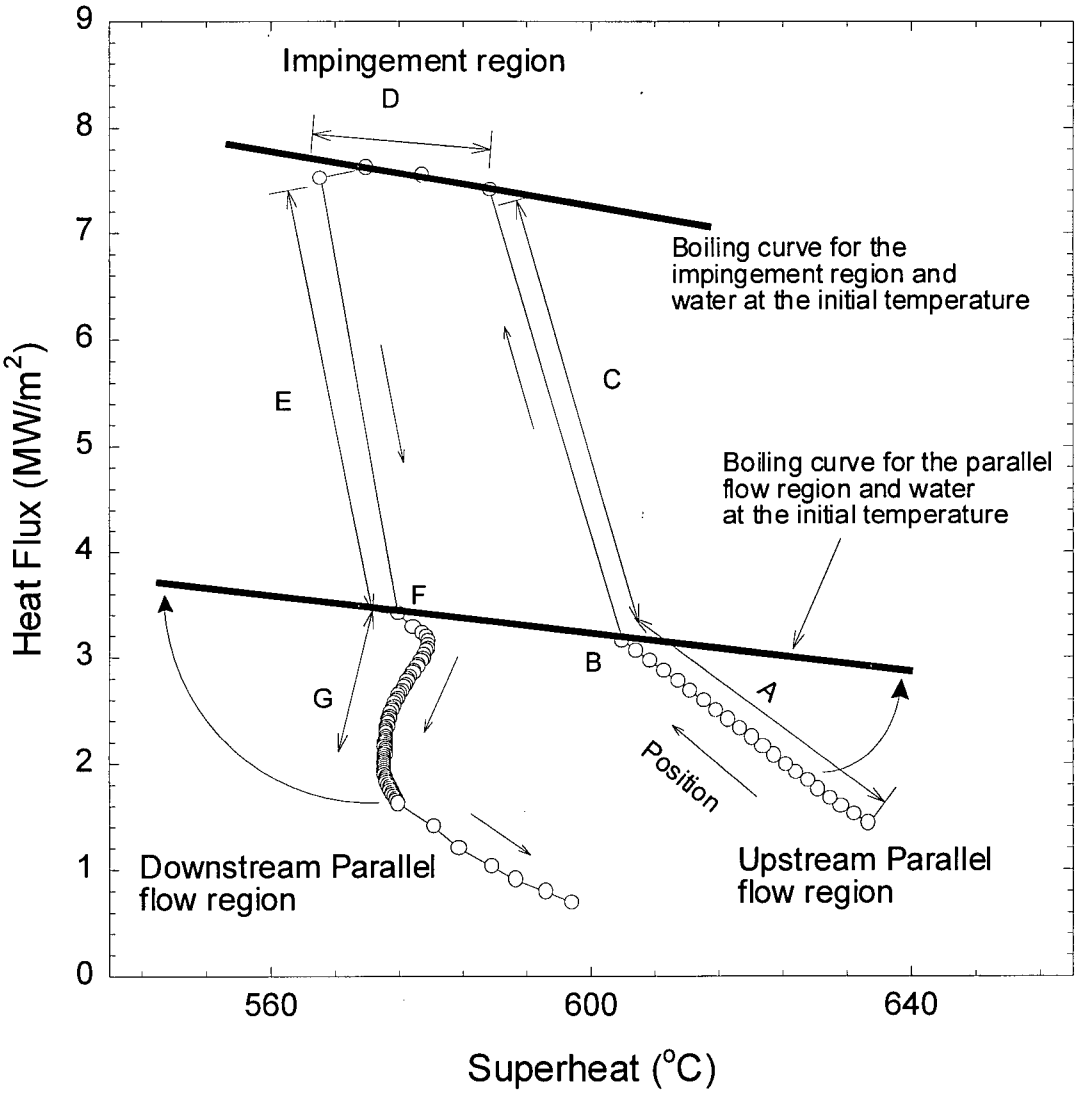

Figure 7.49: Heat Transfer Map for a jet line in Run 1 of Company A. Cooling pattern as shown in Table 7.6.

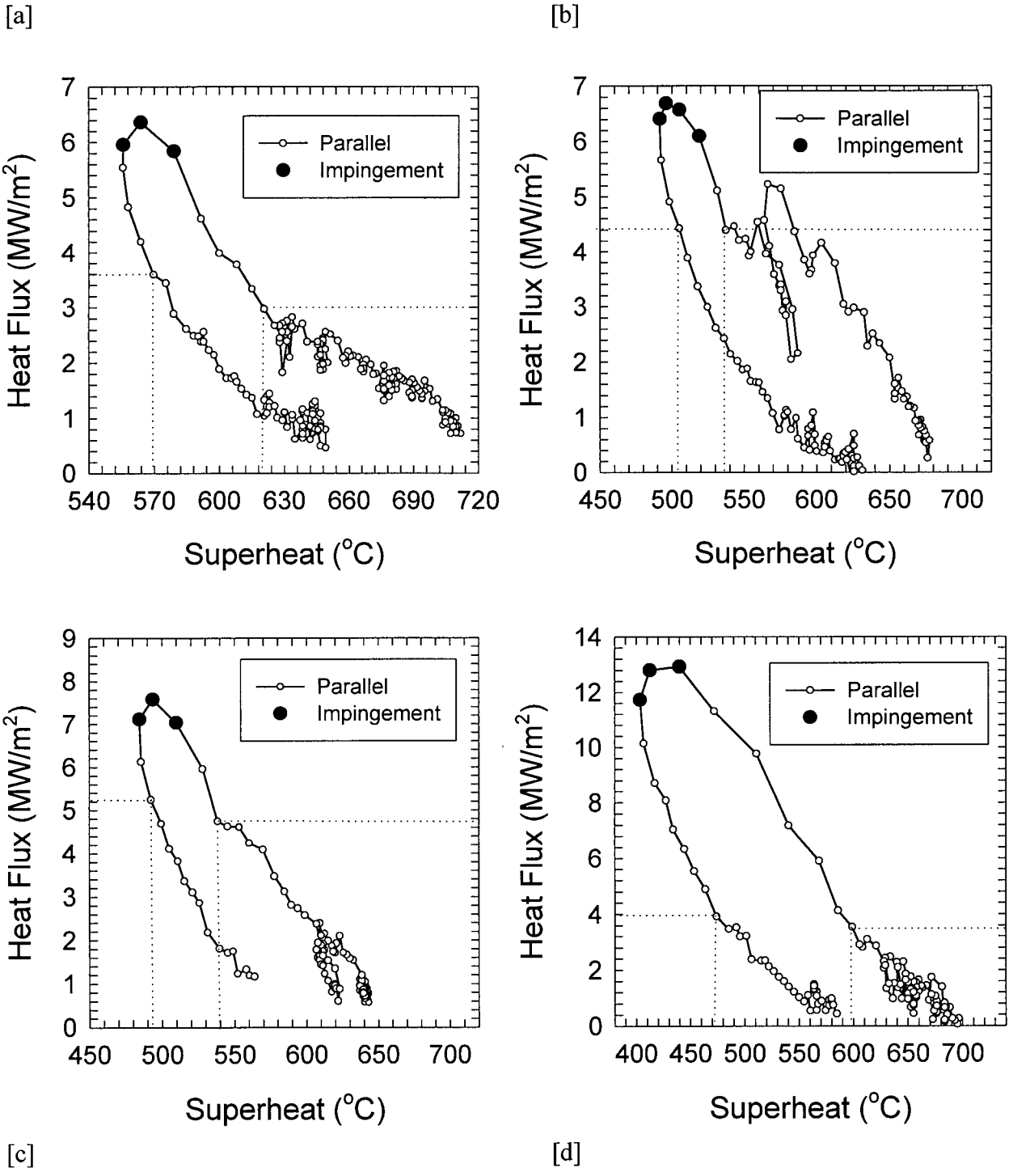

Figure 7.50: Heat Transfer Maps from the pilot-plant measurements during the cooling of a moving plate, for:[a] Jet 2, [b] Jet 3, [c] Jet 4, [d] Jet 5.

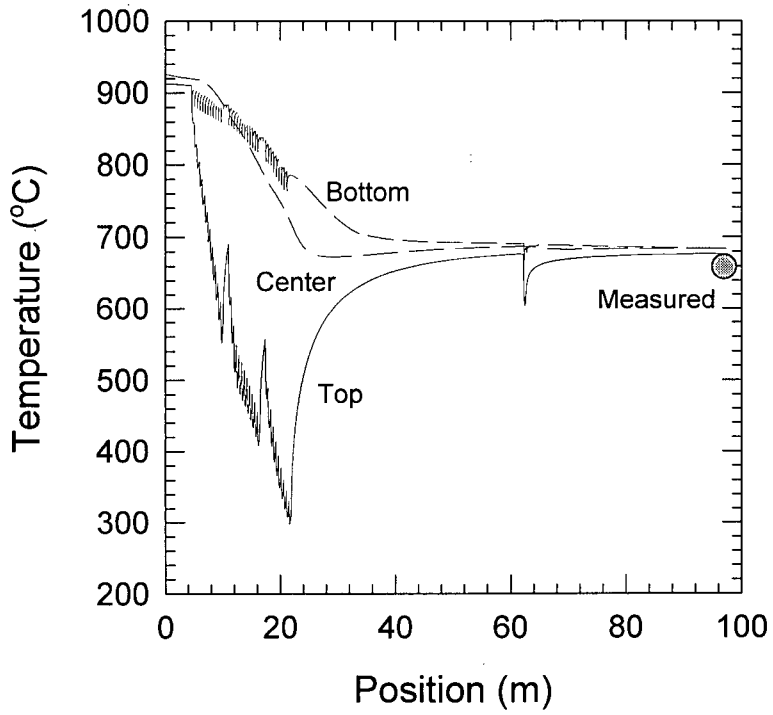

Figure 7.51: Thermal and microstructural evolution of a 9.5mm A36 strip manufactured by company C (coil c934848m).

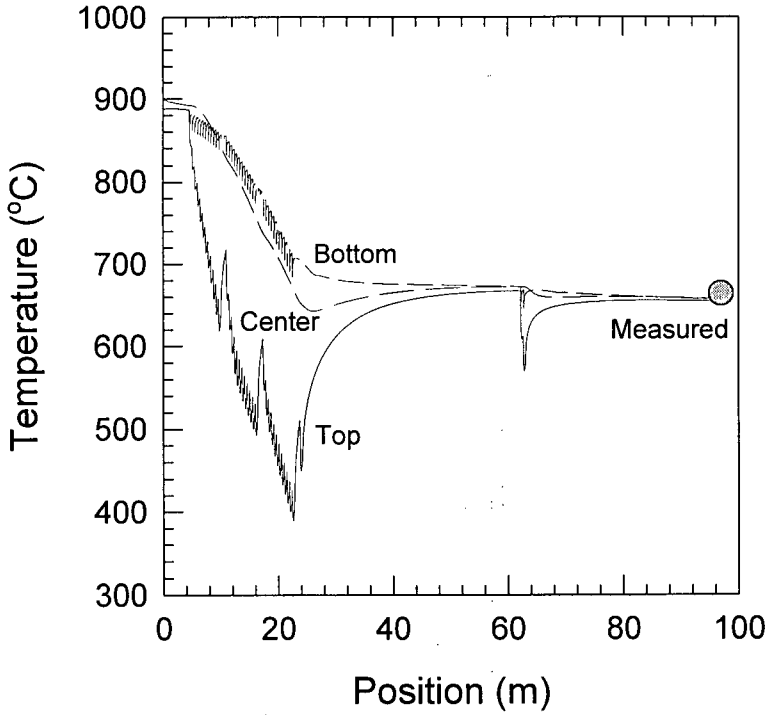

Figure 7.52: Thermal and microstructural evolution of a 6.0mm A36 strip manufactured by company C (coil c162331).

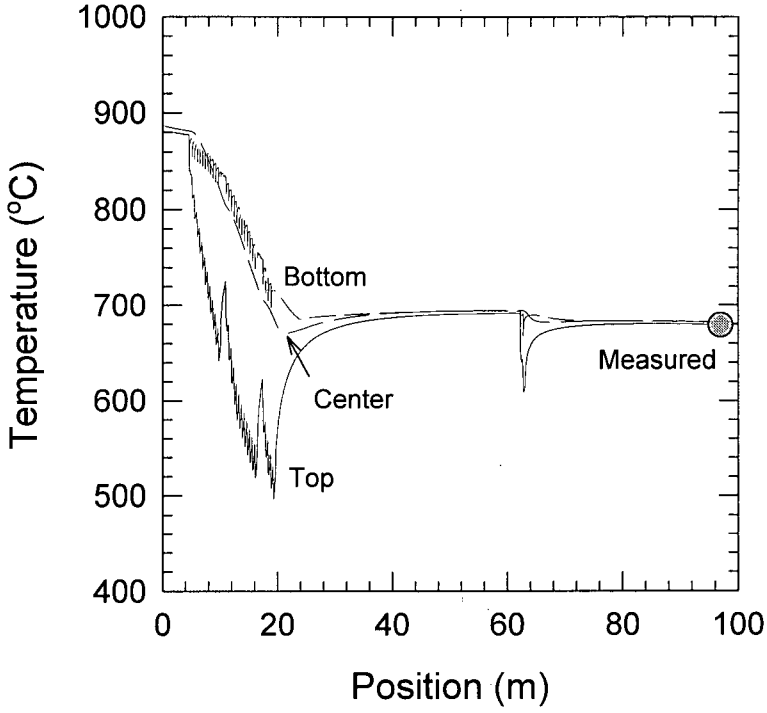

Figure 7.53: Thermal and microstructural evolution of a 4.8mm A36 strip manufactured by company C (coil c163715).

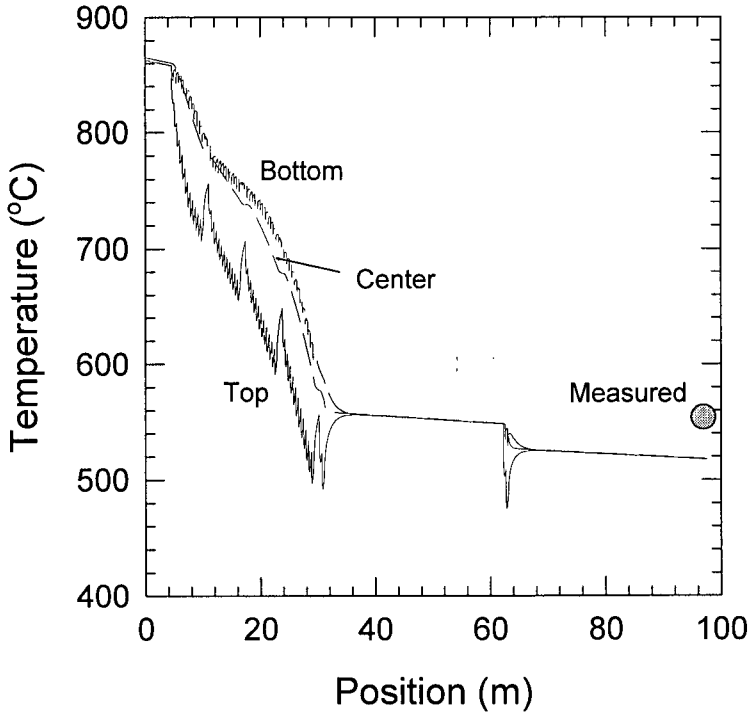

Figure 7.54: Thermal and microstructural evolution of a 2.5mm DQSK strip manufactured by company C (coil c301978).

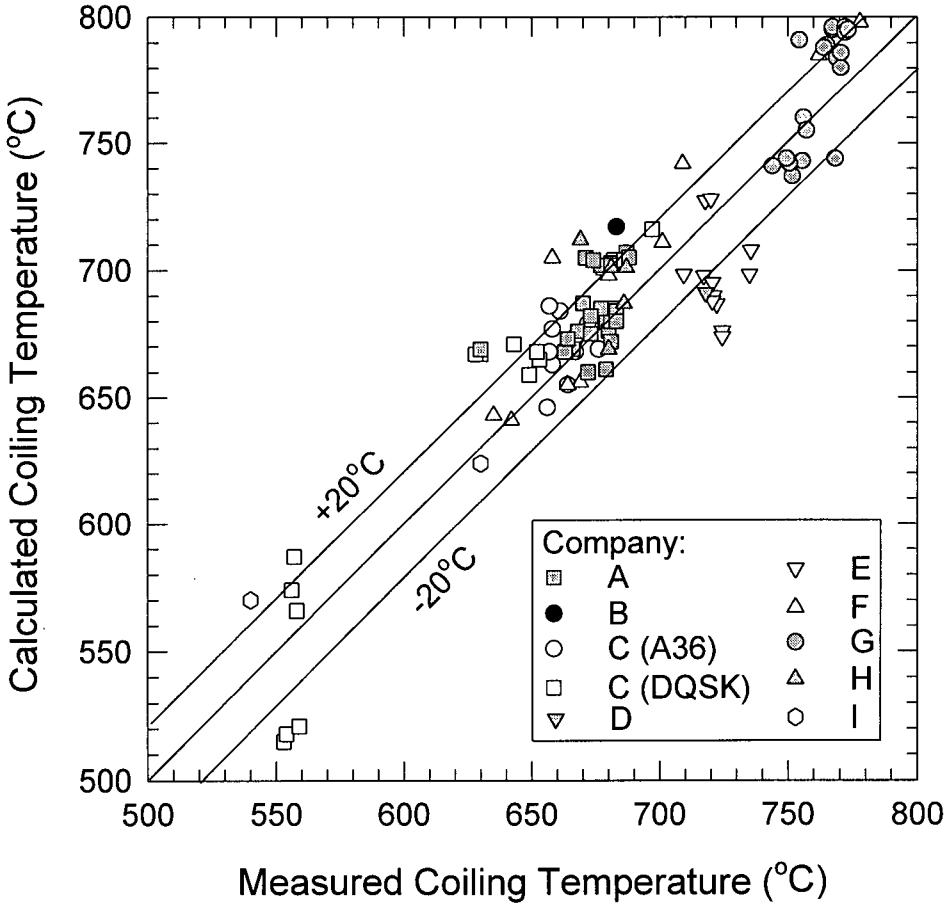

Figure 7.55: Comparison between the predicted and measured coiling temperatures for different companies.

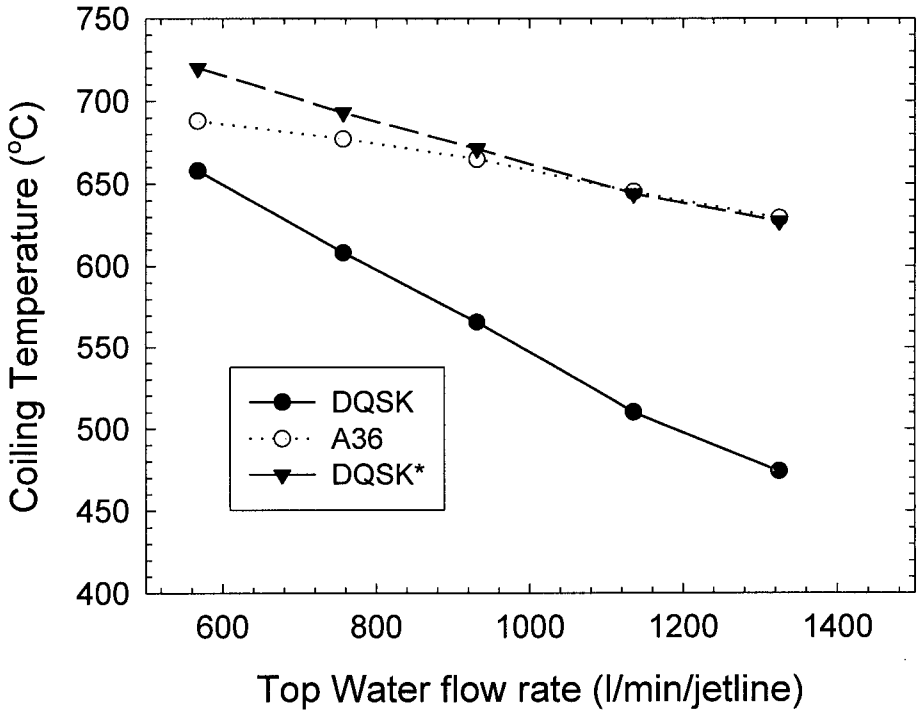

Figure 7.56: Effect of top water flow rate on the coiling temperature. Conditions for company C.

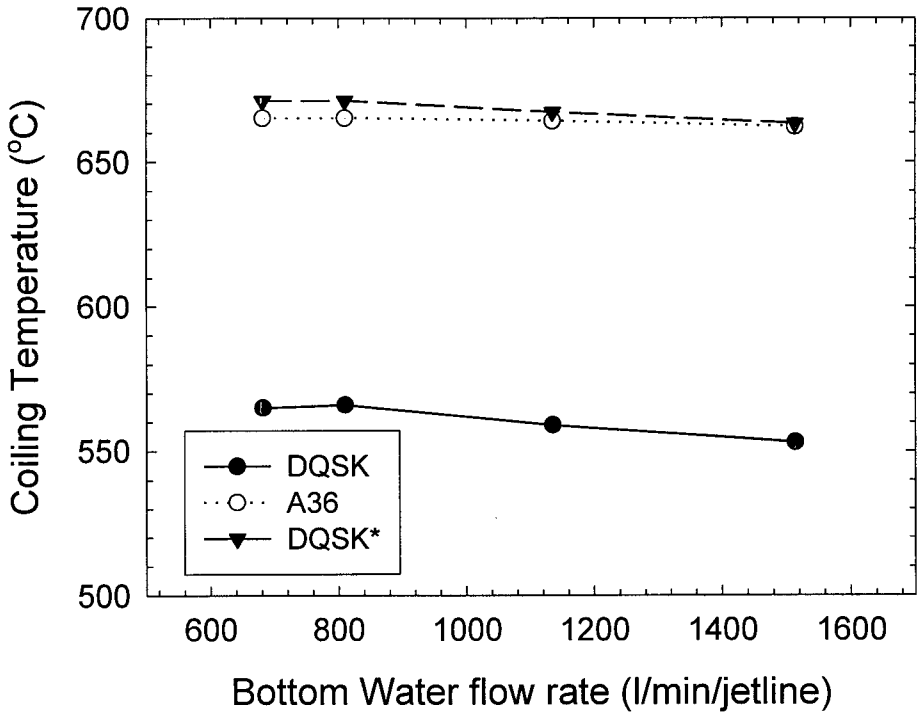

Figure 7.57: Effect of bottom water flow rate on the coiling temperature. Conditions for company C.

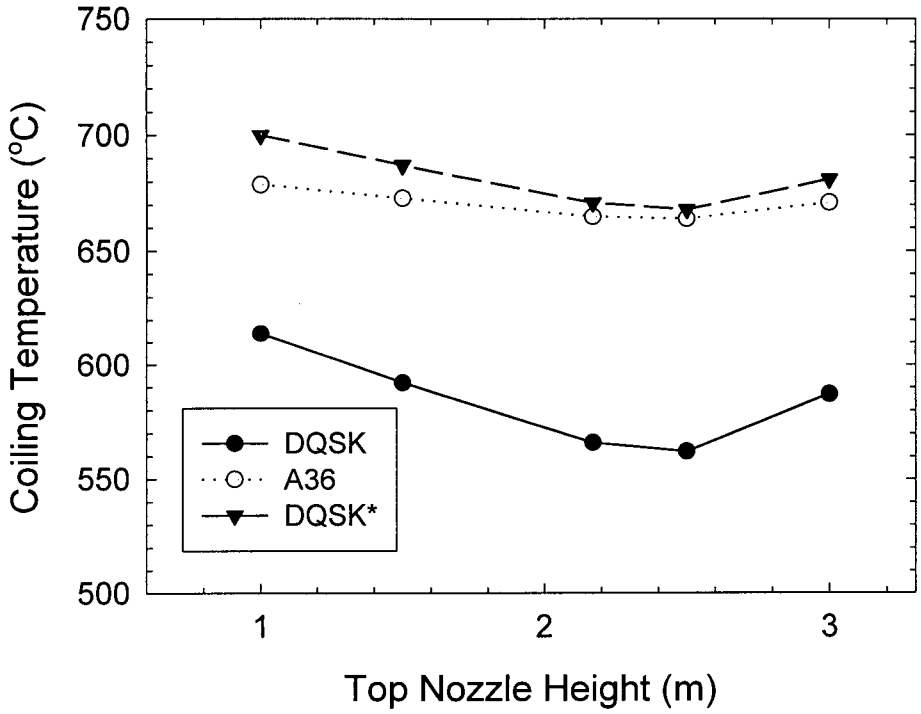

Figure 7.58: Effect of top nozzle height on the coiling temperature. Conditions for company C.

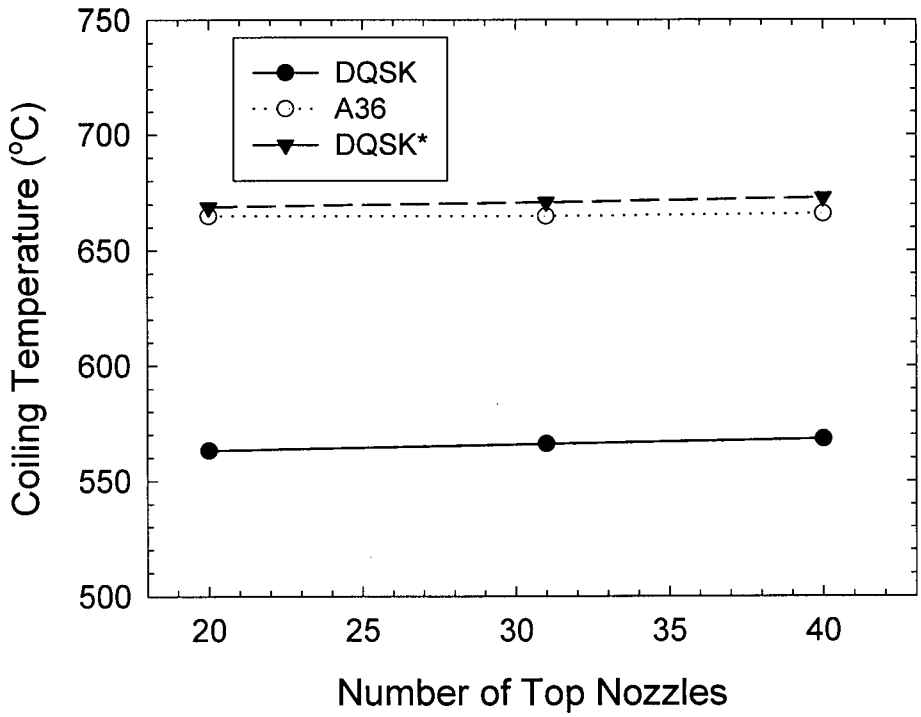

Figure 7.59: Effect of the number of top nozzles (constant flow rate per jetline) on the coiling temperature. Conditions for company C.

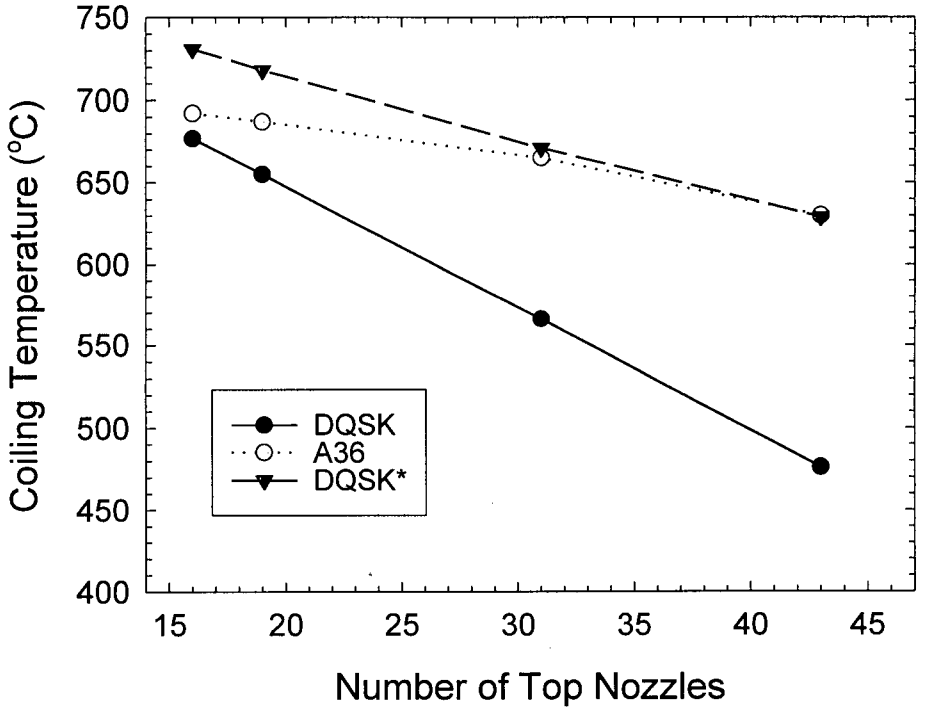

Figure 7.60: Effect of the number of top nozzles (variable flow rate per jetline) on the coiling temperature. Conditions for company C.

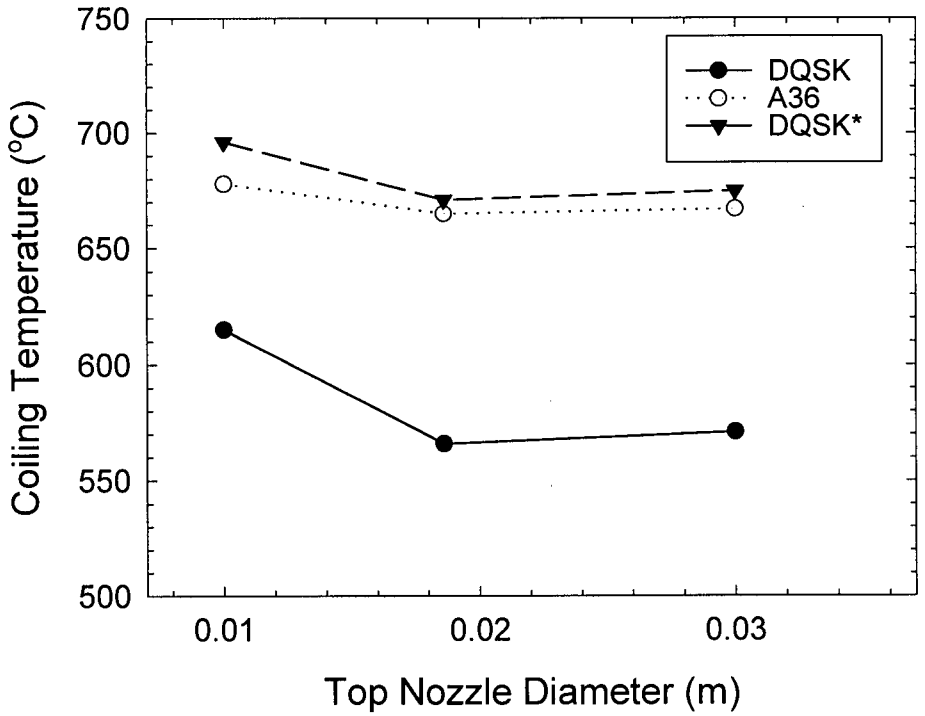

Figure 7.61: Effect of the top nozzles diameter on the coiling temperature. Conditions for company C.

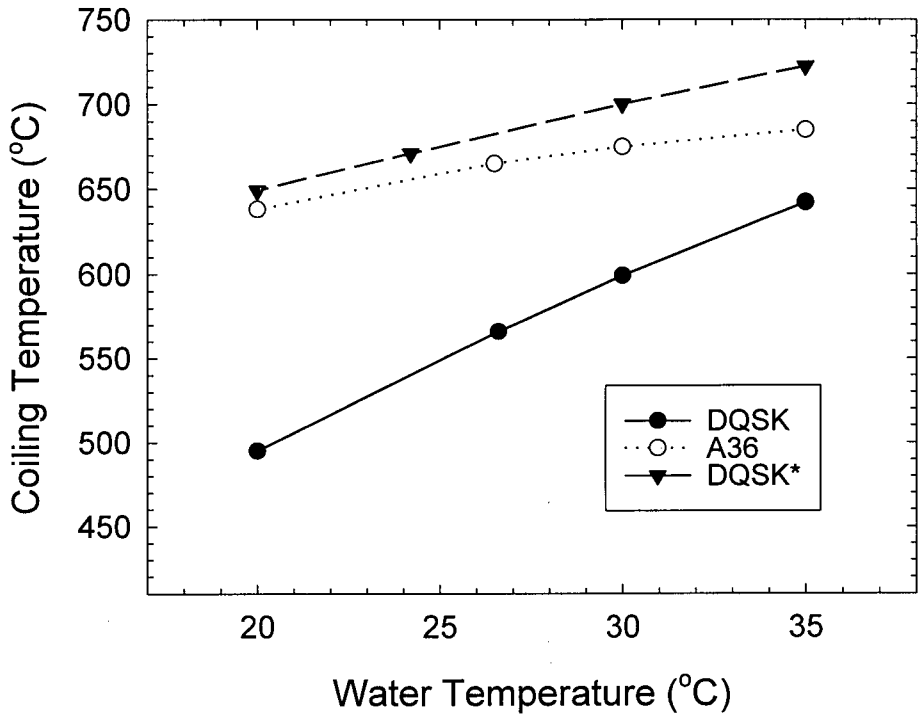

Figure 7.62: Effect of water temperature on the coiling temperature. Conditions for company C.

Table 7.7: Verification of some empirical rules of operation

Operating Parameter	Plant Observation	Conditions of application	Plant Measurement	Model Prediction
Water Temperature[24]	Increment in the required number of working headers due to an increment in water temperature	Water temperature range of 25-35°C	≈1%/°F	1.6%/°F (DQSK) 1.6%/°F (A36) 1.5%/°F(DQSK*)
Water Flow Rate and Nozzle Diameter[24]	An increment of 50% in water flow rate and nozzle diameter decreases the number of working headers required	Unspecified	≈25%	18%(DQSK) 17%(A36) 15% (DQSK*)
Chemistry[21]	Higher water consumption for lower carbon steels to reach a certain coiling temperature	0.09<%C<0.30	≈24%	13%(DQSK) 17%(A36) 18% (DQSK*)

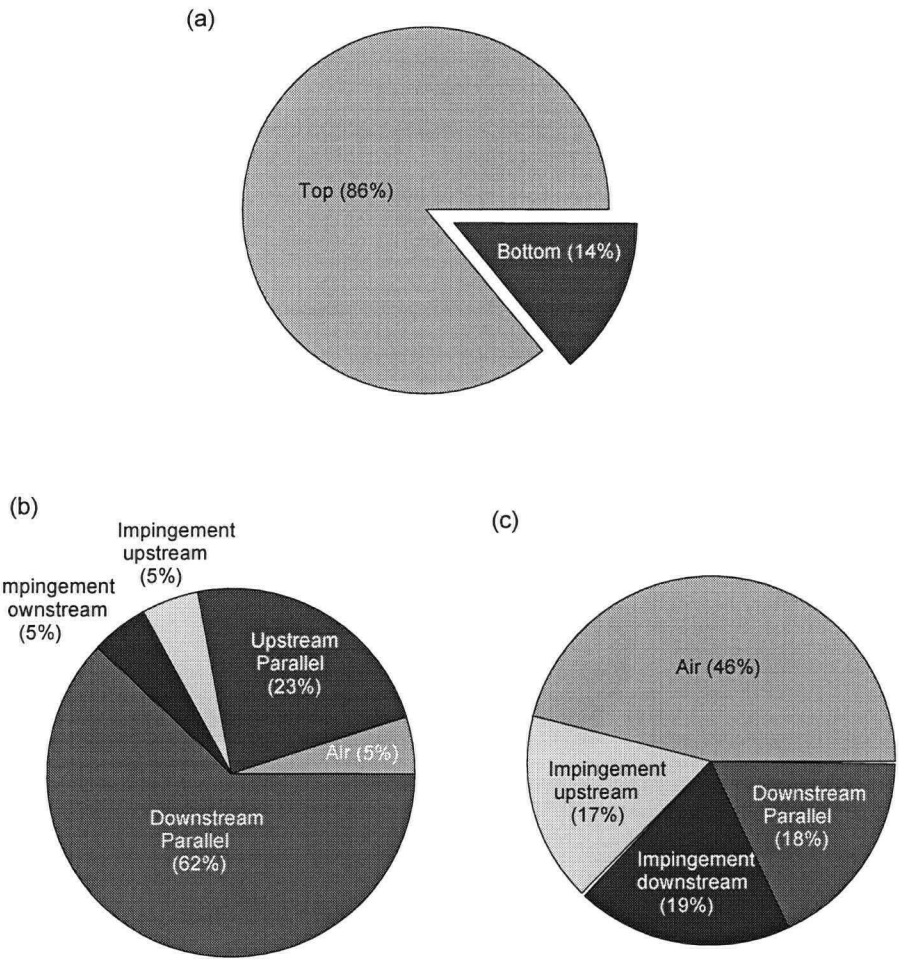

Figure 7.63: Relative importance of each cooling zone on the heat extraction during the processing of coil c162331. [a] Percent of the total heat extracted by each surface, [b] Percent of the heat extracted at the top surface in each cooling zone, [c] Percent of the heat extracted at the bottom surface in each cooling zone.

Table 7.8: Effect of variations in some heat transfer parameters on the predicted coiling temperature for the processing of coil c162331. (Predicted $T_{coiling}$=655°C, Measured $T_{coiling}$=664°C)

Parameter	$T_{coiling}$ (°C) for +20%	$\Delta T_{coiling}$(°C)	$T_{coiling}$ (°C) for -20%	$\Delta T_{coiling}$(°C)
q_{l-s}	602	-53	684	29
q_{v-s}	646	-9	663	8
F	603	-52	684	29
$H_{trans.}$	670	15	632	-23

8. SUMMARY, CONCLUSIONS AND RECOMMENDATIONS FOR FUTURE WORK

8.1 Summary

The runout table process has been studied in detail during this work, and as a result, important observations leading to a better understanding of this operation were obtained. The heat extraction in each of the cooling zones identified on the runout table was characterized by careful examination of video-recorded operations obtained from several different mills. Once the main different cooling regions were established, the quantification of the heat transfer was done by the application of data reported in the literature and mill measurements to the mathematical modelling of the heat transfer events taking place.

A mathematical model for the runout table cooling was developed, which solves the transient 1-D heat transfer in a piece of steel moving through the cooling units in the runout table. The model takes into account the individual fluid flow characteristics of each jet such as its velocity, diameter, temperature, and the geometry of the nozzle arrays, and relates them to other process variables, such as strip speed, chemistry, and thickness, to predict the thermal evolution of the steel. The model was validated by comparing the predictions of the model for the processing of two plain carbon steels, A36 and DQSK, with measurements in ten different runout table operations. Very good agreement with measurements in these mills was obtained.

The runout table model required boundary conditions during water jet cooling, which needed to be very general and accurate. The mathematical modelling of the boiling curves during water jet cooling was considered to be the best alternative to obtain such boundary conditions. The boiling curves were obtained by a simple model of the macrolayer evaporation mechanism together with a semi-empirical fitting procedure to obtain the fractional liquid-solid contact area and a model for the vapor-solid heat fluxes. The boiling curve model provided predictions of the boiling curves that compared well with most of the reported measurements in the literature. The boiling curves were linked to a simple model of the water flow on the strip, based on the video-recorded observations, to obtain the heat transfer coefficients in the runout table model.

Specifically, the key findings of this work as summarized as follows:

[1] The observation of five different runout table operations revealed that the actual flow in each of mill is very unique. However, some general observations were obtained.

When the cooling was done by water bars, the highest heat extraction was seen at a relatively small area, the impingement band, followed by the cooling in the parallel flow regions at the top surface in areas of higher water flow density, such as the countercurrent zone, water stripes in the downstream flow, and in regions of interaction between the parallel flow and sweepers.

[2] The regions of higher cooling in the parallel flow appear only when the local water thickness is relatively high. It was concluded that a lower local water temperature is responsible for the higher cooling. At low water temperatures, such as at the

beginning of the parallel flow region, the heat transfer is high. At higher local water temperatures, low transition boiling or film boiling heat transfer takes place.

[3] In most of the operations, the heat is mainly extracted from the top surface of the strip.

[4] From the literature review and the effect of some operating parameters such as water temperature on the coiling temperature, it became evident that transition boiling is the main mechanism of heat transfer during runout table cooling, in both, the impingement region and the parallel flow regions.

[5] The complexity of the transition boiling regime can be better explained through the understanding of the film boiling regime. All the important effects of the process variables on the heat transfer during film boiling can be explained in terms of their effect on the vapor layer thickness. The heat transfer coefficients in film boiling are inversely proportional to the vapor layer thickness. On the other hand, the effect of the process variables on the transition boiling regime are qualitatively the same as in the film boiling regime, but quantitatively are more important because of the higher heat fluxes caused by the liquid-solid contact during transition boiling.

[6] The fundamental process variables with an effect on the heat transfer are: (1) Strip surface temperature, (2) Water jet temperature, (3) Jet width or diameter, (4) Jet velocity, and (5) Strip speed, and their relative importance in the boiling curves is in that order. The strip surface temperature determines the boiling regime and consequently the local heat fluxes in a very strong manner. The local water temperature has also an important effect because at lower water temperatures the vapor-layer thickness is decreased considerably, which increases the liquid-solid

contact and also heat transfer during these contacts. When the jet diameter or width of the jet is small, the pressure gradient is increased because it is inversely proportional to the jet diameter, resulting in a higher heat transfer in the impingement region. An increase in the jet velocity provides an enhancement in the heat transfer, specially in the impingement region, whereas in the parallel flow regions its effect is smaller. The effect of strip speed is important in film boiling, but apparently it is smaller in transition boiling. Probably, the effect of strip speed on the boiling curves is masked by the effect of this variable on the actual water flow distribution on the strip. Also the surface condition is important. From the film boiling predictions, it was estimated that the strip roughness should be higher than 2-20μm to have a relevant effect.

[7] Cooling in air during the runout table processing represents a small fraction of the total heat extracted during the process. Radiation is the main mechanism of heat extraction during cooling in air. In the processing of strips by air cooling exclusively, the coiling temperature increases linearly with increasing the finishing temperature provided that the chemical composition of the strip, the speed and the thickness remain constant and in the absence of austenite decomposition. When austenite decomposition takes place, the coiling temperature is increased according to the fraction of the steel that has transformed. Coiling temperatures are very sensitive to the chemical composition of the steel when partial austenite decomposition happens.

[8] Runout table rolls chilling is a minor contributor to the overall cooling. Its effect can be neglected at least for strips with a thickness higher than 4mm.

[9] An empirical relation between the temperature drop in the strip during water cooling with the number and the distance between the working jet lines, the strip thickness and speed was developed. The temperature drop is proportional to length of the water coverage, while it is inversely proportional to the strip characteristics. The proportionality constant found in this relationship allows to compare the relative capabilities of the different mills and also to determine the effect of chemistry on the amount of water needed to reach a specific coiling temperature. This proved to be an important tool to verify the consistency of the mill data.

[10] A 1-D model (through the thickness of the strip) was good enough to study the actual 2-D heat transfer because the heat conduction across the width is negligible, except perhaps for thick plates. Regardless of the operating conditions, the coiling temperatures predicted by the model assuming homogeneous water flow distribution across the width and along the length are very close to those predicted for fixed positions across the width under real water flow patterns found in the runout table, as long as the average water distribution along the length assumed in the model coincides with the real.

[11] Besides the strip temperature, the single most important parameter in the operation in the runout table is the local water temperature, which is in practice a function of the designs of headers, nozzle arrangement design and the flow rate and temperature of the water supplied. Predictions of the water temperature agree very well with measurements in plant operations.

[12] A heat transfer map, similar to the boiling curve, was developed in order to have a simple method to characterize the effect of variables such as strip thickness, speed

and surface temperature, residence time under cooling, jet diameter, height, velocity and temperature, and their effect on the local thermal events during jet cooling. Two major applications of this map were found. One in the optimization of the water flow rate of the jet to attain certain cooling characteristics, and another in the measurement of the boiling curves during moving-strip experiments.

[13] A sensitivity analysis of the effect of top water flow rate, bottom water flow rate, top nozzle height, the number of top nozzles/jet line, top nozzle diameter, and water temperature on the coiling temperature was done. For the range of the operation conditions adopted, the top water flow rate has a strong effect on the coiling temperature, which decreases linearly with increasing the top flow rate. The bottom water flow rate has a much smaller effect. It was seen that there is an optimum top nozzle height for a given water flow rate and nozzle diameter, for which the coiling temperature is a minimum. The number of nozzles/jet line was not important for the coiling temperature, provided that the water flow rate per jet line was constant. When the water flow rate was varied according to the number of nozzles used, the effect was the same as the one found by just increasing the water flow rate. The effect of nozzle diameter was restricted to relatively small nozzle diameters, and becomes negligible for higher diameters. An increase in the nozzle diameter resulted in a decreased coiling temperature. Increasing the input water temperature increases considerably the coiling temperature. The effect of all these variables were more pronounced at lower target coiling temperatures, and almost independent of the chemical composition.

Comparison of the effect of some of these parameters with observations in plant operations was very good. The number of working jet lines has to be increased by

about 1% per 1°F increase on the water temperature. The number of jet lines operating also needs to increase by around 20% when the carbon equivalent of the steel is reduced from 0.30% to 0.09%, and by approximately 20% when increasing the water flow rate and nozzle diameter by 50%.

8.2 Conclusions

From the results of this work, the following conclusions can be drawn:

[1] It is possible to develop an accurate runout table model by the application of the fundamentals of boiling heat transfer to real observations in the mill. The model developed was general enough to predict the thermal and microstructure evolution and mechanical properties of two plain carbon steels during their processing in ten different mills.

[2] The complexity of the heat transfer involved can be better understood by a detailed study of the film boiling, and then the transition boiling processes during quenching. This was accomplished satisfactorily by the solution of the convective heat transfer problem during film boiling coupled with a simple model of the macrolayer evaporation mechanism. In this way it is possible to explain the effect of the different process variables and the substantial experimental work published in the literature. This analysis can provide a foundation to design future experimental work.

[3] The incorporation of an accurate mathematical description of the austenite decomposition is very important to predict properly the thermal events.

8.3 Recommendations for future work.

There are many important areas of research to be done in the runout table processing. With respect to the thermal events, the following recommendations are suggested:

[1] Measurement of the thermal events during the cooling of a moving strip. This should include not only the temperatures in the steel, but if possible, in the water streams. In order to capture some of the complexity of the fluid flow patterns found in operation, the cooling system should include several nozzles per jet line and several jet lines.

[2] A systematic study of the effect of chemistry on the thermal events. This should include more plain carbon steels, and the extension of the present model to the modeling of HSLA and IF steels.

[3] The development of an on-line model from the model presented in this work. Since the model developed in this work is very general, many important relationships such as the empirical ones verified can be developed.

[4] From a more fundamental point of view, it is recommended an analysis of the instability of the liquid-vapor interface. Firstly, it is recommended to obtain visual observations of the interface, by photography or video, as it has been done in other systems. Then, the solution of the film boiling problem can be pursued coupled with the solution of the non-linear Kelvin-Helmoltz instability problem. In this way, characteristics of the interface such as the wavelength and amplitude can be determined and linked to the prediction of transition boiling heat fluxes.

Appendix A

I. Crank-Nicholson Finite Difference Equations of the Runout Table Model

1. Internal Nodes:

$$-1/2\,A_i^n T_{i-1}^{n+1} + (1+B_i^n)T_i^{n+1} - 1/2\,D_i^n T_{i+1}^{n+1} = 1/2\,A_i^n T_{i-1}^n + (1-B_i^n)T_i^n + 1/2\,D_i^n T_{i+1}^n + G_i^n$$

where

$$A_i^n = \frac{k_{i-1/2}^n}{(\rho Cp)_i^n}\frac{\Delta t}{(\Delta x)^2};\quad D_i^n = \frac{k_{i+1/2}^n}{(\rho Cp)_i^n}\frac{\Delta t}{(\Delta x)^2};\quad B_i^n = 1/2\left(A_i^n + D_i^n\right)$$

$$k_{i\pm 1/2}^n = 1/2\left(k_i^n + k_{i\pm 1}^n\right);\quad G_i^n = \frac{g_i \Delta t}{(\rho Cp)_i}$$

2. Top Node (node=0):

$$1/2\left(2/r_0^n + x_{t,0}^n + 2\right)T_0^{n+1} - T_1^{n+1} = 1/2\left(2/r_0^n - x_{t,0}^n - 2\right)T_0^n + T_1^n + x_{t,0}^n T_{w,0}^n + G_i^n$$

where

$$r_0^n = \frac{k_{1/2}^n}{(\rho Cp)_0^n}\frac{\Delta t}{(\Delta x)^2};\qquad x_{t,0}^n = \frac{2\Delta x h_{w,0}^n}{k_{1/2}^n};\quad G_0^n = \frac{g_0 \Delta t}{(\rho Cp)_0}\frac{1}{r_0^n}$$

3. Bottom Node (node=M):

$$-T_{M-1}^{n+1} + 1/2\left(2/r_M^n + x_{t,M}^n + 2\right)T_M^{n+1} = T_{M-1}^n + 1/2\left(2/r_M^n - x_{t,M}^n - 2\right)T_M^n + x_{t,M}^n T_{w,M}^n + G_M^n$$

where $\quad r_M^n = \dfrac{k_{M-1/2}^n}{(\rho Cp)_M^n}\dfrac{\Delta t}{(\Delta x)^2};\qquad x_{t,M}^n = \dfrac{2\Delta x h_{w,M}^n}{k_{M-1/2}^n};\quad G_M^n = \dfrac{g_M \Delta t}{(\rho Cp)_M}\dfrac{1}{r_M^n}$

Appendix B

Runout Table Mill Data

The development of the runout table model required validation with measurements from hot strip mill operations. The mill data presented in this work was obtained from eleven companies during the production of A36 and DQSK steels or for steels close to these chemistries. The chemical compositions of the A36 and DQSK steels used as reference for this work are presented in Table B.1.

Due to the confidential nature of the information obtained and used during the progress of this research, selected data is presented in this section with the name of the source companies deleted. Instead, the companies are designated as A, B, C, etc. to identify the individual sets of data.

The collection of the data was carried out with the cooperation of several companies. The model was developed as an interactive process, where personnel from the companies tested the computer model with their own mill information. Comments, recommendations and information was exchanged mainly by this interactive process. In most of the cases, the information was provided according to questionnaires provided to them to compile the information, and/or by the information introduced directly by users of the model. In a few cases, the data was taken directly from blue prints and engineering logs.

Runout Table Full-Scale Data.

A detailed compilation of the runout table top and bottom cooling configurations under study is presented in Table B.2 to Table B.9. Most of these cooling systems consist of water bars (axisymmetric jets) at both the top and bottom of the strip. It is also evident that there are important differences in the placement of the jet lines (the array of the nozzles across the width), and the distance between jet lines, which in practice markedly affects the cooling performance.

The data under the heading "Jet flow characteristics" was obtained by analysis of the data presented under the heading "Nozzle arrangement and characteristics". The jet velocity was calculated by the equations:

$$u_{nozzle} = \frac{Q_{nozzle}}{\left(\pi/4\, d^2_{nozzle}\right)} \qquad [B.1.1]$$

$$u_{nozzle} = \frac{Q_{nozzle}}{\left(w_{nozzle} L_{nozzle}\right)}$$

for water bars and curtains respectively. Given the effect of gravity, the water stream accelerates, so the velocity at impingement is different from that at the nozzle. Because of mass conservation, the diameter or the width of the jet changes according to the Bernoulli's equation, as follows:

$$u_{jet} = \left(u_n^{\,2} \pm 2gH_n\right)^{1/2}$$

$$d_{jet} = \left(\frac{u_n}{u_{jet}}\right)^{1/2} d_n \qquad \text{[B.1.2]}$$

$$w_{jet} = \left(\frac{u_n}{u_{jet}}\right) w_n$$

The impingement zones were calculated assuming that the strip motion has no effect on the pressure gradient caused by the impingement of the jet. According to the information presented in the literature review, the radius of the impingement zone of a water bar is $r = 1.3d_{jet}$, whereas the length (one side) of the impingement zone of a curtain is $x = 1.75w_{jet}$. In order to account for the 2-D nature of the nozzle arrangements, an interaction factor has been defined as the radio of the distance between nozzle centers minus the distance between impingement regions over the distance between nozzle centers. The closer to unity is the interaction factor, the more one-dimensional the arrangement behaves.

A summary of the range of operation of these cooling configurations is presented in Table B.10. It is interesting to note that the most typical impinging jet velocity at the top varies only from 5.5 to 6.5 m/s; only in a few cases operations is the velocity outside this range. The main reason for this is the fact that the top jet impingement velocity is controlled mainly by gravity. Another similarity was found for the common top nozzle diameter. Consequently, the associated impinging jet diameter are similar. However,

Table B.10 also shows that more variations exist in the type of bottom cooling employed.

The relevant processing data for the coils analyzed in this study are presented for each company in Table B.11 to Table B.18. Whenever possible the specific for a particular piece of steel (sample) is presented, and the sample number within the coil was included, to have an idea of the relative position along the length. When three sample numbers are given for a coil, they represent head-middle-tail conditions, except in few cases, where more focus was paid on variation within the middle samples.

The finishing mill exit temperature, $T_{initial}$, varies in most cases between 850 and 950°C during the production of strips and plates of gauges ranging from 1.8 to 16 mm. The initial strip speed into the runout table, Up_o, ranges from 2 to 18 m/s, while the acceleration in the runout table, **a**, varies from 0 to 0.16 m/s^2, and represent a small contributor in the overall speed of the strip. The coiling temperatures, T_{final}, are commonly within 540-740°C. However, under special circumstances such as air cooled A36 products, the coiling temperatures may be as high as 870°C. Generally, the range of coiling temperatures for the A36 is narrower since no special hardening by strain aging due to nitrogen in solution is desired, and typically they lie in the range of 650-690°C. The supplied water temperature may vary significantly from plant to plant, and it is usually from 15 to 35°C. The number of working jet lines, top and bottom jets, is probably the parameter that varies the most from plant to plant and, also increases with increasing strip speed, thickness and decreasing carbon content of the steel.

Table B.1: Chemical Composition of the A36 and DQSK steels

Steel	%C	%Mn	%P	%S	%Si	%Cu	%Ni	%Cr	%Al	%N
A36	0.17	0.74	0.009	0.008	0.012	0.016	0.010	0.019	0.040	0.0047
DQSK	0.038	0.30	0.010	0.008	0.009	0.015	0.025	0.033	0.040	0.0052

Table B.2: Top Cooling Configuration for Companies A, B, and C.

Company	**A**	**B**	**C**
Parameter			
Nozzle arrangement and characteristics			
Kind of nozzle	Pipe, circular	Pipe, circular	Pipe, circular
Nozzle diameter (m)	0.02	0.013	0.0186
Nozzle height (m)	1.75	1.92	2.17
Distance between nozzles across center-center (m)	0.048	0.051	0.068
Distance between nozzles (edge-edge)	0.028	0.038	0.049
Water flow rate per nozzle (l/sec)	0.359	0.315-0.630	0.501
Distance between jet lines (m)	0.46 and 0.92	0.15 and 2.74	0.457
Number of nozzles/jet line	70	40	31-32
Jet Flow characteristics			
Jet velocity at nozzle (m/s)	1.03	2.37-4.75	1.83
Impinging jet velocity (m/s)	5.95	6.58-7.76	6.78
Impinging jet diameter (m)	0.0074	0.0078-0.0101	0.0097
Impingement zone radius (m)	0.010	0.010-0.013	0.0126
Calculated reduction in jet diameter (%)	59	40-22	48
Distance between jets edge-edge (m)	0.041	0.043-0.041	0.0583
Distance between impingement regions edge-edge (m)	0.028	0.031-0.025	0.0428
Interaction Factor	0.417	0.392-0.510	0.371

Table B.3: Bottom Cooling Configuration for Companies A, B, and C.

Company	A	B	C
Parameter			
Nozzle arrangement and characteristics			
Kind of nozzle	Pipe, circular	Banks 1-2 (Pipe, circular) Banks 3-8 (Flat spray nozzle) d_{noz}=0.003m, d_{across}=0.41m, cone angle=80°, Q_{noz}=0.126 l/sec,	Pipe, circular
Nozzle diameter (m)	0.0095 (0.008)*	0.02	0.0104
Nozzle height (m)	-0.12	-0.15	-0.074
Nozzle angle (°)	5	5	15
Distance between nozzles across center-center (m)	0.049	0.041	0.025
Distance between nozzles (edge-edge)	0.041	0.021	0.015
Water flow rate per nozzle (l/sec)	0.178	0.630	0.161
Distance between jet lines (m)	0.46	0.92	0.46
Number of nozzles/jet line	68	12-13	80
Jet Flow characteristics			
Jet velocity at nozzle (m/s)	3.44**	2.01	2.05
Impinging jet velocity (m/s)	3.08	1.05	1.66
Impinging jet diameter (m)	0.0085	0.0277	0.011
Impingement zone radius (m)	0.011	0.036	0.014
Distance between jets edge-edge (m)	0.0405	0.0133	0.014
Distance between impingement regions edge-edge (m)	0.027	overlap	overlap
Interaction Factor	0.449	1.0	1.0

*The actual nozzle diameter may be the diameter of the nozzle minus two times the thickness of hardness deposits or the equivalent nozzle diameter that gives the flow rate and height of the jet observed in video recordings.

**Calculated to match flow rate, and jet height observed in video recordings.

Table B.4: Top Cooling Configuration for Companies D and E.

Company	D	E
Parameter		
Nozzle arrangement and characteristics		
Kind of nozzle	Slot, rectangular	Slot, rectangular
Nozzle length (m)	2.59	1.372
Nozzle width (m)	0.01	0.0064
Nozzle height (m)	1.22	1.372
Water flow rate per nozzle (l/sec)	50.4	23.34
Distance between jet lines (m)	2.74	3.20
Jet Flow characteristics		
Jet velocity at nozzle (m/s)	1.95	2.662
Impinging jet velocity (m/s)	5.27	5.83
Impinging jet width (m)	0.0037	0.003
Impingement zone length (one side) (m)	0.007	0.005
Calculated reduction in jet width (%)	63	53

Table B.5: Bottom Cooling Configuration for Companies D and E.

Company	D	E
Parameter		
Nozzle arrangement and characteristics		
Kind of nozzle	Slot, rectangular	Slot, rectangular
Nozzle length (m)	2.59	1.372
Nozzle width (m)	0.01 (0.006*)	0.0064 (0.004***)
Nozzle height (m)	-0.08	-0.09
Nozzle angle (°)	10	20
Water flow rate per nozzle (l/sec)	50.4	11.67
Distance between jet lines (m)	2.74	0.91
Jet Flow characteristics		
Jet velocity at nozzle (m/s)**	3.18	2.11
Impinging jet velocity (m/s)	2.92	1.64
Impinging jet width (m)	0.0065	0.0051
Impingement zone length (one side) (m)	0.011	0.009

*The actual nozzle width may be the width of the nozzle minus two times the thickness of hardness deposits or the equivalent nozzle width that gives the flow rate and height of the jet observed in video recordings.

**Calculated to match flow rate, and jet height observed.

***Estimated according to operator observations.

Table B.6: Top Cooling Configuration for Companies F, G and H.

Company	F	G	H
Parameter			
Nozzle arrangement and characteristics			
Kind of nozzle	Pipe, circular	Pipe, circular	Pipe, circular
Nozzle diameter (m)	0.0186	0.02	0.03
Nozzle height (m)	2.49	1.47	1.79
Distance between nozzles across center-center (m)	0.0508	0.070	0.076
Distance between nozzles (edge-edge)	0.032	0.050	0.046
Water flow rate per nozzle (l/sec)	1.34	0.380	0.784
Distance between jet lines (m)	0.46	0.61	0.07 and 1.37
Number of nozzles/jet line	40	28	25-26
Jet Flow characteristics			
Jet velocity at nozzle (m/s)	4.93	1.21	1.11
Impinging jet velocity (m/s)	8.55	5.51	6.03
Impinging jet diameter (m)	0.0141	0.0094	0.0129
Impingement zone radius (m)	0.018	0.012	0.017
Calculated reduction in jet diameter (%)	24	53	57
Distance between jets edge-edge (m)	0.037	0.061	0.063
Distance between impingement regions edge-edge (m)	0.015	0.046	0.042
Interaction Factor	0.706	0.343	0.447

Table B.7: Bottom Cooling Configuration for Companies F, G and H.

Company	F	G	H
Parameter			
Nozzle arrangement and characteristics			
Kind of nozzle	Pipe, circular	Pipe, circular	Slot, rectangular
Nozzle diameter (m)	0.0102	0.02	Width = 0.0095 (0.0059*), length = 2.00
Nozzle height (m)	-0.051	-0.27	-0.10
Nozzle angle (°)	10	18	15
Distance between nozzles across center-center (m)	0.0226	0.238/0.107***	-
Distance between nozzles (edge-edge)	0.012	0.218/0.087	-
Water flow rate per nozzle (l/sec)	0.77	0.844/0.868	19.6 and 39.2
Distance between jet lines (m)	0.457	0.63	1.44
Number of nozzles/jet line	90	8/17-18	1
Jet Flow characteristics			
Jet velocity at nozzle (m/s)	9.80	2.69/ 2.76	1.65**/3.32
Impinging jet velocity (m/s)	9.75	1.39 / 1.52	0.87/3.01
Impinging jet diameter (m)	0.010	0.028 / 0.027	Width=0.011/0.0065
Impingement zone radius (m)	0.013	0.036 / 0.035	length (one side)= 0.019/0.011
Distance between jets edge-edge (m)	0.012	0.08	-
Distance between impingement regions edge-edge (m)	overlap	0.037	-
Interaction Factor	1.0	0.654	1.0

*The actual nozzle width may be the width of the nozzle minus two times the thickness of hardness deposits or the equivalent nozzle width that gives the flow rate and height of the jet observed in video recordings.
**Calculated to match flow rate, and jet height observed.

Table B.8: Top Cooling Configuration for Companies I and J.

Company	I	J
Parameter		
Nozzle arrangement and characteristics		
Kind of nozzle	Pipe, circular	Pipe, circular
Nozzle diameter (m)	0.0180	0.0186
Nozzle height (m)	1.6	1.98
Distance between nozzles across center-center (m)	0.046	0.051
Distance between nozzles (edge-edge)	0.028	0.032
Water flow rate per nozzle (l/sec)	0.320	0.501
Distance between jet lines (m)	0.60	0.457
Number of nozzles/jet line	30	31-32
Jet Flow characteristics		
Jet velocity at nozzle (m/s)	1.26	1.83
Impinging jet velocity (m/s)	5.74	6.50
Impinging jet diameter (m)	0.0084	0.0099
Impingement zone radius (m)	0.011	0.0128m
Calculated reduction in jet diameter (%)	53	47
Distance between jets edge-edge (m)	0.038	0.041
Distance between impingement regions edge-edge (m)	0.024	0.0254
Interaction Factor	0.478	0.502

Table B.9: Bottom Cooling Configuration for Companies I and J.

Company	I	J
Parameter		
Nozzle arrangement and characteristics		
Kind of nozzle	Pipe, circular	Slot, rectangular
Nozzle diameter (m)	0.012	Width=0.0064, Length=1.575
Nozzle height (m)	-0.02*	-0.10
Nozzle angle (°)	5	8
Distance between nozzles across center-center (m)	0.046	-
Distance between nozzles (edge-edge)	0.034	-
Water flow rate per nozzle (l/sec)	0.183	25.236
Distance between jet lines (m)	0.30	0.91
Number of nozzles/jet line	30	1
Jet Flow characteristics		
Jet velocity at nozzle (m/s)	1.62**	2.50
Impinging jet velocity (m/s)	1.49	2.07
Impinging jet diameter (m)	0.0125	width, 0.0053
Impingement zone radius (m)	0.016	Length (one side)=0.0093
Distance between jets edge-edge (m)	0.034	-
Distance between impingement regions edge-edge (m)	0.014	-
Interaction Factor	0.696	1.0

Table B.10: Summary of the Jet Cooling operating conditions.

Operation Parameter	Range	Most Typical
Top		
Jet velocity at nozzle (m/s)	1.03-4.93	1.0-2.0
Jet velocity at impingement (m/s)	5.27-8.55	5.5-6.5
Nozzle Diameter (m)	0.01-0.03	0.019
Jet width (curtains) (m)	0.0064-0.010	0.0064-0.01
Impinging Jet diameter (m)	0.0074-0.0141	0.0074-0.010
Impinging Jet width (curtains) (m)	0.003-0.0037	0.003-0.0037
Bottom		
Jet velocity at nozzle (m/s)	1.26-9.8	2.0-3.5
Jet velocity at impingement (m/s)	0.06-9.75	1.0-3.0
Nozzle diameter (m)	0.008-0.020	0.0095-0.012
Jet width (curtains) (m)	0.0064-0.010	0.0064-0.010
Impinging Jet diameter (m)	0.0085-0.028	0.01-0.02

Table B.11: Data of the production of an A36 steel for Company A.

A36	$T_{initial}$	Thickness	Up_o	a	T_{water}	T_{final}	Top Jets	Bottom Jets
Coil ID	°C	mm	m/s	m/s^2	°C	°C		
c500486	932	4.648	5.04	0.00	29.4	677	24	3
c500494	939	4.699	5.06	0.00	29.4	671	24	3
c500500	934	4.699	5.01	0.00	29.4	681	24	3
c500487	934	4.648	5.02	0.00	29.4	683	24	3
c999274	946	6.858	5.49	0.00	29.4	681	52	7
c999280	959	6.858	5.46	0.00	29.4	687	52	7
c999279	966	6.858	5.51	0.00	29.4	686	56	8
c998396	972	9.389	3.25	0.00	29.4	667		
c999269	961	9.601	3.33	0.00	29.4	672		
c998383	934	9.423	3.73	0.00	29.4	681	52	7
c998380	933	9.423	3.67	0.00	29.4	679	52	7
c998385	928	9.423	3.59	0.00	29.4	680	52	7
c998402	1001	9.449	3.34	0.00	29.4	674	52	7
c998382	943	9.423	3.72	0.00	29.4	681	56	8
c998384	933	9.423	3.64	0.00	29.4	681	56	8
c998403	1011	9.449	3.42	0.00	29.4	688	56	8
c998381	972	9.398	3.65	0.00	29.4	683	60	9
c998393	960	9.423	3.68	0.00	29.4	630	64	9
c998394	998	9.423	3.59	0.00	29.4	670	64	9
c999993	927	12.700	2.41	0.00	29.4	672	48	7
c999988	962	12.624	2.43	0.00	29.4	668		
c500005	969	12.700	2.42	0.00	29.4	672	52	7
c500002	958	12.700	2.42	0.00	29.4	666	52	7
c500010	976	12.700	2.42	0.00	29.4	683	52	7
c500011	969	12.700	2.42	0.00	29.4	673	52	7
c500022	965	12.700	2.45	0.00	29.4	663	68	10
c500021	963	12.700	2.44	0.00	29.4	664	68	10
c500029	959	16.043	1.99	0.00	29.4	672		
c500043	940	15.875	1.99	0.00	29.4	679	64	9
c500030	974	15.875	2.00	0.00	29.4	677	64	9
c500039	972	16.027	1.99	0.00	29.4	673	64	9

Table B.12: Processing data of a DQSK and A36 steels for Companies B, D, H, I and J.

A36	$T_{initial}$	Thickness	Up_o	a	T_{water}	T_{final}	Top Jets	Bottom Jets
Coil ID	°C	mm	m/s	m/s^2	°C	°C		
Company B								
GLD1	933	4.29	8.30	0.04	15.5	683	25	5
Company D								
C1	840	9.61	1.87	0	21.7	704	5	1
Company H								
BDF	915	10.64	0.00	0.00	37.7	680	52	2
DMV	919	7.06	0.00	0.00	27.2	669	24	1
CNZ	915	6.55	0.00	0.00	35.0	681	40	2
FPZ	911	7.06	0.00	0.00	27.2	686	30	1
FNB	911	6.55	0.00	0.00	30.4	687	34	1
Company I								
c140753	884	2.52	7	0.00	36	540	28	5
c140751	912	2.54	6.95	0.00	36	630	27	5
Company J								
Coil1	850	1.665	9.17	0.037	21.6	685	2	
Coil2	900	4.65	6.23	0.057	24.0	540	54	2
Coil3	826	9.97	2.78	0.04	24.7	624	54	2
Coil4	896	4.65	6.67	0.052	29.1	572	78	3

Table B.13: Data of the production of a DQSK steel for Company C.

DQSK	Smp	$T_{initial}$	Gauge	Up_o	a	T_{water}	Up_f	T_{final}	top jet		Bottom jet	
Coil ID		°C	mm	m/s	m/s^2	°C	m/s	°C	main	v	main	v
907518	2	885	3.134	9.37	0.06	23.4	9.99	697	23	2	25	
	56	878	3.175	11.32	0.10		12.13	674	34	2	37	
	111	892	3.162	13.32	0.00		13.32	665	47	2	51	
907519	3	891	3.218	9.37	0.07	23.3	10.07	662	24	2	27	
	60	883	3.172	11.54	0.10		12.34	678	37	2	40	
	116	888	3.175	13.42	0.00		13.40	669	47	2	52	
907618	2	857	2.512	10.33	0.07	26.6	10.94	577	35	2	40	
	4	864	2.535	10.31	0.08		11.03	553	35	2	40	
	80	879	2.527	13.80	0.00		13.78	553	54	6	63	
	158	883	2.563	13.81	0.00		13.81	557	54	6	60	
907619	2	854	2.512	10.57	0.07	26.6	11.19	566	36	2	42	
	80	869	2.530	13.99	0.00		13.98	558	54	6	63	
	159	864	2.522	13.98	0.00		13.98	602	53	6	58	
907620	2	858	2.515	10.43	0.07	26.6	11.01	583	35	2	41	
	77	871	2.550	14.01	0.00		14.03	556	54	6	63	
	152	875	2.545	14.01	0.00		14.03	570	54	6	60	
907927	2	911	4.260	7.26	0.06	24.2	7.97	648	31	2	33	
	45	889	4.275	8.84	0.07		9.51	652	42	2	46	
	87	906	4.280	10.22	0.00		10.22	640	54	6	61	
907928	2	908	4.277	7.30	0.06	24.2	7.97	646	31	2	33	
	45	887	4.270	8.83	0.07		9.52	649	42	3	45	
	87	918	4.293	10.02	-0.31		6.56	648	54	6	62	
907929	2	906	4.242	7.29	0.06	24.2	7.97	647	30	2	33	
	42	893	4.252	8.70	0.07		9.39	653	42	2	46	
	82	916	4.270	10.04	0.00		10.06	641	54	6	62	
907968	2	864	2.172	10.41	0.08	24.2	11.08	662	21	2	23	
	77	893	2.187	14.05	0.16		15.08	643	37	3	41	
	152	921	2.200	17.13	0.00		17.16	636	51	0	56	
908209	2	897	3.401	8.85	0.07	24.6	9.54	616	43	2	46	
	47	888	3.434	10.46	0.01		10.53	559	54	6	60	
	93	878	3.404	10.52	0.00		10.53	546	52	6	59	
908348	2	911	3.602	8.96	0.07	24.1	9.64	686	27	2	29	
	45	903	3.548	10.46	0.08		11.19	682	38	2	42	
	89	918	3.564	11.56	-0.01		11.50	672	49	1	53	
908418	2	879	4.856	6.25	0.03	22.6	6.73	628	26	2	28	
	38	864	4.874	7.22	0.06		7.96	630	33	2	36	
	75	891	4.882	8.54	0.00		8.53	637	47	2	51	
908419	2	887	4.887	6.26	0.03	22.6	6.74	633	27	2	29	
	38	879	4.879	7.18	0.06		7.96	628	35	2	38	
	74	891	4.879	8.52	0.00		8.55	631	47	3	51	
301978	55	862	2.525	12.68	0.11	17.9	13.48	569	48	2	52	
	63	863	2.535	13.02	0.11		13.82	554	50	2	54	
	73	866	2.537	13.38	0.06		13.80	561	52	2	56	
301979	55	861	2.532	13.03	0.11	18.0	13.80	559	50	2	54	
	61	863	2.537	13.20	0.09		13.83	553	51	2	55	
	73	862	2.532	13.67	0.02		13.83	566	52	2	57	

Table B.14: Processing Data of an A36 steel for Company C.

A36	Smp	$T_{initial}$	Gauge	Up_o	a	T_{water}	Up_f	T_{final}	top jet		Bottom jet	
Coil ID		°C	mm	m/s	m/s^2	°C	m/s	°C	main	v	main	v
907272	2	875	2.558	10.09	0.07	26.5	10.68	662	25	2	27	
	37	893	2.583	11.42	0.16		12.67	656	33	2	36	
	71	903	2.593	13.09	0.01		13.15	654	42	3	46	
907454	2	896	4.265	7.26	0.05	22.8	7.93	657	27	2	30	
	21	890	4.171	7.88	0.07		8.64	658	31	2	33	
	41	895	4.161	8.64	0.02		8.82	658	36	2	39	
908390	2	939	9.774	4.12	0.02	23.0	4.64	677	34	2	37	
	17	932	9.954	4.51	0.03		5.01	667	39	2	42	
	32	951	9.957	4.88	0.01		5.01	669	45	3	49	
908391	2	930	7.940	4.63	0.03	23.0	5.12	677	29	2	31	
	21	909	7.945	5.09	0.03		5.63	667	32	2	35	
	41	919	7.955	5.61	0.01		5.82	662	41	2	45	
908440	2	912	5.304	6.22	0.04	22.4	6.76	657	28	2	32	
	30	887	5.319	6.95	0.06		7.68	656	33	2	36	
	57	894	5.324	7.95	0.01		8.08	656	43	2	46	
908495	2	927	4.529	7.25	0.06	22.3	7.95	651	37	2	40	
	49	927	4.610	8.93	0.07		9.63	656	48	2	55	
	96	930	4.615	9.85	0.00		9.86	645	54	6	60	
913581	2	899	7.874	4.58	0.03	20.4	5.09	669	24	2	26	
	15	891	7.955	4.94	0.02		5.22	661	28	2	31	
	28	896	7.953	5.22	0.00		5.22	674	30	1	33	
913582	2	901	7.945	4.62	0.02	20.4	5.10	672	24	2	26	
	15	907	7.932	4.92	0.02		5.23	667	28	2	30	
	28	894	7.965	5.23	0.00		5.23	665	29	2	31	
913583	2	897	7.976	4.69	0.02	20.6	5.09	679	23	2	25	
	15	895	7.943	4.91	0.02		5.24	672	26	2	29	
	28	892	7.935	5.24	0.00		5.24	677	28	2	31	
914699	2	911	5.525	6.18	0.02	24.8	6.53	660	30	2	32	
	16	919	5.545	6.43	0.02		6.73	657	33	2	36	
	30	916	5.537	6.64	0.01		6.73	663	35	2	38	
934848	2	936	9.479	4.12	0.02	24.8	4.62	667	31	2	33	
	18	913	9.520	4.51	0.02		4.92	658	34	1	37	
	35	921	9.538	4.92	0.00		4.92	660	39	1	43	
162331	19	887	6.043	6.95	0.02	24.9	7.21	664	37	2	40	
163634	27	886	8.969	5.18	0.06	27.7	6.21	676	39	1	44	
163715	25	881	4.757	7.68	0.06	27.7	8.38	679	29	2	32	

Table B.15: Processing information of a DQSK steel for Company E.

DQSK	$T_{initial}$	Thickness	Up_o	a	T_{water}	T_{final}	Top Jets	Bottom Jets
Coil ID	°C	mm	m/s	m/s^2	°C	°C		
o729841	909	3.55	9.17	0.09	26.6	736	18	3
o738486	889	2.6	12.68	0.16	22.2	718	18	3
o738491	899	2.6	12.68	0.16	22.2	717	18	3
o738492	892	2.6	15.32	0.16	22.2	718	18	3
o738975	897	2.59	15.08	0.16	22.2	720	18	3
o739719	892	3.2	10.00	0.12	21.1	724	18	3
o739720	888	3.2	10.03	0.12	21.1	724	18	3
o739721	903	3.3	9.90	0.12	21.1	721	18	3
o739722	906	3.33	9.77	0.12	21.1	721	18	3
o742987	897	4.5	7.15	0.12	23.4	735	18	3
o745391	881	2.4	13.53	0.15	26.7	721	18	3
o745396	874	1.8	18.05	0.15	26.6	722	18	3
o745397	876	1.8	18.05	0.15	26.6	721	18	3
o745558	893	3.27	9.92	0.12	26.6	709	18	3

Table B.16: Processing information of a DQSK steel for Company F.

DQSK	$T_{initial}$	Thickness	Up_o	a	T_{water}	T_{final}	Top Jets	Bottom Jets
Coil ID	°C	mm	m/s	m/s^2	°C	°C		
c1	960	3.250	10.08	0.00	21.7	739	16	1
c2	950	3.500	11.32	0.00	21.7	701	42	5
c3	958	3.410	10.08	0.00	21.7	778	8	
c4	944	3.260	10.05	0.00	21.7	762	8	
c5	950	3.510	11.18	0.00	21.7	709	32	4
c6	956	3.430	11.75	0.00	21.7	783	8	1
c7	940	3.250	10.08	0.00	21.7	658	44	5
c8	951	3.460	11.23	0.00	21.7	635	58	7
c9	956	3.430	11.75	0.00	21.7	669	58	6
c10	942	3.220	10.08	0.00	21.7	664	40	5
c11	952	3.470	11.23	0.00	21.7	642	58	7
c12	960	3.360	11.80	0.00	21.7	680	48	6
c13	949	3.180	10.12	0.00	21.7	687	60	5
c14	949	3.530	11.22	0.00	21.7	626	68	6
c15	956	3.430	11.82	0.00	21.7	676	64	5

Table B.17: Processing data of air cooled A36 steel for Company G.

A36	Initial Temperature	Thickness	Initial Speed	Acceleration	Exit Temperature
Coil ID	°C	mm	m/s	m/s^2	°C
Cair1	910	4.724	4.19	0	790
Cair2	887	4.724	4.19	0	771
Cair3	870	4.724	4.19	0	760
Cair4	850	4.724	4.19	0	752
Cair5	840	4.724	4.19	0	747
Cair6	830	4.724	4.19	0	743
Cair7	820	4.724	4.19	0	740
Cair8	810	4.724	4.19	0	742
Cair9	805	4.724	4.19	0	740
Cair10	790	4.724	4.19	0	738
Cair11	784	4.724	4.19	0	734
Cair12	950	9.525	4	0	871
Cair13	940	9.525	4	0	862
Cair14	931	9.525	4	0	857
Cair15	923	9.525	4	0	851
Cair16	918	9.525	4	0	843
Cair17	905	9.525	4	0	831
Cair18	899	9.525	4	0	827
Cair19	890	9.525	4	0	819
Cair20	880	9.525	4	0	812
Cair21	869	9.525	4	0	800
Cair22	861	9.525	4	0	793
Cair23	858	9.525	4	0	790
Cair24	853	9.525	4	0	786
Cair25	965	12.7	3.7	0	899
Cair26	945	12.7	3.7	0	872
Cair27	923	12.7	3.7	0	857
Cair28	900	12.7	3.7	0	835
Cair29	874	12.7	3.7	0	820

Table B.18: Processing Data of an A36 steel for Company G.

A36	$T_{initial}$	Thickness	Up_o	a	T_{water}	T_{final}	Top Jets	Bottom Jets
Coil ID	°C	mm	m/s	m/s^2	°C	°C		
Cnew1	842	9.550	3.14	0.00	19.4	744	6	0
Cnew2	838	9.525	3.13	0.00	19.4	743	6	0
Cnew3	847	9.525	3.13	0.00	19.4	769	0	9
Cnew4	842	9.525	3.14	0.00	19.4	771	0	9
Cnew5	856	9.500	3.14	0.00	19.4	767	0	4
Cnew6	857	9.500	3.14	0.00	19.4	767	0	4
Cnew7	849	9.525	3.13	0.00	19.4	765	0	4
Cnew8	853	9.500	3.15	0.00	19.4	768	6	0
Cnew9	854	9.500	3.13	0.00	19.4	764	0	8
Cnew10	857	9.525	3.13	0.00	19.4	772	0	4
Cnew11	854	9.525	3.16	0.00	19.4	772	0	4
Cnew12	855	9.525	3.16	0.00	19.4	773	0	4
Cnew13	845	9.525	3.13	0.00	19.4	771	0	4
Cnew14	851	9.525	3.16	0.00	19.4	754	0	4
Cnew15	801	6.350	4.17	0.00	20.6	752	0	9
Cnew16	810	6.350	4.14	0.00	21.1	756	0	9
Cnew17	807	6.350	4.17	0.00	21.1	751	0	9
Cnew18	823	6.350	4.17	0.00	20.6	756	0	4
Cnew19	818	6.350	4.15	0.00	20.6	757	0	4
Cnew20	804	6.350	4.18	0.00	20.6	749	0	4

Appendix C

Austenite Decomposition Kinetics

The model described in this section was developed by researchers of The Centre for Metallurgical Process Engineering, UBC. This consists on: [a] Start temperature of the austenite to ferrite transformation, [b] Initiation of pearlite formation, and [c] Kinetics of ferrite and pearlite growth.

[a] Start temperature of the austenite to ferrite transformation.

Early growth of ferrite is described by:

$$\frac{dR}{dt} = D_C \frac{c_\gamma - c^o}{c_\gamma - c_\alpha} \frac{1}{R} \qquad [C.1]$$

solved with the initial condition

$$R(T_N) = 0$$

by finite differences using 10 time steps within each runout table model time step. T_{start} is reached when:

$$R \frac{c_\gamma - c^o}{c_* - c_\alpha} = \frac{d_\gamma}{\sqrt{2.1}} \qquad [C.2]$$

where

$$c_* = \left\{ 1.08 + \frac{1.7}{d_\gamma} + 0.2 \exp\left[-0.0002 * \left(T_N - T \right)^{2.2} \right] \right\} c^o; \quad \text{(A36 steel)} \qquad [C.3]$$

$$c_* = \left\{ 1.147 + \frac{9.126}{d_\gamma} + 0.15 \exp\left[-0.000292 * \left(T_N - T \right)^{2.2} \right] \right\} c^o; \quad \text{(DQSK steel)} \qquad [C.4]$$

$$D_C = D_{0C} e^{-q} \qquad [C.5]$$

$$q = \left(17767 - 26436c^o\right)\left(1/T - 2.221x10^{-4}\right)$$

$$D_{0C} = 4.53x10^5 \left\{1 + c^o(1 - c^o) * 8339.9/T\right\}$$

$$T_N = 1033K;\ \text{(A36)} \qquad [C.6]$$

$$T_N = 1116K;\ \text{(DQSK)} \qquad [C.7]$$

$$c^o = 0.00793;\ \text{(A36)}$$

$$c^o = 0.00177;\ \text{(DQSK)}$$

$$c_\alpha = \alpha_0 x10^{-3} - \alpha_1 x10^{-6} T \qquad [C.8]$$

$$\alpha_0 = 6.4668 - 1.5852(\%Mn) + 0.9340(\%C) + 1.3612(\%C)(\%Mn)$$

$$\alpha_1 = 5.4812 - 1.2718(\%Mn) + 0.9288(\%C) + 0.8839(\%C)(\%Mn)$$

$$c_\gamma = \gamma_0 - \gamma_1 x10^{-3} T + \alpha_2 x10^{-7} T^2 \qquad [C.9]$$

$$\gamma_0 = 1.1417 - 0.0893(\%Mn) + 2.3999(\%C) - 4.8483(\%C)^2 + 0.5185(\%C)(\%Mn) - 4.117(\%C)^2(\%Mn)$$

$$\gamma_1 = 1.8764 - 0.1054(\%Mn) + 4.5524(\%C) - 9.0994(\%C)^2 + 0.9129(\%C)(\%Mn) - 7.9834(\%C)^2(\%Mn)$$

$$\gamma_2 = 7.7013 - 0.2571(\%Mn) + 21.5056(\%C) - 42.4328(\%C)^2 + 4.2027(\%C)(\%Mn) - 39.1015(\%C)^2(\%Mn)$$

and all the temperatures are in K.

[b] Initiation of pearlite formation.

The austenite to pearlite transformation is considered for the A36 steel, since in the DQSK steel the volumetric fraction of this constituent is negligible.

Pearlite starts to form when the α-γ interface velocity is less than the critical velocity for cementite nucleation. This critical velocity is given by:

$$v_{\alpha\beta} = 0.164 T c_I D_C \left\{ ln\left(\frac{c_I}{c_P}\right)\right\}^2 \quad [C.10]$$

where

$$c_I = I_0 - I_1 x10^{-3} T + I_2 x10^{-6} T^2 \quad [C.11]$$

$$I_0 = 1.171 - 0.5122E - 25.5E^2$$

$$I_1 = 1.962 - 0.654E - 43.85E^2$$

$$I_2 = 0.822 - 0.1925E - 18.82E^2$$

$$D_C = D_{0C} e^{-q} \quad [C.12]$$

$$q = \left(17767 - 26436 c_I\right)\left(1/T - 2.221x10^{-4}\right)$$

$$D_{0C} = 4.53x10^5 \left\{1 + c_I (1 - c_I) * 8339.9 / T\right\}$$

$$c_P = 4.65391x10^{-2}\left(3.40334x10^{-4} T_C + 3.678037x10^{-7} T_C{}^2 + 8.357222x10^{-10} T_C{}^3\right) \quad [C.13]$$

$$T_C = T - 273$$

$$T_{AE3} = 1097K$$

T is in K

In the runout table model calculations, the velocity of the α-γ interface is carried out by:

$$\frac{dR_{\alpha,t}}{dt} = \left\{ \left(1 - F_{\alpha,t+\Delta t}\right)^{-2/3} \frac{(F_{\alpha,t+\Delta t} - F_{\alpha,t})}{\Delta t} \frac{d_\gamma}{6} \right\} \qquad [C.14]$$

[c] Kinetics of ferrite and pearlite growth.

The kinetics of the austenite decomposition is described by:

$$F_{i,t+\Delta t} = F_{eq,i} \left\{ 1 - \exp\left[-b_i\left(T_{t+\Delta t}\right)\left[t_v + \Delta t\right]^{n_i} \right] \right\} \qquad [C.15]$$

$$t_v = \left[\frac{\ln\left(1 - F_{i,t} / F_{eq,i}\right)}{-b_i\left(T_{t+\Delta t}\right)} \right]^{1/n_i} \qquad [C.16]$$

and the heat of transformation is given by:

$$g = \rho_s H_t \frac{\partial F}{\partial t} \qquad [C.17]$$

where in the case of the austenite to ferrite transformation:

$$\ln b_\alpha = \frac{(3.96 + 0.22 d_\gamma)}{100}\left(T_{AE3} - T\right) - (5.35 + 0.66 d_\gamma)\,; \text{ (A36 steel)} \qquad [C.18]$$

$$\text{if } T < T_{\min} \text{ then } b_\alpha = b_\alpha(T_{\min})$$

$$T_{min} = 655^o C$$

$$ln b_\alpha = \frac{(2.54 + 0.00597 d_\gamma)}{100}\left(T_{AE3} - T\right) - (2.15 + 0.0234 d_\gamma)\,; \text{ (DQSK steel)} \qquad [C.19]$$

$$T_{AE3} = 842.0. - 150.3(\%C) + 216.0(0.765 - (\%C))^{4.26} - (37.6586 + 44.871(\%C) - 57.8658\sqrt{(\%C)})(\%Mn)$$

$$F_{eq,\alpha} = \frac{c_\gamma - c^o}{c_\gamma - c_\alpha} \qquad [C.20]$$

$$c_\gamma == 1.171 - 1.962x10^{-3}\,T + 0.822x10^{-6}\,T^2;\ \text{(A36 steel)}$$

$$c_\alpha = (55.7428 - .047651T)x10^{-4};\ \text{(DQSK steel)}$$

c_α and c_γ for DQSK are calculated by Equations [C.8] and [C.9]. For the austenite to pearlite transformation:

$$\ln b_p = z - 0.0154T_C$$

$$z = 9.372 + (8.453 - 9.372)/(92 - 46) * (d_\gamma - 46)$$

$$n_\alpha = n_p = 0.9$$

$$F_{eq,p} = 1 - F_{\alpha,t}$$